

Technische Universität München

Ingenieur fakultät Bau Geo Umwelt

Lehrstuhl für Astronomische und Physikalische Geodäsie

**Spectral Solutions to the Topographic Potential
in the context of
High-Resolution Global Gravity Field Modelling**

Moritz Rexer

Vollständiger Abdruck der von der Ingenieur fakultät Bau Geo Umwelt der Technischen Universität München zur Erlangung des akademischen Grades eines

Doktor-Ingenieurs (Dr.-Ing.)

genehmigten Dissertation.

Vorsitzender: Univ.-Prof. Dr.rer.nat T. Kolbe

Prüfer der Dissertation: 1. Hans-Fischer-Fellow Dr.-Ing. C. Hirt
2. Univ.-Prof. Dr.techn. R. Pail
3. Prof. Dr.-Ing. P. Novak, University of West Bohemia

Die Dissertation wurde am 08.03.2017 bei der Technischen Universität München eingereicht und durch die Ingenieur fakultät Bau Geo Umwelt am 19.05.2017 angenommen.

Zusammenfassung

Globale Schwerefeldmodelle sind fundamentale Informationsquellen in der Geodäsie und Geophysik, und relevant für eine Reihe von Anwendungen in unterschiedlichen Disziplinen, wie z.B. Ozeanographie oder Luft- und Raumfahrt. Die vorliegende Dissertation untersucht, in welchem Maße das topographische Potential (TP) zur Verbesserung globaler Schwerefeldmodelle im kurzwelligen Bereich, d.h. bis zur räumlichen Auflösung herkömmlicher Modelle (~ 10 km) und darüber hinaus, beitragen kann. Dabei werden ausschliesslich spektrale Vorwärtsmodellierungsmethoden, die auf sphärisch-harmonischer Reihenentwicklung beruhen, für die Berechnung des TPs unter Einbindung aktueller digitaler Höheninformation herangezogen. Die spektrale Analyse höchstauflöster kontinentaler Schwerefeldkarten aus topographischer Vorwärtsmodellierung – kondensiert in ein neues empirisches Gradvarianz-Modell bis Grad 90,000 – zeigt, dass signifikante Schweresignale in diesem spektralen Bereich existieren. Dieses Ergebnis rechtfertigt das Ziel der Arbeit, die kurzwelligen spektralen Bestandteile des Schwerefelds, die aus der Nahfeldanziehung der topographischen Massen resultieren, global zu modellieren. Zu diesem Zweck wird eine umfassende Auswahl an verschiedenen spektralen Vorwärtsmodellierungsansätzen verglichen, die der Berechnung sphärisch-harmonischer Kugelfunktionskoeffizienten der unkompensierten gravitativen Nahfeldanziehung der topographischen Massen dienen. Bestehende strenge und effiziente Ansätze unter Verwendung von einer oder mehrerer Masseschichten werden untersucht und angepasst, z.B. durch arithmetische Erweiterung und Parallelisierung der Algorithmen, um Berechnungen bis zu ultra-hohen Graden zu realisieren. In diesem Zusammenhang wird eine neue spektrale Methode hergeleitet, die es ermöglicht, das TP mehrerer Masseschichten in ellipsoidischer Approximation zu bestimmen. Dabei wird die Integration auf ein abgeplattetes Rotationsellipsoid bezogen. Die Methode führt zum ellipsoidisch-topographischen Potential (ETP), welches im Gegensatz zum häufig verwendeten sphärisch-topographischen Potential (STP) sphärische Approximationen vermeidet. Alle Methoden werden mit einem neu zusammengesetzten Massenmodell mit einer Auflösung von einer Bogenminute (Earth2014), welches die Grenzflächen zur Definition der Masseschichten für festes Krustengestein, Ozeane, größere Süßgewässer und polare Eisschilde bereitstellt, bis zu den Graden 5,400 und 21,600 untersucht. Eine der zentralen unter mehreren Erkenntnissen dieses Experiments ist, dass die spektrale Vorwärtsmodellierung mit den effizienten Ansätzen in der hier gewählten Implementierung (double-precision Umgebung) zu sphärisch-harmonischen Graden der Größenordnung von etwa 10,800 sinnvoll ist. Hauptgrund für diese Beschränkung ist der enorme Rechenaufwand, der mit der vollen Konvergenz der dabei auftretenden Binominalreihen zusammenhängt. Für diese Auflösung werden z.B. $k_{max} = 46$ und $j_{max} = 94$ Binominalterme der k - und j -Reihe benötigt. Zusätzlich wird für die Potenzierung der oberen und unteren Grenzfunktionen der Masseschichten bis zur Potenz k_{max} eine Überabtastung benötigt, um Aliasing zu vermeiden. Dies kann zu extrem großen Gittern führen, die nur mit massiver Parallelisierung sphärisch-harmonisch analysiert werden können. Letzteres ist der zeitkritischste Prozess der spektralen Vorwärtsmodellierung, welcher in dieser Arbeit mit Hilfe effizienter und exakter Quadratur-Techniken gelöst wird. Auf kurzen Skalen ($2160 < n \leq 5480$) führt die sphärische Approximation lokal über gebirgigem Gelände zu Fehlern von einigen mGal Amplitude (~ 0.4 mGal globaler RMS), weshalb die ETP Modellierung zur allgemeinen Praxis werden, und die rein sphärischen Ansätze ersetzen sollte. Der Fehler, der durch das Konzept der rock-equivalent-topography (RET) in der

Einzelschicht-Modellierung entsteht, liegt im kurzwelligen Bereich (< 10 km) bei etwa ~ 0.5 mGal (globaler RMS). Über kontinentalem und maritimen küstennahem Gebiet ist der RET-Effekt in diesem Auflösungsbereich vernachlässigbar klein, deshalb scheint eine Modellierung mit mehreren Masseschichten nur über großen bathymetrischen Massen oder tiefen Ozeangraben gerechtfertigt. Dieses Erkenntnis macht die rechentechnisch weniger aufwendigere Einzelschicht-Modellierung basierend auf dem RET-Konzept zu einer attraktiven Methode für eine hochauflösende globale Modellierung über Landflächen und im Küstenbereich, was durch das rein additive Konvergenzverhalten, welches einen frühzeitigen Abbruch der k -Reihe erlaubt, bekräftigt wird. Bereits eine einfache Kombination mit herkömmlichen beobachtungsbasierten Schwerefeldmodellen (GOCO05s und EGM2008) zeigt, dass das kurzwellige gravitative Signal der ETP-Modelle bis Grad 5480 die Übereinstimmung zu gravimetrischen Kontroll-Messpunkten (KMP) um ~ 6 bis ~ 46 % verbessern kann. Die Verwendung von über 1 Million KMP über unterschiedlichsten Regionen der Erde erlauben robuste und weit differenzierte Aussagen. Mit aufwendigeren Kombinationstechniken, z.B. durch Einführung der ETP-Modelle als Vorinformation oder mit allgemeinen Ausgleichungsansätzen, sind durch die Möglichkeit einer regionalen Gewichtung bessere Ergebnisse zu erwarten. Problematisch für letzteres ist der damit verbundene enorme Rechenaufwand und eine fehlende stochastische Modellierung der hier verwendeten und entwickelten Methoden.

Abstract

Global gravity field models are fundamental resources in geodesy and geophysics and required for a range of applications in different fields, such as aeronautics/astronautics and oceanography. The dissertation investigates to which extent the topographic potential (TP) – based on spectral spherical harmonic forward modelling techniques – together with up-to-date topographic elevation data is a means to improve global gravity field models at short scales, i.e. up to and beyond the resolution of present day models (~ 10 km). The analysis of high-resolution continental gravity maps of near-global coverage – condensed into a new empirical degree variance rule up to degree 90,000 – shows that significant gravity signal amplitudes are present at those scales, justifying the attempt to model the high-resolution constituents of the gravity field implied by the topographic masses in this work on global scale. For this purpose a variety of spectral forward modelling techniques that can be used to compute the short-scale gravitational attraction in terms of solid spherical harmonic coefficients of the uncompensated TP are studied in a comparative manner. Existing rigorous and efficient single- and multi-layer methods are reviewed and adapted, e.g. by embedding arithmetic extensions and parallel structures into the algorithms, to accommodate ultra-high degree computations. In this context a new spectral approach has been derived that allows to compute the TP from a multitude of volumetric-layers in ellipsoidal approximation, i.e. by an integration with respect to an oblate reference ellipsoid. This method leads to the ellipsoidal topographic potential (ETP) that in contrast to the widely used spherical topographic potential (STP) avoids spherical approximations. All methods are studied up to degree 5,400 and 21,600 using a new 1 arc-min source-mass model (Earth2014) that provides the geometric boundaries for the definition of layers of the solid crust, the oceans, lake water masses and polar ice sheets. Amongst a number of new insights, the experiments revealed that the efficient methods in their presented form (double precision environment) are useful to model the complete TP to degrees not much further than 10,800. Main reasons are large computational costs associated with a full convergence of the involved binomial series expansions that in this case require $k_{max}=46$ and $j_{max}=94$ binomial terms of the k - and j -series, respectively. Additionally, raising the boundary functions to the k^{th} power also requires oversampling of the boundary functions in order to avoid aliasing which may result in extremely large grids, demanding massive parallelisation in the spherical harmonic analysis. The latter is found to be the "bottleneck" of spectral forward modelling in terms of computation time and is facilitated efficiently with the help of exact numerical quadrature algorithms in this work. At short scales ($2160 < n \leq 5480$) the spherical approximation locally leads to errors of up to several mGal amplitude over mountainous terrain (~ 0.4 mGal global RMS), therefore ETP modelling should become common practice and replace spherical approaches. The error introduced by the rock-equivalent-topography (RET) concept of single-layer modelling techniques is in the range of ~ 0.5 mGal (global RMS) at short scales (< 10 km). However, at these scales the RET effect is negligible over continental and coastal marine areas. Only for large bathymetric features, such as deep-ocean trenches, multi-layer modelling seems justified at short scales. This makes single-layer ETP modelling based on RET an attractive method when aiming at high-resolution global modelling of land and coastal areas, underpinned further by its additive convergence behaviour that allows an early truncation of the k -series. Simple combinations with state-of-the-art observation-based satellite-only and combined gravity models (GOCO05s and EGM2008) show that the short-scale gravitational signal from ETP models up to

degree 5480 improves the agreement with ground-truth gravity observations (at more than 1 million points) over various regions of Earth between ~ 6 and ~ 46 %. Further improvements can be expected using more sophisticated combination techniques that allow for regional weighting. However, the latter is complicated by enormous computational costs and lacking stochastic modelling within the here used and proposed spectral techniques.

Contents

Zusammenfassung	III
Abstract	V
Contents	VIII
Abbreviations	IX
1 Preamble	1
1.1 Motivation and Scope	1
1.2 Structure and Research Aims	4
2 The Topographic Potential	9
2.1 Definition and geodetic perspective	9
2.1.1 Topographic masses	9
2.1.2 Isostatic masses and isostatic hypothesis	10
2.1.3 The uncompensated topographic potential	12
2.2 Spherical harmonic parametrization	13
2.2.1 Spherical harmonic series expansion	13
2.2.2 Spherical harmonic integration and SHCs of the topographic potential	15
2.2.3 Spherical harmonic truncation, spatial resolution and signal strength	15
2.3 Signal strengths and spherical harmonic characteristics at short-scales	17
2.3.1 Estimating short-scale signal strengths from an analysis of GGMplus	17
2.3.2 Understanding topographic potential models and spherical harmonics at high-degrees	18
2.3.3 Estimating short-scale signal strengths from high-degree global topographic potential models	23
2.4 Summary and evaluation of the chapters's research aims	25
3 Forward Modelling	27
3.1 General	27
3.2 Source-mass models of Earth's topographic masses	29
3.2.1 Available source-mass data and its quality	29
3.2.2 Earth2014: a 1' composite source-mass model	30
3.3 Spectral forward modelling	32
3.3.1 Modelling techniques and most important equations	32
3.3.2 Analysis techniques	41
3.4 Global spectral forward modelling with high resolution	44
3.4.1 A complete degree-5400 model (~ 4 km resolution)	44
3.4.2 An experimental degree-21,600 model (~ 1 km resolution)	51

3.5	Summary and evaluation of the chapter's research aims	58
4	Application and Validation of Spectral Forward Modelling	61
4.1	Strategies for the combination of topographic potential and observed gravitational potential . . .	61
4.1.1	Combination based on least-squares and normal-equations	64
4.1.2	Combination based on a regularisation of normal-equations	65
4.1.3	Combination in space and spectral domain	66
4.2	Demonstration and validation of global high-resolution combined gravity modelling	67
4.2.1	Area with large topographic features: Switzerland	67
4.2.2	Areas with medium topographic features: Northern Canada	69
4.2.3	Areas with small topographic features: Australia	71
4.2.4	Performance over Antarctica	72
4.2.5	Performance over the ocean	76
4.3	Other applications of spectral forward modelling of the topographic potential	79
4.3.1	Height unification and realisation of a global vertical datum	79
4.3.2	Bouguer coefficients and global maps of Bouguer gravity	82
4.4	Summary and evaluation of the chapter's research aims	84
5	Discussion and Future Directions	85
6	Conclusions	89
	Bibliography	97
	Acknowledgments	99
A	Appendix A	101
A.1	Truncation and filtering of topographic potential models	101
B	Appendix B	105
P.1	Publication I	105
P.2	Publication II	131
P.3	Publication III	133
P.4	Publication IV	164
P.5	Publication V	207
P.6	Publication VI	210

Abbreviations

AGAG	Antarctic Gravity Anomaly Grids
ALF	Associated Legendre Functions
ASTER	Advanced Spaceborne Thermal Emission Reflection Radiometer
ANGD	Australian National Gravity Database
BC	Bouguer Coefficients
BD	Block-Diagonal
BED	Bedrock layer of Earth2014
BT	Binomial Term
BVP	Boundary Value Problem
CGIAR	Consultative Group for International Agricultural Research
CPU	Central Processing Unit
CSI	Consortium for Spatial Information
DEM	Digital Elevation Model
DFT	Discrete Fourier Transform
DH	Driscoll/Healy
DHQ	Driscoll/Healy Quadrature
DVs	Degree Variances
Earth2014	1 arc-minute global shape, topography, bedrock and ice-sheet model
EGM2008	Earth Gravitational Model 2008
EGM96	Earth Gravitational Model 1996
EIGEN	European Improved Gravity model of the Earth by New techniques
EIGEN-6C	combined gravity model version 6 of the EIGEN group
ETOPO1	1 arc-minute global relief model
ETP	Ellipsoidal Topographic Potential
EXP	Exponential
FFT	Fast-Fourier Transform
GBT	Greenland Bedrock Topography
GGM	Global Gravity Field Model
GGMplus	Global Gravity Model Plus
GL	Gauss-Legendre
GLQ	Gauss-Legendre Quadrature
GOCE	Gravity Field and steady-state Ocean Circulation Explorer

GOCO	Gravity Observation Combination
GOCO05s	combined satellite-only model version 5 of GOCO group
GPS	Global Positioning System
GRACE	Gravity Recovery And Climate Experiment
GRS80	Geodetic Reference System 1980
HDF	Height Density Function
IAG	International Association of Geodesy
ICE	Ice-sheet thickness layer of Earth2014
ICGEM	International Centre for Global Earth Models
LB	Lower-Bound
LCA	Layer Correction Approach
LRA	Layer Reduction Approach
LRZ	Leibniz-Rechenzentrum
LSQ	Least-Squares
MDT	Mean Dynamic Ocean Topography
MSL	Mean Sea Level
Moho	Mohorovicic discontinuity
NEQ	Normal-Equation matrix
NGA	National Geospatial-Intelligence Agency
P-XX	Publication-Number
RAM	Random Access Memory
RET	Rock-Equivalent-Topography
RET2014	RET layer of Earth2014
RMS	Root Mean Square
RTM	Residual Terrain Modelling
SHA	Spherical Harmonic Analysis
SHCs	Spherical Harmonic Coefficients
SHS	Spherical Harmonic Synthesis
SRTM	Shuttle Radar Topography Mission
SS	Sanso/Sideris
STP	Spherical Topographic Potential
SUR	Surface layer of Earth2014
TanDEM-X	TerraSAR-X add-on for Digital Elevation Measurement
THF	Topographic Height Function
TP	Topographic Potential
UB	Upper-Bound
VMM	Vening-Meinesz-Moritz isostatic model

Chapter 1

Preamble

1.1 Motivation and Scope

The gravitational force that causes the apple to fall to the ground and that defines the orbit geometry of celestial bodies – as discovered by Isaac Newton in 1686 in his *Philosophiae Naturalis Principia Mathematica* – can be represented in mathematical models.

In geodesy and geophysics these so called *global gravity field models* (GGM) or *potential models* are fundamental resources and are needed, e.g., to establish the vertical datum of global reference systems and to realize global height unification (*Sideris and Fotopoulos, 2012*) or to explore the interior structure and retrieve the geologic evolution of Earth (*Wieczorek, 2015*). Also in many other disciplines the precise knowledge of the Earth's gravity field is of great importance: in aeronautics/astronautics gravity models are used to simulate perturbing forces that act on (space) vehicles and predict orbits (*Chao, 2005*); inertial navigation needs precise information on deflections of the vertical that can be derived from gravity field models (*Wu et al, 2016*); the exploration of minerals or fossil fuels and geophysical models rely on gravity inversion (*Oldenburg et al, 1998; Bosch and McGaughey, 2001*); orthometric heights are measured w.r.t. to the *geoid* – an equipotential surface of the gravity field – and are relevant for a wide field of applications and sciences, such as construction or hydrological modelling; melting of ice-covered regions and ground-water depletion can be observed through spatio-temporal gravity variations (*Tapley et al, 2004*); or in oceanography where the geostrophic ocean circulation is derived from the dynamic ocean topography that is given by the difference of the heights measured by satellite altimetry and the geoid heights of a static gravity field model (*Bosch and Savcenko, 2010*).

Today, available satellite, aerial and terrestrial gravity observations at global scale are sufficing in terms of resolution and quality to describe the Earth's gravitational potential in models down to scales no smaller than ~ 10 km, generally (cf. Fig. 1.1). Truth is that some remote areas (mostly found in Asia, Africa and South America) lack sufficiently dense observations or the inaccuracies of the observations over those areas actually don't support such a high resolution (*Pavlis et al, 2012, 2013*). However, in global environmental sciences – mainly driven by the political commitment to understand global phenomena such as the climate change and driven by available high-resolution satellite data (other than space gravimetry) – a demand for finer scale gravity models exists.

A means to increase the resolution of gravity field models is to extend observation based models with forward modelled gravity – which is subject of this work. In brief, forward modelling describes the process of computing values of the gravitational attraction based on a given mass model – knowing or assuming a certain geometry and density – of Earth. Forward models therefore (only) serve as estimates of the actual gravitational field,

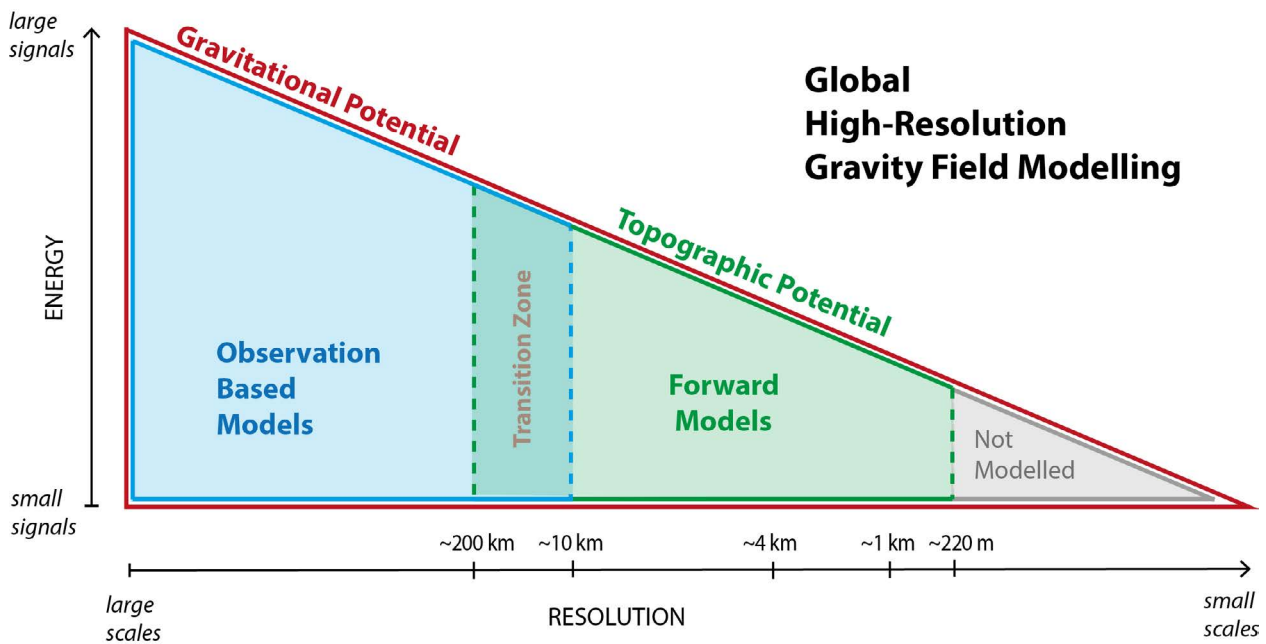


Fig. 1.1 – Scheme of the topographic potential in the context of global high-resolution gravity field modelling.

but their application can be useful if carefully considered. Up-to-date satellite-based digital elevation models provide detailed knowledge of the geometry of the uppermost masses of Earth – the so called topographic masses: visible topography, oceans, lakes and ice-sheets – down to scales of tens to hundreds of metres. Due to the attenuation of gravitational force with distance, it is exactly those uppermost masses that cause most of the short-scale gravity variations at Earth’s surface. With this in mind, the gravitational information hidden in global digital elevation models is of key importance to high-resolution gravity modelling and deserves to be unveiled.

This is obvious, since the gravitational potential implied by the topographic masses, hereafter referred to as *topographic potential* (TP), is used successfully to improve current global potential models, e.g. regionally as fill-in data where terrestrial observations are scarce (Pavlis *et al*, 2012, 2013; Fecher *et al*, 2013). The combination of observation based models and forward models plays a key role in combined high-resolution gravity field modelling. During the combination it is crucially important to ensure that the information content of observation-based gravity at large and medium scales is not substituted by the estimated gravity in forward models. With appropriate combination methods it can be achieved that the topographic potential only accounts for short-scale (=high-resolution) gravitational variations, coming into play in a transition zone ranging from scales of ~200 km to ~10 km in present day models (Pavlis *et al*, 2012, 2013; Fecher *et al*, 2013, 2017) (cf. Fig. 1.1). Optimally, the transition is held regionally variable during the combination since the scales where forward modelled gravity is introduced depends on the coverage of a region with terrestrial observations and since the quality of the (observation) data often is heterogeneous (Fecher *et al*, 2017).

Beyond the zone of transition, forward-modelled gravity alone is deemed to add significant information of the gravitational potential at short-scales (Fig. 1.1). In a near-global attempt gravity has been forward modeled for most parts of Earth’s continental areas to a so far unprecedented scale of ~220 m, recently (Hirt *et al*, 2013). However, towards short-scales the diminishing amplitude of gravity signals makes forward modelling more and more challenging since modelling errors and assumptions need to be reduced to a minimal level. This is accompanied by increased computational costs, not least because higher resolution means more data points.

Different approaches exist for forward modelling of the topographic potential. They may be grouped according to the respective domain where the integration over Earth's masses is performed:

- the *space domain* (e.g. *Mader (1951); Nagy (1966); Forsberg (1984); Papp (1996); Kuhn and Seitz (2005)* and others), or
- the *spectral domain* (e.g. *Lee and Kaula (1967); Balmino et al (1973); Rummel et al (1988); Novak (2010); Balmino et al (2012); Claessens and Hirt (2013)* and others).

While both domains have successfully been used to model Earth's topographic potential at ~ 10 km scale (e.g. *Grombein et al (2016b); Rexer et al (2016)*) and were shown to be mutually consistent (*Hirt et al, 2016*), this work is dedicated to the approaches in the spectral domain (=spherical harmonic domain). These techniques are designated global approaches since they inherently are defined globally, due to their parametrization in spherical harmonics. Further, it is believed that spectral methods are efficient, which will be investigated in the course of this work. Efficiency is not the only, but in this case the determining criterion regarding the enormous amount of data present in global high-resolution modelling and given that both domains were shown to result in exactly the same potential (*Hirt et al, 2016*). The spectral methods benefit computationally from Fast-Fourier Transforms (FFT) that efficiently facilitate analysis and synthesis steps. Note that for geographically-limited modelling space domain integration most likely is faster, simply due to less data.

Recently a spectral approach has been used to model the topographic potential globally down to scales of ~ 2 km, i.e. degree 10,800 (*Balmino et al, 2012*). In the course of this dissertation it will be shown that the models created by *Balmino et al (2012)* lack spectral completeness. Moreover, their modelling is subject to systematic errors since it relies on a spherical approximation of the rather ellipsoidal Earth and it is devoid of most recent elevation data, especially over Greenland and Antarctica. Modelling in ellipsoidal approximation has only recently been proposed (*Claessens and Hirt, 2013*), but neither been adapted for modelling the topographic masses explicitly in a multi-layer approach nor applied at high resolution. A systematic and comparative investigation of different spectral solutions to the topographic potential at high resolution is missing in the literature and shall be performed in this work.

Condensed into one sentence, the scope of this work is the following:

The dissertation shall answer the question to which extent spectral forward modelling together with up-to-date topographic elevation data is a means to improve global gravity field models at short scales, i.e. up to and beyond the resolution of present day models (~ 10 km).

In more detail, breaking the scope of this work down into three defined goals of research, in this work it envisaged to

- G1 - improve the understanding of the short-scale characteristics of the topographic potential,
- G2 - study different spectral forward modelling approaches, involved approximations and available source-mass data down to a resolution of ~ 1 km and identify the best spectral approach,
- G3 - create a complete high-resolution topographic potential model using the best spectral approach and elaborate whether the created forward model can successfully be used in global high-resolution gravity modelling using simple combinations methods.

As argued above, optimal combination strategies are vital for global high-resolution gravity modelling but beyond the scope of this dissertation. In the next section the concept and structure of the dissertation are presented, explaining the methods and strategies in order to meet the above research goals G1 - 3.

1.2 Structure and Research Aims

The thesis is of cumulative type, since parts of the research and of the results have been published in articles in peer-reviewed scientific journals. This manuscript contains the synthesis and synoptic discussion of all publications plus additional research, and is meant to fulfill the overall research goals. First author papers are reprinted in the appendix together with a declaration of own contribution, since the publications were conducted with one or more co-authors. Publications with co-authorship are not reprinted, but own contributions are declared in the appendix. The original article of co-authored papers can be found in the respective issues of the journals or in the publishers' online repositories (see Appendix).

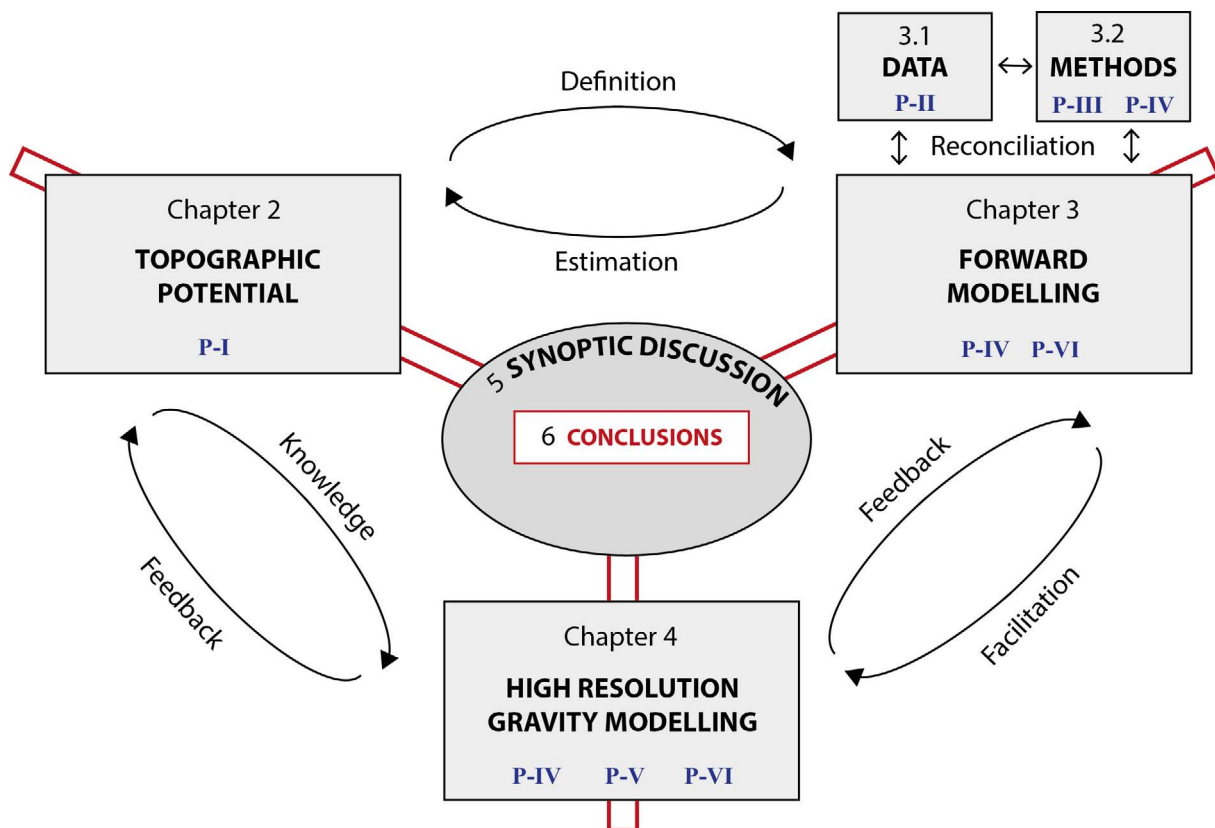


Fig. 1.2 – Scheme of the thesis structure, highlighting links and interaction between chapters (black numbers) and included publications (blue numbers).

The research is subdivided into the three topics *topographic potential*, *forward modelling* and *high-resolution gravity modelling*, closely aligned to the research goals G1-3 that cover the entire scope of the dissertation (see end of previous section). This structure is reflected by the three chapters of the main part of the manuscript (Chpts. 2, 3 and 4). At the end of each chapter the respective research goal, and more detailed research questions and aims (further down) are evaluated. Then the results of the three chapters and all publications are synoptically discussed and future directions are given (Chpt. 5). Finally, conclusions are drawn from the main findings and the discussion (Chpt. 6), forming the central outcome of the dissertation. (cf. Fig. 1.2) Essentially, the single chapters are not treated separately in the course of the research. Interactions are permitted and encouraged by the structure of the dissertation, leading to a symbiosis and an exchange of knowledge across the topics (Fig. 1.2). For example, the clear definition of the topographic potential is required to set up adequate forward modelling data and techniques. The forward modelling itself provides estimates of

the topographic potential which improves our knowledge about it. With the knowledge about the characteristics of the topographic potential we may improve its application in high-resolution gravity field modelling. The combined models contain valuable feedback about the characteristics of the topographic potential as a result of their validation. Further, forward modelling facilitates the increase in resolution in high-resolution gravity models, while the validation of the combined models returns valuable feedback about the applied forward modelling data and techniques.

The main part starts with an introduction to the topographic potential (Chpt. 2), being the elementary subject of the research. Its parametrisation in terms of spherical harmonics is introduced and discussed. The focus in the first section is placed on the investigation of the short-scale characteristics of gravity disturbances and geoid heights represented by the topographic potential. The characterisation and improved understanding of topography related gravity effects at short scales are vital for the purpose of high-resolution gravity modelling. The following research questions shall be answered in this section:

Q1 - How is the topographic potential defined?

Q2 - Is the topographic potential relevant for high-resolution gravity field modelling?

In order to answer the questions the following aim can be stated for Chpt. 2:

A1 - Quantify the signal strength and examine the spectral characteristics of the topographic potential at short scales.

The second chapter of the main part deals with the forward modelling of the topographic potential with spectral methods (Chpt. 3). It can be subdivided into 1) one section about the data required for the forward modelling (Sect. 3.2) and 2) a methodological section about different spectral forward modelling approaches and their mathematical and computational realisation (Sect. 3.3). At the end of this chapter the methods and data are applied to develop topographic potential models with high- and ultra-high resolution (Sect. 3.4). The treated research questions that will be answered in these sections are the following:

Q3 - Which acquisition techniques, geophysical data and models exist that would allow the generation of an appropriate mass model that can be used for the forward modelling of the topographic potential at short scales and on a global scale?

Q4 - Can spectral forward modelling be further improved and is it a feasible technique for global high-resolution forward modelling?

From these questions two related aims may be defined for the Chpt. 3:

A2 - Review existing global topographic data sets and mass models in order to create a truly global and up-to-date mass model at best means that is suited for the purpose of forward modelling.

A3 - Review existing spectral forward modelling techniques in order to further develop and test the best suited approaches for high-resolution modelling.

A4 - Define challenges and limitations of spectral forward modelling with regard to resolution.

The third chapter in the main part is dedicated to the application of the developed data and methods in the context of high-resolution combined gravity modelling (Chpt. 4). The combination of gravity observations and forward modelled topographic gravity is discussed and simple combination schemes are tested to exemplify the benefit of including topographic information in high-resolution gravity field modelling. The section serves as a validation of forward modelled gravity, on the same time demonstrating the application of forward

Paper ID	Research Questions					Research Aims					
	Q1	Q2	Q3	Q4	Q5	A1	A2	A3	A4	A5	A6
<i>P-I</i>	x	x				x					
<i>P-II</i>	x		x				x				
<i>P-III</i>				x				x	x		
<i>P-IV</i>	x	x		x	x			x	x	x	
<i>P-V</i>					x					x	x
<i>P-VI</i>	x			x	x				x		

Tab. 1.1 – Assignment matrix showing the dedication of publications used in the dissertation to research questions and research aims.

modelling in combined gravity field modelling. The chapter can be summarised by the following research question:

Q5 - Are spectrally forward modelled topographic potential models useful for high-resolution combined gravity field modelling or other applications at global scale?

The questions leads to the following research aims for Chpt. 4:

A5 - Find combination strategies for a combination of observed and high-resolution forward modelled gravity and show the added value of the latter to combined gravity field modelling, globally.

A6 - Elaborate the usage of such a combination, the developed data and methods in other applications.

In total, six publications *P-I* to *P-VI* that contain important results and findings are used in this cumulative dissertation – three first author papers and three papers with co-authorship. They are an active part of the above described interactive and symbiotic research structure. Since the papers have to form a complete research on their own, i.e. they deal with theory, data, methods and practical experiments, they in some cases address more than one topic of the dissertation (cf. blue numbers in Fig. 1.2). Still each paper has a clear focus and is closely linked to one (or more) of the research questions and aims of the chapters (Tab. 1.1).

On the next two pages all involved publications are listed with title, authors, journal and a short summary of the paper's content and role in the dissertation.

P-I Spectral analysis of the Earth's topographic potential via 2D-DFT: a new data-based degree variance model to degree 90,000

Moritz Rexer, Christian Hirt
in: Journal of Geodesy

The publication focuses on the investigation of the short-scale characteristics of the topographic potential as implied by near-global gravity maps of ~ 220 m resolution. With an approximate transformation of the maps into the spherical harmonic domain via 2D-DFT and by a parametrization in terms of degree variances models, signal strengths at different scales and over different types of terrain are studied. The paper can be regarded as pre-study and is meant to give answers to Q1 and Q2 and to meet the research aim A1. In essence the paper shows that significant gravitational energy may be implied in Earth's topographic masses at short-scales, therefore its modelling and inclusion in high-resolution gravity field models is relevant. More information and a reprint of the publication are found in appendix P.1.

P-II Earth2014: 1' shape, topography, bedrock and ice-sheet models - Available as gridded data and degree 10,800 spherical harmonics

Christian Hirt, Moritz Rexer
in: International Journal of Applied Earth Observation and Geoinformation

The publication is dedicated to the creation and description of an up-to-date geometric data set of Earth's topographic masses. The data set is named Earth2014 and comprises the boundary surfaces of Earth's bedrock, ocean, lakes and ice-sheets at 1' (arc-min) resolution. Moreover, the boundary functions are represented in sets of high-resolution surface spherical harmonics. All data sets have been made publicly available. As such, Earth2014 is a formidable input data set for (spectral) forward modelling of Earth's topographic potential and other global applications in geosciences. The publication provides answers to Q1 and Q3, and is closely linked to research aim A2. More information and a declaration of own contribution are found in appendix P.2. The Earth2014 data set has been made available to the public and to the scientific community here: <http://ddfe.curtin.edu.au/models/Earth2014/>.

P-III Ultra-high-degree surface spherical harmonic analysis using the Gauss-Legendre and the Driscoll/Healy quadrature theorem and application to planetary topography models of Earth, Mars and Moon

Moritz Rexer, Christian Hirt
in: Surveys in Geophysics

In this publication two harmonic analysis methods, quadrature based on sampling theorems of Gauss-Legendre and of Driscoll/Healy, are investigated, improved and evaluated for their application at high resolution, i.e. high spherical harmonic degree (> 2700). Both methods are shown to enable accurate high-degree spherical harmonic transforms (up to some 10,000s of degrees), after employing X-numbers in order to achieve extended arithmetics that are needed to avoid under/overflow in the computation of the associated Legendre Functions (ALFs). A parallelisation of certain analysis steps leads to acceptable computation times, while the Gauss-Legendre quadrature is found to be the more efficient technique. The development and implementation of a method for high-resolution spherical harmonic analysis is a prerequisite for high-resolution spectral forward modelling. In this respect, this paper is dedicated to the research aims A3 and A4 and helps to give an answer to Q4. More information and a reprint of the publication are found in appendix P.3.

The code and all routines used for ultra-high degree analysis in this publication are available to the public and to the scientific community here: https://www.researchgate.net/publication/291102839_ultra_high_degree_extension_v1_SHT00LS.

P-IV Layer-based modelling of the Earth's gravitational potential up to 10km-scale in spherical harmonics in spherical and ellipsoidal approximation

Moritz Rexer, Christian Hirt, Sten Claessens, Robert Tenzer
in: Surveys in Geophysics

This publication deals with different methods and various important aspects of spectral forward modelling. Existing spectral forward modelling techniques and underlying assumptions are inter-compared and new expressions for the rigorous modelling of volumetric layers with respect to a reference ellipsoid are derived. Contrary to the modelling w.r.t. a reference sphere, the ellipsoidal modelling can be associated with less approximation errors and is spectrally compatible with observation based models. Further, the importance of avoiding aliasing errors and paying proper attention to the convergence behaviour of involved binominal series expansions during the modelling is highlighted. Concluding, layer-based volumetric modelling improves over single-layer modelling and the use of an ellipsoidal reference is desirable for applications of high accuracy and high resolution. The paper is important for answering the research questions Q1, Q2, Q4 and Q5. It also helps to meet the research aims A3, A4 and A5. More information and a reprint of the publication are found in appendix P.4.

The spherical harmonic topographic potential models developed in this publication were made available to the public and to the scientific community via ICGEM (<http://icgem.gfz-potsdam.de/ICGEM/>) and http://ddfe.curtin.edu.au/models/Earth2014/potential_models.

P-V A new degree-2190 (10 km resolution) gravity field model for Antarctica developed from GRACE, GOCE and Bedmap2 data

Christian Hirt, Moritz Rexer, Mirko Scheinert, Roland Pail, Sten Claessens, Simon Holmes
in: Journal of Geodesy

The publication describes the development of a degree-2190 gravity field model that apart from latest satellite gravity observations includes forward modelled gravity from a recent Antarctic bedrock and ice-sheet data set (Bedmap2). It is shown how the spectral forward model that is defined w.r.t. a reference ellipsoid can be combined with the normal equations of a satellite-only gravity field solution by means of regularisation. The transition between observed and forward modelled data is steered by empirical weighting schemes that are meant to provide optimal combination results over the region of Antarctica. The benefit of this kind of combination is demonstrated by comparison with ground truth data from the IAG Subcommission 2.4f "Gravity and Geoid in Antarctica". The paper provides answers to the research question Q5 and is closely linked to research aims A5 and A6. More information and a declaration of own contribution are found in appendix P.5.

The combined potential model developed in this publication is available to the public and to the scientific community here: <http://ddfe.curtin.edu.au/models/Antarctica/>.

P-VI Topographic gravity modelling for global Bouguer maps to degree 2,160: Validation of spectral and spatial domain forward modelling techniques at the 10 microgal-level

Christian Hirt, Elisabeth Reußner, Moritz Rexer, Michael Kuhn
in: Journal of Geophysical Research

This publication is dedicated to the mutual validation of global forward modelling in the spatial and in the spectral domain. Starting from a degree-2160 input topographic function it is shown that amongst other aspects 1) over a dozen integer powers and frequencies far beyond the input band-width of the topographic function are required in spectral forward modelling and 2) a high oversampling of the topographic function is needed in spatial domain modelling in order to avoid discretisation errors for achieving a perfect agreement between both modelling domains. The costly numerical experiments involve the modelling of short-scale gravity signals to ultra-high degree 21,600. Spectral domain modelling is found to be the more efficient variant, while it seems to be at the edge to convergence issues for selected points. The paper is useful for answering research questions Q1, Q4 and Q5 and contains important contributions to research goal A4. More information and a declaration of own contribution are found in appendix P.6.

Chapter 2

The Topographic Potential

2.1 Definition and geodetic perspective

In simple words the gravitational field induced by the *topographic potential* describes the gravitational attraction that is caused by the Earth's topographic masses along with some assumptions on their mass-density. In contrast, the term *gravitational potential* generally refers to the gravitational field that is generated by the entire masses of Earth, i.e. the topographic masses and the masses below with their actual densities. The atmospheric masses shall be disregarded at this stage. For a precise definition of the topographic masses it helps to visualize Earth's geophysical structure (Fig. 2.1).

2.1.1 Topographic masses

In good approximation the inner masses of Earth can be described by concentric layers of constant thickness. While the density is not homogenous within the layers, the mass density generally increases towards Earth's center of mass. Drastic jumps in density or changes of the aggregate phase (e.g. from solid to fluid) are expressed by so called discontinuities forming the boundaries between the layers. The outermost masses of Earth are not well described by a concentric layer model, since there exist significant deviations from a simple spherical shell. The *topography* describes the morphological surface that represents the boundary of the physical body of Earth with the atmosphere. The topographic masses are therefore found at the uppermost part of the lithosphere, the crust.

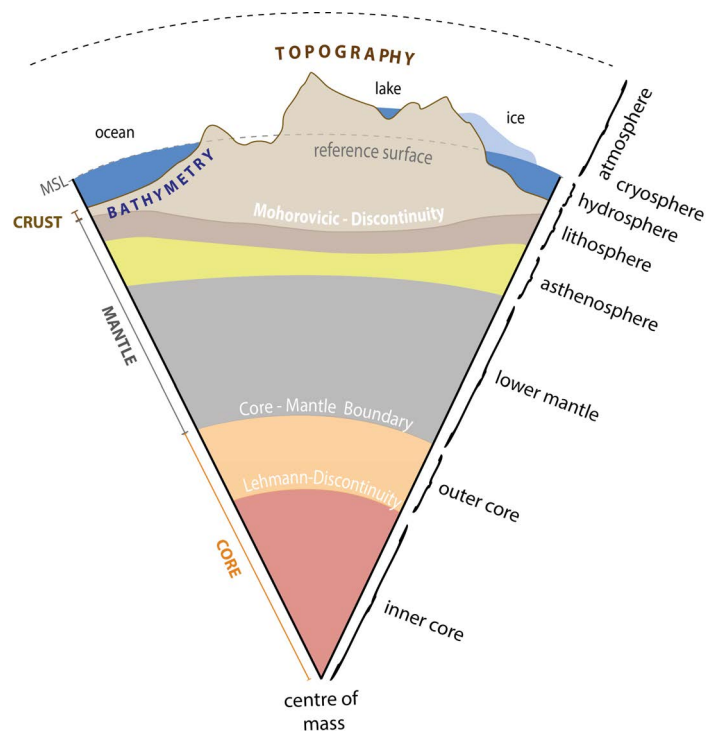


Fig. 2.1 – Scheme of Earth's structure including the topographic masses comprised by the topographic potential (not to scale).

Generally (and in this work), the topographic masses comprised by the topographic potential are the masses of sediments and solid rock of the crust, hydrospheric and cyrospheric masses, i.e. ocean water, lake water and ice-sheets. Vegetation cover or human buildings as well as small rivers or small snow/ice caps are not considered, due to their (comparatively) small gravitational impact. While the upper bound of the topographic masses is clearly defined by the topography, the lower boundary is a matter of definition and subject to discussion. The crustal layer can reach depths of 60 to 80 km in extreme cases (below Cenozoic mountain ranges), but in average the Mohorovicic discontinuity (Moho) is found at ~ 35 km depth below continental areas and at ~ 10 km below oceanic areas (Torge, 2003).

Using the Moho as lower bound of the topographic masses would without doubt be a very logical and geophysical definition which in addition is closely linked to the actual structure of Earth. Conventionally, however, the definition of the topographic masses is done differently. They are defined as mass surpluses (e.g. mountain peaks or highland) or deficits (e.g. valleys or oceans) relative to a defined reference body (Fig. 2.2). The surface of the reference body is mostly chosen to coincide with mean sea level (MSL) – which is expressed by the geoid over land – and sometimes approximated by a sphere or an ellipsoid. The effect of these approximations is studied intensively in *P-IV*. The density of the reference body often is assumed to be constant and approximated by Earth's mean density.

This definition of the topographic masses appears very geodetic, and here two reasons are given that might explain its evolution. The first reason is data-driven and related to the incomplete knowledge of the Moho. Especially at short scales (< 10 km) no global model of the Moho is available. At best the Moho is described globally with 1° in (seismic) geophysical models, corresponding to ~ 111 km resolution (*P-IV*). Higher resolution models of the Moho are derived from gravity and still lack reliability (see further down). Additionally, introducing gravimetric Moho depths as a priori information to estimate gravity would mean a loop that preferably is to be avoided. The second reason is related to the geodetic methods that historically have been used to recover the geoid given gravity measurements at Earth's surface. The problem is manifested in the *boundary value problem* (BVP) of physical geodesy, often referred to as *Stokes' problem* (Torge, 2003). In order to solve it gravity variations caused by the topographic masses outside the geoid, which often is approximated by a mean sphere or ellipsoid of revolution in the first place, need to be removed. For this purpose it is common geodetic practice to apply Bouguer modelling (Torge, 2003). Thereby a spherical slab (in the past) or a spherical shell of distinct height is used as a zero-degree approximation of the topography. The residual parts of the topography – masses above and below the upper boundary of the Bouguer shell – are accounted for by a so called *terrain correction* (Torge, 2003). The terrain corrections may e.g. be approximated via *residual terrain modelling* (RTM) (Forsberg, 1984), with the upper bound of the shell serving as reference surface.

2.1.2 Isostatic masses and isostatic hypothesis

The immediate consequence of not including the Moho in the definition of the topographic masses is that isostatic compensation, i.e. the equilibrium state of the solid lithosphere with the elastic asthenosphere (indicated in Fig. 2.1) is disregarded. The isostatic compensation mechanism may be imagined as crustal roots ranging into the mantle (e.g. below mountain ranges) and so called anti-roots, where the Moho is shifted upwards into the crust (e.g. below the oceans, see Fig. 2.2). The roots and anti-roots are often referred to as *isostatic masses* that (to some extent) compensate topographic mass surpluses or deficits (Fig. 2.1); the distance between reference surface and Moho is called *compensation depth*. More generally isostasy means the interaction of the elastic upper mantle with the masses of the more rigid crust.

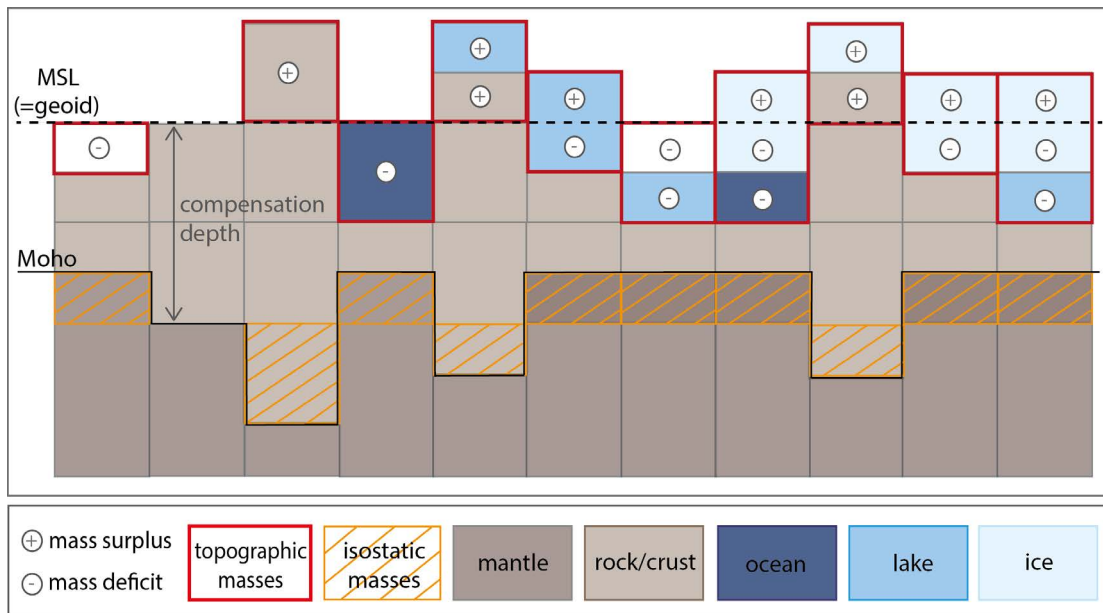


Fig. 2.2 – Scheme of the topographic and isostatic masses.

During the modelling of the topographic potential isostatic compensation can be accounted for by including isostatic hypothesis (see e.g. *Rummel et al* (1988); *Göttl and Rummel* (2009); *Tsouliis* (2013)). Prominent geodetic hypothesis, such as those by *Pratt-Hayford* (*Pratt*, 1855; *Hayford*, 1909) or *Airy-Heiskanen* (*Airy*, 1855; *Heiskanen and Vening Meinesz*, 1985), assume local compensation, with a column-wise compensation of the topographic load. Thus, the elastic flexural rigidity of the crust is ignored in this models (*Göttl and Rummel*, 2009) and it is, e.g., not accounted for isostatic compensation taking place within the lithospheric mantle (cf. *Bagherbandi and Sjöberg* (2012)). Not astonishingly, the results produced by these hypothesis are not satisfactory on regional and global scale, e.g. when evaluated against satellite gravity data (*Hirt et al*, 2012) or seismic Moho depths (*Bagherbandi and Sjöberg*, 2012). But isostatic hypothesis exist that also try to account for isostasy on regional and even global scale e.g. in the form of consolidated crust models or after the Vening-Meinesz-Moritz (VMM) model (*Vening Meinesz*, 1931; *Moritz*, 1990). In the latter model, an isostatic gravity disturbance equivalent to zero is postulated that represents the balance between gravitational attraction given by gravity disturbances, corrected for topography, and the isostatic compensation masses. The VMM is often used to recover the crustal thickness since it shows a strong correlation to the Moho-layer geometry (*Bagherbandi et al*, 2013). However, applying the VMM leaves deviations in the order of several kilometres ($RMS = 3.4$ km) compared to the best seismologic models at scales of ~ 220 km (*Bagherbandi et al*, 2013). In essence, all different hypotheses were found to lead to substantially different results (*Novák et al*, 2016), which means that for different applications different isostatic models may be suitable. This makes it hard to justify the usage of a certain hypothesis during forward-modelling. Therefore modelling of the uncompensated topographic potential is considered in the frame of this work (see below).

2.1.3 The uncompensated topographic potential

The potential of uncompensated topographic masses leads to an overestimation of the actual gravitational potential of Earth, especially over mountain ranges and at large scales. However, due to the rather smooth structure of the Moho and due to its distance to Earth's surface (gravity signals are attenuated with reciprocal powers of the Euclidean distance), the compensation plays a decreasing role towards short scales. This is exemplified in Fig. 2.3 using a potential model of the isostatic masses that is based on an improved *Airy-Heiskanen* hypothesis that incorporates seismic Moho depths (Grombein *et al*, 2014). At scales of ~ 10 km the signal of the isostatic potential (yellow line) already is about 5 orders of magnitude below the signal of the actual gravitational potential (black line).

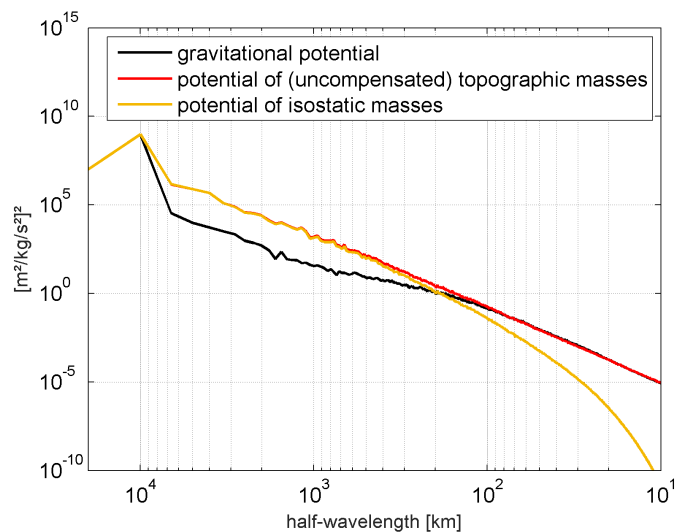


Fig. 2.3 – Energy of gravitational potential, (uncompensated) topographic potential and isostatic potential in terms of degree variances; black line: EGM2008 (Pavlis *et al*, 2012); red line: dV_ELL_Earth2014 (Rexer *et al*, 2016); yellow line: RWI_ISOS_2012 (Grombein *et al*, 2014).

Similar differences in magnitude between the topographic and the isostatic potential at this scale based on the *Airy-Heiskanen* concept were also found by Pavlis *et al* (2007) (Fig. 3 *ibid*). This is supported by Göttl and Rummel (2009) who state " (...) it is known that only larger mountains are compensated, while local topographic features with an extension of less than 100 km are supported by the lithosphere underneath (TORGE, 2003) (...)". In contrast, the topographic potential (red line) shows the same level of energy at scales of ~ 100 km and smaller, suggesting that the gravitational potential is correlated with the topographic potential at short scales. This is also confirmed by Jekeli (2010) who finds that neglecting isostatic effects is justified at very short scales (only).

As an immediate consequence of the above, isostatic compensation mechanisms are not included in the definition of the topographic masses and the corresponding topographic potential in this work. Strictly speaking, all herein produced or investigated topographic potential models are *uncompensated* topographic potential models. The main reasons are the diminishing, or even negligible, relevance of isostatic effects for the short-scale gravity field and the still existing differences and shortcomings of present isostatic compensation models. Their improvement is beyond the scope in this work.

2.2 Spherical harmonic parametrization

Since the topographic potential V^t , similar to the gravitational potential V , is a harmonic function outside of Earth's masses (it fulfills the Laplace condition: $\Delta V^t \equiv 0$) it can be expressed conveniently as a series expansion of solid spherical harmonic base functions. In geodesy the spherical harmonic concept is a common instrument for global analysis and global modelling of harmonic functions, such as the gravity field or the magnetic field (*Barraclough, 1978*). Alternatively, other base functions (e.g. spherical radial basis functions (*Bucha et al, 2016*)) or discretisations (e.g. gridded maps (*Hirt et al, 2013*)) can be used to represent the topographic potential or its functionals, such as derivatives of the potential. The advantage of the concept of spherical harmonics for the purpose of global modelling is its inherent global support. This means the concept allows to represent gravity values at every location of the globe (outside of all masses) in one set of solid spherical harmonic coefficients (SHCs). Since the spherical harmonic base functions are orthogonal, the exact separation of frequencies/SHCs is possible. Another alternative to spherical harmonics with global support are *ellipsoidal harmonics*, also referred to as *oblate spheroidal harmonics* in Literature, which employ the ellipsoidal coordinates instead of the (radial) spherical coordinates (see e.g. *Jekeli, 1988*). Although not applied commonly in the geodetic community – which may be due to the somewhat larger complexity associated with ellipsoidal harmonic computations – the ellipsoidal harmonic concept bears certain advantages which are discussed in the course of this work. For the difference between ellipsoidal and spherical harmonics and the transformation between the two domains it is referred to *Jekeli (1988)* and *Sebera et al (2012)*.

2.2.1 Spherical harmonic series expansion

Let W be the Earth's gravity potential, being the sum of gravitational potential V and the potential of the centrifugal force Z . Then the gravitational potential becomes

$$V = W - Z. \quad (2.1)$$

The disturbing potential T denotes all the anomalous gravitational potential that occurs with respect to the potential of a reference potential U and is derived by (*Torge (2003)*, Eq. 6.1 *ibid*)

$$T = W - U. \quad (2.2)$$

Usually U is defined by the potential of a rotating reference mass-ellipsoid – conventionally the Geodetic Reference System 1980 (GRS80) plus Earth's centrifugal force potential Z (*Moritz, 2000*). Then the gravitational potential V and the disturbing potential T – as well as the topographic potential $V^{(TP)}$ – can be described as the solid spherical harmonic series expansions (cf. *Torge (2003)*, Eq. 6.4 *ibid*)

$$V(r, \lambda, \theta) = \frac{GM}{r} \sum_{n=0}^{\infty} \sum_{m=0}^n \left(\frac{R}{r}\right)^n \bar{V}_{nm} \bar{Y}_{nm}(\lambda, \theta) \quad (2.3)$$

and

$$T(r, \lambda, \theta) = \frac{GM}{r} \sum_{n=0}^{\infty} \sum_{m=0}^n \left(\frac{R}{r}\right)^n (\bar{V}_{nm} - \bar{U}_n) \bar{Y}_{nm}(\lambda, \theta) \quad (2.4)$$

at any location outside the Earth's masses defined by the point $P(r, \lambda, \theta)$ in spherical coordinates with co-latitude $\theta = \pi - \varphi$, where

- G : universal gravitational constant,
- M : Earth's mass,
- R : spherical harmonic reference radius, conventionally often chosen to coincide with the semi-major axis a of the GRS80 reference ellipsoid,
- \bar{V}_{nm} : fully normalised solid SHCs of the gravitational potential of degree n and order m ,
- \bar{U}_n : fully normalised solid SHCs of the reference potential of degree n , conventionally given by the J2, J4, J8 and J10-terms of the GRS80,
- \bar{Y}_{nm} : fully normalised Laplace's (surface) spherical harmonic functions of degree n and order m (e.g. *Heiskanen and Moritz*, 1967, Sect. 1.10 *ibid*)

$$\bar{Y}_{nm}(\lambda, \theta) = \bar{P}_{nm}(\theta) \begin{cases} \cos(|m|\lambda) & \text{for } m \leq 0 \\ \sin(m\lambda) & \text{for } m > 0 \end{cases}, \quad (2.5)$$

- \bar{P}_{nm} : fully normalised associated Legendre functions (ALFs) of the first kind (e.g. *Abramowitz and Stegun* (1972)).

The infinite character of the series in Eqs. 2.3 and 2.4 ($n \mapsto \infty$) and their truncation at a distinct maximum degree n_{max} is discussed further down (Sect. 2.2.3). Further, one often finds the series starting at $n = 2$ which assumes that the total mass and the centre of mass of the actual Earth and the reference ellipsoid coincide. The applied normalisation of the ALFs (and of the potential coefficients) is a function of degree n and order m (cf. *Heiskanen and Moritz*, 1967, Sect. 1.14)

$$\bar{P}_{nm} = P_{nm} \begin{cases} \sqrt{(2n+1)} & \text{for } m = 0 \\ \sqrt{2(2n+1) \frac{(n-|m|)!}{(n+|m|)!}} & \text{for } m \neq 0 \end{cases}, \quad (2.6)$$

and is also referred to as *geodetic* or 4π -normalisation, where P_{nm} are the non-normalised ALFs. The normalisation means that the average square value of these normalised harmonics integrated over the sphere is unity according to (cf. *Heiskanen and Moritz*, 1967, Sect. 1.14)

$$\frac{1}{4\pi} \int_{\sigma} \bar{Y}_{nm}(\lambda, \theta) \cdot \bar{Y}_{n'm'}(\lambda, \theta) d\sigma = \delta_{nn'} \delta_{mm'} \quad (2.7)$$

where

δ_{ij} : Kronecker delta which is 1 for $i = j$ and 0 otherwise .

2.2.2 Spherical harmonic integration and SHCs of the topographic potential

In this work it is focused on the determination of \bar{V}_{nm} or more precisely the SHCs of the topographic potential $\bar{V}_{nm}^{(TP)}$ in the spectral domain (see Chpt. 3). Generally, this is achieved by an integration over Earth's masses after Newton's law of gravitation which translates into spherical harmonics as follows (cf. *Rummel et al*, 1988)

$$\bar{V}_{nm}^{(TP)} = \frac{3}{\bar{\rho}R^3(2n+1)} \frac{1}{4\pi} \int_B \left(\frac{r_Q}{R}\right)^n \rho(\lambda_Q, \theta_Q) \bar{Y}_{nm}(\lambda_Q, \theta_Q) dB(\lambda_Q, \theta_Q), \quad (2.8)$$

where

- $\bar{V}_{nm}^{(TP)}$: fully normalised solid SHCs of the topographic potential of degree n and order m ,
- $\bar{\rho}$: Earth's mean mass-density,
- B : volume of Earth's gravitating masses,
- Q : source-mass point Q given at the spherical coordinates $\langle r_Q, \lambda_Q, \theta_Q \rangle$ with $Q \in B$,
- ρ : mass-density (at point Q), and
- dB : infinitesimal spherical volume element.

The introduction of different reference surfaces – a sphere or an ellipsoid – for the geometric description of the masses during the integration leads to different spherical harmonic topographic potential models. Taking some ellipsoid as a reference surface gives the SHCs of the *ellipsoidal topographic potential* (ETP) \bar{V}_{nm}^{ETP} whereas taking some sphere of constant radius as a reference surface leads to the SHCs of the *spherical topographic potential* (STP) \bar{V}_{nm}^{STP} . In the course of this work ETP and STP models are also referred to as *ellipsoidally approximated* and *spherically approximated* topographic potential models, respectively. While the ETP at least theoretically can be used to determine Earth's topographic potential exactly, the STP always is subject to (spherical) approximations. The publication *P-IV* is dedicated to the computation of \bar{V}_{nm}^{ETP} and \bar{V}_{nm}^{STP} , and to the interpretation and use of both types of models, which is also discussed in publication *P-I*, Sects. 2.3.2 and 3.3.1.6.

2.2.3 Spherical harmonic truncation, spatial resolution and signal strength

The SHCs of the gravitational potential \bar{V}_{nm} are often referred to as gravitational/gravity field model or geopotential model. Although the series in Eqs. 2.3 and 2.4 theoretically is infinite it commonly is truncated at the maximum degree n_{max} of \bar{V}_{nm} , which defines the spatial resolution of the model. In this work it is aimed to increase the parameter n_{max} (and thus the resolution) of potential models, and to investigate the behavior and suitability of spherical harmonics and spectral modelling approaches at short scales. The relation between spatial resolution x and degree n is provided in good approximation by the spherical harmonic half-wavelength at the equator of Earth following (see e.g. *Jekeli*, 2010, p.840, Eq. 34)

$$x = \frac{\pi \cdot R}{n} \approx \frac{20000 \text{ km}}{n}. \quad (2.9)$$

Giving a simple example, up-to-date satellite gravity missions resolve the gravity field up to degree $n = 250$ (roughly) which translates into spatial scales of $x \approx 80$ km (half-wavelength) or a full-wavelength of 160 km. The high resolution gravity signal that is lost by a truncation of the spherical harmonic series at a distinct n_{max} is called *omission error*. It describes all the signal contained in the omitted frequencies ranging from $n_{max} + 1$ to ∞ . The omission error is an important quality indicator for gravity field models, because the lower it is the closer the model is to the actual potential (at least theoretically). In the same way it also quantifies how much (valuable) gravitational signal can be expected at different scales. In publication *P-I* new empirical estimates

of the omission error at short scales are given, and a degree variance rule that can be used to retrieve the omission error at arbitrary scales between ~ 10 km and ~ 200 m has been formulated. The (dimensionless) spherical harmonic degree variance c_n^2 reflects signal power of the model per degree/resolution and is given by the square sum over all coefficients of the same degree

$$c_n^2 = \sum_{m=-n}^n \bar{V}_{nm}^2, \quad (2.10)$$

and can be related to physically meaningful quantities by scaling factors given, e.g., in *P-I* (Eq. 3 and Table 1 *ibid*). Having the degree variances at hand the (dimensionless) omission error ϵ_{OM} can be expressed as

$$\epsilon_{OM} = \sqrt{\sum_{n=n_{max}+1}^{\infty} c_n^2}. \quad (2.11)$$

The omission error can be translated to physically meaningful quantities (see *P-I*), such as geoid heights N (m)

$$\epsilon_{OM} (N) = R \cdot \epsilon_{OM} \quad (2.12)$$

or gravity disturbances T_r (mGal)

$$\epsilon_{OM} (T_r) = \frac{GM}{R^2} \cdot \sqrt{\sum_{n=n_{max}+1}^{\infty} (n+1)^2 c_n^2} \cdot 10^5. \quad (2.13)$$

2.3 Signal strengths and spherical harmonic characteristics at short-scales

For studying the signal strengths and the characteristics of the topographic potential at short scales (≤ 10 km), either a densely sampled set of observations of a gravity field quantity or forward modelled gravity quantities are needed. Interesting properties are the general variability of the field (e.g. extreme values and the average variability), the decrease of the signal magnitude with increasing resolution as well as regional characteristics and dependencies. However, adequate dense observations are available only locally or regionally. As described in more detail in publication *P-I* (Sect. 2.1 *ibid*) few studies based on high-resolution gravity data for spatially limited test areas exist, e.g. by *Jekeli* (2010). Their findings are relevant for the respective area under investigation but do not give a global picture. At global scale observations are available at best with a resolution of $5'$ and represented in the gravity field model EGM2008 (*Pavlis et al*, 2012), but the used original gravity anomalies are proprietary data of the *NGA* (National Geospatial-Intelligence Agency) and are not available. Therefore, in this work high-resolution gravity quantities computed from forward modelling are used to retrieve short-scale properties of the gravity field. Also other studies use forward modelled gravity to retrieve information about the gravitational field, but global studies are limited to scales of ~ 10 km (*Pavlis et al*, 2007) and shorter scales are only investigated locally (*Voigt and Denker*, 2007). Larger scale terrain effects, by contrast, have been studied more intensively, e.g. path-breaking by *Forsberg* (1984) or *Vassiliou and Schwarz* (1987).

2.3.1 Estimating short-scale signal strengths from an analysis of GGMplus

Here the short-scale gravitational signal is investigated based on the recently published 220m-resolution *Global Gravity Model Plus* (GGMplus) (*Hirt et al*, 2013) that provides discrete gravity values at Earth's physical surface over land areas between $\pm 60^\circ$ latitude. This means modelled gravity is not available over polar areas and oceans, thus the corresponding short-scale signal characteristics found over those areas are not studied here. Today, GGMplus is unprecedented in coverage at this high resolution and therefore allows a broad and detailed view of Earth's gravity field at the same time. In detail, GGMplus combines

- satellite gravity observations from the *Gravity Recovery and Climate Experiment* (GRACE) (*Tapley et al*, 2004) and *Gravity Field and Steady-State Ocean Circulation Explorer* (GOCE) (ESA, 1999) satellite missions in low and mid-frequencies ($n \leq \sim 200$),
- terrestrial and altimetric gravity observations from EGM2008 in mid- to high frequencies ($200 < n \leq 2160$) and
- forward modelled gravity in high to ultra-high frequencies ($n > 2160$).

See *Hirt et al* (2013) for more details on the combination of the gravity information from different sources and frequencies. The forward modelling in GGMplus – in contrast to this work – has been performed by an integration in the space domain and in planar approximation. It follows the RTM principle (*Forsberg*, 1984) and its computation is associated with a huge computational effort, taking estimated $\sim 180,000$ CPU hours, roughly (*Hirt et al*, 2013). The forward modelling is based on the assumption of constant rock-density (the crustal mean density of $2670 \frac{\text{kg}}{\text{m}^3}$ is used) and the topography geometry as given by the 220m-resolution digital elevation model (DEM) from the *Shuttle Radar Topography Mission* (SRTM) (*Farr et al*, 2007). The high and ultra-high frequency characteristics of GGMplus's near-global discretisations of geoid heights and gravity anomalies are studied and analyzed in *P-I* using a 2D-DFT procedure (*Forsberg*, 1984; *Flury*, 2006). The DFT method was

Degree range (Scale)	2161 to 90,000 ($\sim 10 - 0.22$ km)	5401 to 90,000 ($\sim 4 - 0.22$ km)	10,801 to 90,000 ($\sim 2 - 0.22$ km)	21,601 to 90,000 ($\sim 1 - 0.22$ km)
T_r [mGal]	8.62	5.26	3.51	2.23
N [cm]	1.53	0.38	0.13	0.02

Tab. 2.1 – Average signal strength as found over continental areas at Earth’s surface between $\pm \sim 60^\circ$ latitude (polar areas and oceans thus are excluded) for different spatial scales as defined by the GGMplus degree variance rule (*P-I*: Eq. 29) in terms of omission errors of gravity disturbances T_r (mGal) (Eq. 2.12) and geoid heights N (m) (Eq. 2.13). Values are based on the assumptions of a uniform rock-density ($2670 \frac{kg}{m^3}$) and uncompensated masses at short-scales.

found to retrieve the spherical harmonic spectrum of a spatially-limited discretisation of the gravity field in terms of degree variances with an accuracy of 10 – 20 % and in spherical approximation. The resolution of GGMplus allows to recover the spherical harmonic spectrum up to degree 90,000. This resolution it is far beyond the resolution of current spherical harmonic gravity models. Since no comparable work is known that could be used for a cross-validation, the results in this work can be considered pioneering. A full account of the analysis technique, the results and their interpretation is given in paper *P-I*. Among others, the latter publication contains detailed investigations concerning the impact of the geographical limitation of GGMplus and the amplification of gravity signals as projected onto the sphere, as is the case for ordinary spherical harmonic degree variances.

Essentially, the analysis of GGMplus suggests that considerable short-scale gravitational energy is contained in the topographic masses of Earth. Following the average signals strengths in different spectral bands listed in Table 2.1 (taken from Tab. 4 in *P-I*), a spherical harmonic expansion up to degree 5400 (at least) is needed for the often envisaged 1cm-geoid over continental areas. Further, models that with a resolution of ~ 10 km, such as EGM2008, omit gravity signals of averagely 8.6 mGal (1.5 cm) magnitude globally due to the early truncation of the series. But the expected signal strengths strongly depend on the presence and nature of topographic masses, i.e. hills, mountain ranges or flat terrain. This was found by analysing the gravity quantities in $2.5^\circ \times 2.5^\circ$ sized tiles as a function of the contained topographic elevation by means of the so called *terrain RMS* (see *P-I*: Tab. 4 and Fig. 11). In the Himalayas omitted signals as large as 38 mGal (7.51 cm) are to be expected due to a truncation at degree 2160, while it is still 2.8 mGal (0.5 cm) in low elevated regions with a terrain RMS of less than 250 m. These numbers indicate a large variability and large signal magnitudes of the topographic potential at short scales and justifies the attempt to model the high-frequency topographic potential globally as is the purpose of this work.

2.3.2 Understanding topographic potential models and spherical harmonics at high-degrees

The spectral modelling techniques and source-mass models introduced further down (Chpt. 3) were used to create new spherical harmonic models of the TP complete up to degree 5400 (~ 4 km spatial resolution). The short scale behaviour of these models, $dV_ELL_Earth2014_5400$ (ETP model) and $dV_SPH_Earth2014_5400$ (STP model), is investigated here anticipatory. The models are interesting because

- 1) they are – in contrast to GGMplus – truly global representations of the topographic potential and
- 2) they exceed degree 2190 of state-of-the-art gravity models and provide signals down to scales of ~ 4 km.

As discussed elaborately in *P-I* the ETP and STP models have different spectral energy, which is a result of the different approximation of the underlying field generating reference source-mass – an ellipsoid or a sphere, respectively. More precisely it is the term

$$\left(\frac{r_Q}{R}\right)^n \quad (2.14)$$

found in the radial integration of Eq. 2.8, that effects the attenuation of gravitational signal of masses located in the interior of the spherical harmonic reference radius (so where $r_Q < R$). Per definition, in case of ETP modelling, the topographic masses are arranged w.r.t. to a reference ellipsoid with the semi-major axis corresponding to the reference radius ($a = R$). Consequently, a large part of the masses, especially near to the poles, are located inside the reference sphere in this case. In contrast, in the case of STP modelling, the topographic masses are mostly close to or above the spherical reference shell and not affected by stark attenuation. Additionally, the attenuation effect is getting stronger towards short scales because the ratio in Eq. 2.14 is taken to the power of n . This is why the spectrum of ETP or the *ellipsoidal approximation* appears to be underpowered as compared to the STP, especially at short scales.

Another important finding in *P-I* is that the surface to which the spherical harmonic spectrum (and the degree variances) refers, changes its spectral signal decay and magnitude. This is relevant since GGMplus provides gravity at Earth's surface and not downward continued to the reference surface. The latter effect is irrelevant at low degrees, say up to degree 200, but is amplified towards high degrees. The reasoning is similar to the above and related to the attenuation term

$$\left(\frac{R}{r}\right)^n \quad (2.15)$$

found in the spherical harmonic series expansion (Eqs. 2.3 and 2.4), which becomes

$$\left(\frac{r_e}{r}\right)^n \quad (2.16)$$

in the case of choosing an ellipsoidal reference. It means a stronger attenuation of the signal with increasing distance from the reference surface (so where $r > R$ or $r > r_e$, respectively) and with increasing resolution n of the model. Thus, at Earth's physical surface (on top of the topographic masses) the gravitational energy is less than that found at the reference surface, especially at high degrees.

For a full picture of these effects, the degree variances of

- 1a): $dV_SPH_Earth2014_5400$ referring to the reference sphere of radius R ,
- 1b): $dV_SPH_Earth2014_5400$ referring to Earth's surface (at height H above reference sphere),
- 2a): $dV_ELL_Earth2014_5400$ referring to the reference sphere of radius R
- 2b): $dV_ELL_Earth2014_5400$ referring to Earth's surface (at height H above reference ellipsoid)

are computed (Fig. 2.4, top panel). The idea of this exercise also is to get degree variances that represent gravity as found on Earth's surface and are suitable for a comparison with GGMplus. The degree variances (DVs) of the cases 1a) and 2a) can be computed straight forward from the actual coefficients of the models (using Eq. 2.10), because they – per definition – refer to the spherical harmonic reference sphere. The DVs of the STP model 1a) (blue) are running above the ETP model 2a) (magenta), as a consequence of their underlying mass arrangement. In case of 1b) and 2b) DVs have been computed by a synthesis of gravity disturbances at Earth's surface using the *gradient approach* (Hirt, 2012) up to the 15th order as implemented efficiently in the *isGraflab* software (Bucha and Janák, 2014) and a consecutive analysis using a solid spherical harmonic variant of the Gauss-Legendre quadrature (*P-III*). In the analysis a sphere of radius R serves as a reference surface in all cases. As to be expected, the DVs at Earth's surface 1b) (light blue) and 2b) (green) almost coincide, since the gravitational signal is attenuated according to the respective reference surface. Their variances are running below those of 1a) and cross/underrun those of 2a) near degree 3100. Their differences

(red dotted line) manifest the spherical (or ellipsoidal) approximation of the topographic potential in STP and ETP models, respectively; in the space domain these differences amount to ~ 0.35 mGal (RMS), see further down.

Additionally, curves have been fitted in least-squares sense for all three cases (1b and 2b coincide), following the exponential-type (EXP) model

$$c_{EXP,n}^2 = a(bn)^{cn-d}, \quad (2.17)$$

where a, b, c and d are the parameters (given in Tab. 2.2) that can be used to retrieve the degree variances. The mathematical models of other degree variance rules, e.g. those proposed by *Kaula* (1966), *Tscherning and Rapp* (1974) or *Sanso and Sideris* (2013), are found to not adequately model the curvature in the degree variances of these high resolution models, at least for cases 1a) and 2a). For comparison purposes also a Sanso/Sideris-type (SS) model ($P-I$)

$$c_{SS,n}^2 = \frac{a \cdot b^n}{(n-1)(n-2)(n+4)(n+17)} \quad (2.18)$$

is fitted for the case 1b&2b (middle panel in Fig. 2.4). For more details on the historically different mathematical parametrisation of degree variance rules see $P-I$ (Sect. 2.3 and Sect. 3.2). Close to the degree of truncation of the topographic potential models (so near degree 5400/5480) the spectrum starts to drop slightly and does not reflect the general trend at high degrees (in the case of the ETP model the stark drop is related to the ellipsoidal reference, see further down). As a consequence the last 100/180 degrees were not used for the estimation of the degree variance rules, thus they are data-based up to degree 5300, strictly. The quality of the fit is indicated by the residuals with the actual degree variances, which are at the level of 10% of the actual signal over large parts of the spectrum for all EXP-type models (Fig. 2.4, lower panel). The SS-type model for case 1b&2b (light green curve) shows a significantly worse fit in low degrees (up to degree ~ 2000), but nicely fits the DVs in the spectral band $\sim 2000 - 5300$, also at the 10% level.

In Fig. 2.5 the degree variances of the above described DV-rules and the GGMplus DV-rule ($P-I$: Eq. 29) are plotted all together up to degree 10,800, scaled to gravity disturbances in mGal^2 (according to the factors given in $P-I$: Tab.1). Additionally – for the sake of orientation – the gravity-related degree variances of the (spherical harmonic) EGM2008 and the transformed ellipsoidal harmonic EGM2008 (see $P-IV$) are plotted to degree 2190 and 2159, respectively. In the spectral window 5301 to 10,800 the DVs of DV-rules are extrapolations. Very striking is the exponential rise of the gravity-DVs of the ETP and STP model (1a and 2a) towards short scales. The turning point (from falling to rising) is around degree ~ 2000 in case of the STP and ~ 3000 in

Model	type	rule	evaluation at	a	b	c	d
1a	STP	EXP	ref. sphere	$4.18478 \cdot 10^{-20}$	$6.94626 \cdot 10^{-4}$	$7.05915 \cdot 10^{-4}$	3.81921
2a	ETP	EXP	ref. sphere	$3.93368 \cdot 10^{-22}$	$2.08525 \cdot 10^{-4}$	$8.52962 \cdot 10^{-4}$	3.82219
1b&2b	STP/ETP	EXP	Earth's surface	$2.47412 \cdot 10^{-23}$	$9.10380 \cdot 10^{-5}$	$3.52286 \cdot 10^{-4}$	3.74328
1b&2b	STP/ETP	SS	Earth's surface	$5.935595 \cdot 10^{-8}$	1.000035	-	-
GGMplus	STP	SS	Earth's surface	$1.79 \cdot 10^{-7}$	0.999995	-	-

Tab. 2.2 – Degree variance rule parameters for the models $dV_SPH_Earth2014_5400$ and $dV_ELL_Earth2014_5400$ using the parametrisation given by Eq. 2.17 (EXP) and Eq. 2.18 (SS) for an evaluation of the models at the reference sphere of radius R or at Earth's surface, respectively. Also shown are the parameters of the GGMplus DV-rule described in $P-I$. All parameters are derived based on the assumptions of a uniform rock-density ($2670 \frac{\text{kg}}{\text{m}^3}$) and uncompensated masses at short-scales.

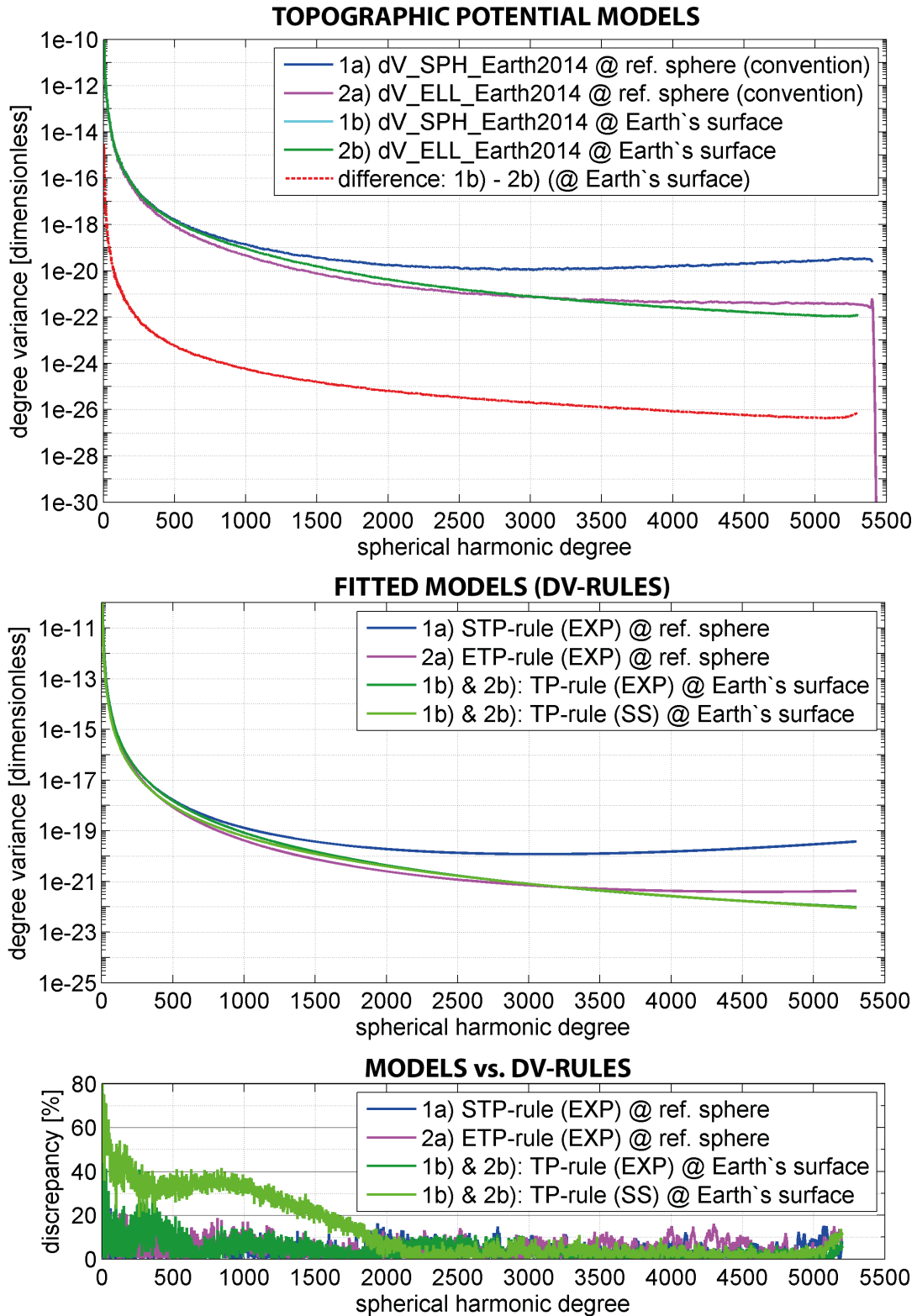


Fig. 2.4 – Dimensionless degree variances of the TP models $dV_SPH_Earth2014_5400$ (STP) and $dV_ELL_Earth2014_5400$ (ETP) referring to the reference sphere (as is convention) and Earth's surface (upper panel); fitted degree variance rules (mid panel) and the accuracy to which the DV-rules represent the actual degree variances in percent (lower panel). Note again that the TP models are based on the assumptions of a uniform rock-density ($2670 \frac{kg}{m^3}$) and uncompensated masses, which is justified only at short-scales.

case of the ETP model. However, as learned from above this is not in contradiction with potential field theory which dictates decreasing energy towards short scales. It simply is a necessity of the spherical harmonic parametrisation that causes the spectrum of the spherical harmonic coefficients to rise with increasing n : since the coefficients, inserted into the spherical harmonic series, must represent the attenuated signal at Earth's surface correctly – and the attenuation is increasing exponentially by n (Eq. 2.15) – they must be amplified accordingly at high degrees n . In other words, the SHCs are consistent amplifications, representing valid surface topographic gravity signals. In contrast – at Earth's surface – the degree variances (light green and red) predict monotonous decreasing energy. This nicely depicts a rather unknown spherical harmonic phenomenon that is present in high-resolution models only and which is found vital for the correct interpretation of the energy of spherical harmonic models (at short scales).

In this context it is found most importantly that the parametrization of the degree variance rules can have a large impact on the extrapolation. This can be seen from the differences between the SS-type and the EXP-type DV-model for $n \geq 5300$ (light green line vs. dotted green line in Fig. 2.5). The EXP-type model in this case falsely predicts rising DVs beyond degree ~ 6000 (dashed green line). Evidence that the EXP-type DV-rule 1b&2b is not correct beyond degree 5400 is also given by the monotonously decreasing GGMplus degree variances which are data-based up to degree 90,000. Certainly, also the extrapolation of SS-type models should be treated carefully. As lesson learned, extrapolations of DV-rules should be handled carefully and the parametrization of the DV-rule must be trustworthy. This finding is underpinned by the diverging results of other DV-rules found in the literature when extrapolated to short scales (*P-I*: Fig. 13).

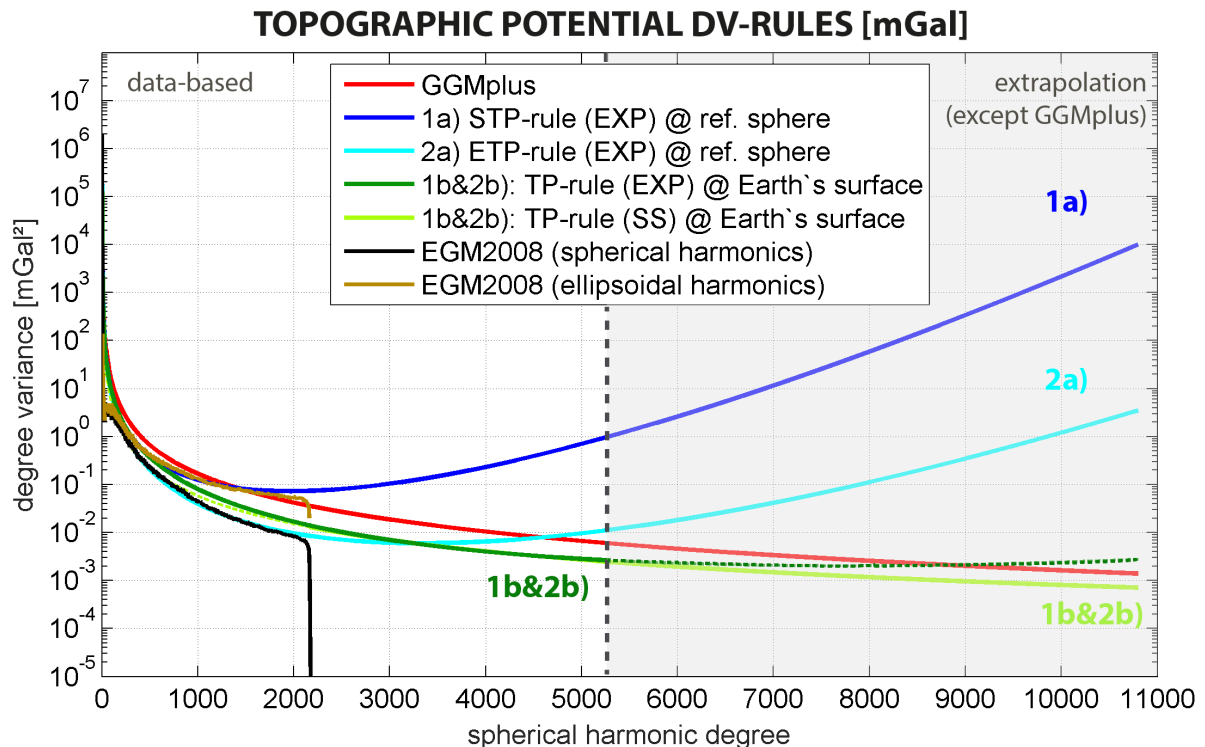


Fig. 2.5 – Degree variances of degree variance rules developed in this work together with the degree variances of the spherical harmonic and the ellipsoidal harmonic EGM2008 in terms of gravity disturbances ($mGal^2$). Beyond degree 5300 the STP and ETP DV-rules are extrapolations.

2.3.3 Estimating short-scale signal strengths from high-degree global topographic potential models

The new analytical models from Tab. 2.2 can be used to estimate the average signal power captured in the spectral band from degree 2161 to 5400 (accumulated via Eq. 2.11) in terms of geoid heights and gravity disturbances (Tab. 2.3). In this band the degree variances are data-based and free of extrapolation errors (see above). The maximum degree of this spectral band exceeds the spatial resolution of up-to-date observation based models by 3210 degrees, i.e. the jump from 10 km scale down to 4 km scale. Generally, the amplitudes in Tab. 2.3 reflect the different level of the degree variances in Figs. 2.4 and 2.5.

The DV-rule 1a with ~ 32 mGal (≈ 5 cm) yields the largest signal in this band. With a considerable gap it is followed by DV-rule 2a with ~ 5 mGal (~ 0.9 cm), and 1b&2b with ~ 4 mGal (~ 0.9 cm). In this spectral band the EXP-type and the SS-type parametrisation of the 1b&2b case deliver the same result in good approximation. The fact that model 1b&2b and 2a provide nearly the same signal strengths can be considered a coincidence, since both differ regarding their approximation level and evaluation surface. Importantly, all models/DV-rules are measures of the signal strength of the (same) topographic potential, but not all of them are useful/valid. Due to the lessons learned from above and from the discussion in *P-I* (Sect. 4.3 *ibid*) the model 1b&2b is considered to deliver the most meaningful signal strengths, because it refers to signal strengths as found at Earth's surface which is needed for most applications in general.

It shall be pointed out explicitly that the STP-rule 1a, the ETP-rule 2a and the actual degree variances of any other observation-based spherical harmonic model are actually not useful to quantify signal strengths at short scales since their spectra refer to the reference sphere of radius R . This leads to an underestimation of the signal strength at $n < \sim 3100$ and to an overestimation for $n > \sim 3100$ in the case of ellipsoidally approximated models. In the case of spherical approximated models the signal strengths are overestimated for $n > \sim 700$.

As an aside, ellipsoidal (spheroidal) harmonic models based on ellipsoidal approximation deliver signal strengths comparable to those of spherical harmonic models based on spherical approximation. The last conclusion is based on the fact that the degree variances of the ellipsoidal harmonic EGM2008 are very close to the STP-rule 1a (EGM2008 slightly dips away beyond degree ≈ 1600 , which might be an effect of underpowered marine gravity in EGM2008 (*Hirt et al*, 2017) and because the degree correlation between the ETP model and EGM2008 only reveal high correlation at high degrees if both are represented in ellipsoidal harmonics (*P-IV*: Fig. 10). In other words, ellipsoidal harmonic models based on ellipsoidal approximation and spherical harmonic models based on spherical approximation are intrinsically consistent and comparable in terms of their spectral energy.

DV-rule	model-type	rule-type	evaluation surface	gravity disturbances T_r [mGal]	geoid heights N [cm]
1a	STP	EXP	ref. sphere	31.73	4.90
2a	ETP	EXP	ref. sphere	4.91	0.92
1b&2b	STP/ETP	EXP	Earth's surface	4.25	0.92
1b&2b	STP/ETP	SS	Earth's surface	4.21	0.91
GGMplus	STP	SS	Earth's surface	6.84	1.49

Tab. 2.3 – Average signal power in the spectral band $2161 < n \leq 5400$ as captured by the degree variance rules created in this work. Values are computed with the omission error formula (Eq. 2.11) and are based on the assumptions of a uniform rock-density ($2670 \frac{kg}{m^3}$) and uncompensated topographic masses at short-scales.

Note, that the SS-type DV-rule 1b&2b equals the GGMplus degree variance rule ($P-I$: Eq.29) in terms of parametrisation, approximation (spherical/STP) and evaluation surface (at Earth's surface). The differences between both (4.25 vs. 6.84 mGal) rules is a result of several effects. Mainly the differences stem from the areas covered by the rules: GGMplus is only based on land data and therefore possesses higher spectral energy (cf. $P-I$: Fig. 6). Apart from that, the computational procedures for the forward modelling differ and the 2D-DFT procedure plus the fitting is able to retrieve the degree variance's energy level with roughly 20% accuracy, only.

2.4 Summary and evaluation of the chapters's research aims

This chapter (Chpt. 2) together with the publication *P-I* are meant to contribute to a better understanding of the topographic potential as used in geodesy and geophysics. The elaboration on Earth's topographic masses, their conceptual usage in geodesy and the distinction from isostatic masses are in the focus of Sect. 2.1 and are fundamental for the correct usage and interpretation of the gravitational attraction that is described by the topographic potential. In this regard the section is an answer to research question Q1. The conventional spherical harmonic parametrisation of the gravitational/topographic potential then is introduced in Sect. 2.2. It is used to analyse, quantify and model the signal strengths at arbitrary scales on a (near) global level in the following section (Sect. 2.3) based on results and findings in *P-I*. Thereby it was found that average signal amplitudes up to ≈ 8.6 mGal in terms of gravity disturbances (≈ 1.5 cm geoid height) are inherent to the continental (=only land) topographic potential at scales smaller than ~ 10 km at Earth's surface. This significant gravitational signal is omitted by current gravity field models that are developed to degree 2190. Based on the investigated data sets up to degree 5400, on global scale the average topography implied signal to be expected in between scales of $\sim 4 - 10$ km amounts to ~ 4.3 mGal (~ 0.9 cm) at Earth's surface. Thus, answering research question Q2, the exploitation of the short-scale topographic potential seems relevant for high-resolution gravity field modelling. Finally, important relationships and short-scale properties that are related to the field-generating reference body, the evaluation surface and the attenuation of the gravitational energy in spherical harmonics could be unveiled, secondarily. Consequently, research aim A1 that reads

"Quantify the signal strengths and examine the spectral characteristics of the topographic potential at short scales."

can be considered to be met, fulfilling also the overall research goal G1.

Chapter 3

Forward Modelling

3.1 General

Forward modelling in the context of this work describes the mathematical and computational process to derive the gravitational potential that is caused by a known source-mass. Here, Earth's topographic potential is sought with the help of an as-detailed-as-possible source-mass model. This requires a solution to Newton's law of gravitation, manifested in an integration over all of Earth's (topographic) masses as, e.g., given by (*P-IV*: Eq.1)

$$V(P) = G \int_B \frac{\rho(Q)}{l(P,Q)} dB(Q), \quad (3.1)$$

where P describes a point exterior to Earth's body B , Q is the source-mass point associated with density $\rho(Q)$, $l(P, Q)$ is the Euclidean distance between P and Q , and the infinitesimal spherical volume element $dB(Q) = r^2 \sin \theta dr d\theta d\lambda$.

Publication *P-II* describes the creation of an up-to-date source-mass model with 1' resolution (~ 2 km) that serves as input data set for all numerical tests and topographic potential models created in this work. The model is briefly presented and input data are discussed in Sect. 3.2.

Numerous forward modelling approaches exist, which typically can be divided into two classes by the respective domain in which the integration takes place: the space domain or the spectral domain. A detailed overview of existing approaches and (selected) relevant literature in chronological order is given in Fig. 3.1, including the placement of the publications of this work. The focus of this work is placed upon forward modelling in the spectral, i.e. spherical harmonic, domain (right side of the chart in Fig. 3.1). In spherical harmonics the integration problem in Eq. 3.1 is derived in spherical coordinates (using geocentric latitudes) and becomes Eq. 2.8, as shown in *P-IV*. Publication *P-IV* is dedicated to a new spectral multi-layer approach for the ETP which is compared to existing spectral approaches of STP and ETP. The principle, important equations, advantages and disadvantages of the different spectral methods are discussed further down (Sect. 3.3). Note that by a different choice of the underlying coordinate system the ETP may also be derived in spheroidal harmonics using reduced latitudes (*Wang and Yang, 2013*) or in ellipsoidal harmonics using geodetic latitudes (*Novak and Grafarend, 2005*), which is not discussed further here.

The spectral methods benefit from efficient transformations (analysis and synthesis) of the so called *height-density functions* (HDFs), sometimes referred to as *topographic height function* (THF), between space and spectral domain by employing FFT-techniques. At high resolution, however, spherical harmonic analysis and synthesis is not a trivial task given the enormous amount of data points, and – numerically as well as arithmetically – intensive operations. Publication *P-III* and Sect. 3.3.2 deal with efficient quadrature techniques as a means for high-resolution spherical harmonic analysis, embodying another thematic focus of this work.

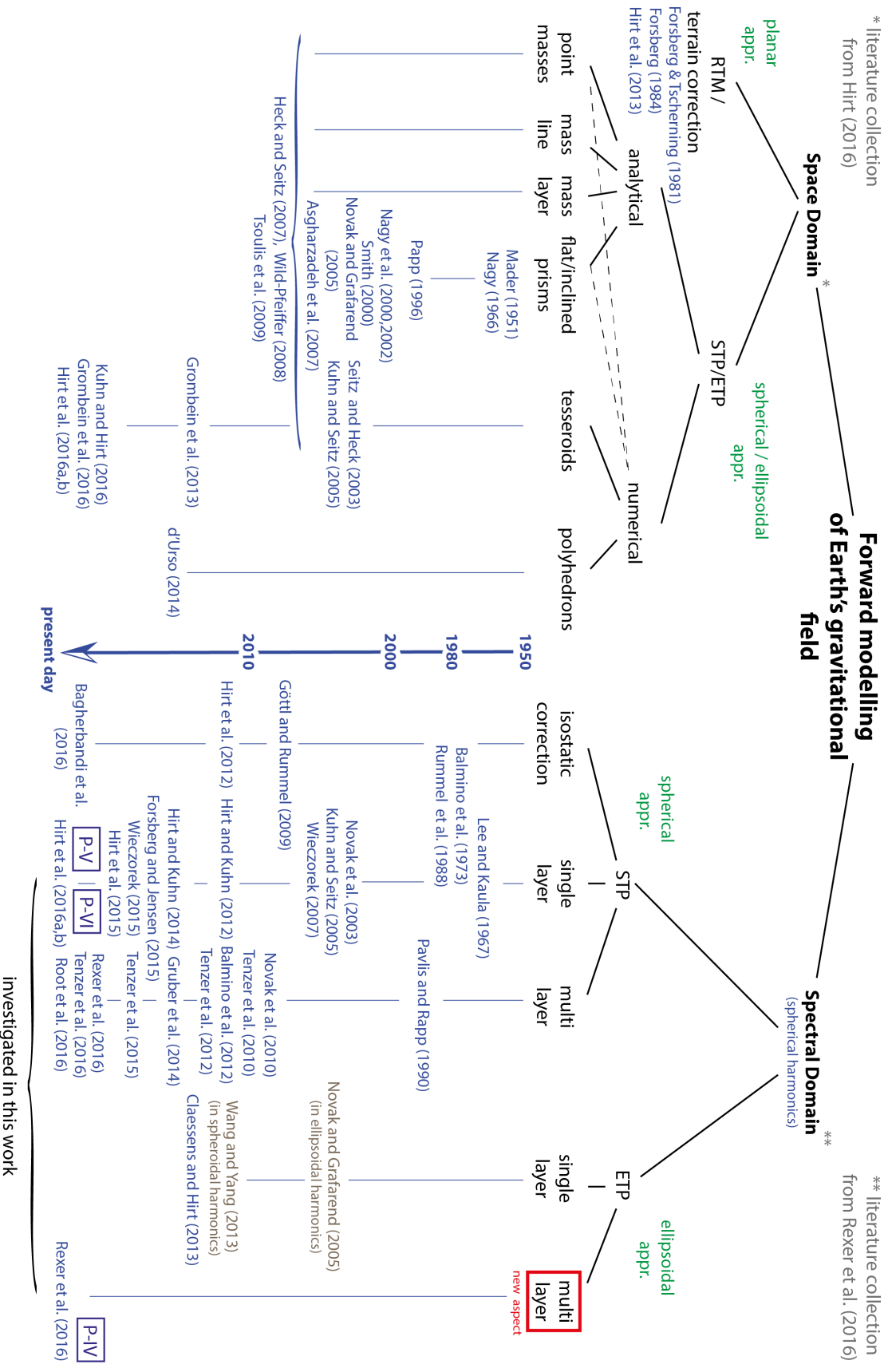


Fig. 3.1 – Tree of forward modelling with (selected) relevant literature in chronological order and placement of the publications that are part of this work.

Finally, the modelling techniques are used and tested to model the topographic potential up to degree 5400 and 21,600, respectively (Sect. 3.4).

3.2 Source-mass models of Earth's topographic masses

A source-mass is defined by a geometric body of known shape and density. A source-mass model accumulates various source-masses in order to describe a more complex body's mass, such as Earth's topographic masses. The gravitational potential originating from that complex body then is the integral effect of all source-masses (Sect. 3.3).

3.2.1 Available source-mass data and its quality

In this work a complete (in the sense of global and 3D) and detailed (in the sense of high-resolution) source-mass model is envisaged. It shall be used to model short-scale gravity effects on global scale. In terms of availability and quality of the source-mass data, the geometric information on the one hand, and the density information on the other hand, have to be treated separately.

In practice, the geometry of Earth's topographic masses is provided in the form of digital elevation models (DEMs) that cover oceanic depths below mean sea level as well as topographic heights above mean sea level. As found in *P-IV* the geometric information is far more reliable as compared to density information, and available in dense grids globally. Over continental and land areas the cell spacing of non-proprietary and non-commercial available elevation grids is at the level of ~ 30 m. The quality and accuracy of up-to-date ~ 30 m resolution DEMs was investigated, e.g., by *Rexer and Hirt (2014)*. They found that the most accurate and reliable of which – the hole-filled CGIAR-CSI SRTM v4.1 – is based on data of the SRTM mission, providing heights with approximately 4.5 m accuracy over the Australian continent on average. Since Australia is sparsely covered by vegetation and is morphologically rather smooth, this is a rather optimistic value. Over mountain ranges the accuracy varies between 8–15 m (*Rexer and Hirt, 2014*). For an overview of current models, space-missions and sensors and their sensor-specific limitations we refer to *Rexer and Hirt (2014)*. Recently, a 12m-resolution DEM with a designated height accuracy of ~ 4 m globally has become available with TanDEM-X's *WorldDEM (Bartusch et al, 2008)*. Already the intermediate releases of WorldDEM were found to outperform any existing global DEM over land (*Rexer and Hirt, 2016*). Unfortunately, WorldDEM is not freely available as a whole for research, thus, in this work SRTM serves as best source for global land elevations.

The ocean's floor, which is described by bathymetric depths, is known with less detail simply due to the fact that it is obscure to optical and radar-based satellite sensors. The depth of the ocean floor "(...) is sensed directly only via local-scale ship soundings and determined globally indirectly via ties to the altimetric gravity field (*Smith and Sandwell 1994*). According to *Sandwell et al. (2014)*, more than 50 % of the ocean is more than 10 km away from the next direct depth measurement. The highest resolution gravity field over the oceans is derived from satellite altimetry, and available models reach $\sim 1'$ (~ 2 km) resolution (*Andersen et al. 2013; Sandwell et al. 2014*) at best. (...) But due to the attenuation of the shorter wavelength (altimetric) gravity signals, the estimation of bathymetric heights from gravity works best in the wavelength band from 12 km to 160 km (*Sandwell et al, 2014*), which means it is of lower quality at scales < 12 km." (*P-III*).

Mainly, however, the creation of a more detailed source-mass model is obstructed by the poor knowledge of the actual density distribution of Earth's masses, at least on global scale. As elaborated in publication *P-IV*, the highest resolution global density model (CRUST1.0) is laterally limited to a spatial scale of ~ 110 km (1°). As

a workaround, density will be assumed homogeneous for defined geophysical layers in the construction of a composite model of Earth's topographic masses in the following. The approximate character of this assumption is discussed further down.

3.2.2 Earth2014: a 1' composite source-mass model

The construction and a detailed description of the source-mass model, Earth2014, which is used throughout this work is given in publication *P-II*. In brief it provides topographic heights, bedrock heights (i.e. solid rock elevations covered by ice, ocean water or water of large lakes) and ice-sheet thickness for polar regions. Its 1 arc-min grid spacing (~ 2 km scale) is reasonable given the available true resolution of bathymetric depth data (see above) and is commensurate to other existing global geometric models such as ETOPO1 (*Amante and Eakins, 2009*). Also two higher resolution global models exist: SRTM30PLUS and its successor SRTM15PLUS (*Becker et al, 2009*). The gain in resolution in the latter models, however, can not be fully exploited by the respective input data, especially over the oceans and over polar regions. Compared to those data sets Earth2014 comprises more recent and improved input-data sets – e.g. the hole-filled SRTM V4.1 topography (*Jarvis et al, 2008*) over land areas between $\pm 60^\circ$ latitude, Bedmap2 (*Fretwell et al, 2013*) for bedrock geometry, bathymetry and ice-sheet thickness over Antarctica, and the Greenland Bedrock Topography (GBTv3) (*Bamber et al, 2013*) – that make Earth2014 a decent representation of Earth's topographic masses. This is confirmed by *Hirt et al (2015)* who show that gravity forward modelled using the Earth2014 data set explains the medium/high resolution gravitational patterns sensed by GOCE satellite better or at least equivalently compared with other available source-mass models.

Earth2014 is composed by the layers

- SUR*: Earth's surface (i.e. lower bound of the atmosphere),
- BED*: bedrock of Earth (i.e. solid rock below water and ice),
- TBI*: Earth's surface over land and bedrock below water masses, and
- ICE*: ice-sheet thicknesses

that represent the boundaries to the volumetric geophysical layers of the solid crust, ocean water masses, lake water masses and ice-sheets, as needed in multi-layer spectral forward modelling approaches. A guide how to use Earth2014 in a multi-layer modelling approach is given in *P-IV* (Sect. 3 *ibid*). The layer boundaries were also expanded to degree-10800 surface SHCs that are needed to facilitate e.g. spherical harmonic filtering and oversampling as required in the forward modelling process.

The complete Earth2014 data set, i.e. 1'-layer grids and their degree-10800 SHCs, is publicly available and can be freely downloaded: http://ddfe.curtin.edu.au/models/Earth2014/potential_model/. It receives quite some attention and is used within the community, e.g. by *Grombein et al (2016b)* and *Tenzer et al (2016)*.

By associating density distributions, i.e. 2D or 3D-functions of mass-density, to the geophysical layers, Earth2014 becomes a source-mass model. As discussed above the poor knowledge of Earth's short-scale density distribution enforce the choice of constant density values for each layer in this work. The density in each layer is defined by state-of-the-art estimates of their average values (see *P-IV*: Tab. 7). Earth's crust is associated with an average value of $\rho_0 \approx 2670 \frac{kg}{m^3}$. Since the crustal layer consists of various types of solid matter in lateral and vertical direction, it is subject to largest approximation errors. The crust hosts materials such as sediments ($\rho \approx 2000 - 2200 \frac{kg}{m^3}$) and basalt ($\rho \approx 2900 \frac{kg}{m^3}$) beneath the ocean floor, granite ($\rho \approx 2500 - 2800 \frac{kg}{m^3}$) in the upper crust, and, basalt and gabbro ($\rho \approx 2700 - 3100 \frac{kg}{m^3}$) in the lower crust (*Torge, 2003*). At maximum, thus,

the crustal density locally may deviate roughly by about 20 – 25% ($+760 \frac{kg}{m^3}$ or $-430 \frac{kg}{m^3}$) relative to the mean density in extreme cases. Over the Canadian Rocky Mountains, the "(...) *relative error of this approximation, reaching up to 10 % [in terms of gravity at Earth's surface], can further be decreased by using a laterally-varying mass density*" (Novak, 2010), as found by Huang *et al* (2001). In general, however, the application of ρ_0 works quite satisfactory (as will be shown) and is common practice. Still, the approximation with mean density values results in differences between forward modelled and observed gravity. Those differences reflect density inhomogeneities that exist in Earth's interior. In geodesy this type of gravity differences are named *Bouguer anomalies* (Torge (2003) and see Sect. 4.3.2).

In reality, also the seawater of the oceans, and ice-sheets do not have homogenous density distributions. In fact seawater density generally increases with depth/pressure, primarily. Secondly, it also varies with temperature and salinity. The effect of vertical density variations in the ocean water has been investigated recently using a simple polynomial to account for the variations during the integration by Tenzer *et al* (2010, 2012). They found that the approximation of the actual seawater with its mean value lead to relative inaccuracies of about 2% translating into a maximum of "(...) $200 \frac{m^2}{s^2}$ and 16 mGal in computed values of the bathymetric potential and attraction, respectively. Extreme values apply particularly to the computation areas situated over the deepest oceans." (Tenzer *et al*, 2012). These small effects seem acceptable given the overall uncertainty of bathymetric depths and are not modelled explicitly in this work.

As an aside the Earth2014 data set contains a rock-equivalent-topography (RET) layer that is the input boundary for single-layer forward modelling. The RET describes Earth's surface in terms of the (constant) density of solid-rock, in this case the crustal mean density ρ_0 . In this concept water and ice masses are compressed by applying the respective density ratio $\frac{\rho}{\rho_0}$ to their vertical geometric extend in each grid cell (see *P-II* for the exact definition). As a consequence the geometry of Earth is changed, but the overall mass balance is retained.

In terms of gravity, the RET leads to approximation errors at the level of 1.8 mGal (RMS) at Earth's surface when modelled up to degree 2190, globally (*P-IV*). Over the oceans the errors are at the level of 10 – 20 mGal and can reach up to +66 mGal or –46 mGal over the deepest parts of the oceans (cf. *P-IV*: Fig. 8).

3.3 Spectral forward modelling

Spectral forward modelling deals with the solution of Eq. 3.1, Newton's integral law, in the spherical harmonic domain. In spherical harmonics the problem is formulated by Eq. 2.8. Different analytical and computational solutions to this problem are presented and reviewed in the following. Thereby attention is directed towards increasing the resolution during the modelling and towards adaptations that are required to realise high-resolution modelling successfully.

3.3.1 Modelling techniques and most important equations

As seen from Fig. 3.1 (right branch) the spectral modelling techniques can be subdivided into modelling of the spherical topographic potential (STP) and ellipsoidal topographic potential (ETP). The first of which uses a sphere, the latter an oblate ellipsoid of revolution as reference body during the modelling. In both cases the coordinate system is truly spherical (with geocentric latitudes) and the modelling relies on spherical harmonic base functions. The reference body serves as the reference source-mass and on the same time defines the geometric reference surface for the description of topographic masses; thus it defines the overall mass-arrangement in the modelling approach.

In both cases a single or a multi-layer approach can be considered. Modelling of isostatic corrections is not done, resulting in uncompensated topographic potential models, generally (Sect. 2.1.2). The single-layer modelling has approximate character since it is commonly used together with the RET-boundary surface, that covers all of Earth's masses condensed into one layer (see above and *P-II*). In contrast, multi-layer modelling is capable of combining the gravitational effects of an arbitrary number of volumetric layers that are bounded by two geometric surfaces, defining the lower-bound (LB) and the upper-bound (UP) of the layers. The multi-layer modelling in the ETP-case is novel and has been developed in the course of this work. In both, multi- and single-layer modelling, a lateral varying density distribution can be applied separately for each layer, while the density must be assumed constant in the vertical direction in each cell. Further, the modelling can be done rigorously (exact) or efficiently using binominal series expansions for some of the involved terms. Both, rigorous and exact solutions, are based on the spectral variant of the Newtonian integral (Eq. 2.8). Assuming constant mass-density (in a layer) the radial integral of the inverse distance can be solved analytically resulting in the rigorous solution. Applying a binominal expression when solving the integral results in the efficient solution, where the infinite binominal series needs to be truncated for its numerical evaluation. This makes the efficient solution a lot faster than the rigorous solution, in general. However, the convergence of the series is not guaranteed for a general geometry. The convergence of all occurring binominal series is comprehensively addressed further down in the dissertation and publication *P-IV*.

For a complete picture of all techniques, the equations of spectral forward modelling are given here in rigorous (exact) and efficient notation (Eqs. 3.2 to 3.21). The expressions are grouped into four tables as follows:

Tab. 3.1 : single-layer STP modelling,

Tab. 3.2 : multi-layer STP modelling,

Tab. 3.3 : single-layer ETP modelling,

Tab. 3.4 : multi-layer ETP modelling.

The derivations of all equations can be found in *P-IV*. The parameters \hat{V}_{nm} denote the rigorous SHCs and \bar{V}_{nm} denote the SHCs given by the efficient expressions. The binominal series expansions in the efficient

modelling procedures with the binominal orders k and j , as well as differences between \hat{V}_{nm} and \bar{V}_{nm} are treated further down. Important parameters are explained below, a full list of all parameters/symbols is given in Tab. 3.5.

Spherical Topographic Potential (STP) single-layer	
rigorous	$\hat{V}_{nm}^{(STP)} = \frac{3}{\bar{\rho}(2n+1)(n+3)} \overline{HDF}_{nnm}^{(STP)} \quad (3.2)$
solution	$\overline{HDF}_{nnm}^{(STP)} = \frac{1}{4\pi} \int_{\lambda=0}^{2\pi} \int_{\theta=0}^{\pi} \rho(\theta, \lambda) \left(\frac{R + D_{RET}}{R} \right)^{n+3} \bar{Y}_{nm}(\theta, \lambda) \sin \theta d\theta d\lambda. \quad (3.3)$

efficient	$\bar{V}_{nm}^{(STP)} = \frac{3}{\bar{\rho}(2n+1)(n+3)} \sum_{k=1}^{k_{max}} \binom{n+3}{k} \overline{HDF}_{knm}^{(STP)} \quad (3.4)$
solution	$\overline{HDF}_{knm}^{(STP)} = \frac{1}{4\pi} \int_{\lambda=0}^{2\pi} \int_{\theta=0}^{\pi} \rho(\theta, \lambda) \left(\frac{D_{RET}}{R} \right)^k \bar{Y}_{nm}(\theta, \lambda) \sin \theta d\theta d\lambda. \quad (3.5)$

Tab. 3.1 – Single-layer expressions for the spherical topographic potential (STP).

Spherical Topographic Potential (STP) multi-layer	
rigorous	$\hat{V}_{nm}^{(STP)} = \sum_{\omega=1}^{\omega_{max}} \hat{V}_{nm}^{(STP, \Omega\omega)} \quad (3.6)$
solution	$\overline{HDF}_{nnm}^{(STP, \Omega\omega)} = \frac{1}{4\pi} \int_{\lambda=0}^{2\pi} \int_{\theta=0}^{\pi} \rho^{(\Omega\omega)}(\theta, \lambda) \left(\left(\frac{R + D_{UB}^{(\Omega\omega)}}{R} \right)^{n+3} - \left(\frac{R + D_{LB}^{(\Omega\omega)}}{R} \right)^{n+3} \right) \bar{Y}_{nm}(\theta, \lambda) \sin \theta d\theta d\lambda. \quad (3.8)$

efficient	$\bar{V}_{nm}^{(STP)} = \sum_{\omega=1}^{\omega_{max}} \bar{V}_{nm}^{(STP, \Omega\omega)} \quad (3.9)$
solution	$\overline{HDF}_{knm}^{(STP, \Omega\omega)} = \frac{1}{4\pi} \int_{\lambda=0}^{2\pi} \int_{\theta=0}^{\pi} \rho^{(\Omega\omega)}(\theta, \lambda) \left(\left(\frac{D_{UB}^{(\Omega\omega)}}{R} \right)^k - \left(\frac{D_{LB}^{(\Omega\omega)}}{R} \right)^k \right) \bar{Y}_{nm}(\theta, \lambda) \sin \theta d\theta d\lambda \quad (3.11)$

Tab. 3.2 – Multi-layer expressions for the spherical topographic potential (STP).

Ellipsoidal Topographic Potential (ETP) single-layer	
rigorous solution	$\hat{V}_{nm}^{(ETP)} = \frac{3}{\bar{\rho}(2n+1)(n+3)} \overline{HDF}_{nnm}^{(ETP)} \quad (3.12)$
	$\overline{HDF}_{nnm}^{(ETP)} = \frac{1}{4\pi} \int_{\lambda=0}^{2\pi} \int_{\theta=0}^{\pi} \rho(\theta, \lambda) \left(\frac{r_e}{R}\right)^{n+3} \left(\frac{r_e + d_{RET}}{r_e}\right)^{n+3} \bar{Y}_{nm}(\theta, \lambda) \sin\theta d\theta d\lambda \quad (3.13)$

efficient solution	$\bar{V}_{nm}^{(ETP)} = \frac{3}{\bar{\rho}(2n+1)(n+3)} \left(\frac{b}{R}\right)^{n+3k_{max}} \sum_{k=1}^{n+3k_{max}} \binom{n+3}{k} \sum_{j=0}^{j_{max}} (-1)^j \binom{-\frac{n+3}{2}}{j} e^{2j} \sum_{i=-j}^j \bar{K}_{nm}^{2i,2j} \overline{HDF}_{klm}^{(ETP)} \quad (3.14)$
	$\overline{HDF}_{klm}^{(ETP)} = \frac{1}{4\pi} \int_{\lambda=0}^{2\pi} \int_{\theta=0}^{\pi} \rho(\theta, \lambda) \left(\frac{d_{LB}}{r_e}\right)^k \bar{Y}_{lm}(\theta, \lambda) \sin\theta d\theta d\lambda \quad (3.15)$

Tab. 3.3 – Single-layer expressions for the ellipsoidal topographic potential (ETP).

Ellipsoidal Topographic Potential (ETP) multi-layer	
rigorous solution	$\hat{V}_{nm}^{(ETP)} = \sum_{\omega=1}^{\omega_{max}} \hat{V}_{nm}^{(ETP, \Omega_{\omega})} \quad (3.16)$
	$\hat{V}_{nm}^{(ETP, \Omega_{\omega})} = \frac{3}{\bar{\rho}(2n+1)(n+3)} \overline{HDF}_{nnm}^{(ETP, \Omega_{\omega})} \quad (3.17)$
	$\overline{HDF}_{nnm}^{(ETP, \Omega_{\omega})} = \frac{1}{4\pi} \int_{\lambda=0}^{2\pi} \int_{\theta=0}^{\pi} \rho^{(\Omega_{\omega})}(\theta, \lambda) \left(\frac{r_e}{R}\right)^{n+3} \left(\left(\frac{r_e + d_{UB}^{(\Omega_{\omega})}}{r_e}\right)^{n+3} - \left(\frac{r_e + d_{LB}^{(\Omega_{\omega})}}{r_e}\right)^{n+3} \right) \bar{Y}_{nm}(\theta, \lambda) \sin\theta d\theta d\lambda \quad (3.18)$

efficient solution	$\bar{V}_{nm}^{(ETP)} = \sum_{\omega=1}^{\omega_{max}} \bar{V}_{nm}^{(ETP, \Omega_{\omega})} \quad (3.19)$
	$\bar{V}_{nm}^{(ETP, \Omega_{\omega})} = \frac{3}{\bar{\rho}(2n+1)(n+3)} \left(\frac{b}{R}\right)^{n+3k_{max}} \sum_{k=1}^{n+3k_{max}} \binom{n+3}{k} \sum_{j=0}^{j_{max}} (-1)^j \binom{-\frac{n+3}{2}}{j} e^{2j} \sum_{i=-j}^j \bar{K}_{nm}^{2i,2j} \overline{HDF}_{klm}^{(ETP, \Omega_{\omega})} \quad (3.20)$
	$\overline{HDF}_{klm}^{(ETP, \Omega_{\omega})} = \frac{1}{4\pi} \int_{\lambda=0}^{2\pi} \int_{\theta=0}^{\pi} \rho^{(\Omega_{\omega})}(\theta, \lambda) \left(\left(\frac{d_{UB}^{(\Omega_{\omega})}}{r_e}\right)^k - \left(\frac{d_{LB}^{(\Omega_{\omega})}}{r_e}\right)^k \right) \bar{Y}_{lm}(\theta, \lambda) \sin\theta d\theta d\lambda \quad (3.21)$

Tab. 3.4 – Multi-layer expressions for the ellipsoidal topographic potential (ETP).

symbol		meaning of symbol
rigorous sol.	efficient sol.	
$\hat{V}_{nm}^{(STP)}$	$\bar{V}_{nm}^{(STP)}$	SHCs of the STP model
$\hat{V}_{nm}^{(STP, \Omega_\omega)}$	$\bar{V}_{nm}^{(STP, \Omega_\omega)}$	SHCs of layer Ω_ω of the STP model
$\overline{HDF}_{nnm}^{(STP)}$	$\overline{HDF}_{knm}^{(STP)}$	surface SHCs of the height density function of a (single-layer) STP model
$\overline{HDF}_{nnm}^{(STP, \Omega_\omega)}$	$\overline{HDF}_{knm}^{(STP, \Omega_\omega)}$	surface SHCs of the height density function of layer Ω_ω of the STP model
$\hat{V}_{nm}^{(ETP)}$	$\bar{V}_{nm}^{(ETP)}$	SHCs of the ETP model
$\hat{V}_{nm}^{(ETP, \Omega_\omega)}$	$\bar{V}_{nm}^{(ETP, \Omega_\omega)}$	SHCs of layer Ω_ω of the ETP model
$\overline{HDF}_{nnm}^{(ETP)}$	$\overline{HDF}_{knm}^{(ETP)}$	surface SHCs of the height density function of the (single-layer) ETP model
$\overline{HDF}_{nnm}^{(ETP, \Omega_\omega)}$	$\overline{HDF}_{knm}^{(ETP, \Omega_\omega)}$	surface SHCs of the height density function of layer Ω_ω of the ETP model
	Ω_ω	layer ω
	ω_{max}	maximum number of layers
	$\bar{\rho}$	Earth's mean density
	$\rho(\theta, \lambda)$	density at the point defined by the spherical coordinates θ, λ
	$\rho^{(\Omega_\omega)}(\theta, \lambda)$	layer's density at the point defined by the spherical coordinates θ, λ
	R	spherical reference radius of the topographic potential model
	r_e	ellipsoidal radius
	D_{RET}	mapped spherical height of the RET function
	D_{UB}	mapped spherical height of the upper bound of the volumetric layer
	D_{LB}	mapped spherical height of the lower bound of the volumetric layer
	d_{RET}	mapped ellipsoidal height of the RET function
	d_{UB}	mapped ellipsoidal height of the upper bound of the volumetric layer
	d_{LB}	mapped ellipsoidal height of the lower bound of the volumetric layer
	$\bar{Y}_{nm}(\theta, \lambda)$	fully-normalised spherical harmonic functions (Eq. 2.5)
	$K_{nm}^{2i, 2j}$	sinusoidal Legendre-weights (see <i>Claessens and Hirt (2013)</i>)
	k	binominal order of k -series (see Sect. 3.3.1.2)
	j	binominal order j -series (see Sect. 3.3.1.3)
	nm	spherical harmonic degree n and order m
	l	spherical harmonic degree $n + 2i$

Tab. 3.5 – List of parameters/symbols used in the STP and ETP expressions in Tabs. 3.1 to 3.4.

3.3.1.1 Geometric parameters

The parameter \overline{HDF}_{knm} and \overline{HDF}_{nnm} denote the surface SHCs of the *height density function* of the respective volumetric layer Ω_ω taken to the power of k or n , respectively. The surface SHCs can be obtained by spherical harmonic analysis (SHA). An exact and efficient SHA is of great importance in spectral forward modelling, especially when aiming at high resolution as explained further down. The Sect. 3.3.2 is dedicated to SHA procedures in the context of forward modelling. The number of layers ω_{max} is arbitrary and depends on the application and available source-mass data.

For a detailed description of the geometric situation and heights applied in ETP and STP modelling it is referred to *P-IV* (Fig. 13 and Tab. 9, *ibid*); the variables are only recalled briefly in the following. In the case of STP modelling, the geometric definition of a layer's boundaries is given by the mapped spherical height D_{UB} and D_{LB} (UB: upper bound; LB: lower bound) that is measured in radial direction from the reference sphere of radius R to the (mapped) surface points. In case of ETP modelling, the layer's boundaries are given by the mapped ellipsoidal height d_{UB} and d_{LB} which is defined as the radial distance between reference ellipsoid (given by the ellipsoidal radius r_e) and (mapped) surface point.

Note that only the ETP expressions can be used with an exact geometric definition of Earth's topographic masses, i.e. without any mapping/projection, when so called *pseudo-ellipsoidal heights* h^l are used. These heights are defined in radial direction, describing the distance between reference ellipsoid and actual surface point, and can be computed from ellipsoidal heights (see appendix 2 in *P-IV*).

Using d instead of h' can be regarded as ellipsoidal approximation and leads to the ellipsoidally approximated ETP. The mapping is discussed in *P-IV* and was found to lead to a surface-point-displacement of 33 m at maximum, which translates into maximum errors in the order of ± 3 mGal ($RMS = 0.04$ mGal) for modelling up to degree 2160/2190.

In practice, often orthometric heights are used in both cases (H replaces D and d), i.e. the geoid height is neglected. The error introduced by this approximation is in the order of ~ 3.7 mGal (RMS), ranging in between $\sim \pm 14$ mGal (not shown). This was found using EGM96 to compute geoid heights that can be used as boundary function in ETP modelling. The effect, however, is mainly of long wavelength character – in fact it shows analogies to the actual geoid structure – and diminishes quickly towards shorter wavelengths. In the spectral band $n = 281 - 2190$ the effect only shows an average signal $RMS \approx 0.04$ mGal, ranging in between $\sim \pm 2$ mGal.

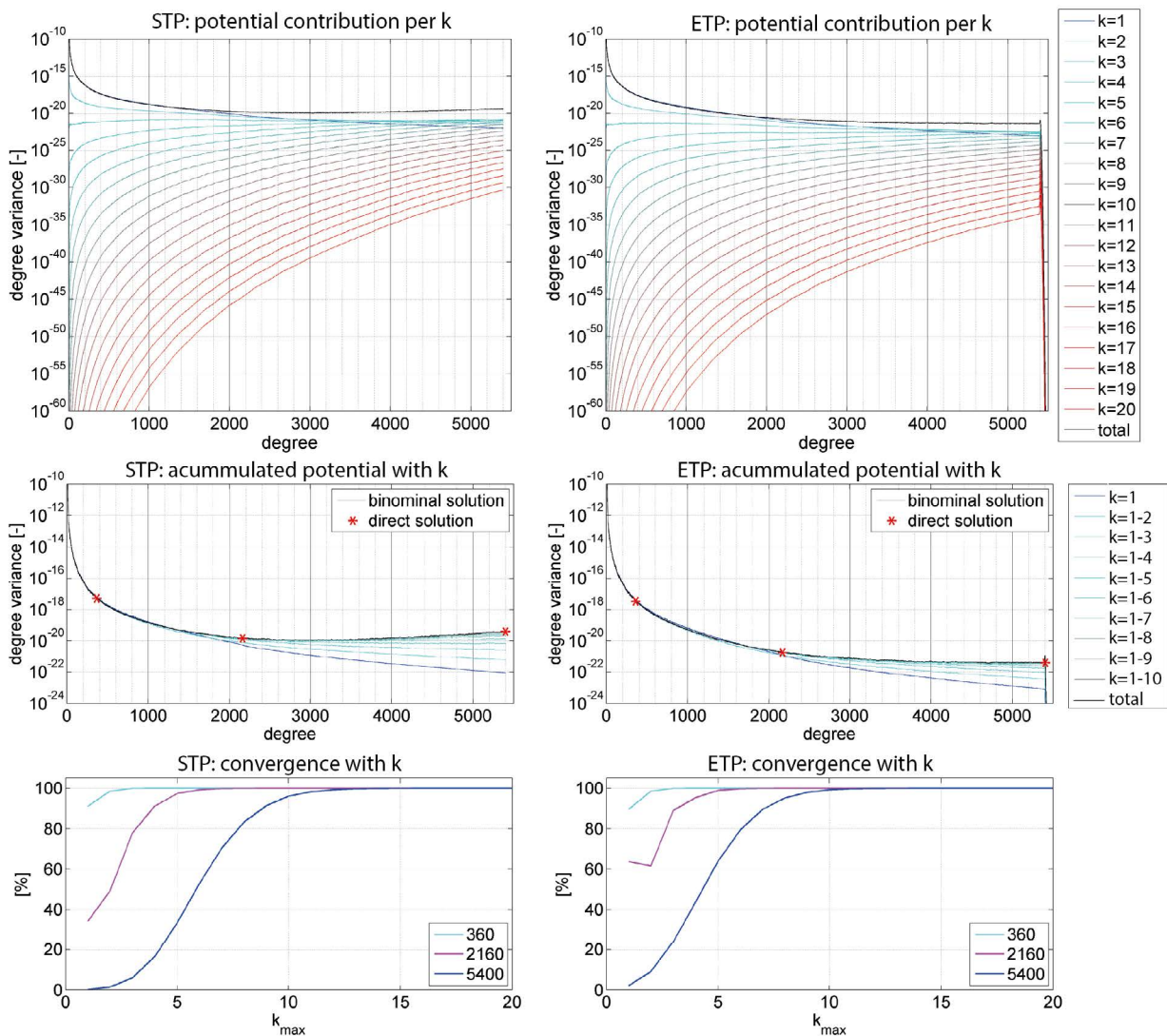


Fig. 3.2 – Meaning and convergence associated with binominal order k used within efficient spectral modelling of STP: \bar{V}_{nm}^{STP} (left plots) and ETP: \bar{V}_{nm}^{ETP} (right plots) in terms of degree variances: potential contribution per order k (upper row); accumulated potential for various orders of k (middle row) together with the direct (rigorous) solutions (\hat{V}_{nm}^{STP} and \hat{V}_{nm}^{ETP}) for degrees 360, 2160 and 5400 (red asterisks); convergence of the efficient modelling method as a function of order k for degrees 360, 2160 and 5400 in percent by comparison against the rigorous value, where 100 % means efficient and rigorous solution coincide (bottom row).

3.3.1.2 Meaning of parameter k and k_{max}

The parameter k denotes the order of the binominal series expansion introduced for the terms $\left(\left(\frac{R+D}{R}\right)^{n+3} - 1\right)$ ($P-IV$: Eq. 17) and $\left(\left(\frac{r_e+d}{r_e}\right)^{n+3} - 1\right)$ ($P-IV$: Eq. 25) in the efficient expressions of STP (Eqs. 3.4/3.10) and ETP (Eqs. 3.14/3.20), respectively. The series expansions and their convergence behaviour were investigated in detail in $P-IV$. The choice of k_{max} depends on the maximum degree n , on the value range of d and D , and to a small extent also on R and r_e , respectively. The theoretical values for the truncation of this series – when the relative error associated with the truncation of the binominal series falls below 1% – for various model resolutions n_{max} are given in $P-IV$: Tab. 1. It tells us that k_{max} generally increases with n_{max} . This is accompanied by an increase of computational costs. There are two main implications of k for the processing: First, k_{max} SHAs are required for each layer boundary. Second, to account for the $(k - 1) \cdot n_{max}$ additional frequencies introduced by the exponentiation of the HDF with k , the grid-size has to be adapted – theoretically up to the maximum frequency $k_{max} \cdot n_{max}$ – in order to avoid aliasing effects during the analysis (see Sect. 3.4.1.2 for further details). The issue: grid size and memory requirements grow non-linearly, approximately by the factor k_{max}^2 . Nevertheless, employing the binominal series is much less costly than the rigorous solution where n_{max} analyses of each HDF are needed and aliasing has to be taken care of, too.

The meaning of parameter k and differences between \hat{V}_{nm} and \bar{V}_{nm} are visualised in Fig. 3.2 for the STP and the ETP case in terms of degree variances of the single-layer solution. The modelling is complete up to degree 5400 and 5480, respectively, and based on the RET2014 layer of Earth2014. The truncation of the k -series is discussed in Sect. 3.4.1.1, where an absolute criterion is suggested instead of the relative criterion in $P-IV$.

3.3.1.3 Meaning of parameter j and j_{max}

The parameter j denotes the order of the binominal series expansion found in the efficient solution to the ETP (Eqs. 3.14 and 3.20). The binominal series replaces the term $\left(\frac{r_e}{R}\right)^{n+3}$ ($P-IV$: Eq. 27) in Eqs. 3.13 and 3.18

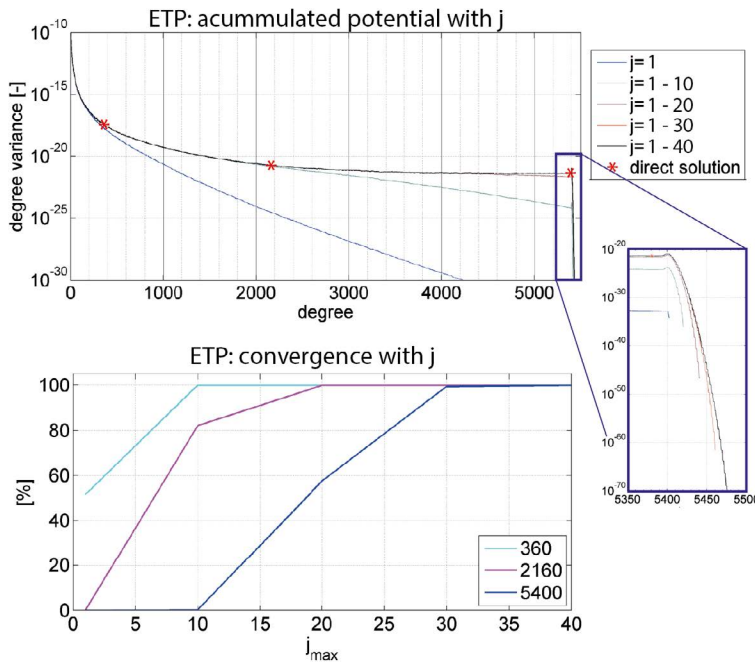


Fig. 3.3 – Meaning and convergence associated with binominal order j used within efficient spectral modelling of the ETP (\bar{V}_{nm}^{ETP}); upper plot: degree variances of accumulated potential for various orders of j together with the direct (rigorous) solution for degrees 360, 2160 and 5400 (red asterisks); lower plot: convergence of the efficient modelling method as a function of order j for degrees 360, 2160 and 5400 in percent through the comparison against the rigorous value \hat{V}_{nm}^{ETP} (100 % means efficient and rigorous solution coincide).

and accounts for the oblateness of Earth during the modelling. The always converging series (*Claessens and Hirt, 2013*) is based on relations with the sinusoidal Legendre-weights $K_{nm}^{2i,2j}$ (*Claessens, 2006*) which can be computed through the recursion relations in *Claessens and Hirt (2013)* (Appendix A, *ibid*). The choice of j_{max} for sufficient convergence was investigated in *P-IV* and the theoretical orders of truncation are given in *P-IV* (Tab. 2). Generally a higher n_{max} in the modelling requires the choice of a higher j_{max} . The series converges faster at the poles than at the equator, therefore the co-latitude $\theta = 90$ delivers the critical truncation value. The series is responsible for (algebraic) correlations among the coefficients (see Sect. A.1) and for additional coefficients of degrees $n_{max} < n \leq n_{max} + 2j_{max}$ and orders $m \leq n_{max}$, that are always required for the correct synthesis of gravity functionals. Those become visible by a "tail" in the degree variances (right-hand side plot in Fig. 3.3).

The meaning and convergence behaviour of j is shown exemplary by the degree variances of the ETP single-layer solution up to degree 5400 in Fig. 3.3. The truncation of the j -series is discussed in Sect. 3.4.1.1 with an absolute criterion instead of the relative criterion in *P-IV*.

3.3.1.4 Workflow and computational demands

The general workflow of spectral topographic potential modelling as done in this work is shown in Fig. 3.4. It starts with the discretised Earth2014 layer boundaries and ends with the synthesised gravity functional in the space domain (white background). The radial integration and summation over k and j is done in the spectral domain (shaded in grey). The computationally most demanding step is the transition from space to spectral

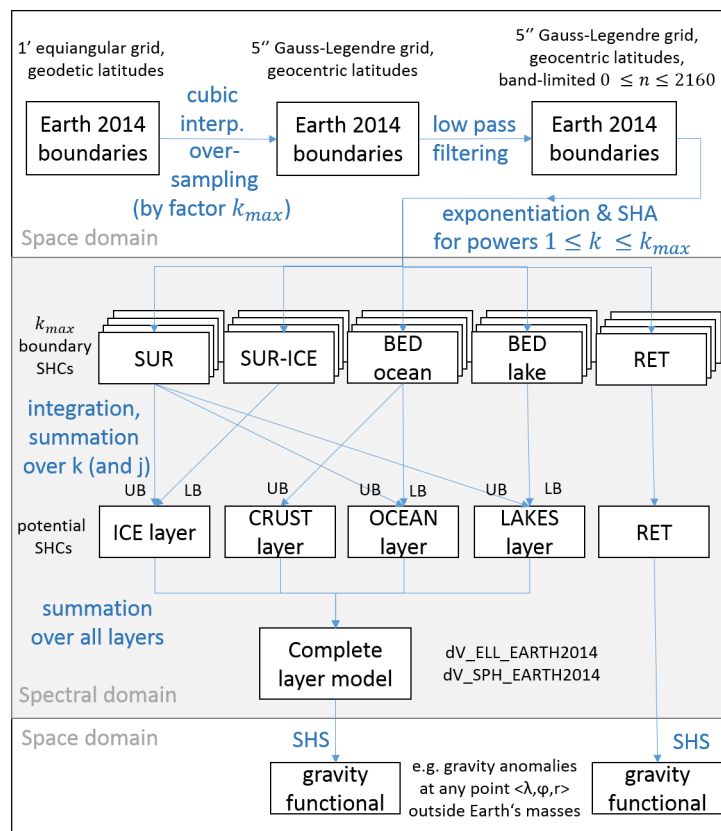


Fig. 3.4 – Scheme of the processing workflow of spectral topographic potential modelling, here exemplary for $n_{max} = 2160$ and $k_{max} = 12$.

model type	n_{max}	k_{max}	j_{max}	layers	SHA time [CPU h]	integration time [CPU h]	total time [CPU h]
STP	2160	12	-	1	1.25	0.02	1.27
				4	6.25	0.08	6.33
	5400	25	-	1	247.33	0.10	247.43
				4	989.33	0.40	989.73
ETP	2160	12	30	1	1.25	0.4	1.65
				4	6.25	2.00	8.25
	5400	25	40	1	247.33	22.5	269.83
				4	989.33	90.00	1079.33

Tab. 3.6 – Computation times for (single and multi-layer) STP and ETP modelling with the efficient expressions (Eqs. 3.4/3.10 and Eqs. 3.14/3.20). *Integration time* here denotes the time required for the summation over k, j and i . CPU hours are calculated as the product of processing time and the number of allocated workers/CPU's for the individual process. Remark to integration times: the STP integration is implemented in MATLAB, while the ETP integration is implemented mainly in FORTRAN (F95).

domain (and vice versa) facilitated by means of SHA (and SHS, see Sect. 3.3.2). Comparing solely the computational demand of the integration of an ETP model to that of an STP model based on the needed CPU hours (Tab. 3.6) shows that at a resolution of $n_{max} = 2160$ the ETP integration is about 25 times more intensive owing to the additional summation over j . At a resolution of $n_{max} = 5400$ it is already about 225 times. Note that the additional computation time is not critical since the overall integration time in the latter case accumulates to roughly 2 CPU h and is much lower than the time needed for the SHA. Note that CPU hours only serve as an estimate of the computational effort associated with a computational process since it depends on various factors, e.g. the quality of the implementation, CPU features and the used compiler/language. Importantly, the computation time increases – in good approximation – linearly with the number of modelled layers in both, ETP and STP.

3.3.1.5 Rigorous vs. efficient expressions

The efficient expressions should always be preferred to the rigorous expressions, especially for high-resolution modelling. There are two main arguments for this suggestion: Firstly, the computational effort is tremendously smaller within the efficient approaches generally since the rigorous approach requires n_{max} instead of k_{max} analyses, where $k_{max} \ll n_{max}$. Secondly, the exponentiation of the boundary functions (or HDFs) by n_{max} would require stark oversampling (theoretically of factor n_{max}) to ensure that no aliasing occurs during the analysis, which results in excessively large grids very soon. Nevertheless, the rigorous expressions can help to cross-validate the efficient modelling with spot-checks (at least approximately), see Fig. 3.2. On the other hand, the efficient expressions require a sound investigation and understanding of the convergence behaviour of involved binomial series expansions to avoid that significant signal contributions are omitted by mistake (see Sect. 3.4).

3.3.1.6 STP vs. ETP modelling

Both, STP and ETP models are valid and usable representations of the topographic potential. However, the respective spherical and ellipsoidal approximations cause characteristic differences that make them more or less suitable, or even deny their usage, for different applications.

First, the different reference surfaces used in the modelling dictate the reference surface that has to be used for their evaluation in the space domain (via SHS): ETP models have to be evaluated on or above the ellipsoid

and STP models have to be evaluated on or above a reference sphere of radius R (Claessens and Hirt, 2013). If an evaluation above the reference surface is deemed, the height – following the spherical harmonic concept with geocentric coordinates – is applied in radial direction.

A detailed comparison of STP and ETP in spectral and space domain up to degree 2160/2190 can be found in *P-IV* and *P-I*. Based on the investigations in these publications, the following advantages, disadvantages and possible applications can be stated:

- The STP is a simple and easy to implement modelling approach, while the ETP is more complex and thus more susceptible for mistakes.
- The STP modelling is the more efficient approach in terms of integration time, especially at high degrees. Nevertheless, the integration time is not critical, i.e. tiny compared with the time needed for the analysis of the boundary functions.
- The ETP with ellipsoidal approximation is less affected by mapping (displacement of masses stays below 33 m) and shows less associated approximation errors as compared with the STP with spherical approximation. In the space domain, the spherical approximation effect/error – which appears in the difference between ETP and STP – amounts to about ± 3 mGal (RMS ≈ 0.4 mGal) at the Earth's surface and shows rather long-wavelength structures that are correlated with topography. Therefore ETP models are desirable for applications that require a high accuracy or need to resolve the topography-implied gravity down to very short scales.
- The spectrum of the ETP is compatible with state-of-the-art gravity field models (cf. <http://icgem.gfz-potsdam.de/ICGEM/>). In contrast, the spectrum of STP models tends to follow Kaula's rule and truly ellipsoidal harmonic gravity models, roughly. Observation-based spherical harmonic gravity models such as EGM2008 represent Earth's actual mass distribution which – in approximation – are given by an ellipsoid of revolution. Thus, they can be considered to inherently rely on an ellipsoidal approximation. This makes the ETP usable for combination strategies based on regularisation (see Sect. 4.1).
- While STP models can be promptly truncated at arbitrary degree in the series expansion, the truncation of the ETP series leads to erroneous patterns in the space domain. These truncation errors, also sometimes referred to as *striations*, are more severe in high latitudes and grow with the harmonic degree of truncation. In principle the errors are very similar to those occurring when truncating EGM2008 at $n_{max} < 2190$. Therefore ETP models should strictly be evaluated up to their maximum degree (n_{max}). The reason are correlations/dependencies among the coefficients of ETP models that require a special filtering when some kind of band-limited usage is envisaged (see appendix A.1). The dependencies in ETP models, e.g., were found to manipulate the degree correlation to other (observation-based) models (see *P-IV*) or lead to misinterpretation when single or a few harmonic coefficients are investigated separately.
- The relation of degree variances to physically meaningful quantities that would allow the realistic estimation of short-scale signal strengths or omission errors is only possible with STP models. Since ETP models represent gravity of an ellipsoidal mass distribution and degree variances refer to the spherical harmonic reference radius R , the ETP spectrum underestimates gravity signals increasingly with rising degree. As a workaround ETP models have to be transformed to ellipsoidal harmonics in order to deliver physically-meaningful degree variances. (cf. Sect. 2.3 and *P-I*)

The differences between ETP and STP at short scales are investigated in Sect. 3.4.1.4.

3.3.1.7 Single vs. multi-layer modelling

The single-layer modelling means a simplification of the modelling process since it compresses all water and ice-masses in a single layer, the RET (see end of Sect. 3.2.2), and is therefore sometimes also called RET-modelling. As explained above this is associated with a geometric rearrangement of Earth's masses. The approximation error associated with this compression is most severely, but not exclusively, found over oceans, lakes and ice covered regions and reaches some tens of mGal – in extreme cases up to ± 70 mGal (*P-IV*). In fact, the approximation also leads to gravity errors over the continents and at global scale (albeit small). These are the outcomes of the investigations in publication *P-IV* (Sect. 4.1 and 4.2) where the comparison to observed gravity from GOCE satellite could be used to validate the benefit of layer-modelling globally down to scales of ~ 80 km. The RET approximation error at short scales ($\sim 4 - 10$ km) is investigated in Sect. 3.4.1.5. The single-layer approach is useful for applications such as geoid modelling based on remove-compute-restore schemes, however, whenever (geo-) physical interpretation sought, the multi-layer approach should be used instead. Note, that at very high elevation (such as satellite orbit height) the numerical values of both approaches may coincide, because of attenuation of gravity signals (and of RET approximation errors) with increasing distance from the spherical reference surface.

3.3.2 Analysis techniques

3.3.2.1 Surface spherical harmonic analysis

In spectral forward modelling the spherical harmonic analysis facilitates the transition from space to spectral domain (see Fig. 3.4). It thus enables the subsequent spectral integration that is based on the relations between the SHCs of the mass-density distribution and the SHCs of gravitational potential. Therefore SHA is an important component of the forward modelling procedure. The importance of the SHA also becomes evident considering that the analysis in the modelling is the time-critical component in the processing (Tab. 3.6).

Here a surface spherical harmonic analysis technique is sought that provides a computational solution to the spherical double integral

$$\bar{F}_{nm} = \frac{1}{4\pi} \int_{\lambda=0}^{2\pi} \int_{\theta=0}^{\pi} f(\theta, \lambda) \bar{Y}_{nm}(\theta, \lambda) \sin \theta d\theta d\lambda \quad (3.22)$$

and results in the fully-normalised surface spherical harmonic coefficients \bar{F}_{nm} of some continuous function f given on the sphere (or a spheroid). In our case the functions that need to be analysed are height density functions of the volumetric layers aiming at their spherical harmonic representation \overline{HDF}_{nm} (below and cf. Eqs. 3.4 to 3.21).

3.3.2.2 Numerical quadrature as means for high and ultra-high degree analysis

The publication *P-III* is concerned with the evaluation of two promising exact quadrature techniques: Gauss-Legendre quadrature (GLQ), see e.g. *Sneeuw* (1994), and quadrature based on Driscoll/Healy's sampling theorem (DHQ) (*Driscoll and Healy*, 1994). In general quadratures denote a numerical integration based on FFT (*Walker*, 1996), see e.g. *Hofsommer* (1957); *Colombo* (1981); *Sneeuw* (1994). Principally also an analysis based on a least-squares (*Sneeuw*, 1994; *Pavlis*, 2011) or collocation techniques (*Moritz*, 1978; *Arabelos and Tscherning*, 1998) can be considered to solve Eq. 3.22. The latter techniques are advantageous because

they additionally provide variance-covariance information and can be applied to arbitrarily sampled functions. However, at high resolutions the normal equation system becomes extremely large and impossible to solve by today's computational means. Inversions of full normal equation systems of degree 720 require large-scale computational resources as demonstrated by *Fecher et al* (2013); no higher degree inversion is known. As this work aims at resolutions ≥ 2160 quadrature techniques become inevitable. Alternatively – if a least-squares formulation is wanted – only a block-diagonal technique (*Gruber, 1999; Pavlis, 2011*) can be used to achieve a computationally solvable least-squares problem. A least-squares block-diagonal formulation, however, is equivalent to quadrature in terms of computational constraints and was shown to deduce into a quadrature formally (*Sneeuw, 1994*). The major disadvantage of quadrature (and of block-diagonal formulations) is that the function needs to be sampled with equi-distant spacing in longitudinal direction (a prerequisite for employing FFTs) and/or according to some other regular spacing in general, at least for exact quadrature formulations. Since the HDFs are available with a regular spacing in terms of dense global grids (in this work Earth2014 is used, see *P-II* and Sect. 3.2) this methodological shortcoming of quadratures is mitigated. Remark: individual existing discretisation (=sampling) differences between Earth2014 and the quadrature prerequisites can be circumvented by means of a 2D-interpolation. In the processing in this work (Fig. 3.4) stark oversampling mitigates interpolation inaccuracies.

During the evaluation of GLQ and DHQ in *P-III* it was shown that both techniques – principally – are analysis techniques suitable for the purpose of forward modelling. Even at a high degree such as 21,600, a precision in the order of $< 5 \cdot 10^{-5}$ m could be achieved by analysing and synthesising band-limited topographic surface functions in a closed-loop environment. Generally, at high-degree the GLQ is advantageous because of minimal requirements regarding memory consumption and less mathematical operations, resulting into shorter computation times. To achieve the latter, i.e. spherical harmonic transforms at resolutions $n_{max} \geq 2160$, two major computational measures were found to be necessary: 1) extension of the arithmetics during the computation of the ALFs and 2) parallel computing. The first modification is needed to ensure a numerically exact evaluation of the ALFs at high degrees which was realised successfully by employing the *X-number* approach (*Fukushima, 2012a,b*). The second adaptation was achieved by embedding OpenMP parallel directives in certain parts of the analysis process in order to achieve acceptable computation times. For details on the modifications it is referred to *P-III* at this point.

The correct operability of DHQ and GLQ up to ultra-high degree has been demonstrated with the Martian ($n_{max} = 23,040$), Earth's ($n_{max} = 43,200$) and the Lunar ($n_{max} = 46,080$) topographic surface functions resolved down to scales of ~ 460 m, ~ 460 m and ~ 120 m, respectively (*P-III*: Sect. 4). Interestingly, Moon's surface depicts the largest variability (in terms of STD applied to its topographic function) and on the same time shows the least residuals errors during the analysis (~ 0.9 m). This is explained as follows: since Moon's spherical harmonic expansion is the highest among the three, the associated truncation error of the spherical harmonic series is expected to be smaller. As an aside, the spectral analysis of the planetary topographic surface functions was used to reveal "(...) artifacts and systematics/characteristics of the observation techniques used for the creation of the elevation data." (*P-III*).

3.3.2.3 Analysis of height-density-functions in forward modelling

In the analysis of the HDFs in Eqs. 3.4 to 3.21 another computational aspect comes into play: the exponentiation with the binominal order k . This supposedly unsuspecting operation has some implications that deserve special attention during the analysis.

First, it leads to large numbers. These large numbers were found to cause overflow in a quadrature (GLQ or

DHQ) implemented in double precision (REAL*8) and for large k . The value of k , where the overflow occurs depends on the numerical range of the HDF itself. As a simple workaround, the HDF can be normalised by its largest absolute value following

$$HDF^*(\theta, \lambda) = \frac{HDF(\theta, \lambda)}{\max(|HDF(\theta, \lambda)|)}, \quad (3.23)$$

prior to the exponentiation so that the function to be analysed stays in the numerical range $[-1 \ 1]$. Then the normalised SHCs \overline{HDF}_{knm}^* of order k have to be renormalised afterwards by

$$\overline{HDF}_{knm} = \overline{HDF}_{knm}^* \cdot (\max(|HDF(\theta, \lambda)|))^k, \quad (3.24)$$

resulting in the SHCs of the HDF taken to the k -th power. Alternatively to a normalisation extended arithmetics similar to the X-number approach (see above) or even quadruple precision could be used to solve the overflow problem. Those solutions were not investigated.

The other implication of the exponentiation is that it increases the number of frequencies – the spectral bandwidth N – covered by the HDF. In fact, it increases proportionally with the exponent k according to (Hirt and Kuhn, 2014)

$$N(k) = kN. \quad (3.25)$$

As discussed above and in publication *P-IV* this causes increased sampling requirements (oversampling) to avoid aliasing problems during the analysis. This can lead to very large grids, since the grid size grows quadratically with finer sampling. However, in most cases oversampling by a factor $k < k_{max}$ can sufficiently ban aliasing effects (see Sect. 3.4.1.2). The actual meaning of Eq. 3.25 – which in brief denotes that a "(...) *band-limited topographic mass distribution generates a full-spectrum gravity field*" (Hirt and Kuhn, 2014) – is explained in more detail in Hirt and Kuhn (2014) and *P-VI*. Importantly, Eq. 3.25 implies that (spherical harmonic) frequency filtering in the domain of source-mass models is not equivalent to frequency filtering in the gravity domain. This is the very reason why RTM (Forsberg, 1984) is not an optimal forward modelling procedure.

3.4 Global spectral forward modelling with high resolution

In this section the global spectral forward modelling techniques and source-mass data presented in Sect. 3.2 and 3.3 are used to demonstrate and investigate the potential of spectral forward modelling for resolutions smaller than 10 km ($n_{max} > 2160/2190$). The methods and data sets were already tested and validated in *P-IV* up to degree 2160/2190. The novelty here solely is the increase in resolution n_{max} during the modelling.

The following demonstrations focus on the efficient multi-layer expressions (Eqs. 3.10/3.11 and 3.20/3.21 for STP and ETP, respectively) by using the layer-reduction-approach (LRA) (*P-IV*). The Gauss-Legendre quadrature technique (*P-III*; Eqs. 2 and 10 - 11) is used for the analysis, since this set-up is most promising in regard of computational demand, smallest level of approximation and increased resolution.

3.4.1 A complete degree-5400 model (~ 4 km resolution)

Here a topographic potential model of degree 5400 is modelled with the efficient spectral expressions (Eqs. 3.10/3.11 and 3.20/3.21). The modelling involves the computation of nearly 30 million SHCs which require 233.3 MByte memory when stored in a double-precision binary variable.

3.4.1.1 Choice of k_{max} and j_{max}

The first step compared with degree-2160 modelling is the consideration of increased maximum orders k_{max} and j_{max} to ensure convergence of the involved binominal series expansions.

According to the theoretical values for truncation, when the relative signal amplitude of the binominal term (BT) of order k (*P-IV*: Eq.17 and 25) and j (*P-IV*: Eq.27) falls below 1% w.r.t. the maximum amplitude (*P-IV*: Tab. 1), $k_{max} = 17$ and $j_{max} = 34$ should be sufficient at degree 5400. Looking at the signal amplitudes of the gravity contributions per k at Earth's surface suggests that the convergence is not reached yet at $k_{max} = 17$ since significant signal is contained for $k = 17$ (up to $\sim \pm 80$ mGal, cf. Tab. 3.7). Those large values must be associated rather with single spikes (at discrete places on Earth) where the convergence is not yet reached, since the global RMS becomes smaller than 1 mGal for $k > 15$. The reason is that the relative 1% criterion is a

k	Min [mGal]	Max [mGal]	Mean [mGal]	RMS [mGal]
1	-942.36	580.85	-284.02	350.23
2	-443.98	427.96	0.21	9.39
3	-780.09	1068.42	-0.02	7.69
4	-1676.63	1512.18	0	8.01
5	-2308.71	2065.93	-0.01	8.58
6	-2490.41	2902.09	0	8.96
7	-3112.88	2764.81	0	8.92
8	-2664.35	2922.52	0	8.29
9	-2445.65	2270.21	0	7.14
10	-1914.91	1849.83	0	5.68
11	-1475.67	1537.15	0	4.19
12	-1132.92	1083.23	0	2.87
13	-735.81	771.73	0	1.84
14	-488.64	465.01	0	1.11
15	-274.71	289.01	0	0.63
16	-160.36	152.33	0	0.34
17	-79.63	83.78	0	0.17
18	-41.36	39.32	0	0.08
19	-18.40	19.35	0	0.04
20	-8.6	8.19	0	0.02
21	-3.47	3.64	0	0.01
22	-1.47	1.4	0	0
23	-0.54	0.57	0	0
24	-0.21	0.2	0	0
25	-0.07	0.08	0	0
1-25	-803.24	669.22	-283.83	349.57

Tab. 3.7 – Descriptive statistics of the gravity signal produced by the order k^{th} STP contribution based on the Earth2014 data set, evaluated at the Earth's surface (in terms of gravity disturbances). Unit is in mGal.

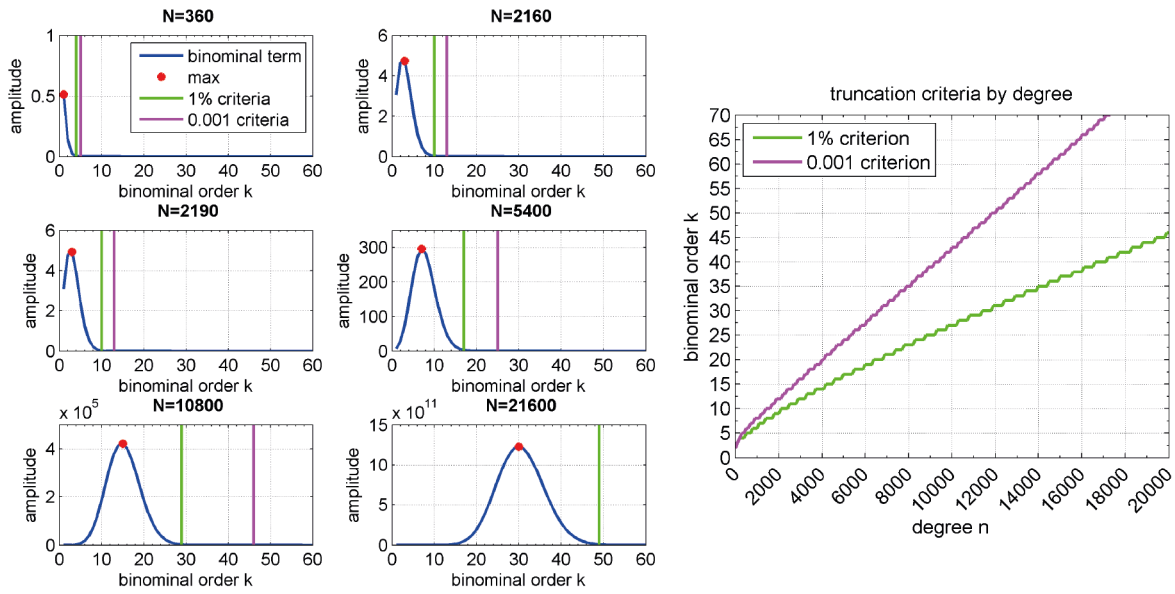


Fig. 3.5 – Left: Amplitude of the binominal term (BT) running over k (P -IV: Eq. 17 and 25) for $d/D/H = +9$ km and $R/r_e = 6378137$ m (blue) together with the relative truncation criterion $BT < 1\%$ (green) and the absolute truncation criterion $BT < 0.001$ (magenta). Right: Both truncation criteria as a function of degree n .

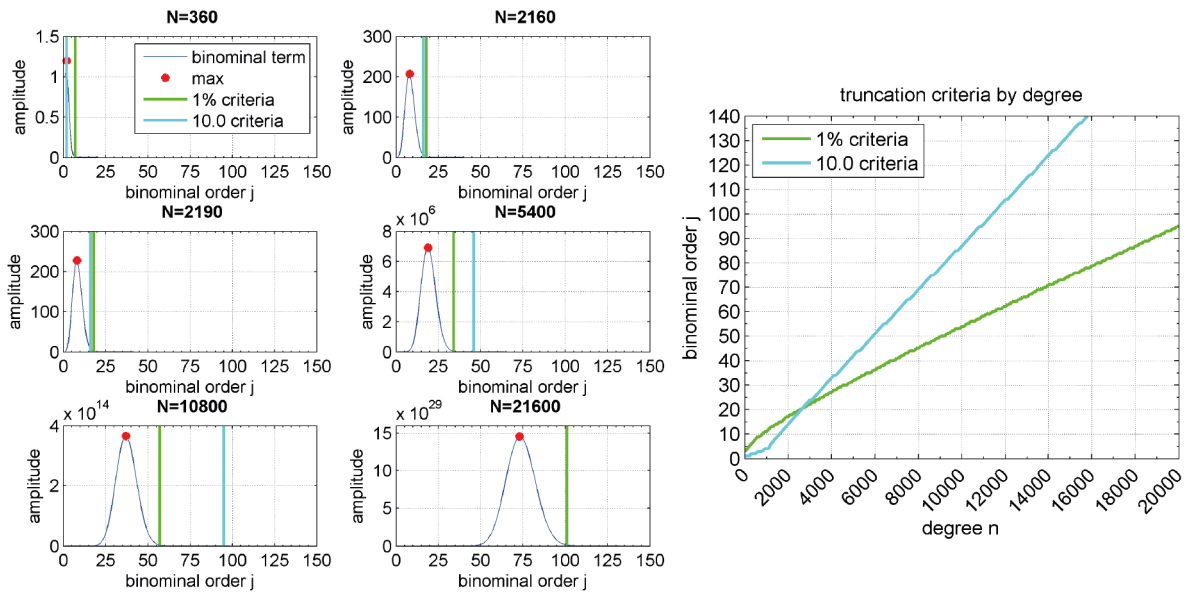


Fig. 3.6 – Left: Amplitude of the binominal term (BT) running over j (P -IV: Eq. 27) for $\theta = 90^\circ$ km, $R = 6378137$ m and $b = 6356752.5$ (blue) together with the relative truncation criterion $BT < 1\%$ (green) and the absolute truncation criterion $BT < 10.0$ (light blue). Right: Both truncation criteria as a function of degree n .

bad criterion at high n_{max} since the amplitudes of the binomial terms grow dramatically with increasing n_{max} (Fig. 3.5: left plot). As a consequence, rather an absolute than a relative truncation criterion should be used to predict the convergence of the k -series. Taking the absolute criterion $BT < 0.001$ which coincides with the amplitude of the BT where the convergence is reached in the case of $n_{max} = 5400$ and $k = 25$ (cf. Tab. 3.7)

suggests higher k_{max} than the relative ones listed in *P-IV*: Tab. 1 (Fig. 3.5: right plot). Note that because of the product

$$\prod_{i=1}^k (n+4-i) \quad (3.26)$$

found in the computation of the binominal coefficient – it runs into an overflow in a double precision environment close to degree $n = 17800$ and $k = 72$ – no BTs for $k > 71$ were computed.

In similar manner, the 1%-criterion also is a bad criterion for the binominal series running over j for $n_{max} > 2160$. The amplitude of the BT (*P-IV*: Eq. 27) also grows dramatically with n_{max} (Fig. 3.6: left plot). In this case an absolute criterion of $BT < 10.0$ seems sufficient and it corresponds to convergence at $j_{max} = 46$ for $n_{max} = 5400$. The 10.0 criterion is rather overcautious as seen from the degree variances differences between the potential based on $j_{max} = 30, 40, 50$ with that based on $j_{max} = 60$ (Fig. 3.7), which suggest that $j_{max} = 40$ should already be enough. However, the j -series is not the critical series in terms of the overall computation time, thus overshooting j_{max} is not a problem in this regard. Note that also the j -series is subject to overflow issues in double precision close to $j > 145$ and $n_{max} = 16500$. The overflow occurs in the computation of the binominal coefficient

$$\binom{-\frac{n+3}{2}}{j} = \frac{1}{j!} \prod_{i=1}^j \left(-\frac{n+3}{2} + 1 - i\right). \quad (3.27)$$

Nevertheless, due to the linear increase of k_{max} with n_{max} according to the 0.001-criterion, and j_{max} with n_{max} according to the 10.0-criterion the following empirical rules of thumb for correct truncations of the binominal series expansions in spectral modelling is postulated for $n_{max} > 2160$:

$$k_{max} = 13 + 3.828 \cdot 10^{-3}(n_{max} - 2160), \quad (3.28)$$

$$j_{max} = 16 + 9.014 \cdot 10^{-3}(n_{max} - 2160). \quad (3.29)$$

These rules of thumb have been derived from the average change rate of k and j by n using the absolute criteria for $n > 2160$ shown in Fig. 3.5 (magenta line) and Fig. 3.6 (light blue line), respectively. From the change rates in the above equations we learn that j_{max} increases faster than k_{max} .

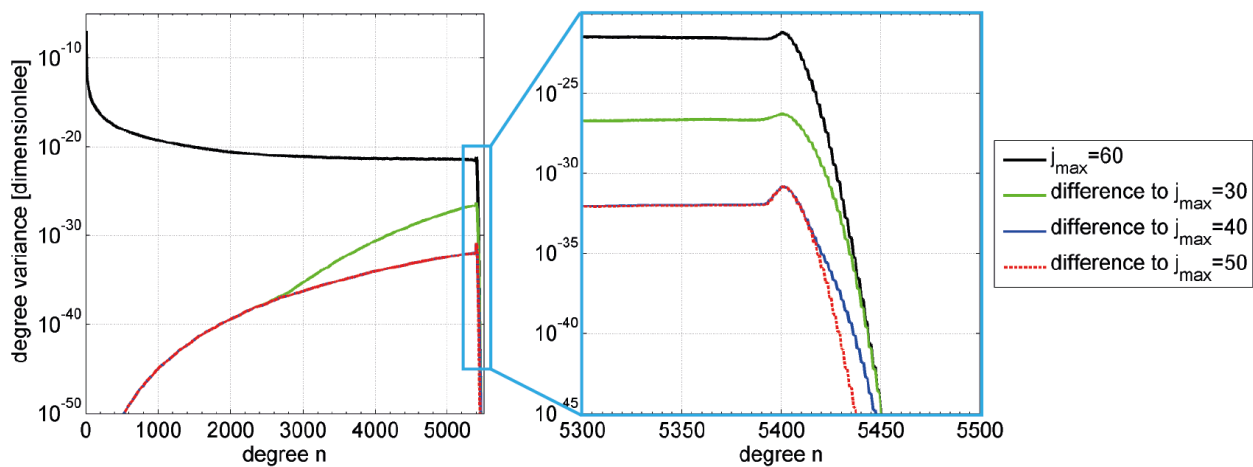


Fig. 3.7 – Degree variances of the RET2014 potential modelled with $j_{max} = 60$ (black) and differences to the respective degree variances corresponding to $j_{max} = 30, 40, 50$.

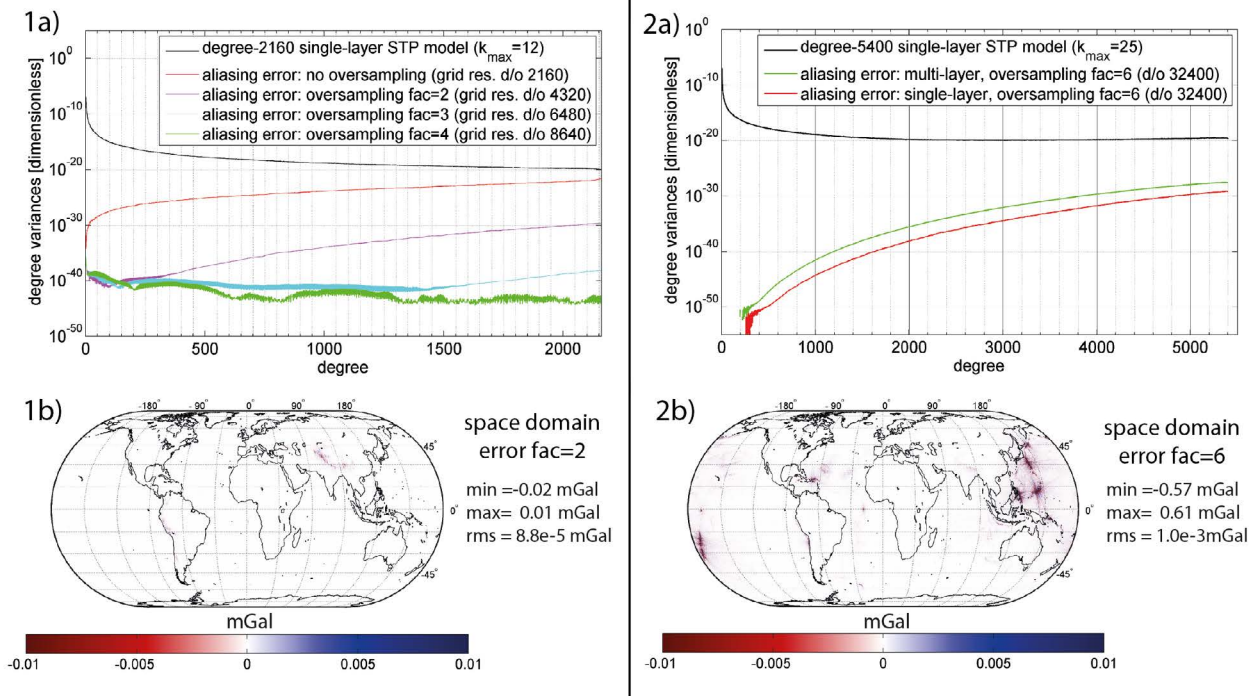


Fig. 3.8 – Aliasing error in terms of degree variances (upper plots) and gravity disturbances (mGal) at Earth’s surface (lower plots). The left panels show the aliasing error for various oversampling of the HDF for single-layer modelling up to degree 2160. The right panels show the aliasing error that is present, when an oversampling of factor 6 was applied (compared to the reference solution with oversampling factor 12) for single- and multi-layer models up to degree 5400.

3.4.1.2 Computational demands, aliasing and realisation of the analysis

The oversampling required to cover all of the additional frequencies entering the HDFs due to the exponentiation exceeds the memory capacities of ordinary computers, and even challenges computing facilities. Representing all frequencies associated with $k_{max} \times n_{max} = 135,000$ degrees correctly would result in a Gauss-Legendre grid of the dimensions $135,001 \times 270,001$, which approximately corresponds to 292 GB memory per HDF/layer boundary. The oversampling, however, can be reduced to acceptable level without yielding any substantial aliasing error in the spectral band $n = 0 - 5400$. This is owed to the fact that during an analysis the aliasing infiltrates the highest frequencies most severely while aliasing errors diminish towards longer wavelengths. This is the result of the following experiment: when modelling to degree 2160 ($k_{max} = 12$) an oversampling of factor 2, i.e. a grid that covers frequencies up to degree 4320, is sufficient to reduce aliasing errors to negligible level in the band $n = 0 - 2160$ (Fig. 3.8, panel 1a and 1b). This more or less confirms the investigations of *Wieczorek* (2015) who found that a grid corresponding to degree 5000 is necessary to mitigate against aliases. As an aside, without oversampling the aliasing errors are up to $\approx \pm 60$ mGal with a global RMS of nearly 1 mGal in this case (not shown).

In the case of modelling to degree 5400 the experiment cannot be repeated to full resolution because of the computational constraints it is aimed to find a solution for. But by comparing a degree-5400 solution generated with oversampling of factor 6 (corresponding to degree 32,400) to one with oversampling of factor 12 (corresponding to degree 64,800), we can see that in the case of a single-layer model aliasing errors in the order of ± 0.6 mGal are present (Fig. 3.8, panel 2a and 2b). In the case of a multi-layer model the aliasing errors are slightly larger (green curve is above the red curve). In this work oversampling of factor 12 is considered suffi-

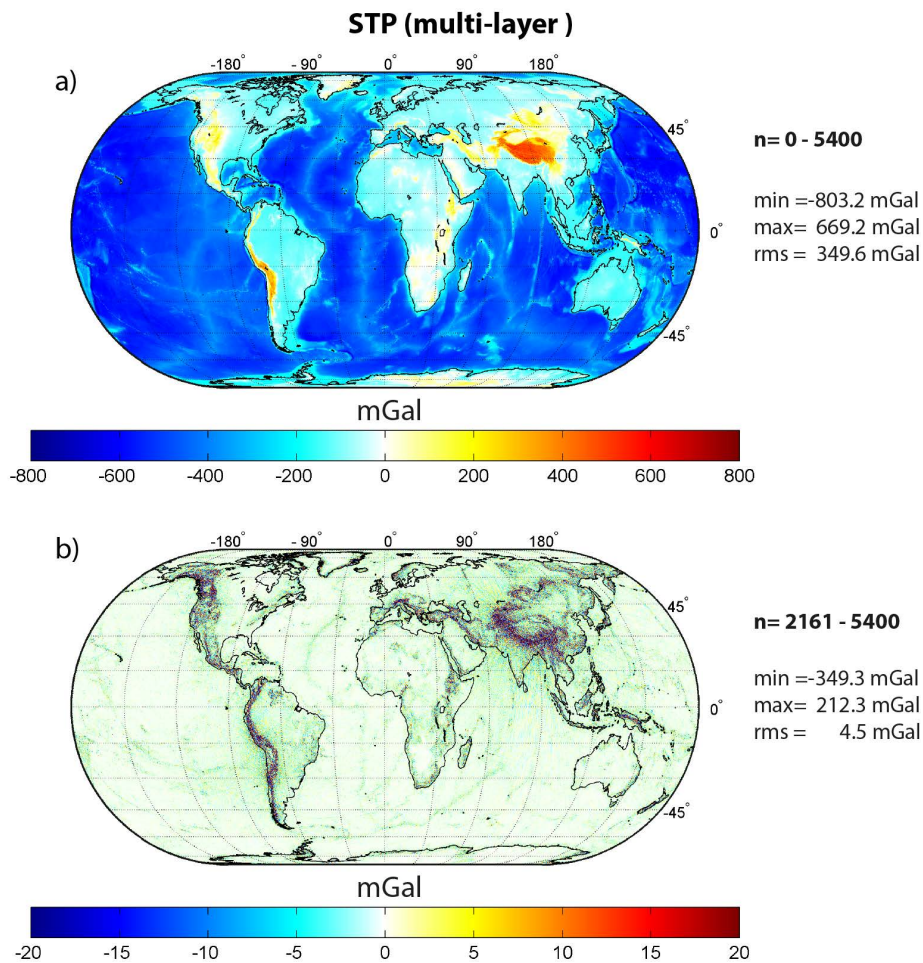


Fig. 3.9 – Variability of the gravitational field implied by the topographic masses as represented in the multi-layer STP model ($k_{max} = 25$) in terms of gravity disturbances (mGal) at Earth's surface: a) full bandwidth ($n = 0 - 5400$) and b) high frequency part ($n = 2161 - 5400$). Unit is mGal.

cient, knowing that the error will be much lower than in the case of oversampling by factor 6. The resulting grid size – 64,801 × 129,601 (~67 GB) – still is demanding but can be handled by supercomputing facilities. In this work the computations were done with the services of the *Leibniz-Rechenzentrum* (LRZ). Together with the parallelisation of the quadrature procedures (*P-III*) a single HDF can be analysed 25 times ($= k_{max}$) in about 240 CPU h (or 30h using 8 CPUs). Note that each latitude-parallel of the grid can be loaded and analysed separately, reducing the general RAM requirements during the analysis to a minimum level.

3.4.1.3 Gravity signal per spectral band and layer up to degree 5400

The multi-layer models based on the Earth2014 source-mass model developed up to degree and order 5400 are modelled with $k_{max} = 25$ and $j_{max} = 40$ (see above). Note that the ETP model in this case is resolved up to $n_{max} = 5480$ due to the j -series. The processing and remaining modelling constants are similar to those of the degree 2160/2190 models created along with publication *P-IV*.

Fig. 3.9 shows the STP multi-layer model for $n = 0 - 5400$ (panel a) and $n = 2161 - 5400$ (panel b) evaluated

spectral band	$0 \leq n \leq 5400$				$2161 \leq n \leq 5400$			
	Min [mGal]	Max [mGal]	Mean [mGal]	RMS [mGal]	Min [mGal]	Max [mGal]	Mean [mGal]	RMS [mGal]
CRUST	-1318.18	579.84	-503.79	584.15	-349.28	212.29	-0.07	4.75
OCEAN	80.51	512.97	208.13	232.49	-36.61	36.4	0	0.64
ICE	-5.51	175.05	11.86	32.75	-26.04	35.54	0	0.42
LAKES	-1.34	66.24	0.02	0.48	-15.38	12.62	0	0.03
EARTH (all layers)	-803.24	669.22	-283.83	349.57	-349.29	212.26	-0.07	4.47

Tab. 3.8 – Global statistics of the gravitational signal per STP layer in the spectral bands $n = 0 - 5400$ and $n = 2161 - 5400$ in terms of gravity disturbances evaluated at Earth's surface. Unit is mGal.

in terms of gravity disturbances at Earth's surface. As before, the gradient approach (*Hirt, 2012*) up to the 15th order (reference height = 4 km) as implemented efficiently in the isGraflab software (*Bucha and Janák, 2014*) is used for this purpose. In the spectral range $n = 2161 - 5400$ all long wavelength features of the gravity field vanish and the small-scale features show a much reduced average signal variability ($RMS = 4.5$ mGal). The signal in this band is correlated with the highest peaks of the topography (Himalayas, Rocky Mountains, Andes) and with deep bathymetric features such as mid-oceanic ridges and deep ocean trenches (Fig. 3.9). The mountain chains of Earth's topography host most extreme values (maxima and minima), i.e. they exhibit the largest variability of the topographic gravitational potential at short scales. Looking at the global signal statistics per layer suggests that – at Earth's surface – the crustal layer is responsible for the major part of the topographic gravitational signal, at least in the bands $n = 0 - 5400$ and $n = 2161 - 5400$ (Tab. 3.8). The ocean layer shows the second biggest signal amplitudes and RMS. This is largely owed to the fact that the ocean does not cover the entire globe, while the crustal layer does. Of course the oceanic water masses also cause attraction over continents (and islands), because the potential of a closed body always leaks over its physical boundaries. But over the continents, the oceanic potential is of smooth character and quickly attenuates with increasing distance to the shoreline (not shown). Thus the ocean layer is hardly contributing to the short-scale topographic potential over land (it does though in long and mid-wavelengths cf. *P-IV*: Fig. 9). In the spectral band ranging from $n = 2161 - 5400$ the RMS of the ocean layer then falls below the 1 mGal level and reaches approximately ± 36 mGal at maximum over the ocean. The ice and especially the lake layer make up even less of the global signal and have extreme values in the order of approximately ± 35 mGal over Earth's ice-sheets and ± 15 mGal over Earth's major lakes, respectively.

Notably, in the spectral band $n = 2161 - 5400$ the complete Earth layer-model shows signal amplitudes of up to ≈ -350 mGal and $\approx +210$ mGal ($RMS = 4.5$ mGal). This means – in view of combined gravity field modelling – that the topographic potential as modelled here is likely to make a significant difference to global potential models that are resolved to degree 2160/2190, at least over some regions with highly-elevated topographic or deeply-layed bathymetric features.

Chapter 4 deals with the combination and validation of the here described degree-5480 ETP model.

3.4.1.4 High-frequency differences between ETP and STP

STP and ETP were shown to have significant differences in the spectral domain up to degree and order 2160/2190 and 5400/5480 (cf. Sect. 2.3, *P-I* and *P-IV*). In the space domain characteristic differences up to degree 2160/2190, investigated first by *Claessens and Hirt (2013)* with a single-layer model, could be confirmed in *P-IV* for multi-layer models (Fig. 16, *ibid* : $RMS = 0.35$ mGal; $min = -4.66$ mGal; $max = 2.84$ mGal; $mean = -0.08$ mGal). The patterns in the differences and their signal amplitudes do not change

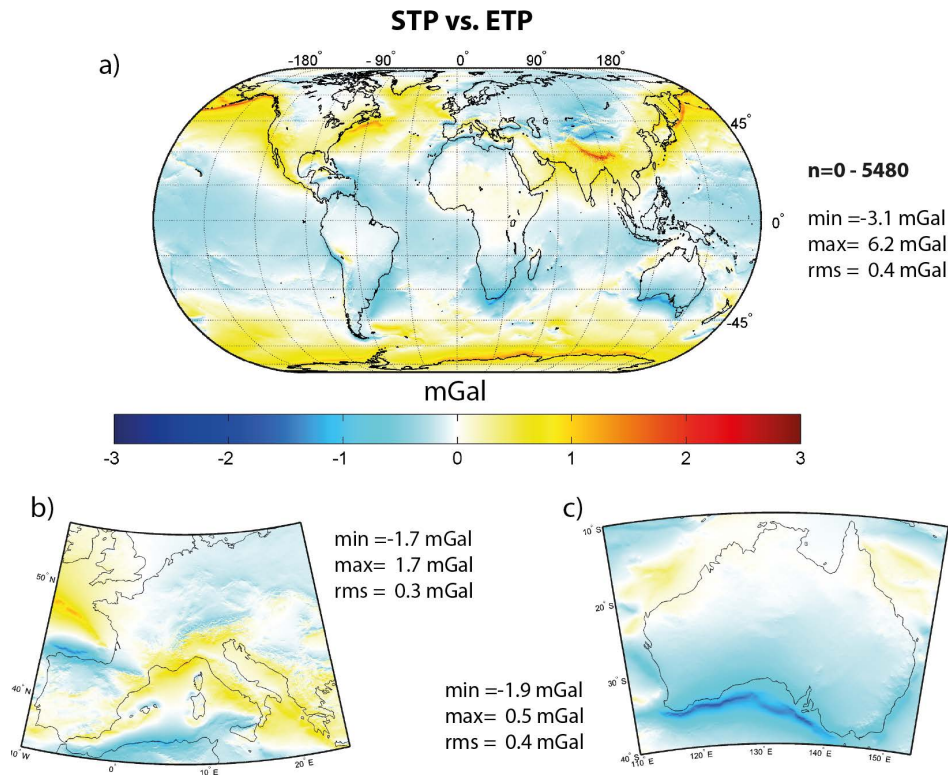


Fig. 3.10 – Differences between ETP and STP in the band $0 \leq n \leq 5480$ in terms of gravity disturbances (mGal) at Earth's surface over a) the entire Earth, c) Europe and Alps and d) Australia. Unit is mGal.

significantly in the case up to degree 5400/5480 (Fig. 3.10: $RMS = 0.36$ mGal; $min = -3.08$ mGal; $max = 6.19$ mGal; $mean = 0.08$ mGal).

In the spectral band ranging from degree 2161 to 5400 (5480 in the case of ETP) all long wavelength signal structures vanish in the differences between ETP and STP – the remaining short-scale signals show an RMS of 0.4 mGal (Fig. 3.11, panel a). The extreme values (minima and maxima) in this band of the spectrum exceed those of the entire spectrum. The short-scale differences are concentrated over the following high elevated mountain chains: the Andes, the Himalayas, the Peg. Maokē/ Central Ra (New Guinea) and the European Alps (Fig. 3.11, panel b). Over those regions short scale fluctuations in the order of ± 30 mGal can exist between ETP and STP. These amplitudes are in the order of to up to $\sim 10\%$ of the maximum short-scale signal found in the band $n = 2161 - 5400$ of the STP model (Fig. 3.9, panel b). Interestingly, over other high-elevated regions such as the Rocky Mountains much smaller differences exist between ETP and STP at short scales. In very low elevated regions, such as the Australian continent, the differences amount to up to $\pm 3 - 5$ mGal at maximum (Fig. 3.11, panel c).

3.4.1.5 High-frequency differences between single- and multi-layer modelling

The RET approximation effect, i.e. the differences between single- and multi-layer modelling, are in the order of ~ 1.8 mGal (RMS) when modelling up to degree and order 2160/2190 ($P-IV$: Fig. 8). The patterns and amplitudes of the differences do not change significantly when modelling up to degree 5400/5480 (Fig. 3.12a). This indicates that the RET approximation effect plays a minor role for $n > 2160/2190$. The differences in the spectral band ranging from degree 2161 to 5400 are in the order of 0.5 mGal (RMS) amount to about ± 30 mGal

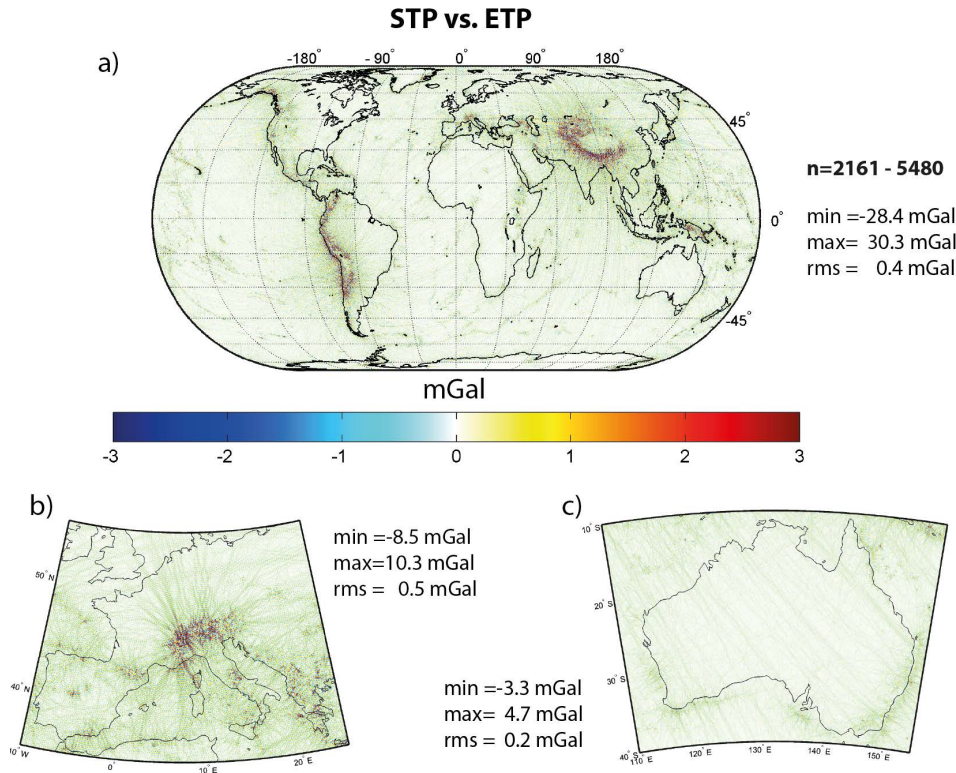


Fig. 3.11 – Differences between ETP and STP in the band $2160 < n \leq 5480$ in terms of gravity disturbances (mGal) at Earth's surface over a) the entire Earth, c) Europe and Alps and d) Australia. The ETP solution has been high-pass filtered according to Eqs. A.2 and A.3 and Tab. A.1. Unit is mGal.

in extreme cases, globally (Fig. 3.12b). The short-scale differences are concentrated along the mid-oceanic ridges and deep ocean trenches, while large parts of the ocean hardly show any RET approximation effect in the spectral band $2161 < n \leq 5400$. It should be considered, though, that the gravitational effects in the this band generally are in the order of 4.5 mGal (RMS), only (Fig. 3.9b). Thus, for a correct representation of the short-scale gravitational effects over the oceans multi-layer modelling is inevitable.

3.4.2 An experimental degree-21,600 model (~ 1 km resolution)

Here an experimental topographic potential model of degree 21,600 is developed with the efficient spectral expressions (Eqs. 3.10/3.11 and 3.20/3.21), the LRA and GLQ. The modelling involves the computation of nearly 467 million SHCs which take 3.7 GByte when stored in a binary variable. In this section the focus is on challenges, issues and possible simplifications during the modelling; it is not aimed to get a complete model in the first place.

3.4.2.1 Challenges associated with large k_{max} and j_{max}

The above postulated rules (Eqs. 3.28 and 3.29) suggest the choice of $k_{max} \approx 87$ and $j_{max} \approx 191$ for a fully converged STP and ETP model with the efficient expressions, respectively. These high values are numerically challenging mainly because of a) the overflow issues associated with the computation of the respective

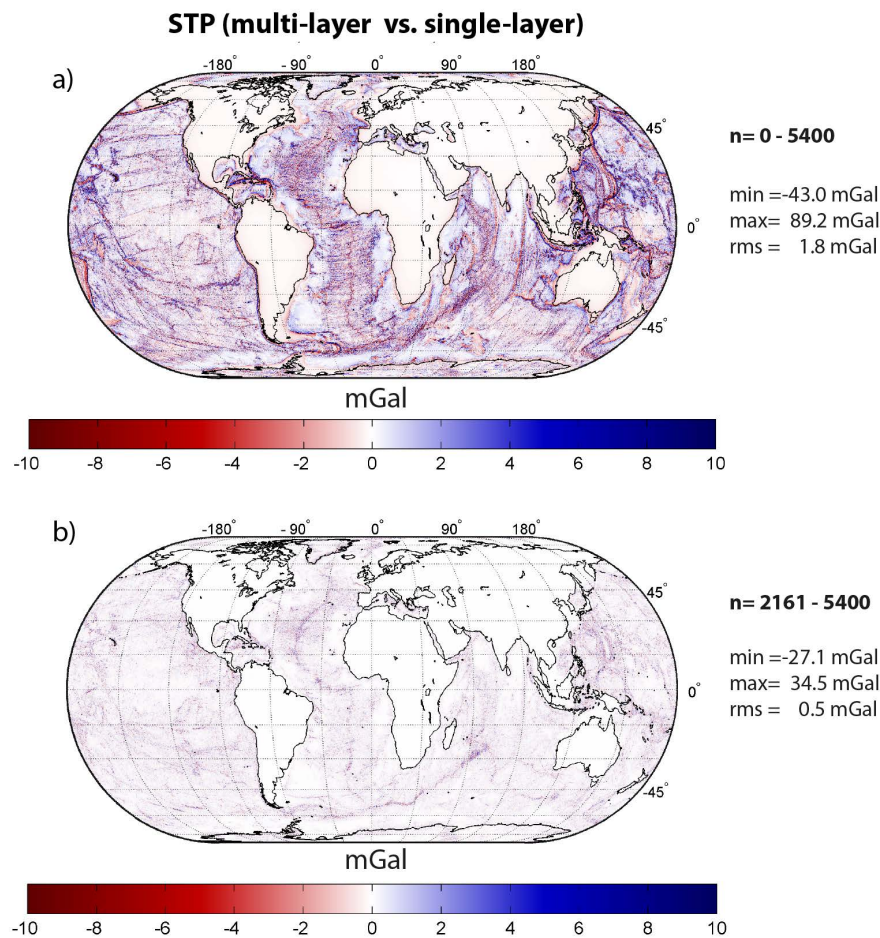


Fig. 3.12 – Differences between single- and multi-layer modelling in terms of gravity disturbances (mGal) at Earth's surface a) in the band $0 \leq n \leq 5400$ and b) in the band $2161 \leq n \leq 5400$. Unit is mGal.

binominal coefficients (see above) and because of the exponentiation of the HDF with k . For both of which theoretically an arithmetic extension, e.g. by choosing X -numbers or quadruple precision, could help to solve the problem in the first place. However, the exponentiation requires massive oversampling which also challenges the memory requirements (and computation times): with an oversampling of factor 30 – which is assumed here to ban aliasing – the grid would have the dimensions 648001×1296001 , which amounts to approximately 6720 GBytes. To get an idea of involved computation times: a degree-21,600 GLQ analysis based on a grid dimensioned 64801×129601 takes approximately 20 CPU-hours, adding up to a total of 1740 CPU hours per layer. In the current implementation the factor 30 oversampled grid would take approximately a factor of 100 longer, so roughly 174,000 CPU-hours per layer are needed, solely for the analysis.

From these considerations we learn that a lot of numerical optimization and further parallelisation of the here presented algorithms and implementations together with access to super-computing facilities are needed to create a fully-resolved and fully-converged topographic potential model of degree 21,600.

3.4.2.2 Modelling multiples of the bandwidth of the input HDF

To study the forward modelling procedures up to degree 21,600 despite some of the above described challenges it is also possible to use the additional frequencies of a degree-2160 (band-limited) HDF – so called

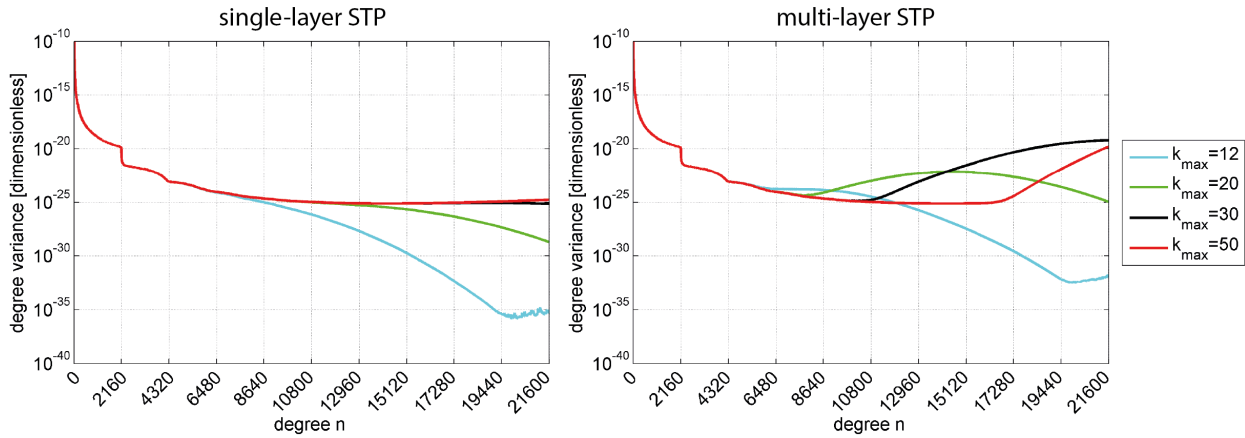


Fig. 3.13 – Degree variances of single- (left) and multi-layer (right) STP models for different degrees of truncation of the k -series in the first 10 multiples of the HDF's band-width of $n_{max} = 2160$ up to degree 21,600.

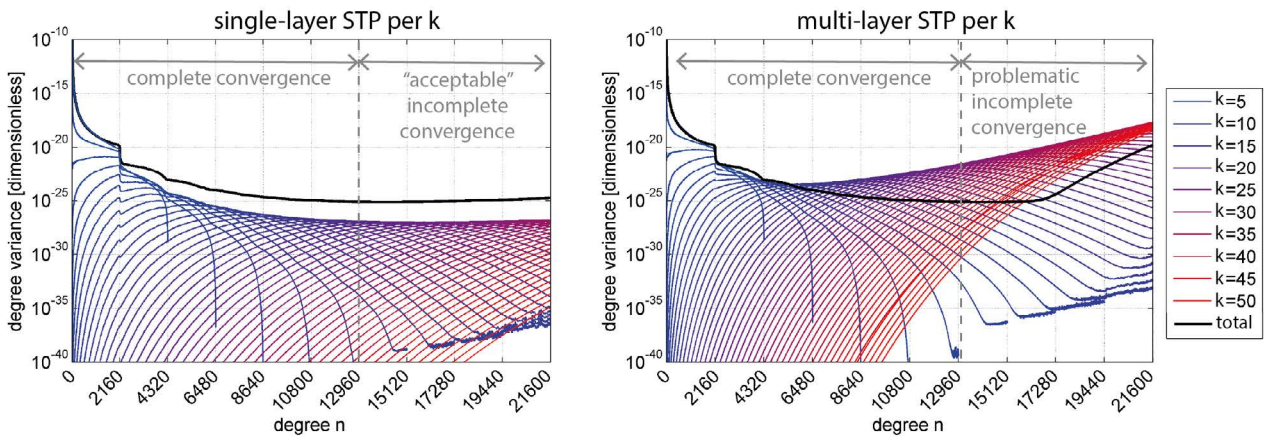


Fig. 3.14 – Degree variances of the potential contributions of a single- (left) and multi-layer (right) degree-21,600 STP model per term of the k -series. In case of the single-layer model, the incomplete convergence is acceptable due to the additive convergence behaviour. In case of the multi-layer model, the incomplete convergence causes large errors because of the eliminating convergence behaviour.

multiples of the input bandwidth – that occur by its exponentiation according to Eq. 3.25. In this way, we exclude issues such as excessively large grids and aliasing problems more easily.

The gravitational signal in the multiples of a band-limited input boundary frequency were first treated in *Hirt and Kuhn* (2014) for single-layer STP modelling. The findings and methods were revisited in *P-VI* under the aspect of Bouguer gravity modelling and it was shown that the multiples of a degree-2160 topographic mass distribution up to degree 21,600 and up to $k = 15$ are needed to achieve successful validation with space domain modelling at the level of $10 \mu\text{Gal}$. In the following the investigations of *P-VI* are expanded to the aspect of multi-layer modelling. Further it shall be clarified whether early truncations of the binomial k -series, which means a great simplification of the modelling procedure, is an acceptable means to enable and justify high-resolution spectral forward modelling. This is also relevant since in the literature the k -series often is truncated at very low k_{max} . For example, *Gruber et al* (2014) and *Balmino et al* (2012) choose $k_{max} = 3$ for STP modelling up to degree 5,400 and to degree 10,800, respectively.

Note that the j -series can never be truncated in an early manner since this always leads to a convergence error reflected in the solution by (large) striations, especially at high latitudes. Since the convergence of the

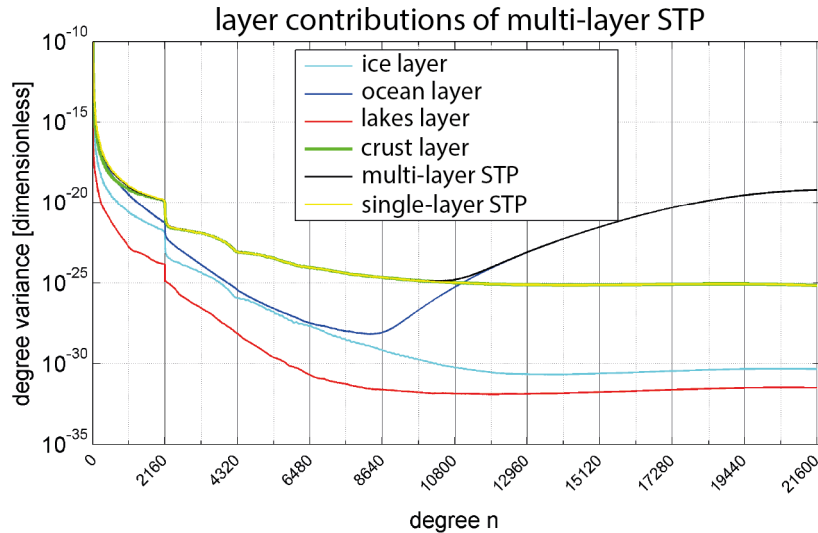


Fig. 3.15 – Degree variances of the layers’ potential contributions (colored lines) to the degree-21,600 STP multi-layer model (black line) in comparison to the single-layer model (yellow line) for $k_{max} = 30$.

k -series in the STP works similar to that in the ETP, it is waived to investigate the ETP model in the following.

3.4.2.3 Early truncation of the k -series at high degrees: global convergence implications of deep ocean masses

For the experimental modelling the degree-2160 HDFs are oversampled by a factor of 30, i.e. a GL grid covering frequencies up to degree 64,800. For $k > 30$ it is assumed that the degree range 21,601 – 64,800 absorbs all or at least big parts of the aliasing error, which is a valid assumption given the investigations in Sect. 3.4.1. Truncating the k -series of the STP at different binominal orders $k_{max} = 12, 20, 30, 50$ leads to very different spectral energy in high degrees of the respective single and multi-layer models based on the Earth2014 source-mass model (Fig. 3.13). In both, at high degree ($n > 8000$) the level of convergence is around 10^{-25} and the higher k_{max} the higher is the degree where the variances break away from this level, in general. An early truncation in case of single-layer modelling leads to falling energy towards higher degrees, e.g. near degree 12,000 for $k_{max} = 20$. In case of multi-layer modelling, an early truncation leads to an increase of the short-scale energy in the degree variances, e.g. near degree 16,500 for $k_{max} = 50$. Each additional k^{th} binominal potential contribution from the k -series has more power at high degrees than the contribution of $k - 1$, at least up to $k = 35$ where the behaviour is reversed (Fig. 3.14). Importantly, the total signal energy (black line) is below that of the single potential contributions at high degrees, i.e. here signal is eliminated incrementally in the total potential with each additional k^{th} contribution.

The increasing signal strengths arise from the incomplete convergence of the oceanic layer that is the dominating layer at those short scales, as seen from the degree variances per layer in Fig. 3.15 (here exemplary for $k_{max} = 30$). The incomplete convergence, due to spherical harmonics, leaks over the bounds of the ocean and contaminates large areas along great arcs that have their origin in seemingly problematic points located in the Pacific ocean (Fig. 3.16a). In contrast, the single layer model is devoid of such problems and shows realistic short-scale gravity in the band ranging from degree 2161 to 21,600 which is in the order of 0.5 mGal RMS (Fig. 3.16b).

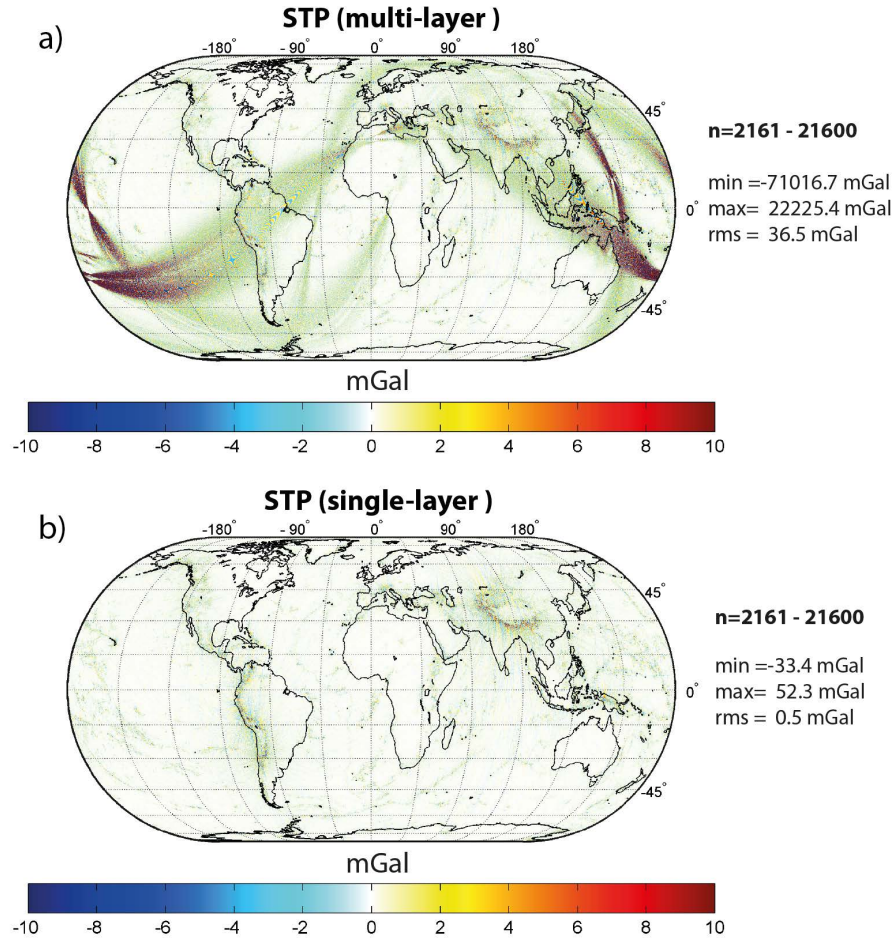


Fig. 3.16 – Gravity disturbances at Earth's surface (mGal) in the degree band $n = 2160 - 21,600$ of the degree-21,600 STP models with $k_{max} = 50$: a) multi-layer model, b) single-layer model.

Picking one of the seemingly problematic locations in the ocean layer over the Pacific – a deep ocean trench in Kiribati – and increasing the maximum degree incrementally by steps of 2160 degrees in the synthesis of gravity disturbances of the single- and multi-layer STP reveals that the erroneous pattern start to appear around $n = 15120$ for $k_{max} = 50$ in the multi-layer modelling, only (Fig. 3.17). This actually is not surprising since the truncation rule for the k -series (Eq. 3.28) predicts that $k_{max} = 62$ is needed for a full convergence at degree 15120. Looking at the boundaries of the source-masses over Kiribati exhibits drastic depth differences of more than 3 km between the RET geometry used in single-layer modelling and the actual bathymetry which is used as lower boundary of the ocean layer (= bedrock), but no other suspicious irregularity (Fig. 3.18). Also at the point on Earth diametrically to Kiribati no irregularity can be found in the bedrock (not shown). In general the bedrock geometry shows larger amplitudes and a higher RMS than the RET (Tab. 3.9), which is an effect of the compression of water masses in the latter, mainly. A premature interpretation is thus that deep masses, as found in the bedrock, generally take longer to converge at high degrees. But as we can see from the degree variances in Fig. 3.13 also the single-layer model has not converged fully at the displayed truncations of the k -series. But the early truncation of the k -series in the case of the single-layer model does not cause large (erroneous) signals (cf. Fig. 3.17). The crucial difference is the way the convergence happens: in single-layer modelling the k -series converges in an additive manner at high degrees, i.e. each additional potential contribution $k_a > k_{max}$ adds spectral energy to the total potential of k_{max} . In contrast, this additive convergence is

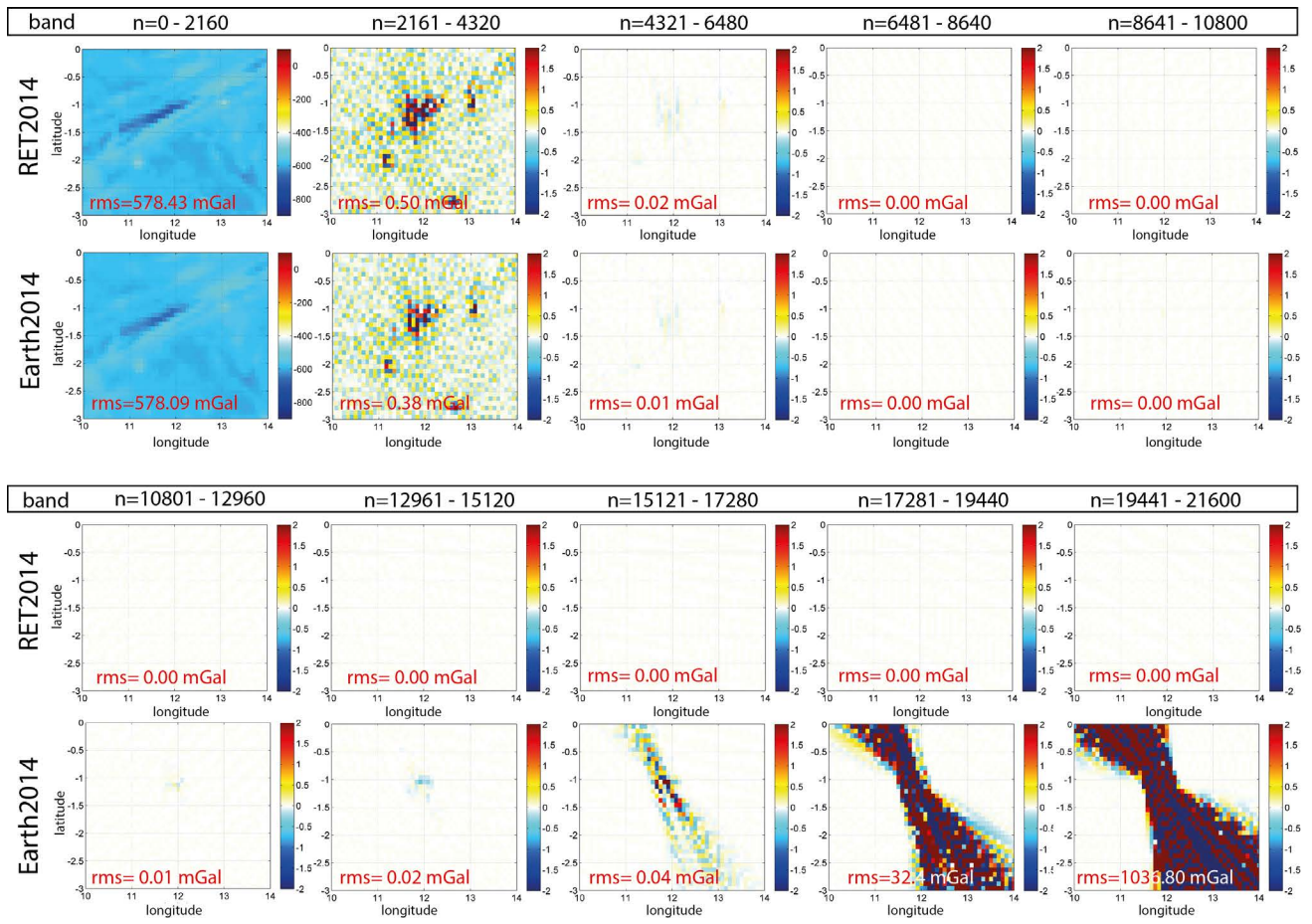


Fig. 3.17 – Single- and multi-layer STP models (RET2014 and Earth2014) for $k_{max} = 50$ in different spectral bands in terms of gravity disturbances at the reference ellipsoid (mGal) over the deep ocean trench located in Kiribati. The multi-layer potential model is affected by incomplete convergence of the k -series and shows severe error patterns for degrees $n > 15120$.

present only up to $k = 8$ in the case of the ocean-layer. Beyond that binomial order each additional potential contribution k_a at high degrees is needed to reduce/eliminate (parts of) the spectral energy of the total potential of $k_{max} < k_a$. This makes an early truncation of the k -series of the single-layer model possible and denies the truncation in the case of the forward modelling of the ocean layer, because it would result in an unusable potential model. This is the very reason why the validation of the single-layer modelling in publication *P-VI* up to degree 21,600 was successful despite the early truncation at $k_{max} = 15$. Whether the signs of divergence over Kiribati between space- and spectral domain modelling stated in publication *P-VI* vanish with additional terms $k_a > 15$ remains an open question, since RET2012 was used in *P-VI* (here RET2014 is used). Concluding: whether the k -series may be truncated or not at high-degrees depends on the respective HDF (more precisely its negative amplitudes). In general, a very early truncation ($k \leq \sim 8$) seems unproblematic as found above. Higher early truncations should be carefully considered, when modelling to high or ultra-high degree.

Note that the here computed experimental model was developed following the LRA, so by reducing density contrasts. In case of the LCA approach, not only the ocean-layer but also the crustal layer would be affected by the problematic (eliminating) convergence, since only then the bedrock depths are used as lower boundary for the crust explicitly. Thus it seems advantageous to use the LRA for ultra-high resolution modelling,

Boundary	Min	Max	Mean	RMS
BED	-10588.11	6709.67	-2117.50	3162.62
RET	-6501.11	6710.46	-1163.00	2005.02

Tab. 3.9 – Statistics of Earth2014's degree-2160 RET (rock-equivalent topography) and the BED (bedrock) boundaries used in single-layer modelling an multi-layer modelling to degree-21600, respectively.

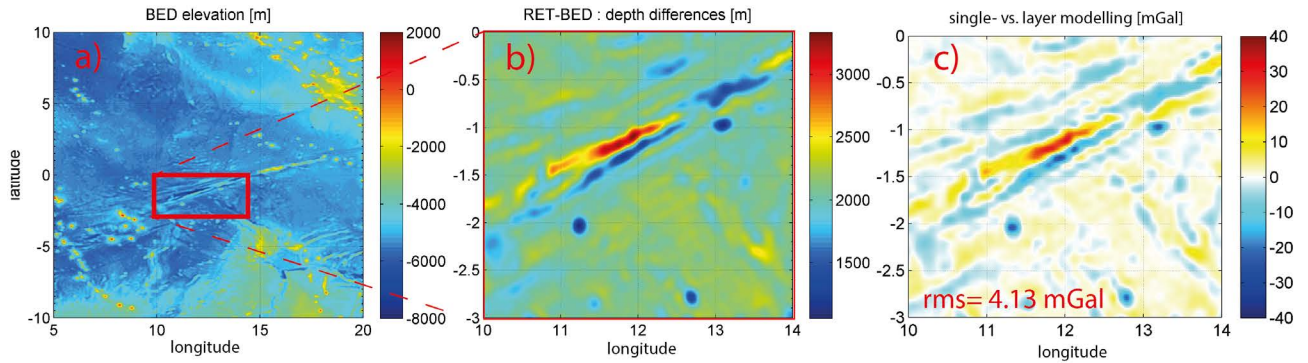


Fig. 3.18 – Elevation of the bedrock layer (bathymetric depths) over the area of Kiribati in the pacific (a), depth differences between bedrock to the rock-equivalent-topography layer (b) and gravity differences between single- and multi-layer modelling ($n_{max} = 12960$, $k_{max} = 50$) evaluated at the ocean's surface ($H = 0$) (c) over the deep ocean trench in Kiribati (depths down to ~ -8600 m). BED: bedrock layer from Earth2014; RET: rock-equivalent-layer from Earth2014.

since it reduces the computational costs, i.e. an excessively high binomial order k is necessary for one layer, only.

3.4.2.4 Meaning and amplitudes of gravitational signal in multiples of the bandwidth of a degree-2160 mass distribution

The value of the gravitational signal in multiples of a (degree-2160) band-limited mass distribution can be estimated roughly from the gravity signal amplitudes in Figs. 3.17 and 3.16b. In Publication *P-VI* the signal strengths at Earth's surface per scale as found in the multiples have soundly been investigated on a global scale (for a single-layer model with $k_{max} = 15$), see Tab. 2 (ibid). Further, it is stated " (...) *the topographic gravity field – as generated by a degree 2160 topographic mass model – reaches significant signal amplitudes at the 20 mGal level beyond degree 2160, while its power is negligible beyond degree $\sim 17,280$. In terms of maximum signals, about ~ 90 % of this short-scale spectral energy is concentrated in the second multiple of the input band (degrees 2161 – 4320), another ~ 8 % in the third multiple, and the remainder beyond harmonic degree 6480.*". As very important finding, the short scale gravity in the band $n = 2161 - 21600$ was found necessary to explain (a big part) of the discrepancies existing between space-domain and spectral-domain modelling in the literature. The reason is that in space-domain modelling the high-frequency gravity signals ($n > 2160$) always are implicitly accounted for. Further, the rest of the discrepancies had their origin in insufficient discretisation of the topographic masses in space-domain modelling (see *P-VI*).

The energy in the multiples also unveils the advantage of spectral topographic potential modelling over residual terrain modelling: spherical harmonic coefficients (\bar{V}_{nm}) enable a filtering in the gravity domain. The energy of the multiples would be disregarded by RTM because filtering takes place in the (geometric) domain of the source-mass models.

3.5 Summary and evaluation of the chapter's research aims

Chapter 3 deals with spectral forward modelling under the aspect of increased resolution, i.e. modelling gravity signals at scales ≤ 10 km. It aims to:

"Review existing global topographic data sets and mass models in order to create a truly global and up-to-date mass model at best means that is suited for the purpose of forward modelling". (A2)

"Review existing spectral forward modelling techniques in order to further develop and test the best suited approaches for high-resolution modelling". (A3)

"Define challenges and limitations of spectral forward modelling with regard to resolution". (A4)

The data and methods for this purpose are described and derived in the publications *P-II*, *P-III* and *P-IV*, mainly. In *P-II* a high-resolution (~ 2 km) and up-to-date global source-mass model (Earth2014) has been created that has been proven to be of adequate quality for the purpose of forward modelling. It especially stands out because of latest geometric information over polar ice-covered regions. A complete overview and comparison between different existing rigorous and efficient spectral forward modelling approaches that rely on different levels of approximation has been carried out. In this context, a new modelling approach, accounting for masses in multiple volumetric layers, that omits spherical approximation effects was developed and shown to deliver improved topographic potential models. The spherical harmonic analysis of height density functions, which can be considered the "bottleneck" of high resolution forward modelling, has been achieved through arithmetic extension and parallelisation of existing exact quadrature techniques. As demonstrated, spherical harmonic expansions up to extremely high degrees close to 50,000 are not a problem any more.

In the second part of chapter 3 the data and most promising spherical harmonic forward modelling approaches were tested up to high-degrees. Complete models up to degree 5400 have been developed unveiling the truly global short-scale topographic potential down to scales of ~ 4 km. In this context an improved empirical rule for the convergence of the involved binomial series expansions at high-degrees could be derived. As another important finding, aliasing errors can be circumvented with adequate oversampling by factors smaller than k_{max} . Full resolution modelling to very high degree, such as 21,600, is not possible in ordinary double precision and requires further arithmetic adaptations of the algorithms along with further parallelisation. Main reasons are numerical overflow of the binomial coefficients (for $k > 72$ and $j > 145$ corresponding to degree $\sim 17,800$ and $\sim 16,500$, respectively) and excessively large grids that are needed to omit aliasing. Modelling to degree 10,800 seems possible in double precision, convergence is reached with $k = 46$ and $j = 94$, but would require massive parallelisation to treat the large grids. The exact oversampling needed in this case has not been determined. Nevertheless, the modelling and early truncation of the k -series were examined up to degree 21,600 using the signal in multiples of the band-width of degree-2160 source mass distributions. Those occur due to the exponentiation of the HDFs by integer powers. Here a different behaviour in the convergence of the k -series between single- and multi-layer modelling was discovered. While the convergence is *additive* in single-layer modelling – the total potential always is larger than the k th potential contribution – the convergence is mainly *eliminating* in the case of multi-layer modelling. More precisely only the ocean layer, reaching the farthest into Earth's interior, is affected by the eliminating convergence. Thus, the deeply located masses of the ocean layer deny an early truncation of the k -series above $k \approx 8$ in the case of multi-layer modelling. In this context, the LRA is preferable compared with the LCA, because the bathymetry is

used as lower bound only once. In general, the energy in the multiples in the band $n = 2161 - 21,600$ was shown to produce significant gravity signals. Importantly, those are needed to explain the discrepancies between space- and spectral domain forward modelling, which is the topic of publication *P-VI*. Concluding, chapter 3 satisfies the research aims A2-A4. As a requirement of the overall research goal G2, the multi-layer ETP approach could be identified as best spectral approach. However, the RET-based single-layer approach, is sufficient if the ETP is sought only over continental and coastal regions, and only at short-scales (≤ 10 km).

Chapter 4

Application and validation of spectral forward modelling in high-resolution combined global gravity field modelling

4.1 Strategies for the combination of topographic potential and observed gravitational potential

In this work it is aimed to examine to which extent (uncompensated) forward modelled gravity – as implied by the topographic masses – is able to improve the knowledge of the gravity field beyond the resolution and coverage of today's observation techniques on global scale. As argued above, global gravity field models that are based on observations are limited to resolutions of about 10 km. In the previous chapter it was shown that – with spectral forward modelling techniques – the gravitational attraction can be modelled down to much shorter scales, albeit relying on some assumptions and approximations. In contrast, at long and mid-wavelengths the observation-based models can hardly (if at all) benefit from forward modelling, mainly because of insufficient knowledge of Earth's (deeper) mass distribution and isostatic compensation mechanisms. In order to use the short-scale gravity information of the topographic potential, measured gravity and forward modelled gravity therefore have to be combined as shown and explained schematically in Fig. 1.1. It is important to understand that this kind of combination model may well be used for the applications that require the model to be as close as possible to the actual (observable) gravitational attraction. A geophysical interpretation of the short-scale spectral constituents, however, is not possible since the models rely on several approximations and geophysical assumptions.

Different theoretical strategies exist for this kind of combination, each of them associated with certain disadvantages and advantages regarding methodological, computational and practical feasibility. A quite complete overview of the different methods and how they relate is given in Fig. 4.1. In principle it can be distinguished between the following 5 types of *merging* (i.e. combination) of topographic potential and observed gravitational potential:

$$\text{C1 - spatial merge: } \Delta\hat{g}^t/\delta\hat{g}^t \oplus \Delta\hat{g}/\delta\hat{g} \rightarrow \Delta\hat{g}^c/\delta\hat{g}^c$$

$$\text{C2 - spectral merge: } \bar{V}_{nm}^t \oplus \bar{V}_{nm} \rightarrow \bar{V}_{nm}^c$$

$$\text{C3 - regularisation merge: } \bar{V}_{nm}^t \oplus A^T PA(V) \rightarrow A^T PA(V^c)$$

$$\text{C4 - block-diagonal merge: } \widehat{A^T PA}(V^t) \oplus A^T PA(V) \rightarrow A^T PA(V^c)$$

$$\text{C5 - least-squares merge: } \Delta g^t/\delta g^t \oplus b = A^T PA(V^t) \oplus A^T PA(V) \rightarrow A^T PA(V^c)$$

where b are observations (e.g. gravity anomalies or gravity gradients), $\Delta\hat{g}/\delta\hat{g}$ are band-limited gravity anomalies/ disturbances, $\Delta g/\delta g$ are not band-limited gravity anomalies, \bar{V}_{nm} are SHCs of a potential model, $A^T PA(V)$ denotes the (full) normal-equation (NEQ) matrix of the potential V and $\widehat{A^T PA}(V^t)$ is the normal-equation matrix assembled in block-diagonal structure of the potential V^t . A superscript t affiliates a variable with the topographic potential, superscript c with the combined potential and no superscript denotes variables of the gravitational potential. All merging variants are discussed briefly in the following sections.

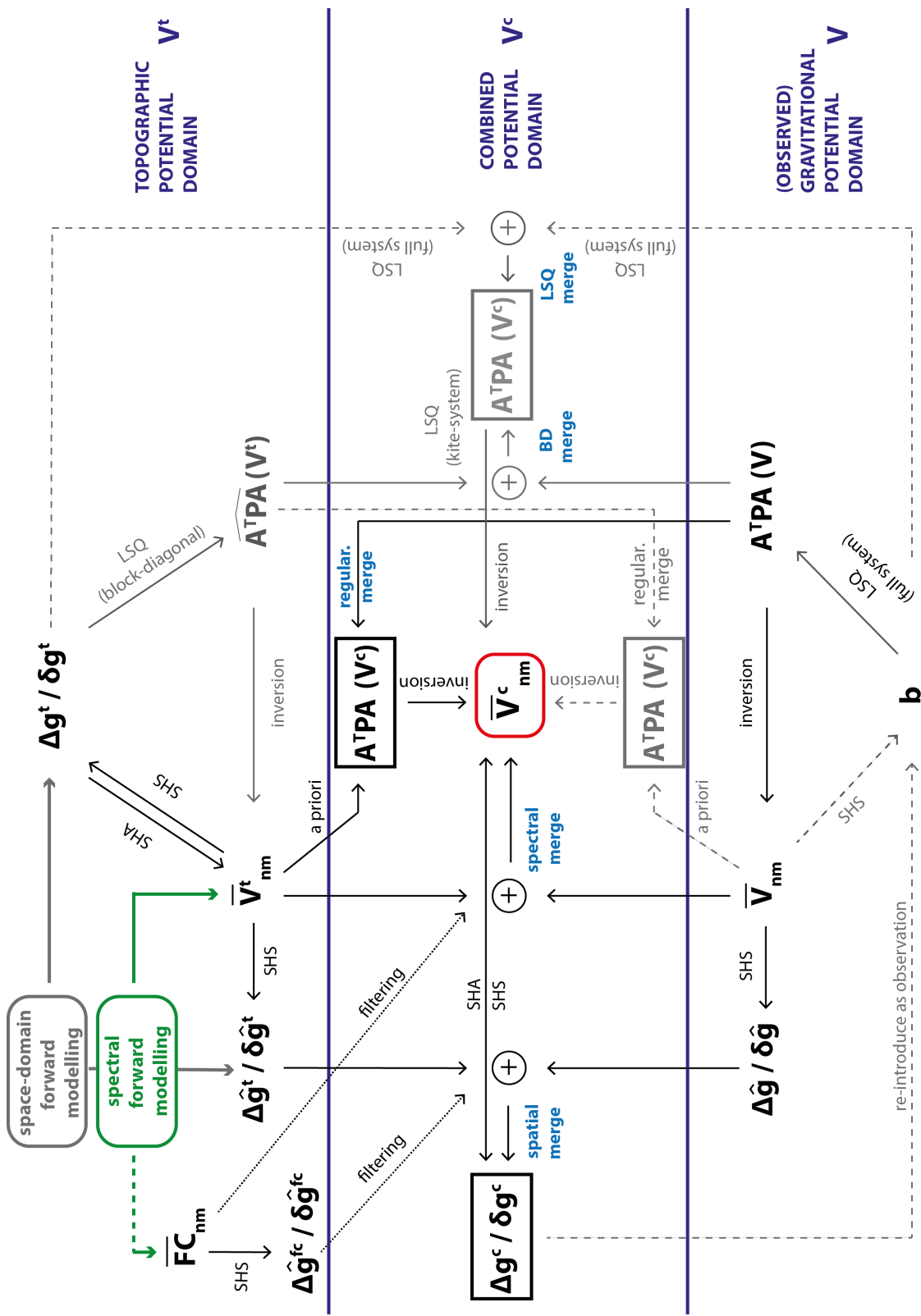


Fig. 4.1 – Flow chart of different combination strategies for a combination of observed b and forward modelled (topographic) gravity $\Delta g^t / \delta g^t$. The combined gravity field model $\bar{V}^{(c)}$ is found in the centre of the chart (embraced by the red box). Black solid lines denote strategies and parameters that have been tested and used in this thesis, grey lines are strategies that have not been tested and dashed lines denote strategies which are theoretically possible but either not considered useful or not feasible due to data-driven or computational limitations. SHS: spherical harmonic synthesis; SHA: spherical harmonic analysis; LSQ: least-squares; BD: block-diagonal; regular.: regularisation; FC: filter coefficients needed for a truncation of ETP models (see appendix A).

4.1.1 Combination based on least-squares and normal-equations

The combination strategy based on least-squares (C5), that involves the assembly of a full (joint) normal equation matrix, certainly is the most powerful in terms of possible data distribution, individual (regional) weighting and stochastic modelling. In this strategy, forward modelled gravity is introduced point-wise (or area-mean-wise) and principally treated similar to observed gravity. This, however, makes C5 the most demanding strategy, especially when aiming at high-resolution modelling. The major disadvantages of C5 are that it requires realistic errors of all input data for a correct regional weighting – the above forward modelling techniques do not provide co-variance information or errors – and the computational costs that are associated with the inversion of large normal-equation systems. Up to today no full NEQ system exceeding degree 720 could be solved (*Fecher et al*, 2013). For more details on this type of combination it is referred to *Fecher et al* (2013); *Fecher* (2015); *Fecher et al* (2017).

The method C4 also is a least-squares combination but it separates the assembly of NEQs of observed and of forward modelled gravity. The two types of gravity then are combined on normal-equation level, i.e. by addition or stacking, where additional relative weighting factors can be introduced. With this method the inversion of high-degree fully-assembled normal equations can be circumvented. Thereby, only the observation based NEQ matrix is fully assembled, e.g. up to degree 720. The NEQ matrix containing the short-scale topographic gravity is assembled in block-diagonal structure (BD), accepting certain restrictions on data distribution and stochastic modelling (see further down), resulting in a sparse system that is solvable even for high maximum degrees (*Gruber*, 1999; *Pavlis*, 2011). During the combination of the full and the BD system the simple sparsity is lost, unfortunately. *Zingerle et al* (2016) therefore suggest a more sophisticated ordering of the combined/stacked NEQ matrix, a so-called *kite-ordering*, for the purpose of efficient computational solving of systems of ultra-high degree. Major drawbacks of the BD-system (and the kite-system) are restricting sampling requirements and limitations for the stochastic models. It, e.g., requires a strong homogenization of the data, i.e. equidistant distribution of the data points at same height above the reference body for each latitude parallel. Controlling the regional influence of the short-scale topographic gravity by weighting (due to explicit stochastic models) is not possible. Individual weighting is solely possible per latitude. However, when assuming equal errors for the topographic gravity this strategy bears an advantage: in the transition zone (where the normal equation matrix is fully-assembled) the regional weighting is indirectly facilitated by the variance co-variance information of the observation data.

These somewhat ambitious combination techniques based on least-squares have not been followed in this research, but deserve to be properly studied. The international GOCO (Gravity Observation Combination) initiative currently is main driver in the field of least-squares and normal-equation-based global gravity combination (<http://goco.eu/>) (*Fecher et al*, 2017). Also other consortia exist for combined gravity-field modelling, such as the EIGEN (European Improved Gravity model of the Earth by New techniques) group and NGA (National Geospatial-Intelligence Agency). They also use techniques similar to some of the techniques described below.

4.1.2 Combination based on a regularisation of normal-equations

In the regularisation merge (C3) – which introduces the topographic potential as prior information at short scales – a full normal equation matrix is regularised with the potential coefficients of a topographic potential model, following (*P-V*)

$$(A^T P A(V) + A^T P^t A(V^t)) \bar{V}_{nm}^c = A^T P b + A^T P^t \bar{V}_{nm}^t \quad (4.1)$$

where P and P^t denote the weight matrix of the observations b and the forward modelled gravity, respectively (i.e. the inverse of the respective variance-covariance matrix), and A is the Jacobian matrix. Since the coefficients of the topographic potential model \bar{V}_{nm}^t are treated as a priori known the Jacobian in this case becomes the identity matrix and thus

$$(A^T P A(V) + P^t) \bar{V}_{nm}^c = A^T P b + P^t \bar{V}_{nm}^t \quad (4.2)$$

which leads to the coefficients of the combined gravity model through inversion

$$\bar{V}_{nm}^c = (A^T P A(V) + P^t)^{-1} (A^T P b + P^t \bar{V}_{nm}^t). \quad (4.3)$$

The diagonal weight matrix P^t contains the inverse variances of each topographic potential coefficient and defines the influence of the forward modelled gravity in the combination. Since the variances are unknown – the forward modelling in Chpt. 3 does not imply stochastic modelling – the weight matrix has to be defined empirically. The main advantages of this approach are twofold: firstly, a full normal equation system has to be solved only to the maximum degree of the observed gravity. Secondly, the forward modelled gravity is weighted indirectly by the variance-covariance information of the observations and principally equal variances can be assumed for the coefficients of the topographic potential model. This makes the approach somewhat comparable to the above combination based on block-diagonal techniques.

This type of combination technique has been successfully applied in the combination of satellite observations from GRACE and GOCE with a single-layer ETP model in *P-V* and with a multi-layer ETP model in *P-IV*, yielding the combined models SatGravRET2014 and SatGravEarth2014. By comparison with ground-truth data it could be shown that the models manifest a better merge of satellite and forward modelled gravity regionally over the area of Antarctica and the polar-gap, that is not covered by GOCE observations. Better is meant in the sense that residuals w.r.t. ground-truth are lower as compared with the merging according to C2 or C1 (described further down). Techniques C4 and C5 were not tested due to the above described obstacles. The empirical weighting thereby ensured that low-degree satellite gravity is not deteriorated by the uncompensated topographic potential (see *P-IV*). Further, it was found that spherical topographic potential models are not eligible for this kind of combination. The level of approximation of a STP model (=spherical) is not consistent with the observations that represent the (actual) ellipsoidal mass-distribution of Earth.

The combination technique has also been successfully used, e.g., in the creation of GGMplus (*Hirt et al, 2013*) where EGM2008 coefficients were used to stabilize the high-frequencies contained in satellite normal equations. In *Rexer et al (2013)* the regularisation approach was used to combine satellite gravity with the SHCs of terrestrial gravity. However, the regularisation approach is not feasible when a combination with dense terrestrial observations is envisaged, since the normal equation systems will get very large, too.

4.1.3 Combination in space and spectral domain

The spectral (C2) and the spatial merge (C1) are mutually consistent/equivalent, if done correctly. Both are based on the concept of spherical harmonic filtering in the potential domain, i.e. the (abrupt) truncation of the spherical harmonic series. In principle, the topographic potential is high-pass filtered according to the maximum degree n_{max}^b of an observation-based potential model \bar{V}_{nm} , i.e. only \bar{V}_{nm}^t of $n > n_{max}^b$ are used. In the spectral domain the relevant coefficients of \bar{V}_{nm} and \bar{V}_{nm}^t are simply stacked together, directly resulting in the combined potential model \bar{V}_{nm}^c . In the space domain the combination is achieved by a superposition of synthesized gravity functionals, e.g. $\Delta\hat{g}/\delta\hat{g}$ and $\Delta\hat{g}^t/\delta\hat{g}^t$, in the relevant spectral band.

Importantly, when ETP models are used for this kind of combinations an abrupt truncation will lead to truncation errors, especially for truncations at mid, high and ultra-high degree. To accommodate such a combination additionally the filter coefficients \overline{FC}_{nm} or corrections $\Delta\hat{g}^{fc}/\delta\hat{g}^{fc}$ are needed. The computation of the filter coefficients \overline{FC}_{nm} and their meaning is explained in the appendix A.1.

This type of combination commonly finds application in the *spectral enhancement method* (Hirt et al, 2011), for the purpose of validation of gravity field models, e.g. Pail et al (2011); Šprlák et al (2012); Hirt et al (2012); Hirt (2012), and for the purpose of height unification (see also Sect. 4.3.1). Thereby, the spectral gap existing between spectrally limited potential models (n_{max}^b) and terrestrial (ground-truth) observations is filled by forward modelled gravity, i.e. topographic potential models or RTM. The major drawback of RTM is that it disregards that filtering in the geometric domain, i.e. spectral filtering of the function that represents the topographic mass distribution, is not equivalent to filtering in the gravity domain (see Eq. 3.25). In case of a residual terrain model based on a degree-2160 high-pass filtered mass distribution the error that occurs due to the incorrect filtering amounts up to some tens of mGal locally and ~ 0.5 mGal on global average (P-VI and Sect. 3.4.2.4: Fig. 3.16b).

Note that the spectral combination between observed and forward modelled gravity in C2 can also be facilitated with the help of some transition function, that omits an abrupt truncation, and tries to achieve a smooth transition in a certain spectral band of width dN . This has been investigated by Grombein et al (2016a) who use a Hanning function for combining satellite-only models with EGM2008. Varying the degree of truncation N of the satellite-only model and the transition band-width dN they found that over Germany and Austria, an abrupt truncation ($dN = 0$) is favorable. Over Brazil, which is not very well modelled in EGM2008, a smooth transition with $dN = 50$ ($N = 220$) delivers best results. It is assumed that these kind of smooth transitions can also be useful for the purpose of combining observation-based and topographic potential models, but they would also be of purely empirical nature. Therefore they always require proper validation. Alternatively, an abrupt truncation can also be omitted by "(...) approaches like a stochastic combination based on the error variances of the SH coefficients, see, for example, Huang and Véronneau (2013) and Ferreira et al. (2016)" (Grombein et al, 2016a). This would require uncorrelated and realistic errors. However, errors (or variances) are not given at all by the forward modelling procedures in this work.

4.2 Demonstration and validation of global high-resolution combined gravity modelling

This section has two purposes: 1) demonstration of the improvements of high-resolution topographic potential models to combined high-resolution gravity field modelling and 2) the validation of the potential models of degree 5,480 that have been computed using the spectral methods and source-mass data (Earth2014) described in chapter 3. Here, only the simplest combination techniques (C1 and C2) are used. This choice is based on the fact that a) no variance-covariance information is available for the topographic potential models, and b) they will be shown to be sufficient for the envisaged purposes (see above). The application of the more sophisticated combination strategy based on regularisation has already been investigated in P - IV and P - V where it was shown to be advantageous e.g. for optimised combinations over polar regions such as Antarctica.

The following comparisons with ground truth data are based on the spectral merges of EGM2008 (up to $n_{max} = 2190$) and the single- and multi-layer ETP ($dV_ELL_RET2014$ and $dV_ELL_Earth2014$) in the band $n = 2160 - 5480$. For a correct high-pass filtering of the ETP models the filter coefficients $\overline{FC}_{nm}^{(ETP,A)}(n_t = 2160)$ and $\overline{FC}_{nm}^{(ETP,B)}(n_t = 2160)$ need to be subtracted and added, respectively. Their computation is given in appendix A. The improvement due to the short-scale topographic potential in this combination is measured by the residual gravity (in the following just denoted *residuals*) that occurs by the comparison with different ground truth data sets against the performance of solely using EGM2008 for the comparison. The results of this investigation are structured by the prevailing topographic features in the area of the respective ground-truth data set.

4.2.1 Area with large topographic features: Switzerland

Exemplifying an area of large topographic features, a dense ground-truth data set with 31,598 gravity observations at sites located in the European Alps over Switzerland (Martí, 2004) has been chosen (Fig. 4.2). Here a large impact of the topographic potential is expected at short scales. The area covers about $550 \times 275 \text{ km}^2$ and the average elevation of the stations is 833.3 m, varying between $\sim 250 - 3550 \text{ m}$ ($RMS = 957,6 \text{ m}$).

In this area, EGM2008 is able to explain roughly 8.3 % of the observed gravity disturbances, while the combination models – with EGM2008 up to degree 2190 merged spectrally with ETP models up to degree 5480 – achieves a reduction of $\sim 50.4 \%$ (Tab. 4.1) in terms of RMS. Both, single-layer and multi-layer models show the same performance. Relatively, the inclusion of the short-scale forward modelled gravity from the ETP models leads to an impressive improvement of about $\sim 46.0 \%$ w.r.t. to EGM2008 in terms of RMS. Thus, over

Statistics over Switzerland	Min	Max	Mean	STD	RMS	red. rel. to	red. rel. to
Gravity data	[mGal]	[mGal]	[mGal]	[mGal]	[mGal]	Obs. [%]	EGM08 [%]
Observations	-145.68	245.19	1.49	43.03	43.06	-	-
Obs. - EGM2008	-224.70	95.08	-18.18	35.06	39.50	8.28	-
Obs. - (EGM2008 \oplus RET2014)	-176.22	62.83	-8.68	19.50	21.35	50.42	45.95
Obs. - (EGM2008 \oplus Earth2014)	-176.21	62.83	-8.68	19.50	21.35	50.42	45.95

Tab. 4.1 – Statistics of the 31,598 ground-truth observations for the area of Switzerland and residuals w.r.t. gravity from EGM2008 and the combination model that includes the short-scale gravity from the single- and multi-layer ETP models. The right side of the table shows the percentage of RMS reduction (=improvement) of the residuals obtained w.r.t. the observations and EGM2008.

Switzerland short-scale gravity from the ETP models on average halves the discrepancies existing between EGM2008 and the terrestrial gravity measurements.

In Figs. 4.3b and 4.3c it can be seen that the additional signal from the ETP models smooths large residual patterns present in the comparison with EGM2008. Especially in the Alpine valleys, where EGM2008 deviates in the order of ~ -100 mGal from the gravity observations, significant reductions (mostly down to $\pm \sim 20$ mGal) are visible. In the northern prealpine lands, the residual patterns in the order of $\sim \pm 20$ mGal are reduced down to $\sim \pm 10$ mGal. Although the patterns are significantly reduced they do not vanish in general. However, they are smaller in their lateral extent and finer in structure.

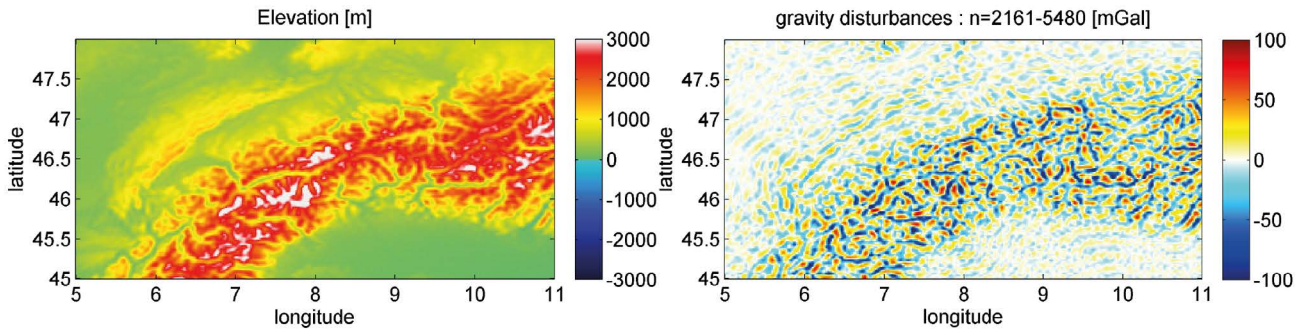


Fig. 4.2 – Elevations (m) and gravity disturbances at Earth's surface (mGal) in the degree band $n \sim 2160 - 5480$ of the degree-5,400 ETP multi-layer model over the European Alps in Switzerland.

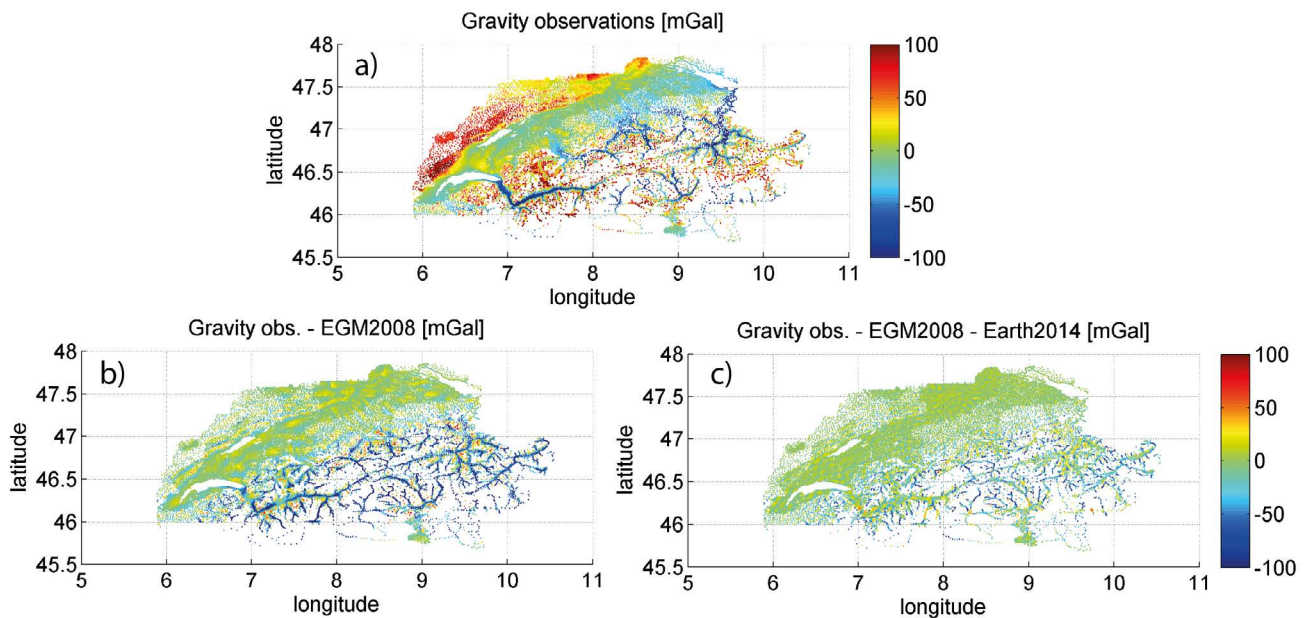


Fig. 4.3 – Gravity observations (a) and residuals at the stations of the ground-truth sites (mGal) over Switzerland obtained with EGM2008 (b) and the combination with the ETP multi-layer model (c). The ground-truth data has kindly been provided by Swisstopo.

4.2.2 Areas with medium topographic features: Northern Canada

The ground-truth data set with 43,422 gravity observations over Northern Canada originates from the Canadian gravity data base maintained by the department of *Natural Resources Canada*. Including near-polar areas, it covers a huge area of about $4880 \times 2750 \text{ km}^2$ (Fig. 4.4) which is characterised with medium topographic features compared with the other investigated regions (see above and below). The average elevation of the stations is 438.4 m, varying between ~ -50 and $+4970$ m ($RMS = 629.3$ m). Despite this test data set shows higher elevated stations than the Swiss data set due to the spur of the Rocky Mountains in the South-West of the region, on average it is much smoother.

In this area, EGM2008 is able to explain roughly 66.2 % of the observed gravity disturbances, while the combination models – with EGM2008 up to degree 2190 merged spectrally with ETP models up to degree 5480 – achieves a reduction of ~ 75.9 % (Tab. 4.2). Again, single-layer and multi-layer models show the same performance. Relatively, the inclusion of the short-scale forward modelled gravity from the ETP models leads to a significant improvement of about ~ 28.7 % w.r.t. to EGM2008.

Largest parts of the improvement due to the ETP models can be found in the higher elevated regions, i.e. the Rocky-Mountains in the south-west, and Ellesmere Island and Baffin Island in the north (Figs. 4.5b and 4.5c). There, residual gravity in the order of $\sim \pm 50$ mGal obtained with EGM2008 are reduced to about $\sim \pm 20$. Still these residual patterns remain dominating compared with the rest of Northern Canada, where residuals are rather in the order of $\sim \pm 2 - 5$ mGal. The latter also reflects that EGM2008 is a very good model over rather flat parts of Canada, since the topographic gravity effects are close to zero there (see right plot in Fig. 4.4).

Statistics over North. Canada	Min	Max	Mean	STD	RMS	red. rel. to	red. rel. to
Gravity Data	[mGal]	[mGal]	[mGal]	[mGal]	[mGal]	Obs. [%]	EGM08 [%]
Observations	-127.74	399.97	-9.4	38.71	39.83	-	-
Obs. - EGM2008	-137.01	106.66	-1.28	13.39	13.45	66.22	-
Obs. - (EGM2008 \oplus RET2014)	-167.76	87.17	-0.34	9.59	9.59	75.92	28.70
Obs. - (EGM2008 \oplus Earth2014)	-167.68	87.18	-0.34	9.59	9.59	75.92	28.70

Tab. 4.2 – Statistics of the 43,422 ground-truth observations over Northern Canada and residuals w.r.t. gravity from EGM2008 and the combination model that includes the short-scale gravity from the single- and multi-layer ETP models. The right side of the table shows the percentage of RMS reduction (=improvement) of the residuals obtained w.r.t. the observations and EGM2008.

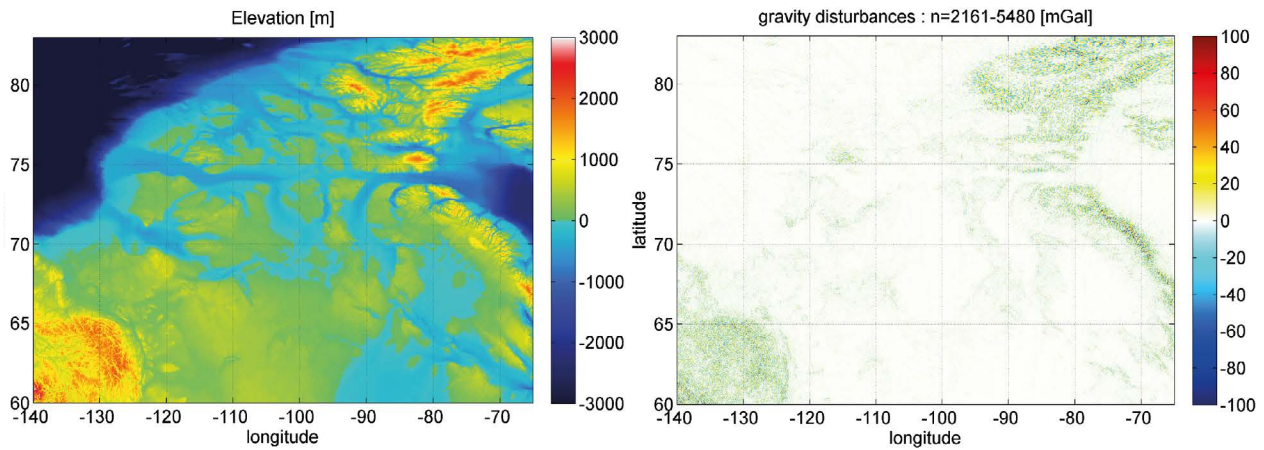


Fig. 4.4 – Elevations (m) and gravity disturbances at Earth’s surface (mGal) in the degree band $n \sim 2160 - 5480$ of the degree-5,400 ETP multi-layer model over Northern Canada.

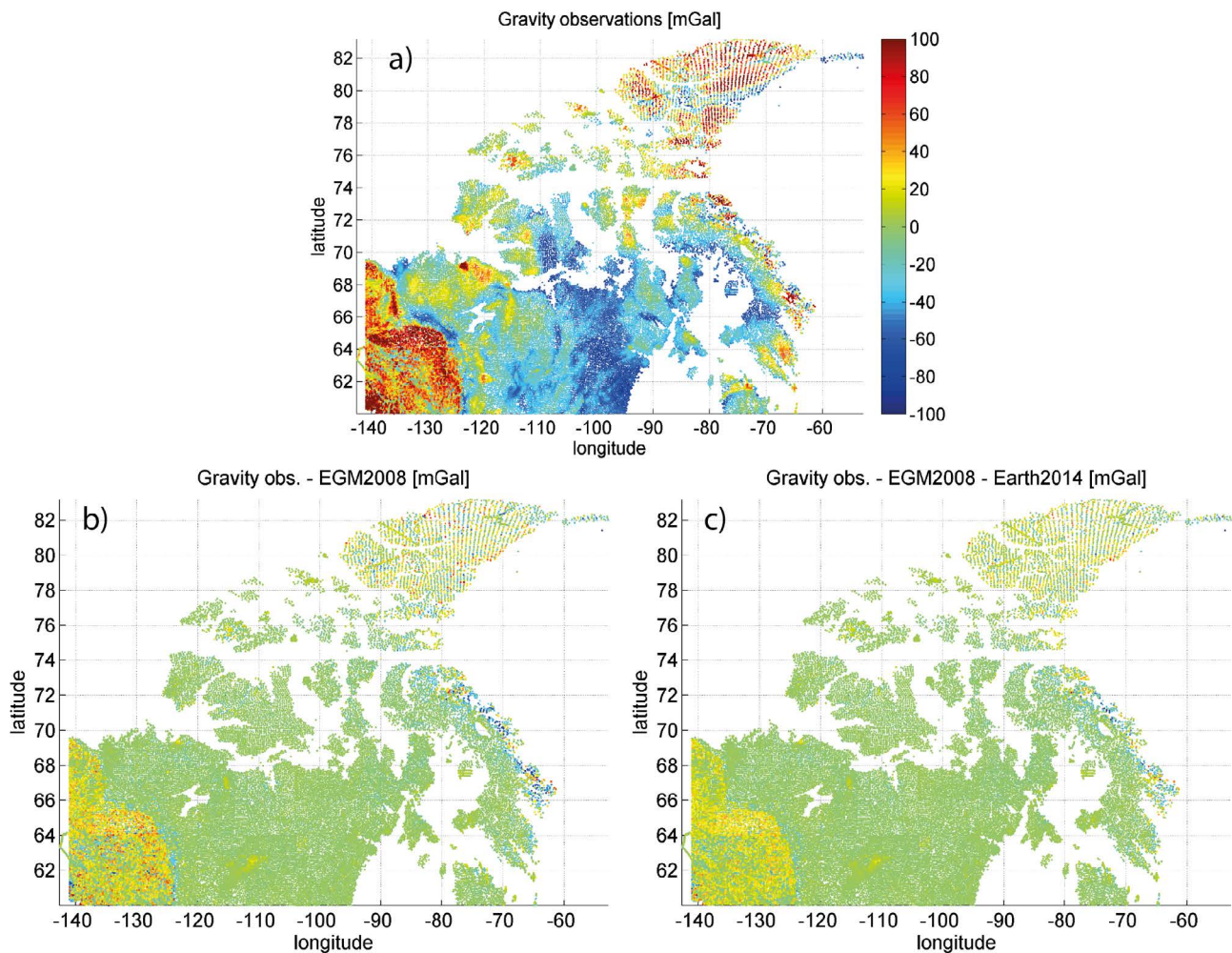


Fig. 4.5 – Gravity observations (a) and residuals at the stations of the ground-truth sites (mGal) over Northern Canada obtained with EGM2008 (b) and the combination with the ETP multi-layer model (c).

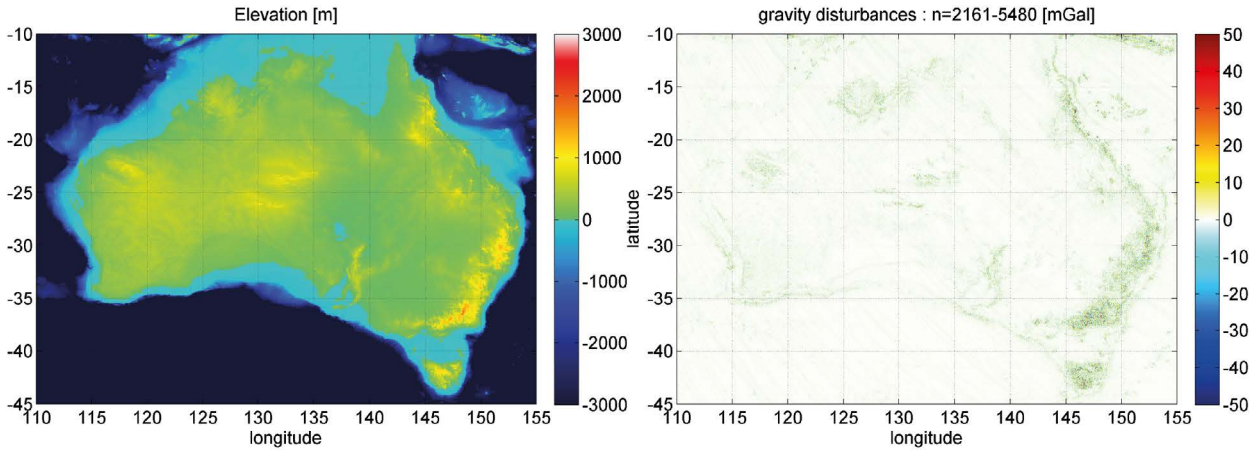


Fig. 4.6 – Elevations (m) and gravity disturbances at Earth’s surface (mGal) in the degree band $n \sim 2160 - 5480$ of the degree-5,400 ETP multi-layer model over Australia.

4.2.3 Areas with small topographic features: Australia

The largest ground-truth data set, with 775,732 gravity observations spread across the Australian continent, covers big parts of an area of about $7,692,024 \text{ km}^2$ (Fig. 4.7a). The ground-truth data set consists of the most reliable terrestrial gravity observations ($\sigma < 1 \text{ mGal}$) of the *Australian National Gravity Database* (ANGD) (Wynne and Bacchin, 2009). The average elevation of the stations is $\sim 311 \text{ m}$, varying between ~ -32 and $+1888 \text{ m}$ ($RMS = 369.3 \text{ m}$, Fig. 4.6). Compared with the other ground-truth data sets (above) it thus represents the smallest and smoothest topographic features.

In this area, EGM2008 is able to explain roughly 81.4 % of the observed gravity disturbances, while the combination models – with EGM2008 up to degree 2190 merged spectrally with ETP models up to degree 5480 – achieves a reduction of $\sim 84.3 \%$ (Tab. 4.3). Again, single-layer and multi-layer models show the same performance. Relatively, the inclusion of the short-scale forward modelled gravity from the ETP models leads to an improvement of about $\sim 16.3 \%$ w.r.t. to EGM2008. Thus, even over a comparatively smooth country (in terms of topography) such as Australia, the gravitational potential of the topographic masses is able to improve the agreement between observed and modelled gravity in combination with up-to-date gravity field models such as EGM2008. However, largest statistical improvements originate from the highest elevated areas such as the Australian Alps in the south-east, seen vaguely from Figs. 4.7b and Figs. 4.7c.

Statistics over Australia	Min	Max	Mean	STD	RMS	red. rel. to	red. rel. to
Gravity Data	[mGal]	[mGal]	[mGal]	[mGal]	[mGal]	Obs. [%]	EGM08 [%]
Observations	-180.22	163.36	7.85	26.66	27.8	-	-
Obs. - EGM2008	-195.87	61.2	-1.23	5.02	5.17	81.40	-
Obs. - (EGM2008 \oplus RET2014)	-193.97	61.47	-1.13	4.18	4.33	84.43	16.31
Obs. - (EGM2008 \oplus Earth2014)	-193.95	61.49	-1.13	4.18	4.33	84.43	16.32

Tab. 4.3 – Statistics of the 775,732 ground-truth observations over Australia and residuals w.r.t. gravity from EGM2008 and the combination model that includes the short-scale gravity from the single- and multi-layer ETP models. The right side of the table shows the percentage of RMS reduction (=improvement) of the residuals obtained w.r.t. the observations and EGM2008.

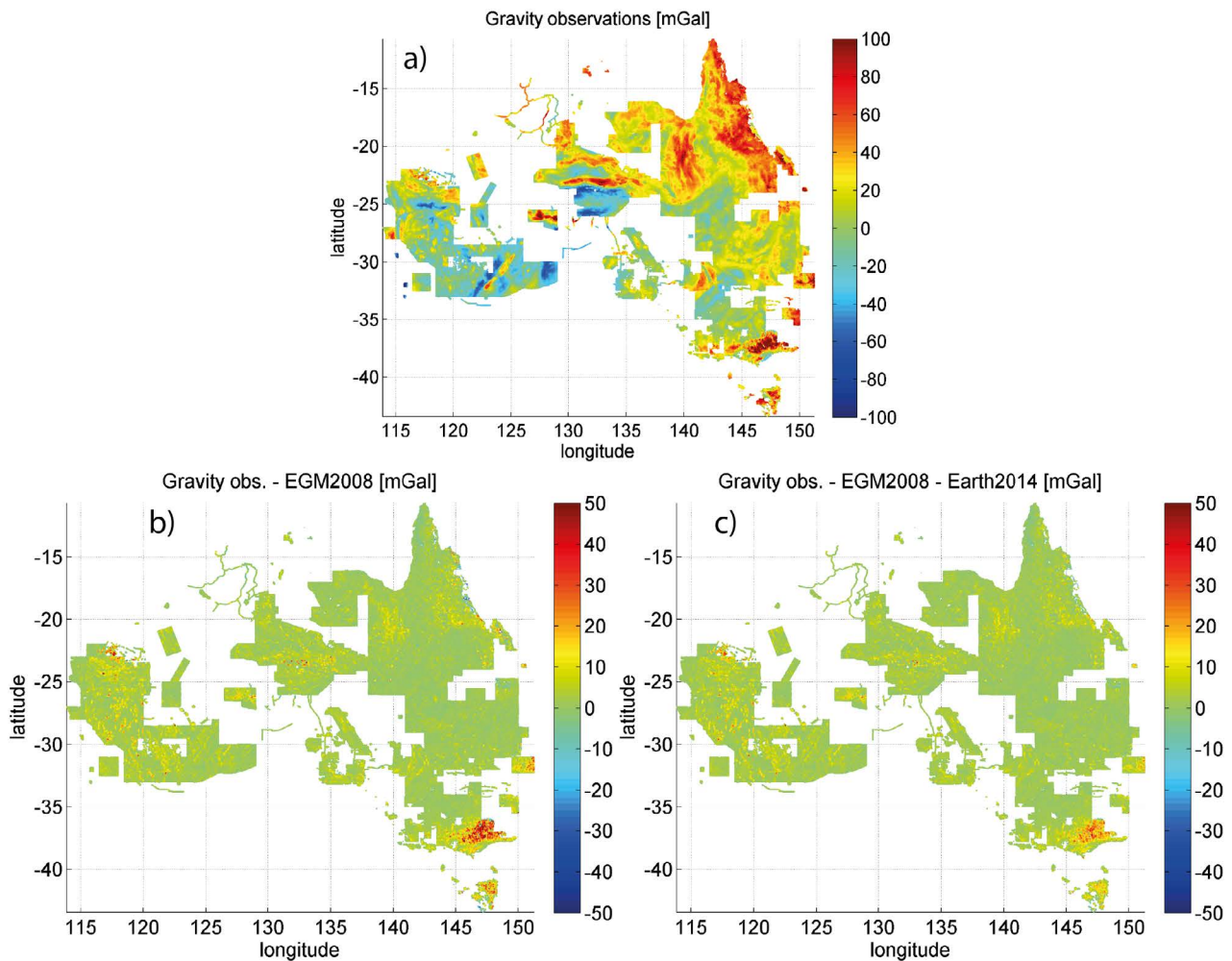


Fig. 4.7 – Gravity observations (a) and residuals at the stations of the ground-truth sites (mGal) over Australia obtained with EGM2008 (b) and the combination with the ETP multi-layer model (c).

4.2.4 Performance over Antarctica

Over Antarctica the observation-based *Antarctic Gravity Anomaly Grids (AGAG)* (Scheinert et al, 2016) serve as ground-truth data for the validation of the topographic potential models and the evaluation of combined high-resolution gravity modelling. Here only the most accurate 24,315 observations (those with a denoted accuracy of $STD < 2$ mGal) are used. The mean elevation at the data points of this excerpt of the AGAG data set roughly is 800 m (RMS= 1313 m), ranging between ~ -60 m to $\sim +3620$ m. See Scheinert et al (2016) and *P-IV* for more general information about AGAG.

In general, Antarctica is a very interesting area for the validation of layer-based spectral forward modelling procedures since Antarctica's topography hosts ice sheets, lake water, ocean water and solid bedrock with considerable elevations (Fig. 4.8). Furthermore, Antarctica is not very well represented in up-to-date gravity field models, mainly because of poor or sparse terrestrial gravity observations and GOCE satellite's orbit inclination that leaves a polar gap unobserved. Thus, the added value by including topographic potential models in combined high-resolution gravity modelling is comparatively large w.r.t. to other areas on Earth. This was shown up to degree 2160/2190 in publication *P-V*, where the improvement due to taking into account a single-layer topographic potential model in the combination with respect to a joint GRACE and GOCE satellite-only

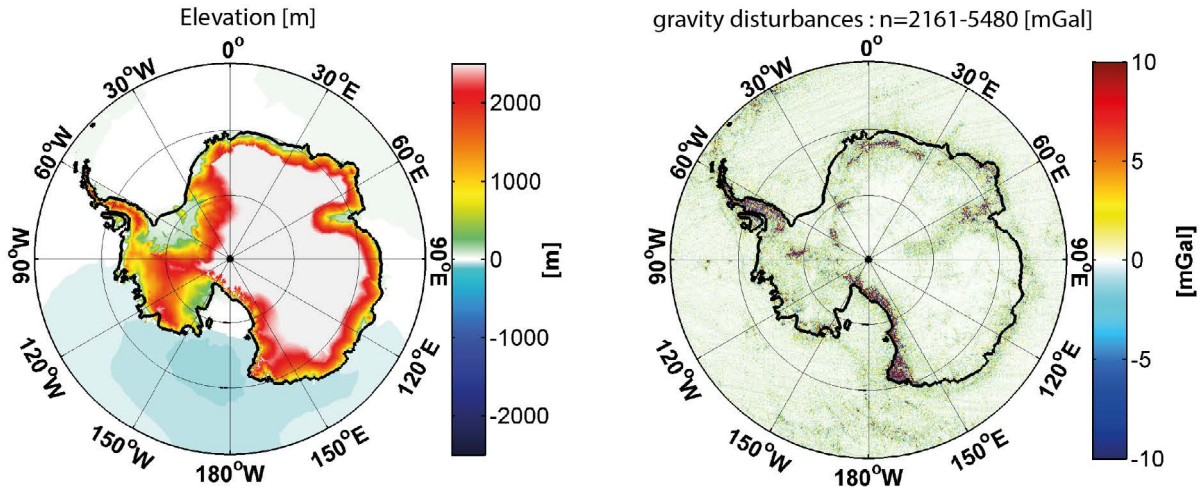


Fig. 4.8 – Surface elevations (m) and forward modelled gravity (mGal) in the degree band $n \sim 2160 - 5480$ of the degree-5,400 ETP multi-layer model over Antarctica.

model was in the order of 8 to 75%. In publication *P-IV*, using a multi-layer model instead of a single-layer topographic potential model, an even higher agreement between the ground-truth data and the combination model was found over Antarctica (by about 2 % on average). Over the Antarctic ocean the improvement due to layer-based forward modelling is slightly higher (around ~ 5 % on average).

Here the same experiment – combining the satellite-only model GOCO05s with the topographic potential models and comparing their performance to the satellite-only model over Antarctica – is repeated up to degree 5400/5480. The topographic potential models thereby are used for the spectral band $280 < n \leq 5480$. The results of this experiment is shown in Fig. 4.9 and numerically in Tab. 4.4. The best agreement with the ground-truth observations is achieved by the combination using the multi-layer topographic potential model, which reduces the observations by ~ 56.7 % (improvement of 9.5 % relative to GOCO05s). The single-layer model achieves a reduction of ~ 55.5 % (improvement of 7.0 % relative to GOCO05s). This confirms the actual, albeit small, advantage of multi-layer modelling. For a more detailed visual inspection of the observed gravity, the residuals and the step-wise improvement, a close-up of the Antarctic Peninsula is given in Fig. 4.10. However, the improvement from panel D to F (left to right in lower row) of Fig. 4.10 is so small that it is visible only

Statistics over Antarctica	Min	Max	Mean	STD	RMS	red. rel. to	red. rel. to
Gravity Data	[mGal]	[mGal]	[mGal]	[mGal]	[mGal]	Obs. [%]	GOCO05s [%]
Observations	-147.4	166.3	-2.02	36.56	36.61	-	-
Obs. - GOCO05s	-98.69	139.69	-0.29	17.52	17.52	52.14	-
ETP models taken for $280 < n \leq 5480$:							
Obs. - GOCO05s + RET2014	-201.58	98.78	-0.13	16.29	16.29	55.50	7.03
Obs. - GOCO05s + Earth2014	-199.71	95.72	-0.13	15.86	15.86	56.68	9.48
ETP models taken for $280 < n \leq 2190$:							
Obs. - GOCO05s + RET2014	-201.79	96.60	-0.17	15.76	15.67	57.20	10.1
Obs. - GOCO05s + Earth2014	-200.29	93.12	-0.17	15.43	15.43	57.85	11.9

Tab. 4.4 – Statistics of the 24,315 ground-truth observations over Antarctica and residuals w.r.t. gravity from the satellite-only model GOCO05s and the combination model that includes the short-scale gravity from the single- and multi-layer ETP models using the full resolution of $n_{max} = 5480$ (cf. Fig. 4.9) and truncating at $n_{max} = 2190$ (from Tab. 8 in *P-IV*). The right side of the table shows the percentage of RMS reduction (=improvement) of the residuals obtained w.r.t. the observations and GOCO05s.

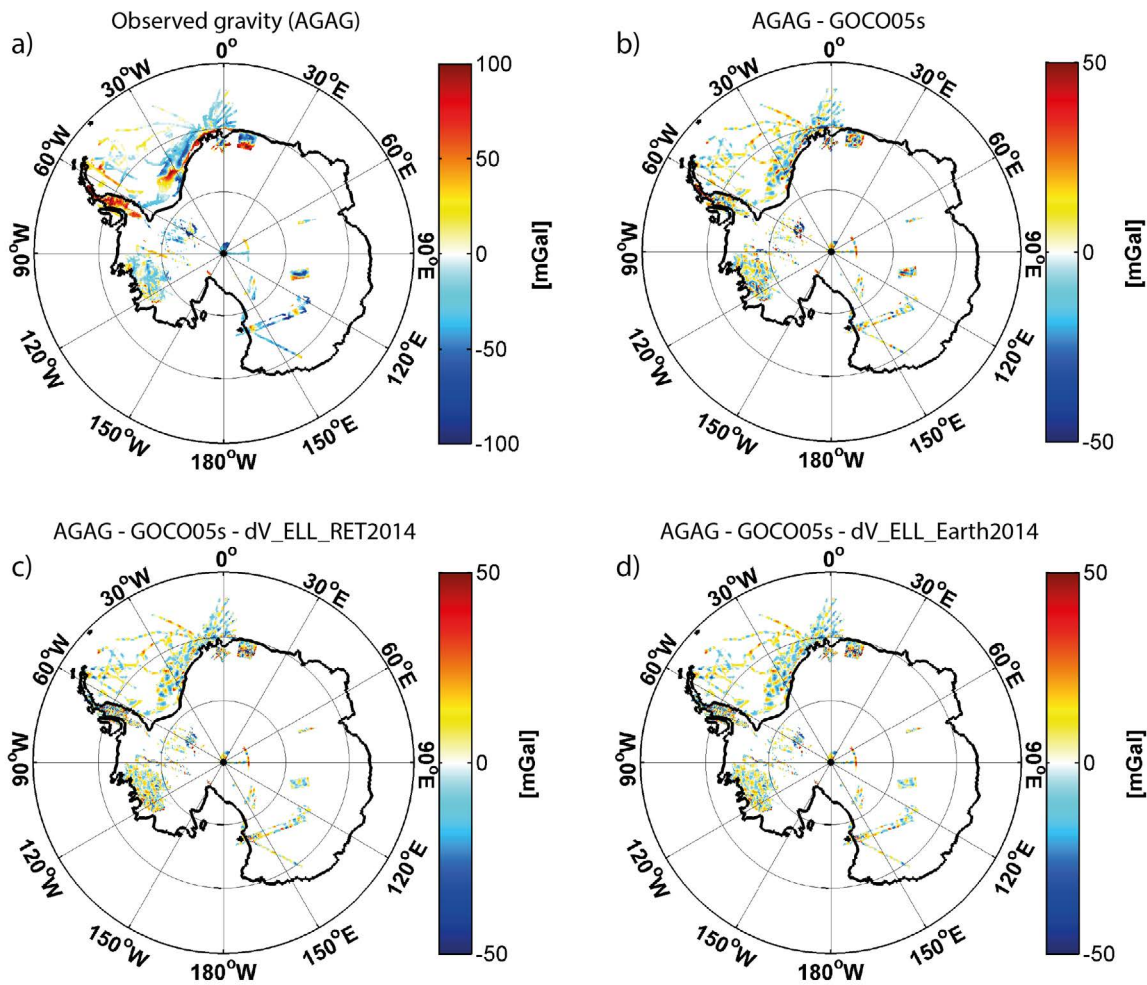


Fig. 4.9 – Observed gravity from the AGAG (where $STD < 2$ mGal) over Antarctica (a) and residual gravity obtained with GOCO05s (evaluated up to degree $n = 280$) (b), the combination with the ETP single-layer model (c) and the combination with the ETP multi-layer model (d). Numerical results to this figure are given in Tab. 4.4. Units are in mGal.

in the statistics.

As interesting outcome, the improvement is better when solely modelling the topographic potential models to degree 2160/2190. Then the improvement relative to GOCO05s is in the order of 10.1 % and 11.9 % on average for single- and multi-layer modelling, respectively (Tab. 4.4), as found in *P-IV*. Thus the gravitational signal of the topographic potential models in the additional spectral window $2160 < n \leq 5480$ seems to worsen the agreement with the observations contained in the AGAG (by about 2 – 3 %). This is in stark contrast to the improvement that was found with all other ground-truth data sets investigated here at scales < 10 km. Even over Northern Canada, that similarly to Antarctica covers polar regions, the short-scale topographic gravity from the spectral forward models could improve the agreement to ground-truth data by about 10 % (cf. Tab. 4.2). Since only the most accurate points of the AGAG have been used for the evaluation over Antarctica it is very likely that the geometric input of the forward modelling over Antarctica is not very reliable at short scales, i.e. between 4 km and 10 km resolution. To be precise, the Earth2014 layers over Antarctica rely on the elevations of bedrock and ice sheets of BedMap2 (Fretwell et al, 2013). The data producers of Bedmap2 state "(...) We provide the ice thickness, bed and surface elevation grids at a uniform 1-km spacing. In creating the ice thickness grid,

however, we initially gridded the direct measurements of thickness at 5 km, primarily because the distribution of these direct measurements does not warrant a higher resolution. (...)" (Fretwell et al, 2013). They justify the choice of a 1 km grid resolution by including detailed available geometric information for outcrops of rocks and mountains. Mostly (over ice-covered bedrock), the actual Bedmap2 resolution does not exceed ~ 5 km, which is confirmed by the above findings (Tab. 4.4). So far, however, Bedmap2 is the state-of-the-art geometric model over Antarctica and was shown to deliver improved elevations as compared to previous Antarctic DEMs, at least up to the resolution of GOCE satellite data (~ 100 km) (Hirt, 2014).

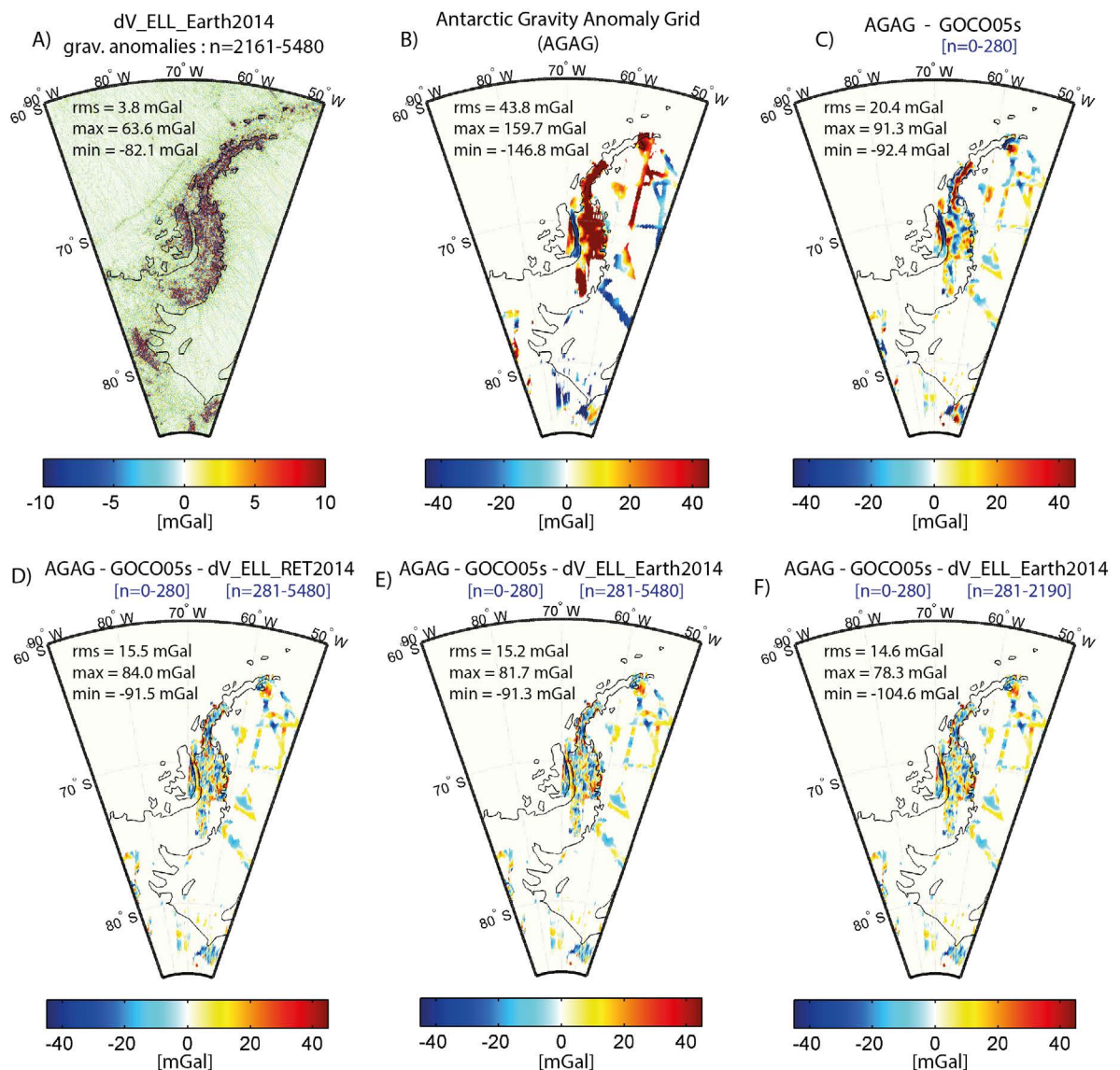


Fig. 4.10 – Gravity anomalies from the multi-layer ETP model in the band $n=2161-5480$ (a), observed gravity anomalies from the AGAG (b) and residual gravity over the Antarctic Peninsula: obtained with GOCO05s (evaluated up to degree $n = 280$) (c), the combination with the ETP single-layer model for $n=281-5480$ (d), the combination with the ETP multi-layer model for $n=281-5480$ (e) and for $n=281-2190$ (f). Units are in mGal.

4.2.5 Performance over the ocean

For the evaluation of the performance of high resolution combined gravity modelling with the help of topographic potential models over the ocean, a large data set with (ship-track) gravity observations that covers big parts of the Arctic (Northern Polar) ocean around Canada is used. As seen from Fig. 4.11, especially the coastal areas are well covered. Also some observations over deep bathymetry (up to -3450 m bathymetric depth) are contained over the Beaufort Sea west of Canada.

The statistics (Tab. 4.5) reveal, that over the Arctic ocean, the improvement of the combination model with gravity up to up to degree 5480 relative to EGM2008 is rather small. EGM2008 alone – without topographic gravity augmentation – already explains about 85.7 % of the observed gravity. The improvement relative to EGM2008 is about ~ 6.4 % for single-layer and ~ 6.6 % for multi-layer modelling, respectively. This amounts to a RMS reduction of about ~ 0.35 mGal. The most significant reduction of observed gravity due to the topographic potential models is found over coastal zones, especially in the fjords found in the north-eastern part of Baffin Island (see Fig. 4.11bc, lower panels).

The fact that over the ocean, the topographic potential models do not seem to contribute to the same extent to combined gravity field modelling as over land in high degrees requires explanation. There are two main reasonings providing such an explanation: signal attenuation of deep bathymetric masses and their (poor) knowledge at shorter scales. Firstly, the bathymetric masses (bedrock) are located further away from the point of evaluation (the ocean's surface) than in case of evaluations over land, where the evaluation point is located directly on the topographic masses. Thus, over the ocean the gravitational signal of the masses of solid rock is attenuated. As learned above (Sect. 2.3.2) the attenuation is of increasing manner towards high- and ultra high degree. As seen from Fig. 4.4 (right plot) there is hardly any short-scale (topographic) signal found over the oceans. The ocean water masses themselves play a subordinate role due to their (comparatively) small associated density contrast despite their immediate vicinity. In other words, at Earth's surface (i.e. at the boundary to the atmosphere) the short-scale gravitational fluctuations are smaller over the ocean than over land, in general. This and the fact that EGM2008 contains homogeneous altimetric measurements over the ocean explains why EGM2008, that resolves the gravity field down to scales of ~ 10 km, gives a better fit to the ship-track gravity observations than to gravity observations over rugged terrain. Also it explains why the reduction of the ground-truth observations is larger in close vicinity to the coast (in shallow water): there satellite altimetry is less accurate and due to coastal topographic masses (fjords) larger signals come into play in the topographic potential. Secondly, inaccurate high-resolution bathymetric depth information in the input topographic data set (Earth2014) would explain the small improvement of topographic potential models to combined gravity field modelling over the oceans. We know that the resolution of bathymetric depth data is very inhomogeneous (see Sect. 3.2.1 and *Sandwell et al (2014)*), however, coastal zones typically are well surveyed.

Statistics over the Arctic ocean	Min	Max	Mean	STD	RMS	red. rel. to	red. rel. to
Gravity Data	[mGal]	[mGal]	[mGal]	[mGal]	[mGal]	Obs. [%]	EGM08 [%]
Observations	-164.85	248.58	-18.76	43.96	37.79	-	-
Obs. - EGM2008	-97.54	106.94	-0.63	5.36	5.40	85.71	-
Obs. - (EGM2008 \oplus RET2014)	-91.7	108.67	-0.49	5.03	5.05	86.63	6.41
Obs. - (EGM2008 \oplus Earth2014)	-91.51	108.52	-0.49	5.02	5.04	86.65	6.56

Tab. 4.5 – Statistics of the 142,167 ground-truth observations and residuals over the Arctic/Northern Polar Ocean and parts of Hudson Bay w.r.t. gravity from EGM2008 and the combination model that includes the short-scale gravity from the single- and multi-layer ETP models. The right side of the table shows the percentage of RMS reduction (=improvement) of the residuals obtained w.r.t. the observations and EGM2008.

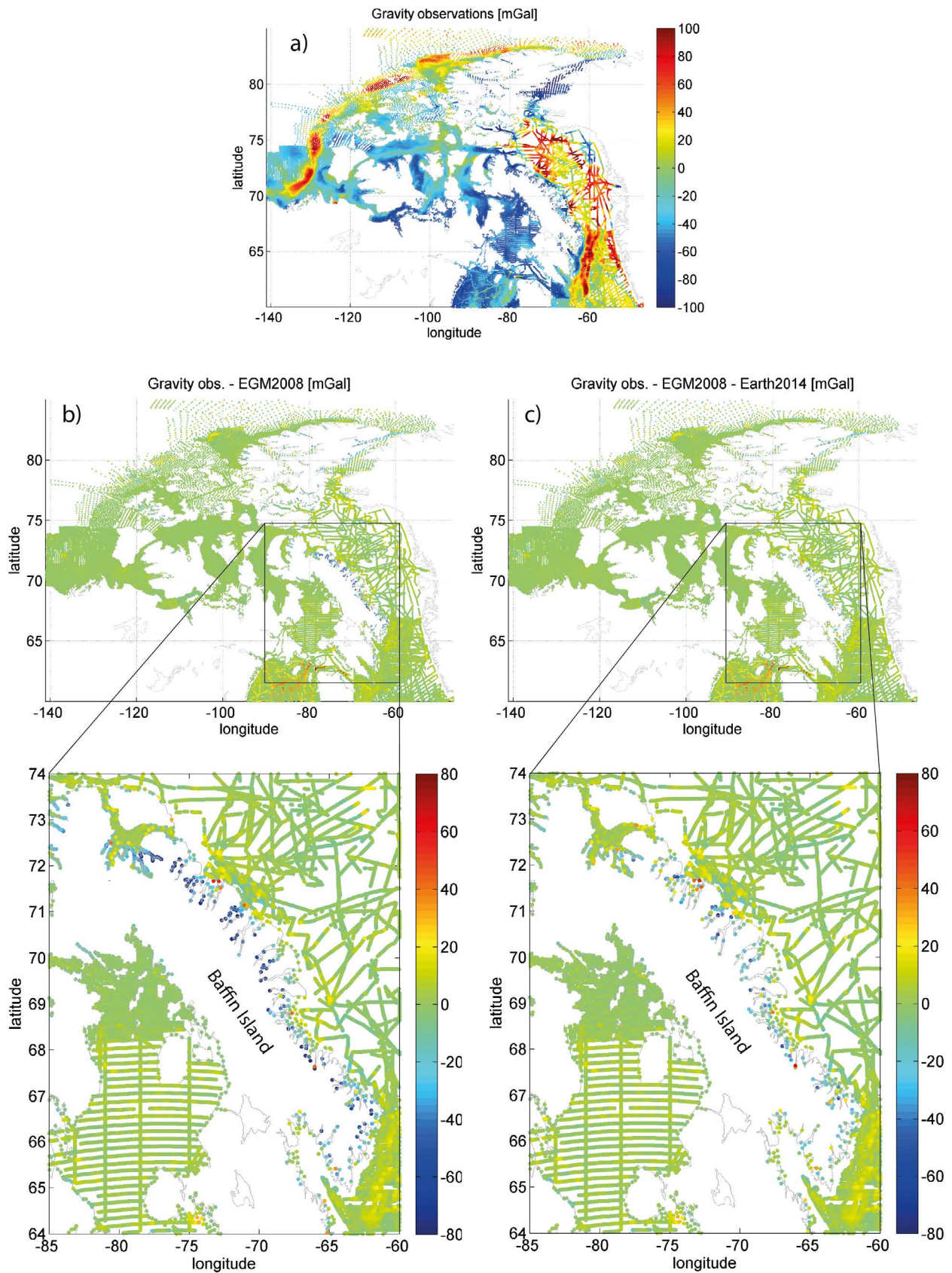


Fig. 4.11 – Gravity observations (a) and residuals (mGal) of along ship-tracks over the Arctic/Northern Polar Ocean and parts of Hudson Bay obtained with EGM2008 (b) and the combination with the ETP multi-layer model (c).

Following the above line of arguments, it becomes clear that to the same reasoning also the RET approximation effect, affecting mainly the oceans, becomes acceptable towards high- and ultra high degrees: the expected signals are small anyway. While at global scale, the RET approximation error is in the order of ~ 0.5 mGal (RMS) in the band $2161 < n \leq 5400$ (Fig. 3.12), it is about ~ 0.01 mGal (RMS) in the here investigated differences to ship-track data. Obviously the impact of the RET approximation diminishes towards high and ultra-high degrees (at least for the here investigated area), given inaccuracies of the ship-track data and of the bathymetric depths, and other prevailing modelling errors. Over deep-ocean trenches and mid-oceanic ridges the picture is different (see Fig. 3.12b), since there the RET approximation is most severe.

4.3 Other applications of spectral forward modelling of the topographic potential

This section deals with other applications for global forward modelling in the spectral domain and its topographic potential models. Spectral forward modelling generally can be used for

- the testing of isostatic hypotheses (e.g. *Göttl and Rummel, 2009*),
- omission error modelling, e.g. in the frame of height unification or validation of gravity field models (e.g. *Gruber et al, 2012*),
- Bouguer gravity computation (e.g. *Wieczorek, 2015*),
- smoothing or reducing the Earth's gravity field or its observations, e.g. in the frame of remove-compute-restore applications or Stokes's geodetic boundary value problem (e.g. *Grombein et al, 2014*),
- geoid-to-quasigeoid separation (e.g. *Tenzer et al, 2016*),
- evaluation of global digital elevation models (e.g. *Rexer et al, 2015*),

and even more applications. Here, only the concepts of two out of these applications are described briefly together with small computational examples. Thereby references to related work, where more examples and details about the applications can be found, are given. Focus is placed on the expected benefits of the here proposed forward modelling procedures for the applications.

4.3.1 Height unification and realisation of a global vertical datum

One of the up-to-date topics of research in geodesy is the realisation of a global vertical datum which can be achieved by a satellite-based height unification with the help of satellite derived global gravity field models. In simple words, height unification involves the determination of height offsets between national vertical datums on regional and inter-continental level. The geoid – the equipotential surface coinciding with a hypothetical global ocean – is provided by global gravity field models and serves as a global vertical reference surface. Height offsets of national, local or regional vertical datums can then be measured relative to this global reference. This typically is achieved by comparing geoid heights obtained by a subtraction of GPS heights and levelling heights with the global reference geoid. Recently, the gradiometer measurements of the satellite mission GOCE have led to a new generation of accurate (global) geoid models initiating new attempts to adjust vertical datums on regional and global scale (see collection of articles in *Sideris and Fotopoulos (2012)*). Another method for the estimation of vertical datum offsets is the *ocean approach* where it is aimed " (...) to connect the MSL at various tide gauges by a model of mean dynamic ocean topography (MDT)." (*Rummel, 2012*), which is not further discussed here.

Given spirit leveling and GPS measurements at each point i belonging to the same local vertical datum A , the connection to the (quasi-) geoid height is given by (*Gruber et al, 2012*)

$$N_i^A = h_i - H_i^A, \quad (4.4)$$

where N_i^A is the observed geoid height, referring to vertical datum A , h_i is the GPS-based ellipsoidal height for point i and H_i^A is the orthometric or normal height for point i from spirit leveling. The datum offset ΔN_i^A relative to the geoid retrieved from a GOCE-based geopotential model at each point then becomes

$$\Delta N_i^A = N_i^A - (N_i^{GOCE} + N_i^{res}) \quad (4.5)$$

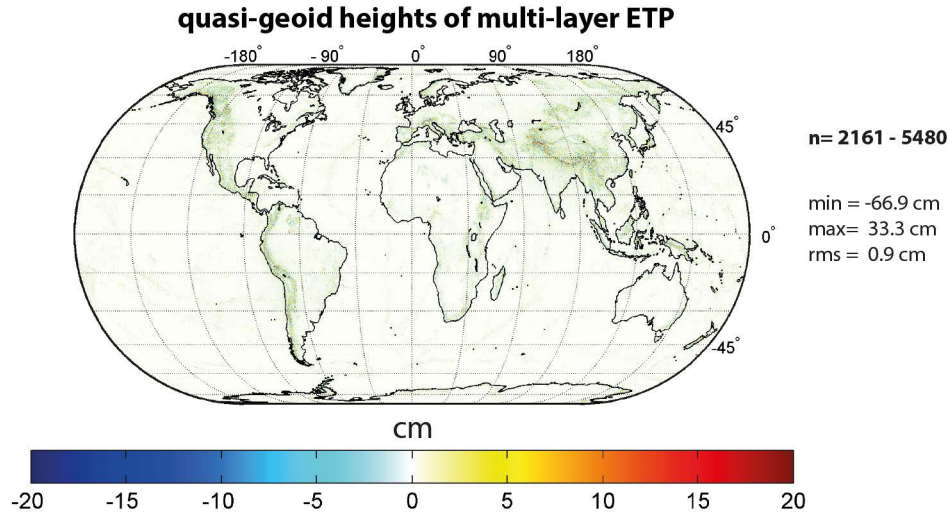


Fig. 4.12 – Omission error in terms of quasi-geoid heights (cm) at Earth's surface computed by a spherical harmonic syntheses of the multi-layer ETP model ($dV_ELL_Earth2014$) in the spectral band ranging from degree 2161 to 5480. The maximum and the minimum are located close to each other in the Himalayas, about 2.9° west of Mount Everest.

from which the mean datum offset $\Delta\bar{N}^A$ of the vertical datum A can be retrieved as

$$\Delta\bar{N}^A = \frac{\sum_i \Delta N_i^A}{n^A}, \quad (4.6)$$

where N_i^{GOCE} is the GOCE-based geoid height at point i , N_i^{res} is the residual geoid signal that is omitted by the GOCE-based geopotential model (i.e. omission error) and n^A is the total number of points referring to the vertical datum A . These relations can be used in least-squares adjustment approaches taking into account stochastic models in order to retrieve optimal height offsets (*Rummel, 2012; Grombein et al, 2016a*). The above relation (Eq. 4.5) "(...) only is correct for ideal situations assuming error-free spirit leveling and gravimetry, error-free GNSS as well as an error-free GOCE geoid (...)" (*Gruber et al, 2012*) and a known omission error. Usually the omission error is unknown. In this case forward modeling of the potential of the topographic masses is a means to get estimates of it and to achieve reasonable datum offsets. Other methods exist for mitigating the residual geoid signal, such as the inclusion of the Stokes integral formula into a least-squares adjustment approach (*Rummel, 2012*).

The principle of omission error modelling is the same as in the *spectral enhancement method* (*Hirt et al, 2012*), where the spectral gap existing between gravity model and terrestrial gravity measurement is filled by (spectrally filtered) forward modelled topographic gravity. Beyond the resolution of GOCE-based gravity models (typically $n > 200 - 250$) first other observation-based gravity models are used to estimate the omission error (e.g. EIGEN-6C or EGM2008). Beyond the actual resolution of these models, i.e. for $n > 2161$, the omission error has to be estimated from other sources, e.g. RTM or forward modelling. The first is a common method (with some disadvantages, see further up) and is freely available with the near-global ERTM gravity model, providing residual gravity maps of ~ 220 m resolution over the continents (*Hirt et al, 2014*). Very recently, omission error modelling successfully has been achieved in a least-squares adjustment approach with the help of local space-domain forward modelling based tesserooids derived from a 7.2 arc-sec resolution topography

(Grombein *et al*, 2016a). The authors found that the estimated height offsets can be changed by up to 3 cm with test data sets over Austria and Brazil, resulting in a reduction of the standard deviation up to 30 – 40 %. Willberg *et al* (2017) showed that over Greece the consideration of the omission error from EGM2008 and forward modelling using the RTM method leads to a significant change of the vertical datum offsets between its different islands (see also further down). Fig. 4.12 shows that the omission error in the spectral window $2161 < n < 5480$ in terms of quasi-geoid heights computed with the here developed degree-5480 multi-layer ETP model (see Sect. 3.4.1) can reach extreme values of up to -67 cm and $+33$ cm ($RMS \approx 1$ cm) on global scale. Looking at a close-up of the omission error over Greece (Fig. 4.13b) reveals significant signals over land as well as over some of the Greek islands, which are well resolved by a degree-5480 (~ 4 km) topographic potential model. The problem of vertical height offsets between the Greek island can be seen as small-scale example for height unification in general, which is directly transferable to global height unification, where the offset between continents is sought. Islands have a high omission error because they often stand out as peaks in the topographic/bathymetric function (especially volcanic islands), which was also observed by Willberg *et al* (2017). For example the island Karpathos exhibits a mean omission error of 2.4 cm, ranging from $+9.0$ cm to -6.9 cm ($RMS=4.8$ cm) in the spectral band $2161 < n \leq 5480$. Thus, the consideration of the omission error at

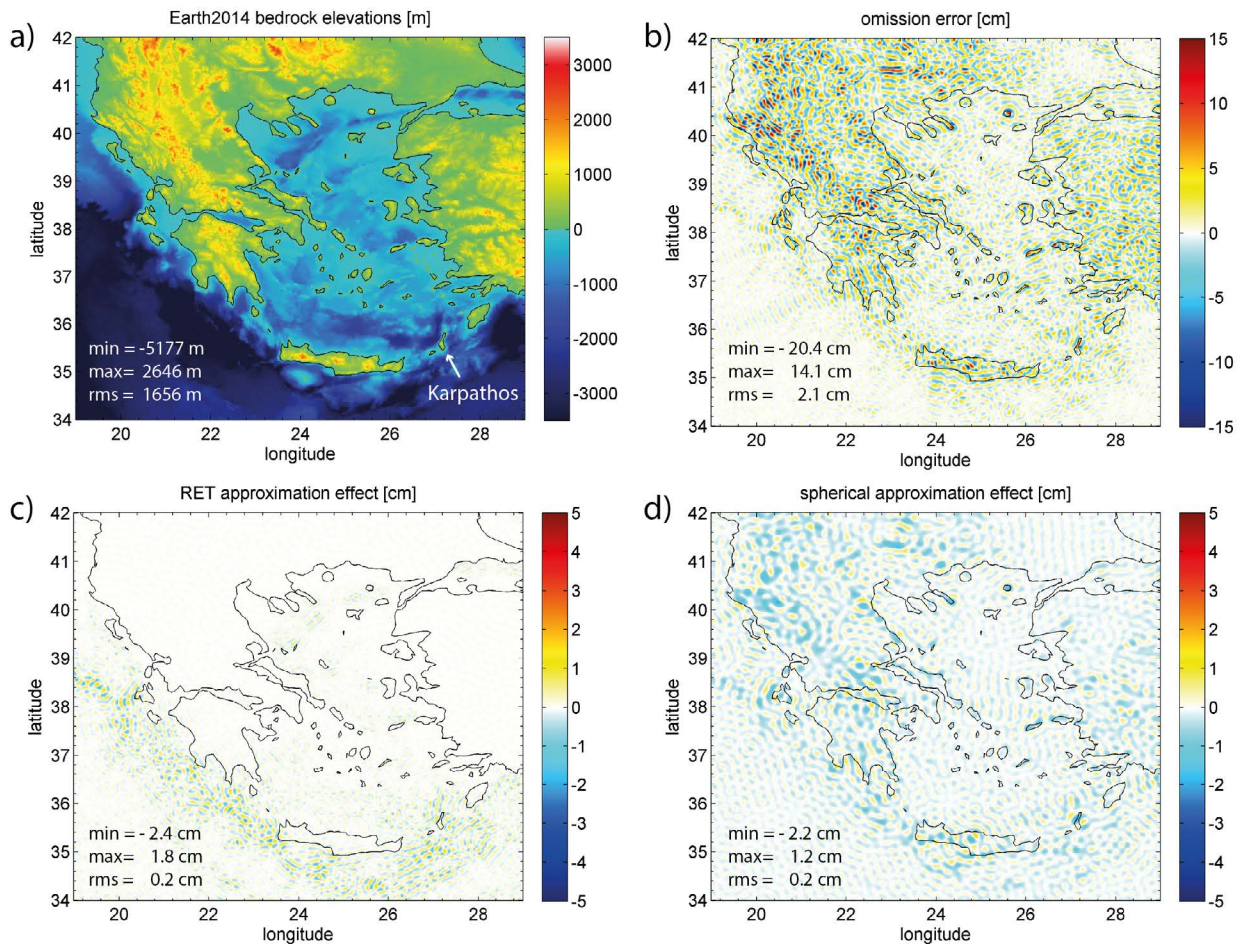


Fig. 4.13 – Example for the omission error as given by the spectral forward modelling techniques in this work over the area of Greece: a) bedrock elevations (m), b) omission error in terms of quasi-geoid heights at Earth's surface of a multi-layer ETP model filtered to $n=2161-5480$ (cm), c) error introduced by the RET approximation (i.e. difference of single- and multi-layer model) and d) by the spherical approximation of STP models (i.e. difference of ETP and STP model) in the same spectral band.

single GPS/levelling-points beyond the resolution of up-to-date observation-based GGMs can make significant changes to the mean vertical offset of Karpathos to the local vertical datum (LVD), which is in the order of -3.2 cm (Willberg *et al*, 2017).

In the context of investigating the omission error over Greece the improvement of the here developed layer-based forward modelling in ellipsoidal approximation over single-layer (RET) modelling and the spherical approximation can be demonstrated: at short scales ($2161 < n \leq 5480$) the RET approximation (as found in single-layer modelling) causes errors in the order of 0.2 cm (RMS), ranging from -2.4 cm to 1.8 cm. The RET error is introduced over the oceans, mainly, and most severely over the north-west to south-east aligned Mediterranean subduction zone (Fig. 4.13c). In contrast, the error introduced by the spherical approximation of STP models is also found over land, but shows similar amplitudes (RMS=0.2 cm) that are concentrated over topographic/bathymetric peaks (Fig. 4.13d).

4.3.2 Bouguer coefficients and global maps of Bouguer gravity

The Bouguer gravity anomaly (or simply *Bouguer anomaly*) is defined as observed gravity reduced for normal gravity and for the gravitational attraction of the topographic masses. In geophysics Bouguer anomalies play an important role for "(...) geophysical studies of interior mass variations associated with geological units (...)" (P-VI) and gravity inversion, e.g. for recovering the Earth's actual density distribution or to recover its crustal thickness, globally (e.g. Wieczorek, 2015) and locally (e.g. Ebbing *et al*, 2001).

Historically Bouguer gravity has been achieved by reducing a planar slab (or spherical shell), representing the mean height of the topography (cf. Torge, 2003). Today, the complete Bouguer gravity anomaly – including the terrain correction – can be achieved conveniently based on global potential models as described in the following.

The Bouguer potential may be defined as the observed gravitational potential V reduced by the gravitational potential of the topographic masses V^t . With the help of the spectral forward modelling techniques and source-mass data developed in this work (see Chpt. 3) V^t is well described by spherical and ellipsoidal topographic potential models on a global scale. The observed gravitational potential V may be represented by any observation-based GGM listed at ICGEM. Then the Bouguer potential, as e.g. shown in Rexer *et al* (2015) with GGMs based on data of the GOCE satellite mission or by Claessens and Hirt (2013)

with EGM2008, conveniently can be expressed through fully-normalised spherical harmonic Bouguer coefficients (BC) \bar{B}_{nm} , following

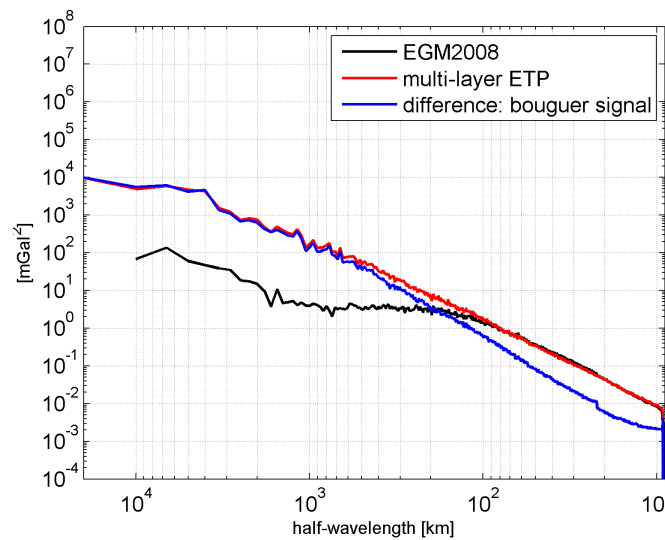


Fig. 4.14 – Degree variances of the Bouguer signal (blue line) as given by the difference of the observation based signal model EGM2008 (Pavlis *et al*, 2012) (black line) and the (uncompensated) multi-layer ETP model (red line) in terms of gravity ($mGal^2$).

$$\bar{B}_{nm} = \bar{V}_{nm} - \bar{V}_{nm}^{ETP}. \quad (4.7)$$

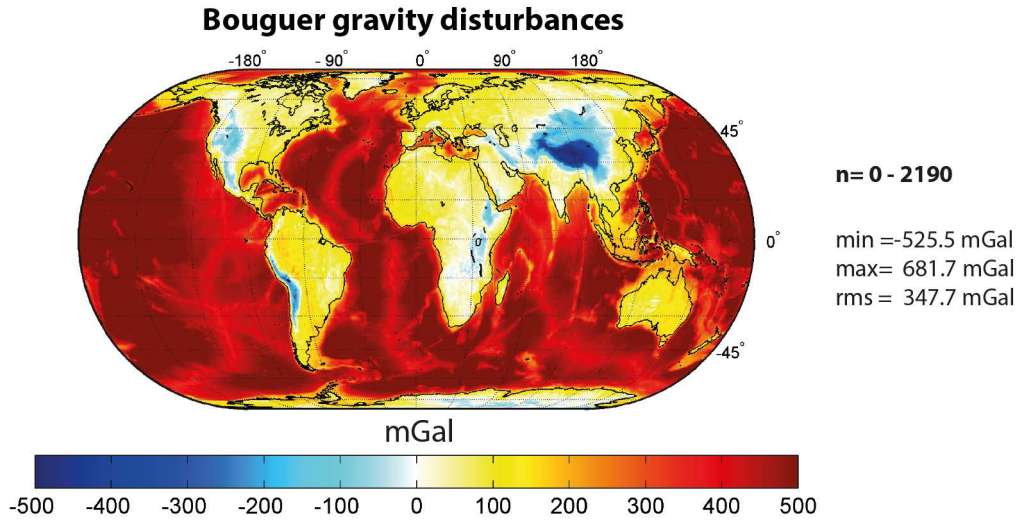


Fig. 4.15 – Bouguer gravity disturbances (mGal) at Earth’s surface as given by the difference of EGM2008 and the here developed multi-layer ETP model in the spectral band $n = 0 - 2190$

Importantly, the constants of the spherical harmonic models \bar{V}_{nm} and \bar{V}_{nm}^{ETP} must be identical (e.g. reference radius and GM) or have to be chosen consistent a priori. Taking EGM2008 as source for \bar{V}_{nm} and the layer-based spectral forward modelling for \bar{V}_{nm}^{ETP} gives the Bouguer signal shown in terms of gravity degree variances in Fig. 4.14. Introduced in the spherical harmonic series (Eq. 2.4) the Bouguer coefficients allow the straight forward computation of global map of Bouguer gravity disturbances (Fig. 4.15), or any other gravity functional.

Note that \bar{B}_{nm} cannot be retrieved with a STP model (\bar{V}_{nm}^{STP}), since the spherical approximation is not compatible with observation based GGMs (see above). The BC in Eq. 4.7 improve conceptually over the classical (planar) definition of Bouguer modelling in geodesy (*Rexer et al, 2015*): they take into account (1) the actual ellipsoidal shape of Earth, (2) the implicit modelling of terrain corrections, (3) the effect of remote masses (*Kuhn et al, 2009*) and (4) ensure spectral consistency (i.e. identical band-widths) of both signals.

Theoretically, in order to compute accurate short-scale Bouguer gravity anomalies it is further important to also consider the signal in multiples of the input bandwidth of topographic source-mass model of topographic potential models, being the main outcome of publication *P-VI*. The gravitational signal in the first 10 multiples (spectral band from degree 2160 to 21,600) has a global RMS of ~ 0.5 mGal and ranges between -33.4 and $+52.3$ mGal (see Sect. 3.4.2.4 and Fig. 3.16b). The relevance of these amplitudes depend on the application, of course.

4.4 Summary and evaluation of the chapter's research aims

This chapter (Chpt. 4) along with (parts of) the publications *P-IV*, *P-V* and *P-VI* dealt with the application and validation of the methods and data compiled and developed in this dissertation in view of the research aims A5 and A6, that read:

"Find combination strategies for a combination of observed and high-resolution forward modelled gravity and show the benefiting of the latter to combined gravity field modelling, globally". (A5)

"Elaborate the usage of such a combination, the developed data and methods in other applications". (A6)

In this context, five strategies for this type of combination were reviewed and assessed comparatively. The most powerful of which, the *least-squares* merge and the *block-diagonal* merge were not tested due to missing stochastic information (i.e. the actual errors) about the computed forward models and their associated enormous computational demands. Nevertheless, these approaches would be the best suited for a regionally controlled impact of forward-modelled gravity in areas devoid accurate terrestrial observations. The *regularisation merge* enables an indirect regional weighting (due to the stochastic model of the observed gravity) via regularisation of the fully assembled normal equation system of the observations. In this procedure the SHCs of an ellipsoidal topographic potential model are introduced as prior information which was shown to deliver regional improvements over the area of Antarctica in publication *P-IV* and *P-V*, compared to the rather simple *spectral* and *spatial merge*. The latter two techniques are mutually consistent and rely on the concept of spectral filtering, which in case of the ETP requires extra filter coefficients instead of a (abrupt) truncation of the spherical harmonic series in order to treat the correlations between coefficients of the same order. For the purpose of demonstration and validation, the simplistic spectral merge was used to generate combined models consisting of EGM2008 to model the gravitational signal for $n \leq 2160$ and forward-modelled gravity for $2161 \leq n \leq 5480$. Those were evaluated over diverse areas at over 1 million ground-truth points in order to get a representative judgment of the quality of the single- and multi-layer ETP models. Over areas with large topographic features such as the alpine country Switzerland, the short-scale information of the multi-layer ETP model improves the RMS agreement with the ground-truth data by about 46 % relative to EGM2008. In Northern Canada, which on average has a smoother topography, the improvement is at the level of 29 %. Over a comparatively flat region such as the Australian continent, the improvement still is significant (~ 16 %). Over Antarctica, the relatively small improvement w.r.t. the satellite-only model GOCO05s is to be explained by rather poor short-scale information of the bedrock and ice sheet geometry as contained in Bedmap2. Over the Arctic (Northern Polar) ocean the positive effect due the combination with the high-resolution ETP models is also comparatively small (RMS reduction of about 6.5 %), which is due to the attenuation of the short-scale gravitational signal of deeply located bathymetric masses at the oceans surface, to inaccurate short-scale bathymetric depth information or to altimetry contained in EGM2008. Generally, the reduction over the oceans is largest in the vicinity to the coastline and in fjords. Over land, the small RET approximation effect visible in the band $0 \leq n \leq 2160$ disappears entirely in the band $2161 \leq n \leq 5480$, while it shrinks to acceptable level over the ocean, at least in comparison with the here used ship-track data. Summarising, the short-scale (topographic) gravitational signal from the here developed data and methods is beneficial to high-resolution gravity modelling, especially over land and over coastal areas in vicinity of large topographic masses, as seen from an investigation up to degree 5480. In this respect, also the overall research goal G3 is fulfilled. Finally, the application of spectral topographic potential models as developed in this work for global Bouguer modelling and height unification was shown and discussed briefly, fulfilling the other research aims of this chapter.

Chapter 5

Discussion and Future Directions

The overall research goals of this work were discussed and evaluated in detail in Chpts. 2.4, 3.5 and 4.4. This chapter is devoted to a synoptic discussion across all chapters and publications of this dissertation, illuminating the key findings in a broader perspective and giving directions for future research.

Dealing with the question up to which scale global forward modelling of the topographic masses is useful can – in the first place – be answered with the help of the created empirical degree variance rule based on GGMplus. Certainly, this has to be done in light of the respective application. The GGMplus rule delivers realistic estimates for the average continental short-scale gravitational signals expected at Earth's surface, being slightly larger than the truly global average signals (when including the oceans). This can be seen from comparisons with the created degree-5400/5480 models and other local estimates of signal strengths in the literature. From this perspective, modelling to at least degree 5,400 is required for the determination of the geoid height with *cm* accuracy on global average. Even modelling up to extremely high degree such as 21,600 seems justified for the purpose of high-resolution gravity field modelling, since GGMplus predicts an omission error still in the order of ~ 2 mGal for the truncation at this degree. Investigations restricted to very mountainous terrain in the Himalayas revealed that in those areas signals in the order of ± 10 mGal are found on average at scales < 1 km.

The available source-mass models lack sufficiently resolved density information to fully exploit the actual capabilities of spectral forward modelling: the techniques generally would allow for much more detailed density information (in the vertical and lateral dimension), than available by current geophysical models (e.g. CRUST1.0). In contrast the lateral resolution of today's satellite-borne digital elevation models provide – for most parts of the world – more details of the topography than exploitable by spectral forward modelling. However, over ice-covered regions such as Antarctica, the resolution (and quality) of the bedrock component still needs to be improved. Generally, the seafloor geometry from bathymetry is of poorer quality than the land geometry from topography. This especially is true for scales smaller than ~ 12 km, i.e. degree ~ 1670 , where the altimetry-based depth recovery is not working very well anymore due to signal attenuation with increasing depth. At these short scales it relies on sparsely available ship soundings, mainly, that are known to show gaps of more than 10 km lateral distance between the measurements for 50 % of the oceans. The degree 10,800 source-mass model Earth2014 is an up-to-date compilation of available information of solid bedrock, lake and ocean water, and major ice sheets close to the actual resolution limits of the methods (see further down). For reasons of simplicity and lack of high-resolution density information, the density is assumed constant and approximated by the estimated mean density for each derived geophysical layer, leading to satisfactory results (see further down). In this respect, future modelling attempts should also include improved mass-density modelling, e.g. over the oceans (*Tenzer et al*, 2012), isostatic compensation based on isostatic hypothesis and actual seismic

Moho depths (e.g. *Grombein et al*, 2014) and might even account for the atmosphere's gravitational potential (e.g. *Novak*, 2010).

The historically and even today widely used spherical approximation in spectral forward modelling affects the gravitational signal not only at scales > 10 km but also at shorter scales, especially over Earth's mountain chains (errors up to ~ 30 mGal). Still STP modelling is useful for some applications (e.g. band- or degree-wise evaluations) and is, apart from that, easy to understand due to rather simple analytical expressions. Generally the ellipsoidal approximation keeps approximations at a minimum level as it allows mapping-free modelling with the source-mass data arranged in appropriate manner (using pseudo-ellipsoidal heights). Further, the additional computational demand of modelling w.r.t. an ellipsoid is not relevant. The time critical task during the processing is the spherical harmonic analysis of multiple height-density-functions, an aspect that equally holds for ETP and STP modelling. Thus, the ETP should become common practice for spherical harmonic forward modelling. ETP modelling becomes crucial for applications such as creating spherical harmonic Bouguer coefficients or a combination with observations-based data via regularisation. In the future, forward modelling in ellipsoidal (or spheroidal) harmonics should be envisaged since the underlying coordinate system fully supports the ellipsoidal shape of Earth's masses and would allow for a wider and more versatile field of applications, e.g. band- or degree-wise evaluations. This is because ellipsoidal harmonic coefficients of successive degrees are arithmetically un-correlated, in contrast to spherical harmonic coefficients that represent an ellipsoidal mass-distribution. First pioneering work in this direction exists, e.g. by *Novak and Grafarend* (2005) or *Wang and Yang* (2013).

If the short-scale ($n < 2160$) gravitational potential over continents is sought, single-layer modelling is sufficient given the up-to-date available source-mass models at global scale that do not provide layers differentiating between different types of rock/sediment or provide the extent of glaciers at scales < 10 km. The error associated with single-layer modelling or the RET approximation at short scales is restricted to the oceans with an average global amplitude of 0.5 mGal (RMS). Even over the oceans, thus, the RET approximation effect only plays a role over rugged or deepest bathymetric features, with amplitudes up to ~ 20 mGal. The investigation with the ground-truth data set over the Arctic ocean shows an influence of the RET approximation effect at the level of 0.01 mGal RMS, suggesting that RET leads to negligible errors at scales < 10 km given the accuracy of the ground-truth and the bathymetric depth data.

Using spectral forward modelling methods up to ultra-high degree seems possible up to degrees close to 10,800 without substantial changes of the here presented double-precision algorithms. The only exception are the ALFs, that require extended arithmetics beyond degree $n \approx 2700$. But taking proper care of sampling requirements in order to ban aliasing it would require access to super-computing facilities and a stark parallelisation of the spherical harmonic analysis step. However, full convergence of the involved binomial k - and j -series at higher degrees will require an arithmetic extension of the algorithms, e.g. to cope with the overflow of the binomial coefficients. Against practice in many works in literature (e.g. *Root et al* (2016); *Gruber et al* (2014); *Balmino et al* (2012)), this work shows that the evaluation of the k -series up to k_{max} -values much larger than three should be considered for $n \geq 2160$, since these terms may lead to significant gravity signal amplitudes at short scales. Further, tests up to degree 21,600 showed a convergence of eliminating character for layers with deep masses (such as bathymetric masses in deep ocean trenches) that prohibits an early truncation of the k -series (for $k > 8$), leaving substantial short-scale signals unmodelled. In contrast, single-layer modelling is devoid of such problems as it shows a purely additive convergence behaviour. Given that the RET approximation effect reaches relevant amplitudes only over deep ocean trenches at scales < 10 km, single-layer modelling (in ellipsoidal approximation) seems to be an advisable method if only the short-scale gravitational signals over land and coastal areas are sought/used. Due to the strong increase of computational

costs – mainly driven by the increasing number of k -terms to be evaluated with rising n_{max} – space domain forward modelling is to be preferred for high-resolution forward modelling applications with only local extent. On global scale, spectral integration methods seem to outperform the space domain integration approaches (e.g. numerical integration of rectangular prisms in *P-VI* or the tesseroid approach in *Grombein et al (2016b)*) in terms of computation time, at least up to degree 2160.

Concerning the stable implementation of ALFs (of the first kind) at high degrees, also other (and faster) approaches than the here used X -number approach (*Fukushima, 2012a,b*) can be used. For example, *Gruber and Abrykosov (2016)* suggest the computation of ALFs in the spectral domain which seems favorable in terms of efficiency for high resolution spherical harmonic transforms, at least if the Fourier coefficients of ALFs are precomputed and stored.

Another interesting aspect that was not treated in this work is the development of the here presented spectral forward modelling methods based on integral values of ALFs (of the first kind). In their current form point ALFs (of the first kind) are used in the analysis of the height-density functions. Since the height values provided by DEMs and satellite observation techniques rather are block-mean values, the employment of integral ALFs seems more adequate and should be investigated in the future.

In view of global combined gravity field modelling with the help of high-resolution spectral forward modelling approaches, least-squares combination techniques are desirable because of the ability to control the regional impact of the forward modelled gravity within the combination. This, however, would require stochastic information which is not given by the spectral forward methods presented here. Indeed, an error propagation or a thorough analysis of individual errors such as DEM inaccuracies or density estimates is missing in this work. Attempts in this direction were made by *Balmino et al (2012)* (Eq. 37, *ibid*) who translates the spherical harmonic representation error of the DEMs into values of uncertainty in terms of gravity or geoid heights: e.g., a ~ 4 m global height representation error would correspond to ~ 0.5 mGal gravity error on global average. Another interesting attempt was made by *Abrykosov et al (2012)* who estimated formal errors of the spherical harmonic coefficients of a $1'$ -grid. A proper error propagation and stochastic modelling for spectral forward modelling approaches warrants for future research.

Indirectly, of course, an analysis of the (overall) error of the forward modelling was done in this work by the comparison to the different ground-truth data sets. Doing so in this work, it was shown that with simple spectral merges that incorporate high-resolution spectral forward models computed with the here compiled methods and data, an improvement over state-of-the-art observation based degree-2190 GGMs by nearly 50 % can be achieved over mountainous areas, i.e. halving the differences between model and terrestrial observation.

As a final remark, by evaluating gravity functionals at the Earth's surface the thesis implicitly assumes the convergence of the spherical harmonic series expansion of the topographic potential at the top of Earth's actual masses. Up to the investigated degrees this seems justified, very small possible signs of divergence were only found in the series up to degree 21,600 (*P-VI*). Theoretically, the convergence of the spherical harmonic series is only guaranteed on or outside the Brillouin sphere (*Jekeli, 2012*) – the sphere encapsulating all of Earth's topographic masses – which might become a limiting factor when raising the spherical harmonic series to higher degrees than investigated here.

Chapter 6

Conclusions

The thesis showed that significant gravitational acceleration signals are caused by the uncompensated topographic masses at short-scale (≤ 10 km). Modelling these signals with the help of efficient spectral spherical harmonic solutions to Newton's integral formula was found to improve high-resolution global gravity field models using up-to-date topographic elevation data.

For example, at scales between ~ 4 and 10 km, gravity signals in the order of ~ 4.5 mGal and ~ 1 cm in terms of geoid heights are found on global average (RMS). Those signals were shown to substantially improve the agreement with ground-truth gravity observations w.r.t. the state-of-the-art observation-based gravity field model EGM2008 by almost 50 % over Alpine areas and ~ 16 % over flat countries such as Australia. Even at finer scales (< 4 km), an omission error in the order of ~ 5 mGal (~ 0.4 cm) is to be expected at Earth's continental surface on average which can be estimated from a newly-derived empirical degree variance model up to degree 90,000.

Reviewing existing spectral forward modelling approaches, a novel approach has been developed that provides some advantages w.r.t. prevailing techniques. It allows the efficient spectral computation of the ellipsoidal topographic potential from a set of volumetric layers of laterally-varying mass-density (i.e. integrated w.r.t. to an oblate ellipsoid of revolution). The method avoids two types of approximations that are commonly found in spectral forward modelling:

- 1) the spherical approximation present in the spherical topographic potential, leading to errors in the order of some mGals (global RMS ≈ 0.4 mGal up to degree 5,400), and
- 2) the RET approximation of single-layer modelling, leading to errors in the order of some tens of mGals (global RMS ≈ 1.8 mGal up to degree 5,400).

At short scales (≤ 4 km) the spherical approximation is most severe over rough terrain/ mountains, while the RET approximation becomes negligible over the continents and in coastal maritime regions. Thus, at short scales multi-layer modelling is only justified when the global topographic potential is sought, i.e. including oceans and deeper bathymetry, where the RET error is most severe.

Efficient spectral forward modelling techniques are equivalent to their rigorous counterparts when enough terms of the involved binominal series expansions are taken into account. Importantly, for high degrees a very large number of binominal terms is required, which has not been accounted for in many related works in literature. The correct amount of terms can be estimated from newly-derived linear relationships between the desired maximum degree of the forward model and the maximum order of the binomial series required for full convergence.

Very or ultra high-degree forward modelling is only possible when the spherical harmonic analysis, being the time critical processing step, is done efficiently. In this work this was achieved by exact numerical quadrature techniques. Principally, the only two major modifications to existing techniques that need to be implemented are numerically stable ALFs, achieved by an arithmetic extension using the X-number approach, and a parallelisation of parts of the code. Then spherical harmonic analyses up to some ten thousands of degrees are well feasible in short time, e.g. ~ 10 h are needed for an analysis to degree 21,600 using only 8 CPUs.

In the first place, limiting factors of spectral forward modelling in terms of maximum resolution are twofold. Firstly, the binomial coefficients of the involved binomial series expansions are running into an overflow. If a full convergence of the k - and the j -series is considered, the overflow occurs close to degree $\sim 17,800$ and $\sim 16,500$, i.e. $k_{max} = 72$ and $j_{max} = 145$, respectively. Secondly, the exponentiation of the topographic boundary functions up to power k_{max} requires an oversampling of the gridded function in order to ban aliasing effects. Although the oversampling factor generally can be chosen smaller than k_{max} , this soon leads to extremely large grids, because the grid size grows quadratically with the oversampling factor. An analysis in reasonable time can only be achieved with the help of massive parallelisation and access to supercomputing facilities.

Testing the forward modelling procedures experimentally up to degree 21,600 (~ 1 km) an eliminating convergence behaviour was detected that prohibits the early truncation of the k -series of layers having the ocean's bathymetry as a lower bound. In contrast, single-layer modelling shows a purely additive convergence behavior, suggesting the use of the RET approximation for very high-degree applications.

Concluding, spectral spherical harmonic forward modelling with the here presented methods that use an ellipsoid as reference surface (ellipsoidal approximation) are a powerful means for global modelling of the uncompensated topographic potential down to scales of about 1.5 – 2 km. This finding is based on the limitations found, and the estimated computational demands for spectral forward modelling. The derived ellipsoidal topographic potential, modelled to degree 5,400 based on data from Earth2014, was shown to positively contribute to combined high-resolution global gravity field modelling and to other applications. Especially, this holds given the steady improving quality of high-resolution digital elevation and source-mass data. Currently, source-mass models are of comparatively poor quality over the oceans and Antarctica, and lack detailed mass-density information on a global scale.

Finally, in light of the next-generation observation-based spherical harmonic gravity field model of degree 2190 (successor of NGA's EGM2008), to be released in 2020 (*Barnes et al, 2016*), the herein proposed multi-layer ETP approach together with source-mass information from Earth2014 are formidable means to generate fill-in gravity in areas devoid terrestrial or air-borne gravity, or to mitigate the omission error beyond the model's resolution, globally. In similar manner, methods and data of this work are believed to provide valuable contributions to global combined gravity field modelling in the frame of the EIGEN and GOCO initiatives.

Bibliography

- Abramowitz M, Stegun I (1972) Handbook of Mathematical Functions. Dover Publications, New York, USA
- Abrykosov O, Förste C, Gruber C, Shako R, Barthelmes F (2012) Harmonic analysis of the DTU10 global gravity anomalies. In: Abbasi A, Giesen N (eds) EGU General Assembly Conference Abstracts, EGU General Assembly Conference Abstracts, vol 14, p 4945
- Airy G (1855) On the computations of the effect of the attraction of the mountain masses as disturbing the apparent astronomical latitude of stations in geodetic surveys. Transactions of the Royal Society of London Series B 145
- Amante C, Eakins B (2009) ETOPO1 1 Arc-Minute Global Relief Model: Procedures, Data Sources and Analysis. NOAA Technical Memorandum NESDIS NGDC-24, National Geophysical Data Center, NOAA
- Arabelos D, Tscherning C (1998) The use of least squares collocation method in global gravity field modeling. Physics and Chemistry of the Earth 23(1):1 – 12, DOI [http://dx.doi.org/10.1016/S0079-1946\(97\)00234-6](http://dx.doi.org/10.1016/S0079-1946(97)00234-6), URL <http://www.sciencedirect.com/science/article/pii/S0079194697002346>
- Asgharzadeh M, von Frese R, Kim H, Leftwich T, Kim J (2007) Spherical prism gravity effects by Gauss-Legendre quadrature integration. Geophysical Journal International 169:1–11
- Bagherbandi M, Sjöberg L (2012) Non-isostatic effects on crustal thickness: A study using crust2.0 in fennoscandia. Physics of The Earth and Planetary Interiors 200-201 pp 37–44, DOI <http://dx.doi.org/10.1016/j.pepi.2012.04.001>
- Bagherbandi M, Tenzer R, Sjöberg L, Novák P (2013) Improved global crustal thickness modeling based on the VMM isostatic model and non-isostatic gravity correction. Journal of Geodynamics 66:25–37, DOI 10.1016/j.jog.2013.01.002
- Balmino G, Lambeck K, Kaula W (1973) A spherical harmonic analysis of the Earth's Topography. Journal of Geophysical Research 78(2):478–521
- Balmino G, Vales N, Bonvalot S, Briais A (2012) Spherical harmonic modelling to ultra-high degree of Bouguer and isostatic anomalies. Journal of Geodesy 86(7):499–520, DOI 10.1007/s00190-011-0533-4, URL <http://dx.doi.org/10.1007/s00190-011-0533-4>
- Bamber J, Griggs J, Hurkmans Rea (2013) A new bed elevation data set for greenland. The Cryosphere 7:499–510
- Barnes D, Factor J, Holmes S, Ingalls S, Presicci M, Beale J (2016) Earth Gravitational Model 2020. In: Presentation at: International Symposium on Gravity, Geoid and Height Systems 2016, 20.09.2016
- Barracough D (1978) Spherical harmonic models of the geomagnetic field. Geomag Bull Inst Geol Sci 8
- Bartusch M, Berg H, Siebertz O (2008) The TanDEM-X Mission. In: Synthetic Aperture Radar (EUSAR), 2008 7th European Conference on, pp 1–4
- Becker J, Sandwell D, Smith W, Braud J, Binder B, Depner J, Fabre D, Factor J, Ingalls S, Kim SH, Ladner R, Marks K, Nelson S, Pharaoh A, Trimmer R, Von Rosenberg J, Wallace G, Weatherall P (2009) Global bathymetry and elevation data at 30 arc seconds resolution: Srtm30_plus. Marine Geodesy 32(4):355–371, DOI 10.1080/01490410903297766, URL <http://dx.doi.org/10.1080/01490410903297766>, <http://dx.doi.org/10.1080/01490410903297766>
- Bosch M, McGaughey J (2001) Joint inversion of gravity and magnetic data under lithologic constraints. The Leading Edge pp 877–881

- Bosch W, Savcenko R (2010) On estimating the dynamic ocean topography. In: Mertikas S (ed) Gravity, Geoid and Earth Observation, IAG Symposia, Springer, vol 135, DOI 10.1007/978-3-642-10634-7_34
- Bucha B, Janák J (2014) A MATLAB-based graphical user interface program for computing functionals of the geopotential up to ultra-high degrees and orders: Efficient computation at irregular surfaces. *Computers and Geosciences* 66:219–227
- Bucha B, Janák J, Papčo J, Bedék A (2016) High-resolution regional gravity field modelling in a mountainous area from terrestrial gravity data. *Geophysical Journal International* 207(2):949–966, DOI 10.1093/gji/ggw311
- Chao CC (2005) Applied Orbit Perturbation and Maintenance. American Institute of Aeronautics and Astronautics
- Claessens S (2006) Solutions to Ellipsoidal Boundary Value Problems for Gravity Field Modelling. PhD thesis, Curtin University of Technology
- Claessens S, Hirt C (2013) Ellipsoidal topographic potential - new solutions for spectral forward gravity modelling of topography with respect to a reference ellipsoid. *Journal of Geophysical Research* 118(11):5991–6002, DOI 10.1002/2013JB010457
- Colombo O (1981) Numerical methods for harmonic analysis on the sphere. Rep. No. 310, The Ohio State University
- Driscoll J, Healy D (1994) Computing Fourier Transforms and Convolutions on the 2-Sphere. *Advances in Applied Mathematics* 15(2):202–250, DOI 10.1006/aama.1994.1008
- D'Urso M (2014) Analytical computation of gravity effects for polyhedral bodies. *Journal of Geodesy* 88:13–29
- Ebbing J, Braitenberg C, Götze HJ (2001) Forward and inverse modelling of gravity revealing insight into crustal structures of the Eastern Alps. *Tectonophysics* 337:191–208
- ESA (1999) Gravity Field and Steady-State Ocean Circulation Mission. Report for the mission selection of the four candidate earth explorer missions (ESA SP-1233(1)), European Space Agency
- Farr T, Rosen P, Caro E, Crippen R, Duren R, Hensley S, Kobrick M, Paller M, Rodriguez E, Roth L, Seal D, Shaffer S, Shimada K, Umland J, Werner M, Oskin M, Burbank D, Alsdorf D (2007) The Shuttle Radar Topography Mission. *Reviews of Geophysics* 45(RG2004), DOI 10.1029/2005RG000183
- Fecher T (2015) Globale kombinierte Schwerefeldmodellierung auf Basis voller Normalgleichungssysteme. PhD thesis, Technische Universität München
- Fecher T, Pail R, Gruber T (2013) Global gravity field modeling based on GOCE and complementary gravity data. *International Journal of Applied Earth Observation and Geoinformation* 35:120–127, DOI 10.1016/j.jag.2013.10.005
- Fecher T, Pail R, Gruber T, GOCO-Consortium (2017) GOCO05c: A New Combined Gravity Field Model Based on Full Normal Equations and Regionally Varying Weighting. *Surveys in Geophysics* DOI 10.1007/s10712-016-9406-y
- Flury J (2006) Short-wavelength spectral properties of the gravity field from a range of regional data sets. *Journal of Geodesy* 79:624–640, DOI 10.1007/s00190-005-0011-y
- Forsberg R (1984) A study of terrain reductions, density anomalies and geophysical inversion methods in gravity field modelling. OSU Report 355, Ohio State University
- Forsberg R, Jensen T (2015) New geoid of Greenland: A case study of terrain and ice effects, GOCE and the use of local sea level data. *International Association of Geodesy Symposia* DOI 10.1007/1345_2015_50
- Fretwell P, Pritchard HD, Vaughan DG, Bamber J, Barrand N, Bell R, Bianchi C, Bingham R, Blankenship D, Casassa G, et al (2013) Bedmap2: improved ice bed, surface and thickness datasets for Antarctica. *The Cryosphere* 7(1)
- Fukushima T (2012a) Numerical computation of spherical harmonics of arbitrary degree and order by extending exponent of floating point numbers. *Journal of Geodesy* 86(4):271–285, DOI 10.1007/s00190-011-0519-2, URL <http://dx.doi.org/10.1007/s00190-011-0519-2>

- Fukushima T (2012b) Numerical computation of spherical harmonics of arbitrary degree and order by extending exponent of floating point numbers: li first-, second-, and third-order derivatives. *Journal of Geodesy* 86(11):1019–1028, DOI 10.1007/s00190-012-0561-8, URL <http://dx.doi.org/10.1007/s00190-012-0561-8>
- Göttl F, Rummel R (2009) A Geodetic View on Isostatic Models. *Pure and Applied Geophysics* 166:1247–1260, DOI 10.1007/s00024-004-0489-x
- Grombein T, Luo X, Seitz K, Heck B (2014) A Wavelet-Based Assessment of Topographic-Isostatic Reductions for GOCE Gravity Gradients. *Surveys in Geophysics* pp 1–24, DOI 10.1007/s10712-014-9283-1, URL <http://dx.doi.org/10.1007/s10712-014-9283-1>
- Grombein T, Seitz K, Heck B (2016a) On High-Frequency Topography-Implied Gravity Signals for a Height System Unification Using GOCE-Based Global Geopotential Models. *Surveys in Geophysics* DOI 10.1007/s10712-016-9400-4
- Grombein T, Seitz K, Heck B (2016b) The Rock-Water-Ice Topographic Gravity Field Model *RWI_TOPO_2015* and Its Comparison to a Conventional Rock-Equivalent-Version. *Surveys in Geophysics* 37(5):937–976, DOI 10.1007/s10712-016-9376-0
- Gruber C, Abrykosov O (2016) On computation and use of Fourier coefficients for associated Legendre functions. *Journal of Geodesy* 90(6), DOI 10.1007/s00190-016-0891-z
- Gruber C, Barthelmes F, Flechtner F, Novak P (2014) Derivation of Topographic potential from global DEM Models. In: Rizos C, Willis P (eds) *Earth on the Edge : Science for a Sustainable Planet : Proceedings of the IAG General Assembly*, Melbourne, Australia, June 28 - July 2, 2011, Berlin : Springer, vol 139, pp 535 – 542
- Gruber T (1999) Hochauflösende Schwerefeldbestimmung aus Kombination von terrestrischen Messungen und Satellitendaten über Kugelfunktionen. PhD thesis, Technische Universität München
- Gruber T, Gerlach C, Haagmans R (2012) Intercontinental height datum connection with GOCE and GPS-levelling data. *Journal of Geodetic Science* 2(4):270 – 280
- Hayford J (1909) *The figure of the Earth and isostasy from measurements in the United States.* , USCGS
- Heck B, Seitz K (2007) A comparison of the tesseroid, prism and point-mass approaches for mass reductions in gravity field modelling. *Journal of Geodesy* 81:121–136, DOI 10.1007/s00190-006-0094-0
- Heiskanen W, Moritz H (1967) *Physical Geodesy*. WH Freeman Comp
- Heiskanen W, Vening Meinesz F (1985) *The Earth and its Gravity Field*. McGraw-Hil Book Company, Inc., New York
- Hirt C (2012) Efficient and accurate high-degree spherical harmonic synthesis of gravity field functionals at the Earth's surface using the gradient approach. *Journal of Geodesy* 86(9):729–744
- Hirt C (2014) GOCE's view below the ice of Antarctica : Satellite gravimetry confirms improvements in Bedmap2 bedrock knowledge. *Geophysical Research Letters* 41(14):5021–5028, DOI 10.1002/2014GL060636
- Hirt C, Kuhn M (2012) Evaluation of high-degree series expansions of the topographic potential to higher-order powers. *Journal of Geophysical Research Solid Earth* 117, DOI 10.1029/2012JB009492
- Hirt C, Kuhn M (2014) A band-limited topographic mass distribution generates a full-spectrum gravity field - gravity forward modelling in the spectral and spatial domain revisited. *Journal of Geophysical Research - Solid Earth* 119(4):3646–3661, DOI doi:10.1002/2013JB010900
- Hirt C, Gruber T, Featherstone W (2011) Evaluation of the first GOCE static gravity field models using terrestrial gravity, vertical deflections and EGM2008 quasigeoid heights. *Journal of Geodesy* 85:723–740
- Hirt C, Kuhn M, Featherstone W, Göttl F (2012) Topographic/isostatic evaluation of new-generation GOCE gravity field models. *Journal of Geophysical Research - Solid Earth* 117:B05,407, DOI 10.1029/2011JB008878

- Hirt C, Claessens S, Fecher T, Kuhn M, Pail R, Rexer M (2013) New ultra-high resolution picture of Earth's gravity field. *Geophysical Research Letters* 40, DOI 10.1002/grl.50838
- Hirt C, Kuhn M, Claessens S, Pail R, Seitz K, Gruber T (2014) Study of the Earth's short-scale gravity field using the ERTM2160 gravity model. *Computers & Geosciences* 73:71–80
- Hirt C, Rexer M, Claessens S (2015) Topographic evaluation of fifth-generation GOCE gravity field models - globally and regionally. *Newton's Bulletin* 5, Special issue on validation of GOCE gravity fields, International Association of Geodesy (IAG) 5:1–24
- Hirt C, Reußner E, Rexer M, Kuhn M (2016) Topographic gravity modelling for global bouguer maps to degree 2,160: Validation of spectral and spatial domain forward modelling techniques at the 10 microgal-level. *Journal of Geophysical Research: Solid Earth* 121, DOI 10.1002/2016JB013249
- Hirt C, Rexer M, Claessens S, Rummel R (2017) The relation between degree-2160 spectral models of Earth's gravitational and topographic potential - a guide on global correlation measures and their dependency on approximation effects. *Journal of Geodesy* (submitted)
- Hofsommer D (1957) On the expansion of a function in a series of spherical harmonics. Rep. No. R344A, Computation Department of the Mathematical Centre, Amsterdam
- Huang J, Vaniček P, Pagiatakis S, Brink W (2001) Effect of topographical density on geoid in the Canadian Rocky Mountains. *Journal of Geodesy* 74:805–815
- Jarvis A, Reuter H, Nelson A, Guevara E (2008) Hole-filled SRTM for the globe v4.1. URL <http://srtm.csi.cgiar.org>
- Jekeli C (1988) The exact transformation between ellipsoidal and spherical harmonic expansions. *manuscripta geodaetica* 13(2):106–113
- Jekeli C (2010) Correlation Modeling of the Gravity Field in Classical Geodesy. In: Freeden W, Nashed M, Sonar T (eds) *Handbook of the Geomathematics*, Springer-Verlag Berlin Heidelberg, DOI 10.1007/978-3-642-01546-5_28
- Jekeli C (2012) Omission Error, Data Requirements, and the Fractal Dimension of the Geoid. In: Sneeuw Nea (ed) VII Hotine-Marussi Symposium on Mathematical Geodesy, International Association of Geodesy Symposia 137, Springer-Verlag Berlin Heidelberg, DOI 10.1007/978-3-642-22078-4_27
- Kaula W (1966) *Theory of Satellite Geodesy*. Blaisdel, Waltham
- Kuhn M, Hirt C (2016) Topographic gravitational potential up to second-order derivatives: an examination of approximation errors caused by rock-equivalent topography (ret). *Journal of Geodesy* (online first) 90(9):883–902, DOI 10.1007/s00190-016-0917-6
- Kuhn M, Seitz K (2005) Comparison of Newton's Integral in the Space and Frequency Domains. In: Sanso F (ed) *A window on the Future of Geodesy - IAG Symposia*, vol 128, pp 386–391
- Kuhn M, Featherstone W, Kirby J (2009) Complete spherical Bouguer gravity anomalies over Australia. *Australian Journal of Earth Sciences* 56:213–223
- Lee W, Kaula W (1967) A spherical harmonic analysis of the Earth's Topography. *Journal of Geophysical Research* 72:753–758
- Mader K (1951) Das Newtonsche Raumpotential prismatischer Körper und seine Ableitungen bis zur dritten Ordnung. *Österreichische Zeitschrift für Vermessungswesen*
- Marti U (2004) High-precision combined geoid determination in Switzerland. In: Presented at Gravity, Geoid and Space Missions (GGSM) 2004 Symposium, Porto, Aug 30 - Sep 03 2004, Porto, Portugal
- Moritz H (1978) Least-squares collocation. *Reviews of Geophysics* 16(3):421–430, DOI 10.1029/RG016i003p00421, URL <http://dx.doi.org/10.1029/RG016i003p00421>

- Moritz H (1990) The Figure of Earth. Wichman, H.
- Moritz H (2000) Geodetic Reference System 1980. *Journal of Geodesy* 74(1):128–162, DOI 10.1007/s001900050278
- Nagy D (1966) The gravitational attraction of a right rectangular prism. *Geophysics* 31:362–371
- Nagy D, Papp G, Benedek J (2000) The gravitational potential and its derivatives for the prism. *Journal of Geodesy* 74:552–560, DOI 10.1007/s00190-006-0094-0
- Nagy D, Papp G, Benedek J (2002) Correction to "the gravitational potential and its derivatives for the prism". *Journal of Geodesy* 76:475, DOI 10.1007/s00190-002-0264-7
- Novak P (2010) Direct modelling of the gravitational field using harmonic series. *Acta Geodyn Geomater* 7(1 (157)):35–47
- Novak P, Grafarend E (2005) Ellipsoidal representation of the topographical potential and its vertical gradient. *Journal of Geodesy* 78(11):691–706
- Novak P, Kern M, Schwarz K, Heck B (2003) Evaluation of band-limited topographical effects in airborne gravimetry. *Journal of Geodesy* 76:597–604
- Novák P, Tenzer R, Bagherbandi M, Chen W, Sjöberg L (2016) Isostatic global gravity fields for geodetic and geophysical applications. Oral presentation, Gravity, Geoid and Height Systems 2016, 19-23 September, Thessaloniki, Greece
- Oldenburg D, Li Y, Farquharson C, Kowalczyk P, Aravanis T, King A, Zhang P, Watts A (1998) Applications of geophysical inversions in mineral exploration problems. *The Leading Edge* 134:231–227
- Pail R, Bruinsma S, Migliaccio F, Förste C, Goiginger H, Schuh WD, Höck E, Reguzzoni M, Brockmann JM, Abrikosov O, Veicherts M, Fecher T, Mayrhofer R, Krasbutter I, Sanso F, Tscherning CC (2011) First GOCE gravity field models derived by three different approaches. *Journal of Geodesy* 85(11):819–843, DOI 10.1007/s00190-011-0467-x, special issue: "GOCE - The Gravity and Steady-state Ocean Circulation Explorer"
- Papp G (1996) Gravity field approximation based on volume element model of the density distribution. *Acta Geod Geoph Hung* 91:339–358
- Pavlis N, Factor J, Holmes S (2007) Terrain-related gravimetric quantities computed for the next EGM. In: Dergisi H (ed) *Proceedings of the 1st International Symposium of the International Gravity Field Service*, vol 18, pp 318–323
- Pavlis N, Holmes S, Kenyon S, Factor J (2012) The development and evaluation of the Earth Gravitational Model 2008 (EGM2008). *Journal of Geophysical Research* 117, DOI 10.1029/2011JB008916
- Pavlis N, Holmes S, Kenyon S, Factor J (2013) Correction to the development and evaluation of the Earth Gravitational Model 2008. *Journal of Geophysical Research* 118(5):2633–2633
- Pavlis NK (2011) *Encyclopedia of Solid Earth Geophysics*, 1st edn, Springer Netherlands, chap Spherical Harmonic Analysis Applied to Potential Fields, pp 1382–1391
- Pavlis NK, Rapp R (1990) The development of an isostatic gravitational model to degree 360 and its use in global gravity modelling. *Geophys J Int* 100:369–378
- Pratt J (1855) On the attraction of the Himalaya Mountains and of the elevated regions beyond upon the plumb-line in India. *Transactions of the Royal Society of London Series B* 145
- Rexer M, Hirt C (2014) Comparison of free high resolution digital elevation data sets (ASTER GDEM2, SRTM v2.1/v4.1) and validation against accurate heights from the Australian National Gravity Database. *Australian Journal of Earth Sciences* 61(2):1–15, DOI 10.1080/08120099.2014.884983, URL <http://www.tandfonline.com/doi/abs/10.1080/08120099.2014.884983>, <http://www.tandfonline.com/doi/pdf/10.1080/08120099.2014.884983>
- Rexer M, Hirt C (2016) Evaluation of intermediate TanDEM-X digital elevation data products over Tasmania using other digital elevation models and accurate heights from the Australian National Gravity Database. *Australian Journal of Earth Sciences* (accepted for publication)

- Rexer M, Hirt C, Pail R, Claessens S (2013) Evaluation of the third- and fourth-generation GOCE Earth gravity field models with Australian terrestrial gravity data in spherical harmonics. *Journal of Geodesy* 88(4):319–333, DOI 10.1007/s00190-013-0680-x, URL <http://dx.doi.org/10.1007/s00190-013-0680-x>
- Rexer M, Hirt C, Claessens S, Braitenberg C (2015) Use of topography in the context of the GOCE satellite mission - some examples. In: Ouwehand L (ed) Proc. '5th International GOCE User Workshop', Paris, France, 25-28 November 2014, ESA Communications, ESA SP-728
- Rexer M, Hirt C, Claessens S, Tenzer R (2016) Layer-Based Modelling of the Earth's Gravitational Potential up to 10-km Scale in Spherical Harmonics in Spherical and Ellipsoidal Approximation. *Surveys in Geophysics* pp 1–40, DOI 10.1007/s10712-016-9382-2, URL <http://dx.doi.org/10.1007/s10712-016-9382-2>
- Root B, Novák P, Dirx M, Kaban M, van der Wal W, Vermeersen L (2016) On a spectral method for forward gravity field modelling. *Journal of Geodynamics* 97:22–30, URL <http://dx.doi.org/10.1016/j.jog.2016.02.008>
- Rummel R (2012) Height unification using GOCE. *Journal of Geodetic Science* 2(4):355 – 362
- Rummel R, Rapp R, Sünkel H, Tscherning C (1988) Comparisons of Global Topographic/Isostatic Models To the Earth's Observed Gravity Field. OSU report 388, Ohio State University
- Sandwell DT, Müller RD, Smith WH, Garcia E, Francis R (2014) New global marine gravity model from CryoSat-2 and Jason-1 reveals buried tectonic structure. *science* 346(6205):65–67
- Sanso F, Sideris M (2013) Geoid Determination - Lecture Notes in Earth Sciences, vol 110, Springer-Verlag Berlin Heidelberg, chap Harmonic Calculus and Global Gravity Models
- Scheinert M, Ferraccioli F, Schwabe J, Bell R, Studinger M, Damaske D, Jokat W, Aleshkova N, Jordan T, Leitchenkov G, Blankenship DD, Damiani TM, Young D, Cochran JR, Richter TD (2016) New antarctic gravity anomaly grid for enhanced geodetic and geophysical studies in antarctica. *Geophysical Research Letters* 43(2):600–610, DOI 10.1002/2015GL067439, URL <http://dx.doi.org/10.1002/2015GL067439>, 2015GL067439
- Sebera J, Bouman J, Bosch W (2012) On computing ellipsoidal harmonics using Jekeli's renormalization. *Journal of Geodesy* 86(9):713–726, DOI 10.1007/s00190-012-0549-4
- Seitz K, Heck B (2003) Efficient calculation of topographic reductions by the use of tesseroids. In: Presentation at the joint assembly of the EGS, AGU and EGU, Nice, France, 6-11 April, 2003
- Sideris M, Fotopoulos G (2012) Special issue on regional and global geoid-based vertical datums. *Journal of Geodetic Science* 2(4)
- Smith D (2000) The gravitational attraction of any polygonally shaped vertical prism with inclined top and bottom faces. *Journal of Geodesy* 74:414–420
- Sneeuw N (1994) Global spherical harmonic analysis by least-squares and numerical quadrature methods in historical perspective. *Geophysical Journal International* 118:707–716
- Tapley B, Bettadpur S, Watkins M, Reigber C (2004) The gravity recovery and climate experiment: Mission overview and early results. *Geophysical Research Letters* 31(9), DOI 10.1029/2004GL019920
- Tenzer R, Abdalla A, Vajda P, Hamayun (2010) The spherical harmonic representation of the gravitational field quantities generated by the ice density contrast. *Contrib Geophys Geod* 40(3):207–223
- Tenzer R, Novák P, Gladkikh V (2012) The bathymetric stripping corrections to the gravity field quantities for a depth-dependant model of the seawater density. *Marine Geodesy* 35:198–220
- Tenzer R, Chen W, Tsoulis D, Bagherbandi M, Sjöberg L, Novák P, Jin S (2015) Analysis of the refined CRUST1.0 crustal model and its gravity field. *Surveys in Geophysics* 36(1):139–165

- Tenzer R, Hirt C, Novák P, Pitoňák M, Šprlák M (2016) Contribution of mass density heterogeneities to the quasigeoid-to-geoid separation. *Journal of Geodesy* 90(1):65–80, DOI 10.1007/s00190-015-0858-5
- Torge W (2003) *Geodäsie*. Walter de Gruyter, Berlin
- Tscherning C, Rapp R (1974) Closed covariance expressions for gravity anomalies, geoid undulations, and deflections from the vertical implied by anomaly degree variance models. 208, Ohio State University
- Tsoulis D (2013) Geodetic use of global digital terrain and crustal databases in gravity field modelling and interpretation. *Journal of Geodetic Science* 3, DOI 10.2478/jogs-2013-0003
- Tsoulis D, Novák P, Kadlec M (2009) Evaluation of precise terrain effects using high-resolution digital elevation models. *Journal of Geophysical Research* 114:B02,404
- Vassiliou A, Schwarz K (1987) Study of the high-frequency spectrum of the anomalous potential. *Journal of Geophysical Research* 92(B1):609–617
- Vening Meinesz F (1931) Une nouvelle méthode pour la réduction isostatique régionale de l'intensité de la pesanteur. *Bulletin Géodésique* 29:33–51
- Voigt C, Denker H (2007) A study of high frequency terrain effects in gravity field modelling. In: Dergisi H (ed) 1st International Symposium of the International Gravity Field Service, "Gravity Field of the Earth", Ankara, Turkey, vol 18, pp 342–347
- Šprlák M, Gerlach C, Pettersen B (2012) Validation of GOCE global gravity field models using terrestrial gravity data in Norway. *Journal of Geodetic Science* 2(2):134–143
- Walker JS (1996) *Fast fourier transforms*, vol 24. CRC press
- Wang Y, Yang X (2013) On the spherical and spheroidal harmonic expansion of the gravitational potential of the topographic masses. *Journal of Geodesy* 87:909–921
- Wieczorek M (2015) *Treatise on Geophysics - 2nd Edition*, vol 10, Elsevier, chap The gravity and topography of the terrestrial planets, pp 153–193
- Wild-Pfeiffer F (2008) A comparison of different mass elements for use in gravity and gradiometry. *Journal of Geodesy* 82:637–653
- Willberg M, Gruber T, Grego (2017) Analysis of GOCE Omission Error and its Contribution to Vertical Datum Offsets in Greece and its Islands. In: submitted to: Proceedings of the International Symposium on Gravity, Geoid and Height Systems 2016 (GGHS) - September 19-23 - Thessaloniki, Greece
- Wu R, Wu F, Han T, Liu P, Li H (2016) Gravity Compensation Using EGM2008 for High-Precision Long-Term Inertial Navigation Systems. *Sensors* 16(2):2177
- Wynne P, Bacchin M (2009) *Index of gravity surveys*. , Geoscience Australia
- Zingerle P, Fecher T, Pail R, Gruber T (2016) High-resolution combined global gravity field modelling: Solving large kite systems using distributed computational algorithms. In: Abstract: International Symposium on Gravity, Geoid and Height Systems 2016, September 19-23, Thessaloniki, Greece

Acknowledgments

Working on this thesis has been a great challenge and a great pleasure on the same time. The latter – to a big part – is owed to the unique atmosphere and multifaceted support at TUM-IAPG and, of course, to all of my colleagues I was able to meet and work with during the last 3.5 years. Although I'm not willing this great experience to end, I am ready to move on and am looking ahead of new challenges to come.

@ Christian: cordial thanks for guiding me all the way through the thesis and for the funding I received via IAS. I have benefited a lot from your scientific experiences, intrinsic curiosity & not-always-easy-to-answer questions. I enjoyed our discussions, also those bringing us much further than science.

@ Roland: many thanks for arranging this work in the first place & for the opportunities and the nice atmosphere that come with being a staff member at IAPG! Also, your wide expertise has been of great help, often pointing me to new ideas and approaches.

@ Sten: thanks for your support from overseas, especially regarding the HC-method and topics related to ellipsoidal modelling and harmonics in general.

@ Thomas G.: thanks for leading me through contracts and helpful scientific & professional advices.

@ Anna, Alex & Steffi: I really enjoyed sharing an office with you!

@ Thomas F.: thanks for sharing your expertise in Fortran and gravity field modelling, as well as your NEQ-solver, which has already been of great help during my Master's thesis.

@ Christian A., Christoph: thanks for your initial support with Linux & server maintenance, topics I was completely novice.

@ Blažej and Juraj: thanks for your excellent GrafLab and isGrafLab synthesis-software that saved a lot of my life-time.

@ Christian A., Michi & Ilias: it was always fun making and talking about music with you!

@ Bingbing, Qingchen, Martin & Peter: thanks for thrilling ping-pong matches during coffee break!

@ Nadja: thanks for your brisk mind & few but awesome mountain bike tours!

@ my friends Phillip & Ferdinand: meeting for lunch with you guys has always been a tasteful and welcome diversion and it was great having you working in close vicinity!

To my family: I am glad to have you! The last years have been a lively time for all of us and I wouldn't have succeeded this work without your persistent support. Especially, I thank my wife Inka, beyond giving me a wonderful daughter.

This work was supported by the Technische Universität München - Institute for Advanced Study, funded by the German Excellence Initiative (and the European Union Seventh Framework Programme under grant agreement N° 291763).

Appendix A

A.1 Truncation and filtering of topographic potential models

As learned in Sect. 4.1 some combination methods afford the truncation of topographic potential models, which in more general words means nothing else than spectral filtering of the gravitational signal. More precisely, the topographic potential often is made spectral complementary to the maximum degree of the observed gravitational potential by high-pass filtering (spectral and spatial merge in Sect. 4.1.3). The filtering principle also applies for the spectral enhancement method (*Hirt et al, 2011*) or omission error modelling.

The truncation of the spherical harmonic series usually is straight forward and defined by the choice of the maximum degree n_{max} in the spherical harmonic series (see 2.2). This holds as long as the spherical harmonic concept is not violated and the harmonic function really is spherical (or spherically approximated). This is e.g. the case for all STP models (cf. Sect. 3.3) that are computed in spherical approximation. On the contrary, this feature of abrupt truncation is lost for spherical harmonic models that represent a potential that originates from an ellipsoidal mass distribution, which is the case for ETP models (cf. Sect. 3.3). Then a more complex filtering is required – a topic rarely dealt with in the community probably because of missing awareness. The reason are (algebraic) correlations among some spherical harmonic coefficients which have already been noted by *P-IV* (Sect. 4.3 *ibid*). The correlations deny that single frequencies (or coefficients) can be treated or investigated independently without having to deal with errors in the form of spherical striation patterns. The correlations also appear in observation-based high-resolution spherical harmonic GGMs, such as EGM2008, because the observations refer to the (actual) ellipsoidal mass arrangement of Earth, i.e. observation-based models can be considered to be of ellipsoidal approximation.

The reason for the correlations in ETP modelling can be found in Eq. 28 in *P-IV*. It expresses the term $\sin \theta^{2j} \bar{Y}_{n,m}$ with the help of fully normalised sinusoidal Legendre weight functions (*Claessens and Hirt, 2013*)

$$\sin^{2j} \theta \bar{Y}_{nm} = \sum_{i=-j}^j \bar{K}_{nm}^{2i,2j} \bar{Y}_{n+2i,m}, \quad (\text{A.1})$$

which are found in the final expression of the (layered) ETP potential (Eq. 31 in *P-IV*). The correlations among certain spherical harmonic coefficients arise from the summation over i from $-j$ to j , since i is found in the degree-index of the fully normalised surface spherical harmonic functions $\bar{Y}_{n+2i,m}$. Thus, any coefficient \bar{V}_{nm} depends on (some of) the equal order coefficients of degree $n - 2j_{max} < n \leq n + 2j_{max}$.

If a truncation of the ETP series for the purpose of high- or low-pass filtering of the gravitational signal at degree n_t is desired, two possible procedures can be suggested to account for correct filtering: 1) compute a full ETP model up to the degree of truncation n_t (and subtract it from the higher degree model in case of high-pass filtering) or 2) compute the correlations that occur for a truncation at n_t explicitly and apply them as filters to the truncated ETP model. The latter variant is the more elegant way, since less computational

filter type	$\overline{FC}_{nm}^{(ETP,A)}$	$\overline{FC}_{nm}^{(ETP,B)}$
low-pass	+	-
high-pass	-	+

Tab. A.1 – Sign for the application of ETP filter coefficients for high- and low-pass filtering

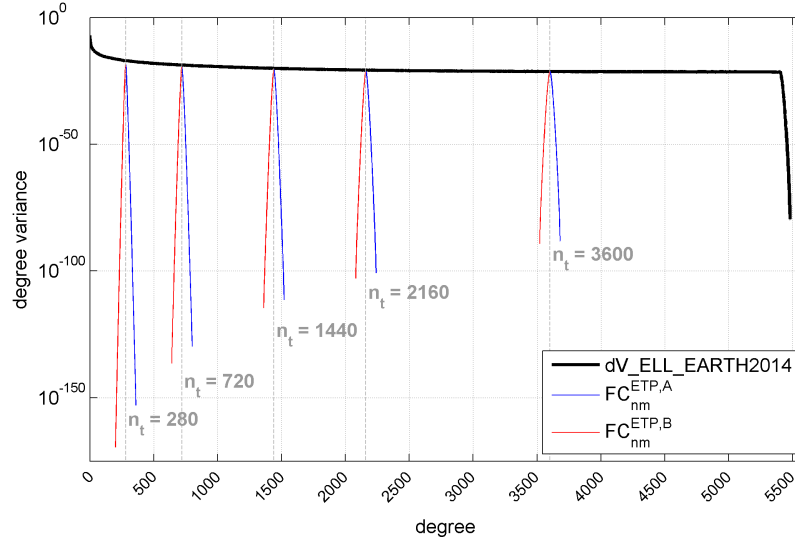


Fig. A.1 – Dimensionless degree variances of the filter coefficients $\overline{FC}_{nm}^{(ETP,A)}$ (in blue) and $\overline{FC}_{nm}^{(ETP,B)}$ (in red) for various degrees of truncation.

resources are required. The explicit computation of the filter coefficients $\overline{FC}_{nm}^{(ETP)}$ depends on n_t and j_{max} and can be derived from Eq. 31 in *P-IV* as follows:

$$\begin{aligned} \overline{FC}_{nm}^{(ETP,A)}(n_t) &= \frac{3}{\bar{\rho}(2n+1)(n+3)} \left(\frac{b}{R}\right)^{n+3} \sum_{k=1}^{k_{max}} \binom{n+3}{k} \\ &\times \sum_{j=0}^{j_{max}} (-1)^j \binom{-\frac{n+3}{2}}{j} e^{2j} \sum_{i=-j}^{\lfloor \frac{n_t-n}{2} \rfloor} \overline{K}_{nm}^{2i,2j} \overline{HDF}_{klm}^{(ETP)} \end{aligned} \quad (\text{A.2})$$

for all correlations occurring at $n > n_t$ and

$$\begin{aligned} \overline{FC}_{nm}^{(ETP,B)}(n_t) &= \frac{3}{\bar{\rho}(2n+1)(n+3)} \left(\frac{b}{R}\right)^{n+3} \sum_{k=1}^{k_{max}} \binom{n+3}{k} \\ &\times \sum_{j=0}^{j_{max}} (-1)^j \binom{-\frac{n+3}{2}}{j} e^{2j} \sum_{i=i_0}^j \overline{K}_{nm}^{2i,2j} \overline{HDF}_{klm}^{(ETP)} \end{aligned} \quad (\text{A.3})$$

where $\begin{cases} i_0 = \lfloor \frac{n_t-n}{2} \rfloor & \text{for } n < n_t \\ i_0 = 1 & \text{for } n = n_t \end{cases}$

for correlations occurring at $n \leq n_t$. How the filter coefficients $\overline{FC}_{nm}^{(ETP,A)}$ and $\overline{FC}_{nm}^{(ETP,B)}$ should be applied to a truncated series (with positive or negative sign) is given in table A.1. Since the correlations need to be added or eliminated depending on the application, respectively.

In terms of degree variances the correlations look like what is often associated with and called "tail" of

coefficients (cf. *Claessens and Hirt (2013)*). While only the correlations $\overline{FC}_{nm}^{(ETP,A)}$ are visible at the end of every ETP model, the correlations contained in $\overline{FC}_{nm}^{(ETP,B)}$ are not visible since they are dominated by the energy of the actual topographic gravity signal (see e.g. degree variances of $dV_ELL_Earth2014$ (black) in Fig. A.1). Computed for various different n_t (and constant $j_{max}=40$) we can see how the energy of the coefficients $\overline{FC}_{nm}^{(ETP,A)}$ and $\overline{FC}_{nm}^{(ETP,B)}$ is rising towards higher degrees of truncation (Fig. A.1). This can be verified in the space domain. In the case of a truncation at $n_t = 280$ the filter signals are in the order of $1 - 3 \text{ mGal}$ while they reach some 100 mGals for $n_t = 2160$. The largest part of the signal in both cases is found in polar latitudes. This reflects the close relation of the correlations with the differences between an ellipsoidally and a spherically shaped Earth, since Eq. A.1 is introduced within a binominal series expansion in order to replace the term $(\frac{r_s}{R})^{n+3}$.

The parameter j_{max} defines the "length" of the tails and the larger it is chosen, the higher is the correlation ratio among the coefficients (Fig. A.3). Note, that the choice of j_{max} is a matter of convergence in ETP modelling, as described in *Rexer et al (2016)* and *Claessens and Hirt (2013)*.

In similar manner as the ETP that employs the sinusoidal Legendre weights also Jekeli's renormalisation (*Jekeli, 1988; Sebera et al, 2012*) introduces correlations into the spherical harmonic series when a transformation from an ellipsoidal harmonic set of coefficients to their spherical harmonic equivalents is performed.

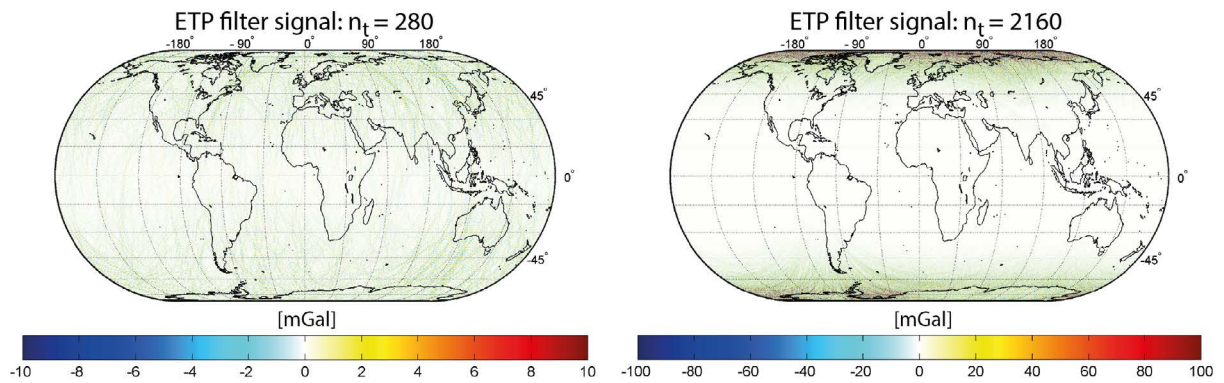


Fig. A.2 – Gravity effect of the ETP filter coefficients (Eqs. A.2 and A.3) synthesised in terms of gravity disturbances at Earth's surface for truncation at degree 280 ($Min = -3.4 \text{ mGal}$; $Max = 3.3 \text{ mGal}$; $RMS = 0.6 \text{ mGal}$) and 2160 ($Min = -300.0 \text{ mGal}$; $Max = 326.2 \text{ mGal}$; $RMS = 23.1 \text{ mGal}$). Unit is in mGal.

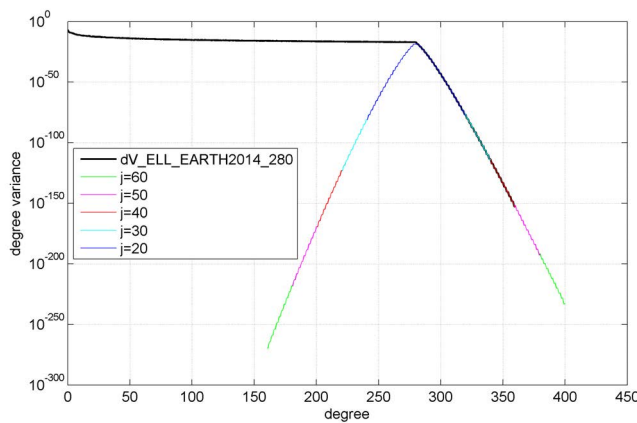


Fig. A.3 – Dimensionless degree variances of the filter coefficients $\overline{FC}_{nm}^{(ETP,A)}$ and $\overline{FC}_{nm}^{(ETP,B)}$ as a function of j_{max} (for constant degree of truncation $n_t = 280$).

Appendix B

P.1 Publication I: Spectral analysis of the Earth's topographic potential via 2D-DFT: a new data-based degree variance model to degree 90,000

Reference:

Rexer M., Hirt C.: Spectral analysis of the Earth's topographic potential via 2D-DFT: a new data-based degree variance model to degree 90,000; Journal of Geodesy, Vol. 89, Issue 9, p.887-909, Springer Berlin Heidelberg, ISSN 0949-7714, ISSN (Online) 1432-1394, DOI: 10.1007/s00190-015-0822-4, 2015.

Copyright

This work originally has been published in Journal of Geodesy, available at <http://link.springer.com/>, and is reprinted here with permissions of Springer. The copyright has been transferred to Springer-Verlag Berlin Heidelberg.

Short Summary

The near-global and freely-available GGMplus gravity grids with 220 m resolution are well-suited to study the spectral characteristics and signal strengths of Earth's topographic potential at short-scales. GGMplus is a composite model consisting of satellite-data and terrestrial data as contained in the model EGM2008 up to scales of ≈ 10 km. At shorter scales gravity signals originate from forward-modelling, thus GGMplus represents the gravity as implied by the topographic masses assuming a constant rock density of $2670 \frac{\text{kg}}{\text{m}^3}$. A commonly used 2D-DFT approach has been chosen to perform the spectral analysis, which was shown to recover the gravity spectral energy only approximatively (error margin of 10 – 20%) and in spherical approximation. The results of the analysis were used to estimate and parametrize a degree variance model complete up to degree 90,000, representing gravity as found at Earth's surface over the continental area ($-56^\circ \leq \varphi \leq 60^\circ$). The model is the only data-driven degree variance model beyond scales of 10 km and shows considerable differences to other models. The degree variance model can be used to estimate omission errors and signal amplitudes over continental areas. Importantly, it suggest larger signal amplitudes at short scales than most of the other models.

Declaration of own contribution

(MR: Moritz Rexer; CH: Christian Hirt)

CH had the idea to spectrally investigate the short-scale signals as contained in GGMplus gravity maps using 2D-FFT transforms. MR and CH mutually designed the study. MR did all software development and performed all calculations. CH had the idea to fit curves to the degree variances and MR selected suitable mathematical models and tools. MR added a lot of aspects to the original idea of the study, e.g. the detailed investigation of the used 2D-FFT method, or the numerical description of the ratio between the spherical and ellipsoidal

approximation. MR drafted all interpretations of the numerical results. Some of the interpretations were the result of discussion with CH, especially those regarding the differences between spherical and ellipsoidal approximation. Text, figures and tables were drafted and created by MR.

The overall own contribution of MR for *P-I* is estimated at 85 %, which is the average value of the percentage values estimated for the six criteria listed in the table below (Tab. P.1).

Criteria	Estimated own contribution
Computation and results	100 %
Ideas and study design	50 %
Analysis and interpretation	70 %
Text	90 %
Figures	100 %
Tables	100 %
Total	85 %

Tab. P.1 – Criteria and estimated contribution share of Moritz Rexer for *P-I*

Confirmation by the Co-Author

I hereby confirm the correctness of the declaration of own contribution by Moritz Rexer for the publication:

Rexer M., Hirt C.: Spectral analysis of the Earth's topographic potential via 2D-DFT: a new data-based degree variance model to degree 90,000; Journal of Geodesy, Springer Berlin Heidelberg, ISSN 0949-7714, ISSN (Online) 1432-1394, DOI: [10.1007/s00190-015-0822-4](https://doi.org/10.1007/s00190-015-0822-4), 2015.

Christian Hirt

Institut für Astronomische und Physikalische Geodäsie, Technische Universität München, Germany.

Signature: Christian Hirt Date: 27/01/2017

Spectral analysis of the Earth's topographic potential via 2D-DFT: a new data-based degree variance model to degree 90,000

Moritz Rexer¹ · Christian Hirt^{1,2}

Received: 30 July 2014 / Accepted: 3 May 2015
© Springer-Verlag Berlin Heidelberg 2015

Abstract Classical degree variance models (such as Kaula's rule or the Tscherning-Rapp model) often rely on low-resolution gravity data and so are subject to extrapolation when used to describe the decay of the gravity field at short spatial scales. This paper presents a new degree variance model based on the recently published GGMplus near-global land areas 220 m resolution gravity maps (Geophys Res Lett 40(16):4279–4283, 2013). We investigate and use a 2D-DFT (discrete Fourier transform) approach to transform GGMplus gravity grids into degree variances. The method is described in detail and its approximation errors are studied using closed-loop experiments. Focus is placed on tiling, azimuth averaging, and windowing effects in the 2D-DFT method and on analytical fitting of degree variances. Approximation errors of the 2D-DFT procedure on the (spherical harmonic) degree variance are found to be at the 10–20 % level. The importance of the reference surface (sphere, ellipsoid or topography) of the gravity data for correct interpretation of degree variance spectra is highlighted. The effect of the underlying mass arrangement (spherical or ellipsoidal approximation) on the degree variances is found to be crucial at short spatial scales. A rule-of-thumb for transformation of spectra between spherical and ellipsoidal approximation is derived. Application of the 2D-DFT

on GGMplus gravity maps yields a new degree variance model to degree 90,000. The model is supported by GRACE, GOCE, EGM2008 and forward-modelled gravity at 3 billion land points over all land areas within the SRTM data coverage and provides gravity signal variances at the surface of the topography. The model yields omission errors of ~ 9 mGal for gravity (~ 1.5 cm for geoid effects) at scales of 10 km, ~ 4 mGal (~ 1 mm) at 2-km scales, and ~ 2 mGal (~ 0.2 mm) at 1-km scales.

Keywords Degree variance · Omission error · Discrete Fourier transform · Ultra-high resolution gravity · GGMplus · Spherical approximation · Ellipsoidal approximation

1 Introduction

Much progress has been made in global gravity field determination with the dedicated satellite gravity field missions GRACE (e.g., Tapley et al. 2004) and GOCE (e.g., Pail et al. 2011). While these missions provide good global data coverage, their resolution is limited to spatial scales of ~ 80 km due to the gravity attenuation with altitude. The fine structure of the field is, therefore, usually retrieved from (a) terrestrial measurements (e.g., gravity anomalies or vertical deflections) and (b) from gravity forward modelling (i.e., computation of gravity effects from topographic mass models), particularly over areas devoid of terrestrial data (Pavlis et al. 2007; Hirt et al. 2010). Due to the fact that terrestrial measurements are neither homogeneously nor completely given on a global scale (e.g., Pavlis et al. 2012), gravity effects implied by the topographic masses are often considered as a means to increase the resolution of a gravity model.

With the help of integration techniques based on Newton's law of gravitation, digital elevation models along with

Moritz Rexer
m.rexer@tum.de

Christian Hirt
c.hirt@curtin.edu.au

¹ Institute for Astronomical and Physical Geodesy, Institute for Advanced Study, Technische Universität München, Munich, Germany

² Department of Spatial Sciences, The Institute for Geoscience Research, Western Australian Geodesy Group, Curtin University, Perth, Australia

mass-density assumptions can be used to approximate the gravity field at very short scales (e.g. scales of few hundreds of meters to tens of kilometers). Recently, this has been done on a near-global scale by [Hirt et al. \(2013\)](#) in the spatial domain. The authors provide GGMplus gravity maps for all land areas between 60° North and 56° South at 220 m ground resolution. The maps incorporate gravity from a combination of GRACE and GOCE satellite observations, terrestrial gravity data from EGM2008 ([Pavlis et al. 2012](#)) and topographic gravity effects beyond the 10-km resolution of EGM2008. The gridded GGMplus gravity maps provide fairly complete information on the topography-generated gravity field over the continents at spatial scales down to 220 m corresponding to spherical harmonic degree of about 90,000.

In order to examine topography-generated gravity signal strengths at different spatial scales, and to describe the decay of these signals as a function of the spatial scale, some spectral representation of the gravity field is required. This can be in terms of spherical harmonic coefficients (SHCs) or degree variance spectra (power law) describing the decay of the field as a function of wavelength. Three techniques suitable for this are:

- Global spherical harmonic analysis transforming gridded gravity data to SHCs (e.g., [Sneeuw 1994](#); [Pavlis et al. 2012](#); [Gruber and Abrikosov 2014](#)).
- Spectral-domain gravity forward modelling transforming a global spherical harmonic topographic mass model to SHCs of the implied potential (e.g., [Rummel et al. 1988](#); [Balmino et al. 2012](#)).
- Application of 2D-Fourier techniques to derive degree variance spectra of gridded gravity data (e.g., [Forsberg 1984a](#); [Flury 2006](#)), which is the scope of this paper.

While the first two methods have been applied to harmonic degree 10,800, or ~ 2 km spatial scales ([Abrikosov et al. 2012](#); [Balmino et al. 2012](#)), there are currently no results from global harmonic analysis or spectral-domain forward modelling reported in the literature that reach sub-km resolution for degree variance spectra. This may be due to significant computational costs associated with ultra-high degree spherical harmonic modelling, particularly with the forward method that involves multiple harmonic analyses (e.g. [Hirt and Kuhn 2014](#)). However, ultra-high resolution spectral representations would be useful to study the short-scale properties of the gravity field, e.g., to derive signal strengths and omission errors.

In this paper we determine degree variance spectra of the topographic potential at short spatial scales as incorporated in GGMplus (harmonic band of degrees 2161 to 90,000) with near-global scope using 2D-Fourier transform and variance model fitting techniques. At long spatial scales the spectra are supported by a combination of satel-

lite gravity (GRACE and GOCE) and terrestrial gravity as contained in EGM2008 (harmonic band of degrees 2 to 2160). The spherical harmonic power spectra are computed from equi-angular GGMplus grids of gravity disturbances (<http://ddfe.curtin.edu.au/models/GGMplus/>). As a major advantage over spherical harmonic modelling, 2D-Fourier techniques can be flexibly applied on regional and global data sets to derive power spectra and are computationally less expensive than the first two methods when going to ultra-high degree. This is evident from the fact that 2D-Fourier techniques were used already few years ago to study the power spectra of local and regional gravity data sets to ultra-high degree (e.g. [Flury 2006](#); [Voigt and Denker 2007](#)), cf. Sect. 2. Different to the first two techniques, 2D-Fourier methods do not yield sets of SHCs as spectral description of the gravity data set, and involve some approximations, which are studied and quantified in this paper. While potential spectra from 2D-Fourier techniques and several degree variance models are reported in the literature, a guide that would describe and analyse all processing steps in detail and investigate the approximations involved and their impact on the estimated spectra was not available to us.

This paper attempts to provide a tutorial-style description for the computation of degree variances and the consecutive fitting of degree variance models using commonly used mathematical models (Sect. 3). We make use of a two-dimensional Discrete Fourier Transform (DFT) approach dating back to [Forsberg \(1984a\)](#) for recovery of potential spectra. This approach is reviewed here and tested in a closed-loop environment in view of application on global and near-global gridded gravity data. We discuss in detail the so-called radial averaging in the 2D-DFT, and focus on the role of the reference surface for spherical harmonic spectra (sphere, ellipsoid or topography). This is rarely dealt with in the literature but crucial for interpretation of degree variances. We further develop a rule of thumb for the transformation of degree variances of the topographic potential from spherical to ellipsoidal approximation and vice versa. With the computed degree variances in hand we are able to define a new degree variance model based on GGMplus which describes the spectral energy of the topographic potential at the surface of the Earth's landmasses to ultra-fine spatial scales (Sect. 4).

Our work extends the study by [Flury \(2006\)](#) who analysed the signal strength of the medium-wavelength part of the gravity field. While Flury studied the spectral properties of topography-reduced gravity by 2D-DFT, he pointed out (in his outlook) the need for investigation of the very-short wavelength components caused by the topographic masses and computed from digital terrain models. This is exactly the purpose of this work.

This paper is structured as follows: In Sect. 2 we start with some introductory comments on the topographic potential at short scales and its computation through forward

modelling techniques. We describe the spherical harmonic modelling concept, elaborate the spherical and ellipsoidal approximation regarding the underlying mass distribution of those models and define degree variances. In Sect. 3 we introduce the mathematical tools and experiments that are needed for the computation and correct interpretation of degree variances recovered from 2D grids of topographic gravity. We elaborate—in the form of a detailed guide—the 2D-DFT approach of Forsberg (1984a) for its global application and discuss the different domains of degree variances (e.g., sphere vs. ellipsoid). Section 4 deals with the approximation of the topographic gravity energy to ultra-short scales of 220 m (equivalent to spherical harmonic degree 90,000) based on GGMplus gravity maps, and omission errors are estimated. Further, we deal with the nature and the interpretation of the computed degree variance models based on spherical and ellipsoidal approximations. Finally, in Sect. 5 we summarise our findings and give an outlook on future work.

2 Background

2.1 Topographic potential and topographic gravity effects

Because of the quadratic attenuation of gravity with distance, the fine structure of the Earth's gravity field is strongly influenced by the mass distribution in the outermost layer of the Earth—the topography. While the Earth's flattening and the masses of core and mantle account for more than 99 % of the total variations in gravity, the topographic masses cause less than 1 % of the global variations (cf. Torge 2001). Locally and particularly in areas of rugged terrain, however, the topographic masses are necessary to explain the full gravitational signal because the contribution of the topography to gravity is dominant at very short scales. Since gravity observations on very short scales are limited, forward modelling of gravity effects is a crucial technique in view of generating high-resolution (global) gravity field models (Pavlis et al. 2012; Hirt et al. 2013).

Besides the visible topographic masses, other components—such as mass anomalies in the Earth's interior, sediments, salt domes—also generate higher-frequency gravity signals. The gravity forward modeling data used in this study are based on the visible topographic masses as represented by the SRTM topography.

Forward gravity field modelling techniques can be classified as follows (Kuhn and Seitz 2005):

- Space domain techniques rely on a numerical evaluation of Newton's law of gravitation to yield topographic

gravity effects (e.g., Forsberg 1984b; Pavlis et al. 2007; Grombein et al. 2014).

- Spectral domain techniques expand the topographic potential into integer powers of topographic heights and require several harmonic analyses or need some rigorous formulation to obtain the SHCs of the topographic potential, and subsequent synthesis to derive gravity effects (e.g., Rummel et al. 1988; Pavlis and Rapp 1990; Novak 2010; Claessens and Hirt 2013).

For more details and an in-depth comparison of both forward modelling techniques we refer to Hirt and Kuhn (2014). Importantly, the approaches are often based on the assumption of an underlying mass sphere with topographic masses assumed to reside on Earth's spherical surface. The topographic gravity constituents of the GGMplus gravity maps which we investigate in this study were generated in the space domain with the well-known residual terrain modelling (RTM) technique by Forsberg (1984b). GGMplus is based on a spherically approximated mass distribution as far as the topography-implied gravity signal (RTM) is concerned (see Sect. 2.2) and a full account of the RTM forward modelling of GGMplus is given in Hirt et al. (2014).

The spectral characteristics of topographic gravity effects on short scales have been investigated in local and regional scale studies e.g., by Voigt and Denker (2007) and Jekeli (2010). Voigt and Denker (2007) investigated topographic gravity effects on gravity anomalies, deflections of the vertical and geoid heights computed from digital terrain models (DTM) with 1'', 3'', 6'', 12'' and 30'' (arc-second) resolution in Germany. Their tests concentrate on three 1° × 1° tiles for which empirical covariance functions and power spectral densities (and degree variances) are computed and analysed. In view of a one centimetre geoid they conclude that at least a 6'' DTM for an alpine region and 30'' DTMs for the non-alpine regions are required. Jekeli (2010) elaborated the disturbing gravity potential as a stochastic process and presents two topographic PSDs generated from 1 arc-min gravity anomaly grids over the mid US. The author analytically derived a linear relationship between the topographic heights and the gravity anomaly, which is confirmed empirically with digital elevation data of 30 arc-sec resolution over the same areas.

2.2 Spherical harmonic models, spherical vs. ellipsoidal approximation

Today, spherical harmonic (SH) representations are the most common way to globally describe the gravity field. Following Sanso and Sideris (2013), a global representation of the disturbing potential T may be written as

$$T(\theta, \lambda, r) = \frac{GM}{R} \sum_{l=2}^{L_{\max}} \left(\frac{R}{r}\right)^{l+1} \sum_{m=-l}^l CS_{lm} Y_{lm}(\theta, \lambda), \tag{1}$$

where CS_{lm} are the SH coefficients of the representation, Y_{lm} are the SH basis functions, R is the scaling parameter associated with the model coefficients (often the semi-major axis a of some reference ellipsoid), GM is the product of the gravitational constant times the Earth's mass, l is the spherical harmonic degree, L_{\max} is the maximum degree (degree of truncation of the series expansion) and m is the spherical harmonic order. Negative and positive orders m ($m < 0$; $m \geq 0$) denote the affiliation to the sine and cosine terms of the base functions, respectively. The geocentric coordinate triplet—geocentric latitude, longitude and geocentric radius θ, λ, r —defines the point of evaluation of the series, usually located outside of the Earth's topographic masses. For more details on the spherical harmonic representation, see, e.g. [Sanso and Sideris \(2013\)](#).

Spherical harmonic potential coefficients can be computed via forward modelling techniques from mass distributions on a sphere, or on an ellipsoid. In either case, the SH coefficients describe the potential field in the domain exterior to the mass distributions, where the field is harmonic.

Spherical harmonic models in spherical approximation are computed from masses arranged on the surface of a sphere of some constant radius. This requires “mapping” of the topography (e.g., taken from an elevation model) onto the surface of the sphere. This approach has been used, e.g., in [Rummel et al. \(1988\)](#), [Balmino et al. \(2012\)](#), and [Hirt and Kuhn \(2012\)](#) to construct models of Earth's topographic potential in spherical approximation. In this paper we use the topographic potential model dV-SPH-RET2012 ([Hirt and Kuhn 2012](#)) as an example for spherical harmonic models in spherical approximation. Besides Earth's visible topography it also models gravity effects of the ocean water masses, those of the major lakes and masses of Earth's ice sheets via the concept of rock-equivalent topography (e.g. [Rummel et al. 1988](#)). While models such as dV-SPH-RET2012 “disregard” the ellipsoidal shape of the Earth, they are useful, e.g., for testing of computational procedures as will be shown in Sect. 3.

When gravity forward modelling is applied to a mass distribution arranged on the surface of some reference ellipsoid, the topographic potential is obtained in ellipsoidal approximation ([Claessens and Hirt 2013](#); [Grombein et al. 2014](#)). An example for a SH model of the topographic potential in ellipsoidal approximation is the dV-ELL-RET2012 model ([Claessens and Hirt 2013](#)). In this type of model, the mass arrangement is much closer to that of the real Earth than in spherical approximation.

Spherical harmonic models of Earth's geopotential, e.g., those available via IAG's International Centre for Global Earth Model (ICGEM) service, are in ellipsoidal approximation too. This is because geopotential models are usually based on gravity field observations, which reflect that the field-generating mass distribution is—in good approximation—ellipsoidal. For instance, the EGM2008 geopotential model ([Pavlis et al. 2012](#)) and those from the GOCE gravity field mission ([Pail et al. 2011](#)), among other geopotential models of the ICGEM, can be considered as ellipsoidal approximation—type.

In summary, the main difference between spherical harmonic potential models in spherical and ellipsoidal approximation in this study is the arrangement of the field-generating masses (sphere vs. ellipsoid), which come into play when forward modelling the gravitational field in spherical harmonics.

2.3 Degree variances

Degree variance models are power laws that describe the decay of the gravity signal in some spectral representation. They are mostly of purely empirical nature and reflect the observable variations in a set of global spherical harmonic coefficients (see Sect. 2.2). As such degree variances are dimensionless (unitless). They are defined as the sum of squared spherical harmonic coefficients per spherical harmonic degree as

$$c_l^2 = \sum_{m=-l}^l CS_{lm}^2. \tag{2}$$

In other words the degree variance of degree l reflects the signal power contained in all the coefficients of same degree (and of different orders $m \in [-l, \dots, +l]$). Degree variances as computed in this work refer to gravity disturbances and are given in mGal^2 . They relate to dimensionless degree variances (Eq. 2) by the (functional-dependent) scaling factor Ψ (Table 1) following

$$c_l^2[\Psi] = \Psi \cdot \sum_{m=-l}^l CS_{lm}^2, \tag{3}$$

Table 1 Gravity functionals and degree variance dimensioning factors together with their unit

Gravity functional	Dimensioning factor Ψ	Unit
None	1	–
N : geoid heights	R^2	m^2
T_r : gravity disturbances	$(l + 1)^2 \left(\frac{GM \cdot 10^5}{R^2}\right)^2$	mGal^2
Δg : gravity anomalies	$(l - 1)^2 \left(\frac{GM \cdot 10^5}{R^2}\right)^2$	mGal^2

Note that the factors may be derived from the spherical harmonic expansion (of the respective gravity quantity, e.g. Eq. (4) in case of gravity disturbances) for $r = R$. The converted degree variances (e.g. in metres or mGal) roughly reflect the signal strength (per wavelength) as expected from a spherical harmonic synthesis with evaluation points residing on the surface of a sphere of radius R .

Degree variances generally can be obtained from

- a set of spherical harmonic coefficients: e.g., of gravity field models as found at the ICGEM and evaluated by Eq. (2).
- degree variance models/rules (based on analytical functions): e.g., [Kaula \(1966\)](#), [Tscherning and Rapp \(1974\)](#), [Heller and Jordan \(1976\)](#), [Moritz \(1977\)](#), [Jekeli \(1978\)](#), [Flury \(2006\)](#), [Sanso and Sideris \(2013\)](#), also see Sects. 3.2 and 4.

3 Recovering the spherical harmonic power spectrum from gridded gravity data by 2D-DFT

3.1 Computation of degree variances by 2D-DFT

In the literature, different ways for computing degree variances from a set of 2D-scattered point gravity values are described. [Flury \(2006\)](#) reviews several approaches to calculate degree variances and elaborates their complementarity (see Fig. 5 in [Flury 2006](#)). In principle one can either choose to estimate the degree variances from the 2D-PSDs (power spectral density) by azimuth averaging (c.f. [Forsberg 1984a](#)) or to calculate the degree variances from the empirical auto-covariance function (or from an analytical auto-covariance model, cf. [Wenzel and Arabelos 1981](#)). Both ways naturally assume homogeneity, isotropy and periodicity of the signals as well as no violations of the sampling theorem in the discretization process. With PSDs, the calculation of the Legendre polynomials can be omitted as the similarity of the shape of the Bessel functions and the Legendre polynomials is exploited ([Forsberg 1984a](#)). The PSDs are generally obtained by Fourier transformation of an equally spaced grid calculated from the 2D scattered point data. Note that PSDs can also be retrieved from the auto-covariance function of the 2D scattered point data by the so-called discrete Hankel transform (c.f. [Flury 2006](#)).

To exemplify the processing steps of the 2D-DFT method, we use a global 5 arc-min grid of topography-implied gravity disturbances (Fig. 1). These were synthesised from the spherical-harmonic topographic potential model dV-SPH-RET2012 ([Hirt and Kuhn 2012](#), Section 2.2) in the spectral band of harmonic degrees 0 to 2160 with the harmonic_synth software ([Holmes and Pavlis 2008](#)) following

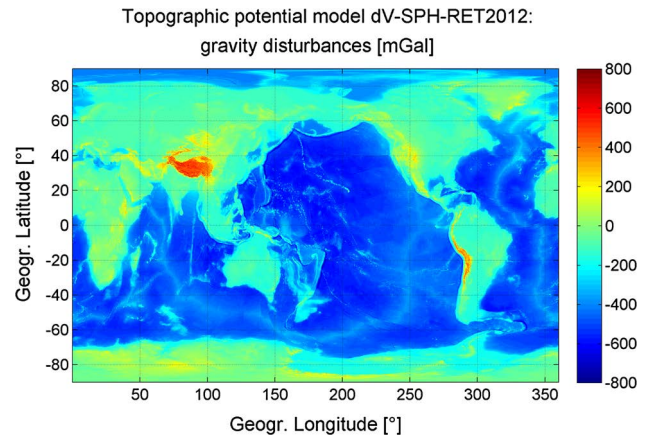


Fig. 1 Global $5' \times 5'$ —gravity disturbance grid of the topographic potential model dV-SPH-RET2012 evaluated from degrees 0...2160 (Eq. 4)

$$\delta g(\theta, \lambda, r) = \frac{GM}{R^2} \sum_{l=0}^{L_{\max}} (l+1) \left(\frac{R}{r}\right)^{l+1} \sum_{m=-l}^l CS_{lm} Y_{lm}(\theta, \lambda). \quad (4)$$

The dV-SPH-RET2012 model is chosen in this study because it allows (1) computation of the true spectrum of potential degree variances to benchmark all approximation errors in the 2D-DFT method, and (2) its approximation level is suitable for testing Forsberg's 2D-DFT formalism which is shown to be based on spherical approximation, too.

In Fig. 2 the flow from 2D gridded data in space domain to the signal representation in frequency domain and finally the transformation to the spherical harmonic frequency domain is shown. Next a detailed description of the five working steps shown in Fig. 2 is given for the computation of degree variances. Following the procedure of [Forsberg \(1984a\)](#) and the description given in [Flury \(2006\)](#), the guide elaborates the details of the 2D-Fourier transform for potential spectrum recovery.

1. Interpolation of 2D scattered gravity data to an equidistant grid with K_x row samples at the equidistant coordinates x_k and K_y column samples at the equidistant coordinates y_j

$$x_k = k \cdot \Delta x \quad (5)$$

$$y_j = j \cdot \Delta y, \quad (6)$$

where $k = 1, 2, \dots, K_x$, $j = 1, 2, \dots, K_y$ and $\Delta x/\Delta y$ is the equidistant spacing of the grid in row-/column direction in metres. The equidistant sampling in metres is related to the spacing in degree by the mean co-latitude θ_{ave} of the grid following

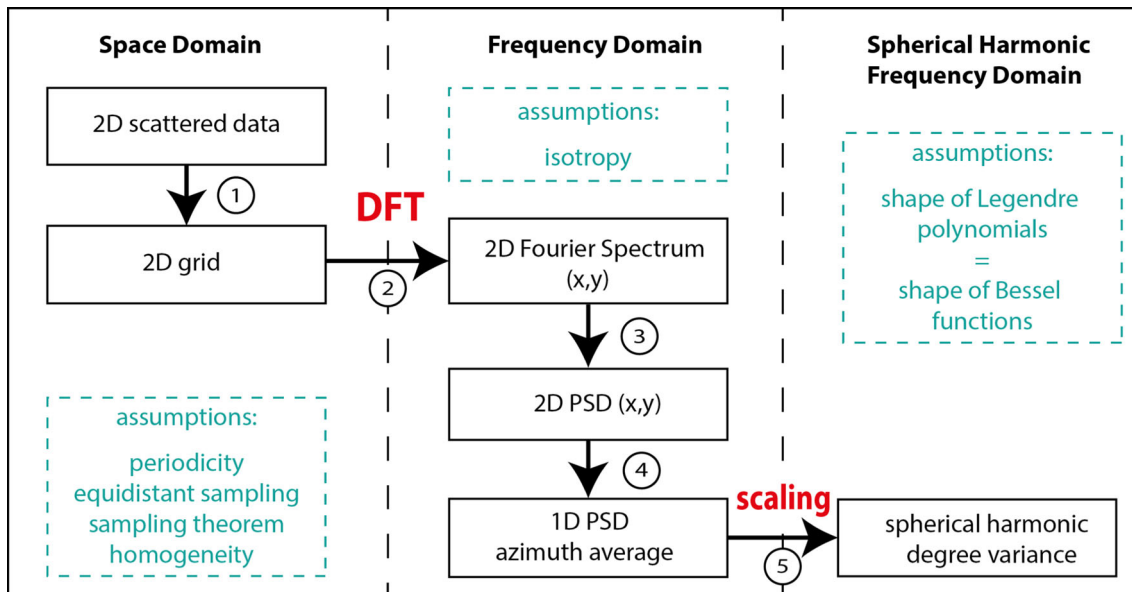


Fig. 2 Flow chart showing the transition of gravity data in Space Domain to PSDs in Frequency Domain and to degree variances in Spherical Harmonic Frequency Domain

$$\begin{Bmatrix} \Delta x \text{ [km]} \\ \Delta y \text{ [km]} \end{Bmatrix} = \begin{Bmatrix} \Delta x \text{ [rad]} \\ \Delta y \text{ [rad]} \cdot \sin \theta_{ave} \end{Bmatrix} \cdot R. \quad (7)$$

We acknowledge that according to the definition in Eq. (7) equidistant sampling is only given in good approximation for small grids; thus one DFT prerequisite is actually violated for regional or global grids. However, closed loop results will show this effect to be non-critical.

- The discrete 2D-Fourier transform of the gridded data $f(x, y)$ is given by

$$F(v_p, v_q) = \frac{1}{K_x K_y} \sum_{k=0}^{K_x-1} \sum_{j=0}^{K_y-1} f(x_k, y_j) \cdot e^{-i2\pi \left(\frac{pk}{K_x} + \frac{qj}{K_y} \right)} \quad (8)$$

returning the 2-dimensional Fourier Spectrum $F(v_p, v_q)$ at the frequencies v_p and v_q for $p = 0, 1, \dots, K_x - 1$ and $q = 0, 1, \dots, K_y - 1$. The Fourier Transform is complex-valued and can generally be described by a real and an imaginary part as

$$F(v_p, v_q) = a(v_p, v_q) - ib(v_p, v_q), \quad (9)$$

where a and b are the Fourier coefficients at the frequencies v_p and v_q .

- The 2D-PSD is then estimated by

$$\phi(v_p, v_q) = D_x D_y |F(v_p, v_q)|^2, \quad (10)$$

as the square of the amplitude spectrum $|F(v_p v_q)|$, where

$$|F(v_p v_q)| = \sqrt{a^2(v_p, v_q) + b^2(v_p, v_q)}, \quad (11)$$

and scaled to the grid dimension $D_x = K_x \cdot \Delta x$ and $D_y = K_y \cdot \Delta y$. The frequencies are defined as $v_p = p/D_x$ in the row direction and as $v_q = p/D_y$ in the column direction (their unit is km^{-1}). Note that only the one-sided spectrum is of interest (corresponding to the upper left quadrant of the 2D-Fourier Transform), as the 2D-PSD is mirrored at its centre. The unit of the PSD is $\text{mGal}^2 \text{km}^2$ for gravity anomalies. As example, Fig. 3 (left plot) shows the corresponding 2D-PSD of the previously introduced dV-SPH-RET2012 gravity disturbance grid, which exhibits the radial decay of the signal power with rising frequency and a sudden drop at $v_p = v_q \approx 0.1078 \text{ km}^{-1}$ which corresponds to the maximum harmonic degree ($=2160$) of the model.

- In order to obtain a 1D-PSD which later can be transformed to degree variances, a so-called ‘‘azimuth averaging’’ (Forsberg 1984a) procedure is applied to the 2D-PSD. Values along equi-frequency circles (values at the same azimuth distance from the upper left corner of the PSD-matrix) are averaged, following

$$\phi(v_i) = \phi \left(\sqrt{v_p^2 + v_q^2} \right) \quad (12)$$

In other words, frequency classes V_i are to be defined containing the average PSD corresponding to the average frequency v_i within the class boundaries $V_i - \frac{\Delta h}{2} \leq$

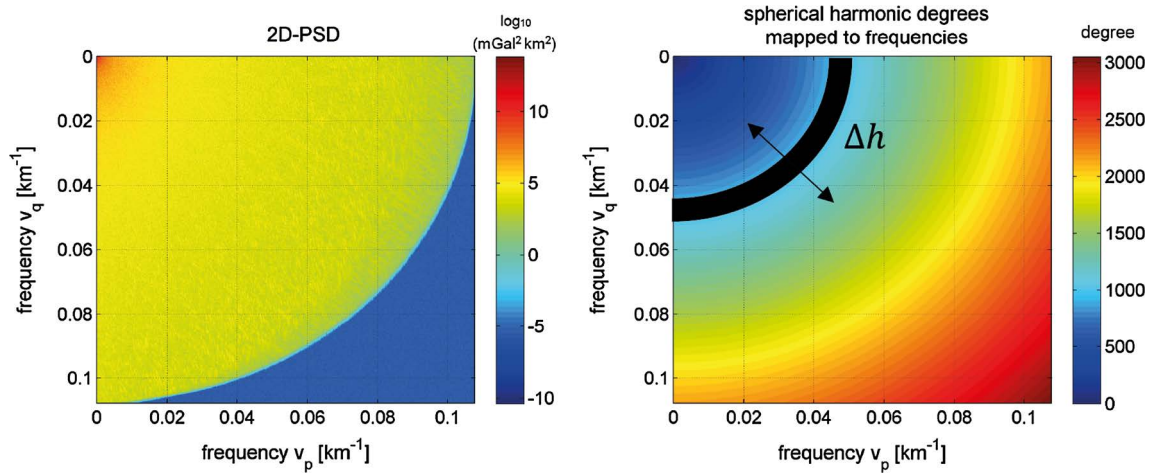


Fig. 3 Two-dimensional power spectrum density $\phi(v_p, v_q)$ in $\log_{10}(\text{mGal}^2 \text{km}^2)$ (left) and the corresponding spherical harmonic degrees (right) of the Fourier Spectrum derived from a global $5' \times 5'$ dV-SPH-

RET2012 grid evaluated from degrees 0...2160; the *black illustration* in the *right plot* shows the meaning of the class-width parameter Δh of the azimuth-averaging procedure

$\sqrt{v_p^2 + v_q^2} < V_i + \frac{\Delta h}{2}$, where Δh is the class width (Fig. 3, right plot). The parameter Δh then defines the spectral resolution of the approach and directly affects the smoothness of the computed degree variance curve (see step 5 and Fig. 4).

- Finally, the obtained azimuth average $\phi(v_i)$ of the 2D-PSD is scaled to physically interpretable quantities related to the signal contained in the coefficients of a spherical harmonic representation of the gravitational potential. The transformation is given in (Forsberg 1984b, pp. 8–10) and is a good approximation especially for high spherical harmonic degrees ($l > 10$). Hence, it is well suited to determine the signal at short spatial scales. It is based on the similarity of the shape of the Bessel functions J_0 and Legendre Polynomials P_l , as shown in Forsberg (1984a): $P_l(\theta) \approx J_0(\frac{2l+1}{2} \cdot \theta)$ with a relative error of 1 % at $l = 10$ and $\theta = 8.1^\circ$. We investigated the approximation errors in detail for various degrees and latitudes. Our numerical investigations show that the relative error of this approximation stays below 10 % for $\theta \leq 60^\circ$ and below 25 % for $\theta \leq 90^\circ$ up to degree 90,000. Degree variances c_l^2 are then (approximately) obtained by

$$c_l^2 \approx \frac{l + \frac{1}{2}}{2\pi R^2} \phi(v_i), \tag{13}$$

where R is Earth's mean radius 6,371,008.77 m (c.f. Moritz 2000) and l denotes the spherical harmonic degree. The degree variances are defined for the “natural” wave numbers, which are the frequencies $v_i = (l + \frac{1}{2}) / (R\pi)$. The frequencies v_i can easily be transformed to the corresponding spherical harmonic degree by the simple relation

$$l = (\pi R) \cdot v_i - \frac{1}{2}. \tag{14}$$

The approach, e.g. finds application in studies by Forsberg (1984a,b), Vassiliou and Schwarz (1987), Flury (2006), Voigt and Denker (2007), Jekeli (2010) and Szűcs et al. (2014), where the high-frequency part of the spherical harmonic power spectrum was retrieved from regional datasets.

The minimum L_{\min} and maximum L_{\max} retrievable spherical harmonic degree depends on the dimension of the grid D_x and D_y and the sampling distance $\Delta_{\lambda,\phi} = \Delta x = \Delta y$, respectively:

$$L_{\max} = \frac{1}{\Delta_{\lambda,\phi} [^\circ]} \cdot 180^\circ - 0.5 = \frac{1}{\Delta_{x,y} [\text{km}]} \cdot \pi R - \frac{1}{2} \tag{15}$$

$$L_{\min} = \frac{1}{D_{\lambda,\phi} [^\circ]} \cdot 180^\circ - 0.5 = \frac{1}{D_{x,y} [\text{km}]} \cdot \pi R - \frac{1}{2} \tag{16}$$

3.2 Fitting degree variance models through analytical models

Spherical harmonic degree variances, e.g. as computed from 2D-DFT (see previous section) can be approximated by an analytical mathematical function relying on a relatively small number of parameters. These so-called degree variance models are convenient to describe the decay of the gravity signal in general, for estimating the signal power of a gravity functional at a specific spatial scale and for extrapolating its power

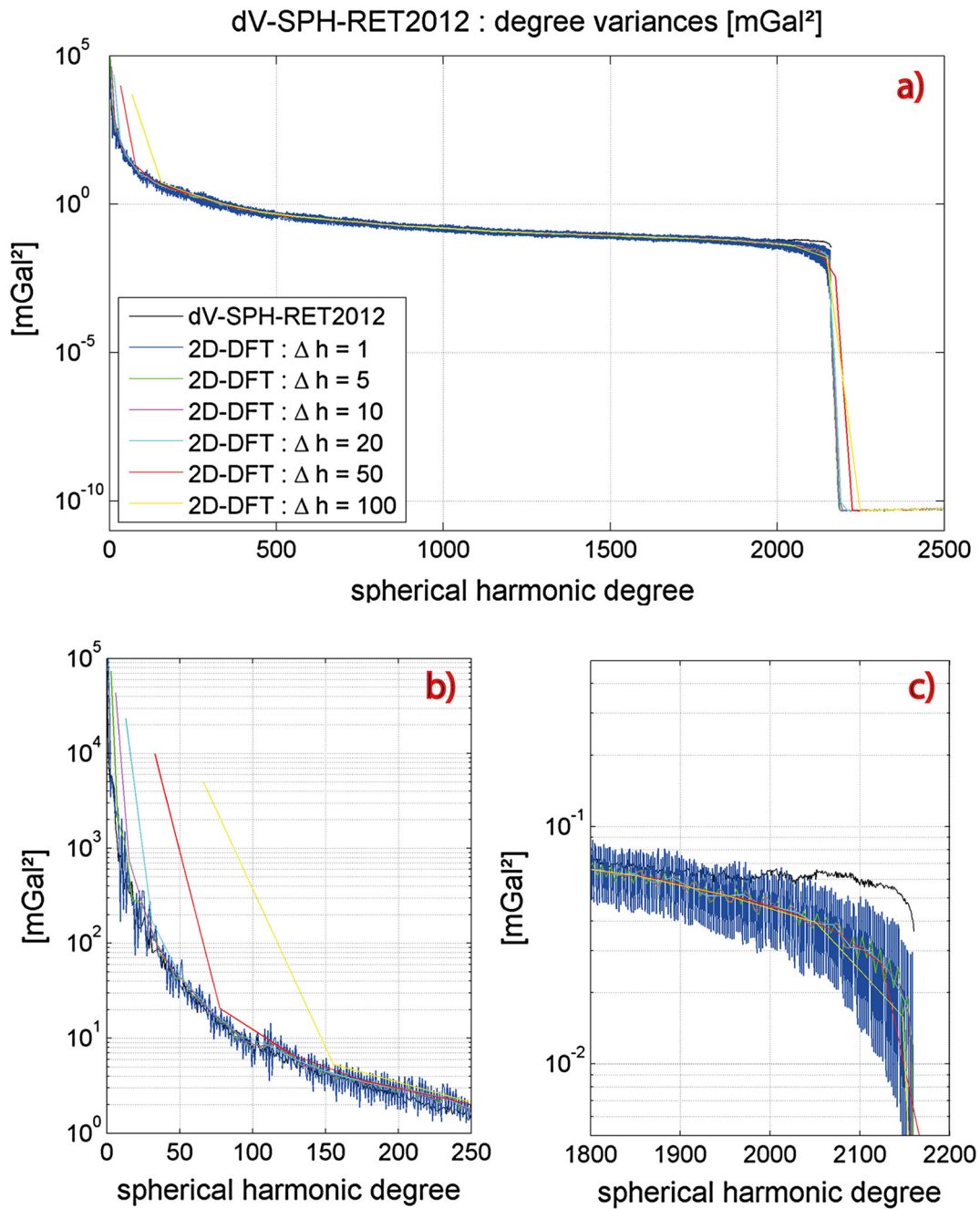


Fig. 4 Degree variances from original topographic potential model dV-SPH-RET2012 (in black) and the degree variances retrieved by 2D-DFT (coloured lines) for various different class widths Δh (in degrees); degree variances are in mGal^2

to shorter spatial scales. Three selected mathematical models are used to represent computed degree variances in this work, which date back to [Kaula \(1966\)](#), [Tscherning and Rapp \(1974\)](#) and more recently [Sanso and Sideris \(2013\)](#). In brackets the gravity functional to which the mathematical models refers to is given along the lines of the notation in Sect. 2.3.

The functional model of Kaula's degree variance model is given by

$$c_K^2(l) = \frac{A}{l^B} (=c_l^2[\Psi = 1]), \tag{17}$$

where $A = 1.6 \cdot 10^{-10}$ (unit: dimensionless) and $B = 3$. The functional model (Eq. 17) is referred to as Kaula-type in the following. The original model of [Tscherning and Rapp \(1974\)](#) refers to gravity anomalies and is parameterised as

$$c_{T Rorig}^2(l) = \frac{A(l-1)}{(l-2)(l+B)} \cdot \sigma_0^{l+2} \left(= c_l^2 \left[\Psi = (l-1)^2 \left(\frac{GM \cdot 10^5}{R^2} \right)^2 \right] \right) \text{ for } l \geq 3$$

$$c_{T Rorig}^2(2) = 7.54 \text{ mGal}^2$$

$$c_{T Rorig}^2(0, 1) = 0, \tag{18}$$

where $A = 425.28 \text{ mGal}^2$, $B = 24$ and $\sigma_0 = 0.999617$ (unit: mGal^2). In Sanso and Sideris (2013) the best fitting Tscherning/Rapp model w.r.t. EGM2008 is parameterised as

$$c_{T R EGM08}^2(l) = \frac{A \cdot B^l}{(l-1)(l+2)(l+4)} (=c_l^2[\Psi = 1]), \tag{19}$$

where $A = 2.8 \cdot 10^{-10}$ (unit: dimensionless) and $B = 0.998365$. Note that this version differs from the original model (Eq. 18). Sanso and Sideris (2013) also present a modified version of their functional model

$$c_{SS}^2(l) = \frac{A \cdot B^l}{(l-1)(l-2)(l+4)(l+17)} (=c_l^2[\Psi = 1]) \tag{20}$$

to better analytically fit the spectrum of the EGM2008 gravity field model. We denote this functional model as Sanso/Sideris type. (Sanso and Sideris 2013, p 158) have published (dimensionless) coefficients $A = 3.9 \cdot 10^{-8}$ and $B = 0.999443$ (ibid, Eq. 3.178) as best fitting analytical description of the EGM2008 spectrum. However, as will be shown in Sect. 4, Sanso and Sideris' numerical values for A and B are erroneous and do not fit the EGM2008 spectrum well. Instead, Eq. (20) evaluated with $A = 5.0 \times 10^{-8}$ and $B = 0.999845$ (derived in this paper with the procedure described next) fits the EGM2008 spectrum in a least squares sense. The functional model in Eq. (20) is well suited to describe spectra of EGM2008 and GGMplus (cf. Sect. 4).

Fitting the above models (Eqs. 17, 19 and 20) to computed degree variances is done in an iterative least-squares adjustment approach. During the fit the observations (i.e., the degree variances) are assumed to be without errors and consequently, the adjustment yields the same results as a regression (residuals are not used to improve observations).

The gravity signal expressed by degree variances shows a characteristic decrease over several orders of magnitude with increasing spherical harmonic degree, most of it happening in the low degrees. This non-linear behavior would lead to a bias of the fitted curve in the adjustment to the low degrees, where the signal is much larger. In order to overcome this issue the degree variance is substituted by its logarithmic value y :

$$y(l) = \log_{10}(c^2(l)). \tag{21}$$

Table 2 Partial derivatives of the functional models (Eqs. 17, 19, 20) by the unknown parameters A and B as needed for the design matrix J

	$\frac{\partial y}{\partial A}$	$\frac{\partial y}{\partial B}$
$y = \log_{10} c_K^2$	$\frac{1}{\ln(10) \cdot A}$	$-\frac{\ln(l)}{\ln(10)}$
$y = \log_{10} c_{T R EGM08}^2$	$\frac{1}{\ln(10) \cdot A}$	$\frac{l}{\ln(10) \cdot B}$
$y = \log_{10} c_{SS}^2$	$\frac{1}{\ln(10) \cdot A}$	$\frac{l}{\ln(10) \cdot B}$

Another alternative (not further used here) would be to linearize the functional models, e.g., using a Taylor series as proposed by Jekeli (1978).

The partial derivatives $\frac{\partial y}{\partial A}$ and $\frac{\partial y}{\partial B}$ of the three functional models which are needed for the development of the respective design matrix J are given in Table 2. When equal and uncorrelated observations $y(l)$ are assumed the weight matrix turns into the identity matrix and the adjustment is given by

$$\Delta \hat{x} = (J'J)^{-1} J'w, \tag{22}$$

where $\Delta \hat{x} = [\Delta \hat{A} \ \Delta \hat{B}]$ is the vector of the adjusted corrections of the initial parameters A_0 and B_0 . The vector w describes the disagreement between observations and the function evaluated with the initial parameters

$$w = y(l) - \log_{10}(c^2(l, A_0, B_0)). \tag{23}$$

Then the adjusted parameters are

$$\hat{A} = A_0 + \Delta \hat{A} \tag{24}$$

$$\hat{B} = B_0 + \Delta \hat{B}. \tag{25}$$

The iterative process is terminated when $\Delta \hat{A} < 10^{-13}$ and $\Delta \hat{B} < 10^{-8}$ (for Kaula-type models $\Delta \hat{B} < 10^{-5}$). Using these criteria four to five iterations are found to be necessary for the fit (up to ten for Kaula-type models), depending on the choice of the initial parameters.

3.3 Empirical investigation of the 2D-DFT approach

3.3.1 Effects of class width, averaging, regional coverage and evaluation height

In the literature, the 2D-DFT approach described above (Sect. 3.1) has been applied on local or regional data sets. The application of the method with global scope needs further investigation. We focus on determining the approximation errors by comparisons between 2D-DFT-recovered spectra from dV-SPH-RET2012-derived gravity against those directly from the dV-SPH-RET2012 SHCs which serve as true reference. This allows us to test the influence of free

parameters in the 2D-DFT (e.g., class width) in a closed-loop environment.

Of particular interest is the effect of tiling of the input gravity grids on the spectra in view of an application of the 2D-DFT to compute degree variances from GGMplus (see Sect. 4.1). It provides gravity at the surface of the topography only over the continental landmasses of the Earth (except for polar regions). We, therefore, compare the global spectra recovered from regional averages with spectra recovered from one global grid processed at once, study the effect of the data extent and investigate the role of the evaluation height in the synthesis of dV-SPH-RET2012 gravity on the degree variances spectra. Next we test a range of simple scenarios based on the global 5 arc-min grid of dV-SPH-RET2012 gravity disturbances (Fig. 1; Eq. (4)) as input for the 2D-DFT.

- Processing a global grid

In this test, we apply the 2D-DFT to the global dV-SPH-RET2012 gravity disturbance grid without any tiling. The mean latitude of the global grid is zero and D_y and D_x become 40,075.0 km and 20,035.5 km, respectively. The recovered degree variances (Fig. 4a) show greatest deviations from the original degree variances (black line) for the very low (<40) and very high degrees (>2000), see detail plots in Fig. 4b, c. In the low frequencies the deviations are directly related to the azimuth averaging and the chosen class width, e.g. $\Delta h = 50$ (cyan line), which in this case indicates that the computed degree variance values are actually averages over ± 25 spherical harmonic degrees of the denoted degree. Thus, the parameter Δh (see Sect. 3.1) defines the spectral resolution of the 2D-DFT approach and $\Delta h = 20$ seems to be a good compromise in terms of smoothness and spectral resolution. As the signal decay is very steep (and exponential) near the low-degree harmonics, the averaged values are rather overestimates.

In the very high frequencies, the signal is underestimated as the recovered degree variances dip away beyond degree ~ 2000 (Fig. 4c). The behavior in the high degrees is related to the chosen gravity grid sampling of 5 arc-min, which is near the Nyquist frequency for high harmonic degrees (the high frequencies near degree 2160 are not well represented at 5 arc-min resolution). By increasing the grid sampling to 1 arc-min (oversampling of factor 5) in the synthesis, the signal power beyond 2000 can be retrieved with almost the same quality as for degrees <2000 (not shown here). The recovered degree variances correctly drop by about eight orders of magnitude around degree 2160, which is the resolution of the input model.

- Role of tiling and averaging

In a second step, the global grid of synthesised gravity disturbances is divided into 2592 $5^\circ \times 5^\circ$ tiles and each of

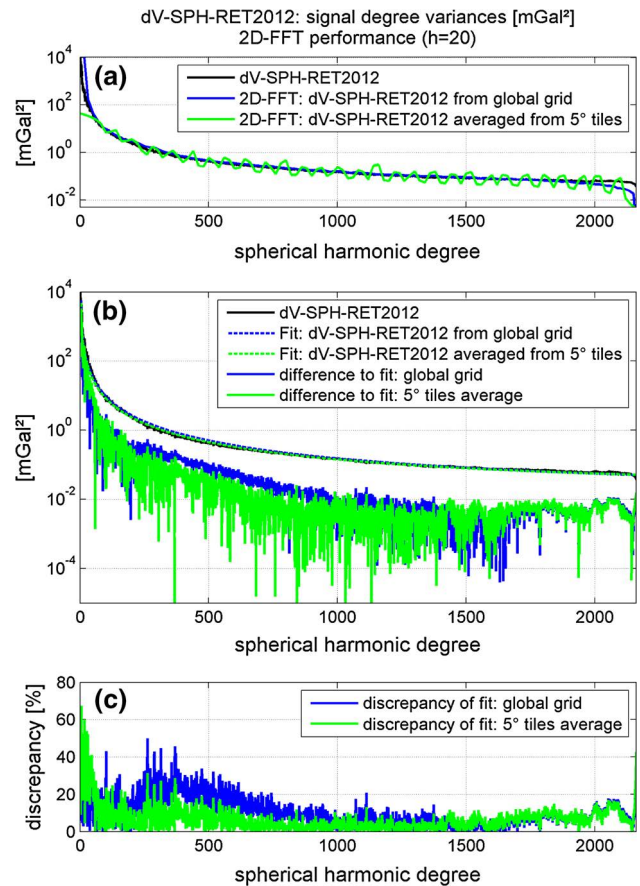


Fig. 5 Closed-loop performance of 2D-DFT approach based on the topographic potential model dV-SPH-RET2012 when applied on global grid (blue lines) and on $5^\circ \times 5^\circ$ tiles with consecutive averaging (green lines) in terms of gravity disturbances (mGal²)

the tiles is evaluated by the 2D-DFT approach. The average of the 2592 computed degree variances (Fig. 5a, green line) oscillates around the true degree variances (black line). For comparison purposes, the 2D-DFT-recovered spectrum of the global dV-SPH-RET2012 gravity grid is shown too (Fig. 5a, blue line), revealing there are no notable oscillations. The amplitude and frequency of the oscillations associated with the tiling are to some extent related to the tile size (decreasing the tile size leads to a lower frequency but a higher amplitude and vice versa). The ability for retrieval of the low-degree harmonics is limited because the maximum wavelength in a $5^\circ \times 5^\circ$ tile is ~ 555 km. Therefore, the spherical harmonic degrees below ~ 36 cannot be recovered, which explains why the low-frequency power cannot be retrieved in the same manner as the 2D-DFT applied to a global grid. However, this effect is non-critical for this study because of our interest in the GGMplus gravity field spectra at short scales.

Fitting a Sanso/Sideris-type model (Eq. 20) to the averaged degree variances between degree 50...2000

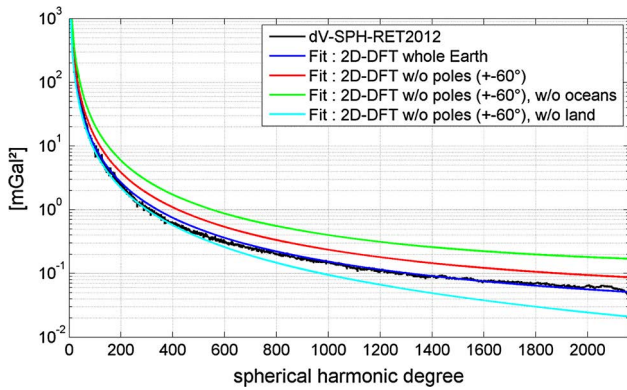


Fig. 6 2D-DFT signal degree variance fits from synthesised dV-SPH-RET2012 gravity disturbance grid in dependence of different global coverage

(Fig. 5b, dashed green line for spectra from tiled data, dashed blue line for grid processed as whole), the differences with respect to the true dV-SPH-RET2012 SHC-derived spectrum are at the 10 % level and hardly exceed 20 % (Fig. 5c).

In summary, the fairly good agreement in the closed loop tests show that the 2D-DFT method is capable of recovering the gravity power spectra with reasonable quality. There are ~10 % errors over much of the spectrum when using regional tiles. The choice of the tile size puts limitations to the minimum recoverable degree and the tiling and averaging leads to an oscillation of the signal around the original degree variance. Most importantly, the oscillations do not deteriorate the fit, and the precision of the tiling and averaging procedure is commensurate or even better compared to processing a global grid at once.

• **Role of coverage**

In view of spectrally analysing GGMplus gravity maps, available only for land areas in between 60° North and 56° South, the effect of different global coverage on the spectra is important. Therefore, the dV-SPH-RET2012 gravity disturbance grid is divided into 10° × 10° tiles and degree variance averages for selected spatial coverages are computed and analysed. The fitted degree variance curves in Fig. 6 indicate the following: polar regions contain less topographic gravity signal over nearly all scales, because excluding tiles North of 60° and South of -60° latitude from the average (red line) leads to more power in the degree variances than the global grid (dark blue line); additionally excluding all tiles entirely located over the oceans (green line) leads to even more power in the degree variances; hence, the continental areas are covered by higher-power topographic gravity features compared to the bottom of the oceans. Conversely, averaging only the degree variances from ocean tiles (light blue line) leads to signal power below the global energy level in

the spherical harmonic domain. Note that these considerations hold for the topographic potential (and probably for gravity at very short scales), but not necessarily for Earth's actual gravity field.

• **Role of evaluation height**

In the experiments above gravity values were synthesised on the sphere ($r = R$). In geodetic practice, gravity is often given on the surface of the topography (e.g. measurements or gravity models such as GGMplus). In spherical approximation, evaluation at the surface of the topography is done by introducing $r = R + H$ in Eq. (4). Gravity signals at the reference surface (e.g. sphere) are downward-continued and thus amplified compared to signals at the surface of the topography. In Fig. 7 the 2D-DFT procedure has been applied to a global grid of gravity disturbances of the spherical topographic potential model dV-SPH-RET2012

- evaluated at the surface of the model's reference sphere (light blue line) and,
- evaluated at the surface of the topography (red line) using an upward continuation technique along with gravity gradients of up to sixth order (see Hirt 2012 for details).

For comparison purposes, the true dV-SPH-RET2012 degree variances computed from SHCs are shown as well (dark blue line). The degree variance curves start to deviate near degree 600 where the red degree variances fall below the energy level of degree variances at the sphere. At degree 2000 the difference between the “topography-residing” and the “sphere-residing” degree variances reaches a factor of ~2.8.

This behaviour is explained by the attenuation of gravity with height. At the reference sphere gravity (e.g. gravity disturbances) is downward continued, thus amplified. With increasing height gravity becomes attenuated. This particularly affects short-scale signals because the attenuation effect becomes stronger the shorter the associated wavelengths. From Fig. 7, it is thus important to discriminate between spectra of gravity provided at the reference sphere, and those at the surface of the topography.

3.3.2 Degree variances in ellipsoidal and spherical approximation

To study the effect of ellipsoidal approximation (see Sect. 2.2 for the definition in our context) in the 2D-DFT technique, we have synthesised gravity from the ellipsoidal topographic potential model dV-ELL-RET2012 (which is the counterpart to the spherical topographic model dV-SPH-RET2012) and investigated the (2D-DFT) recovered spectra. The original degree variance spectra of dV-ELL-RET2012 (green line) and dV-SPH-RET2012 (blue line) already differ, and

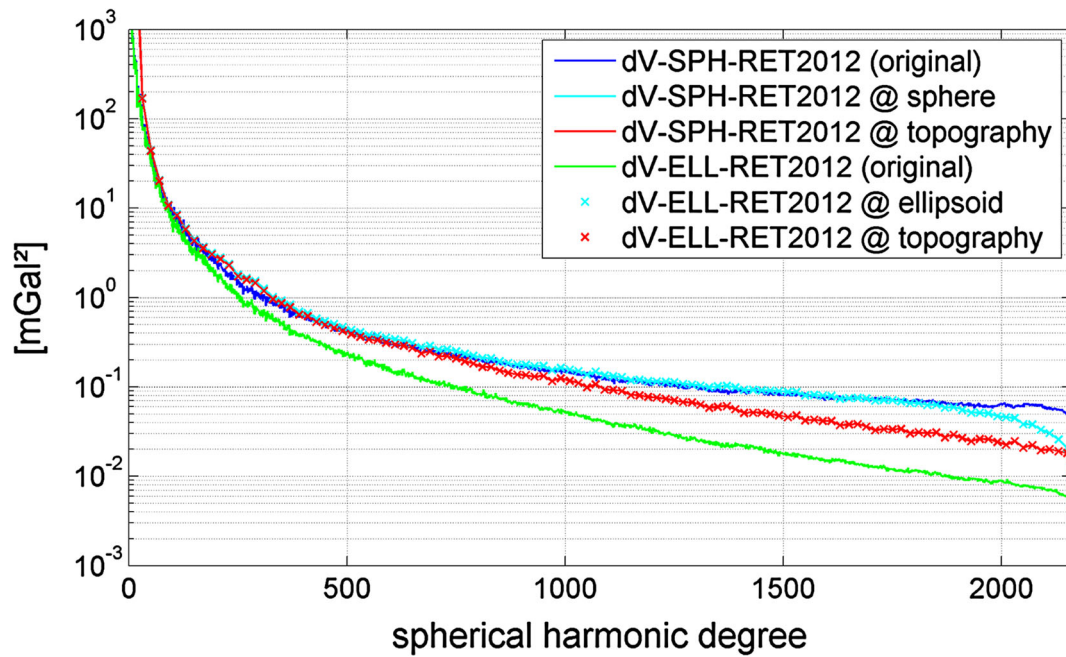


Fig. 7 Results of 2D-DFT experiments using two different models evaluated on different surfaces such as sphere, ellipsoid and topography: (1) topographic potential model dV-SPH-RET2012 (blue line) recovered from gravity disturbances evaluated at the sphere (cyan line),

at the topography (red line), (2) topographic potential model dV-ELL-RET2012 (green line) recovered from gravity disturbances evaluated at the ellipsoid (cyan cross), at the topography (red cross); unit in mGal^2

the decay of the ellipsoidal approximated spectra (green) is stronger than the spherical approximated spectra (blue) with increasing degree (Fig. 7). This is due to different attenuation factors $((a/R)^{l+1}$ vs. $(a/r_e)^{l+1}$) that are implicitly contained in the spherical harmonic coefficients (c.f. Claessens and Hirt 2013). In Fig. 7 the 2D-DFT technique has been applied to a global grid of dV-ELL-RET2012 gravity disturbances

- evaluated on the surface of the model's reference ellipsoid (light blue crosses); $r = r_e$ [see Eq. (4)]; and
- evaluated at the surface of the topography using the gradient continuation technique as above (red crosses); $r = r_e + H$ [see Eq. (4)].

Importantly, the recovered spectra of dV-ELL-RET2012 (light blue/red crosses, Fig. 7) almost exactly follow the recovered spectra of dV-SPH-RET2012 (light blue/red line) (see last paragraph of previous subsection). This is due to the spherical nature of the 2D-DFT approach, given by applying a constant radius R in Eq. (13). Hence, the 2D-DFT refers to a truly spherically approximated Earth and cannot be used to recover degree variances in ellipsoidal approximation. When applying the 2D-DFT approach to a grid of gravity disturbances from the ellipsoidal topographic potential model dV-ELL-RET2012 (2...2190), we obtain degree variances which are (quasi) transformed/compatible to their spherical counterpart (dV-SPH-RET2012).

The distinctly different decay between spherical and ellipsoidal approximation can be expressed by the ratio $\frac{c_l(\text{dV-ELL-RET2012})}{c_l(\text{dV-SPH-RET2012})}$ (black line, Fig. 8). For the very low degrees the approximations nearly coincide while the gap becomes larger (non-linearly) towards the high degrees, where the spectra differ in the order of 10^{-1} at degree 2160.

Describing this ratio by $\alpha_l^{e/s}$, a 1st order polynomial (as exponent to 10) as a function of the degree l with $k_0 = -4.5511 \times 10^{-2}$ and $k_1 = -4.1104 \times 10^{-4}$ following

$$\frac{c_l(\text{dV-ELL-RET2012})}{c_l(\text{dV-SPH-RET2012})} \sim \alpha_l^{e/s} = 10^{(k_0+l \cdot k_1)} \quad (26)$$

yields quite a good fit for degrees larger than 150 (see red line, Fig. 8). In Eq. (26) the superscripts e/s indicate it is a ratio between degree variances of ellipsoidal and spherical approximation. In approximation the ratio $\alpha_l^{e/s}$ can now be used as an empirically derived rule of thumb for a transformation of degree variances of any degree $l > 150$ from spherical to ellipsoidal approximation of the underlying mass distribution, and vice versa.

Note that the empirical law is derived from degree variances of the topographic potential and, therefore, it is primarily applicable to any functional derived from this topographic potential. As the dimensioning factor Ψ in Eq. (3) cancels out in the ratio, the rule is valid for any gravity functional. As an aside, fitting an 8th order polynomial to the ratio yields a very good fit for degrees $l < 150$ (see green line, Fig. 8);

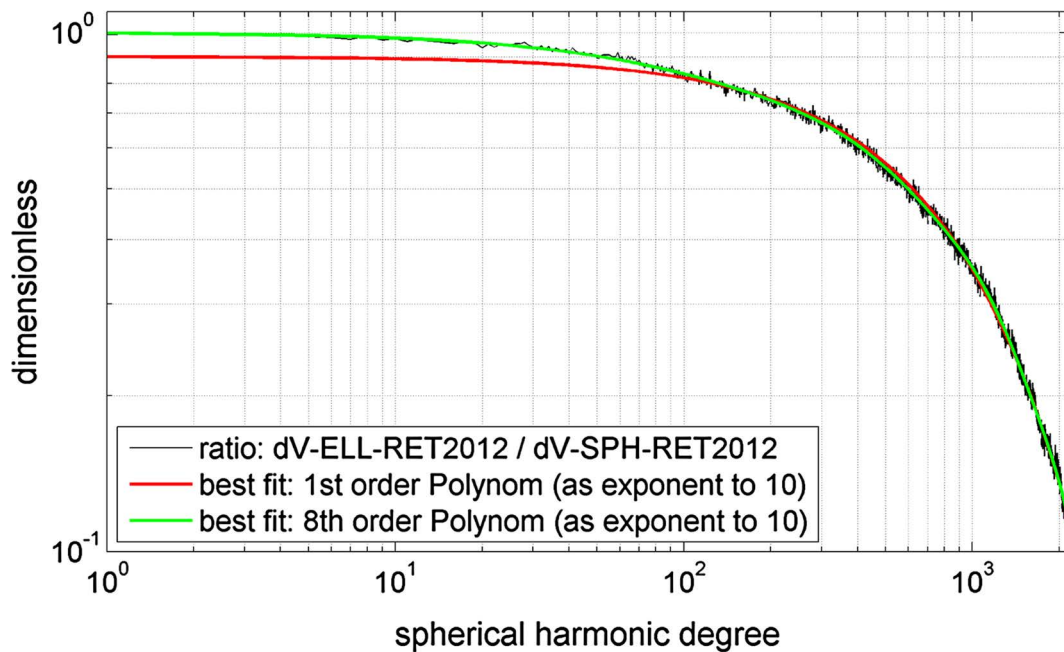


Fig. 8 Ratio between the spherically and the ellipsoidally approximated degree variances of the topographic potential (dimensionless)

however, eight parameters are not considered very handy for a rule of thumb.

The rule of thumb applied to both RET2012 topographic potential models (Fig. 9) shows an average disagreement of 2.1 % (over all degrees) to the respective other model, with discrepancies per degree hardly exceeding 10 %. The rule of thumb allows generation of a spherically approximated spectrum of EGM2008 (or any other potential model) at degree variance level (grey line, Fig. 9), which closely follows the spherically approximated model dV-SPH-RET2012 (for degrees > ~250).

Besides, Fig. 9 shows that the spectrum of the Earth Gravitational Model 2008 model (black line) can be directly compared with that of the dV-ELL-RET2012 model. The very close agreement over most part of the spectrum demonstrates that EGM2008 is in ellipsoidal approximation (as expected).

3.3.3 Discussion

The above experiments investigating the 2D-DFT approach provide valuable insight into the interpretation of degree variances of the topographic potential and the applicability of the 2D-DFT approach for recovery of these spectra.

In general, the experiments show that due care is needed in the interpretation of degree variances obtained from gravity values measured/synthesised on the topography. At the reference surface ($r = R$) the gravity is amplified (for all functionals), e.g. gravity disturbances according to $(\frac{R}{r})^{l+2}$. Therefore, the 2D-DFT spectra generated from gravity at the

topography ($r > R$) exhibit less energy than those retrieved directly from the original spherical harmonic models that refer to the underlying reference body, especially in the high degrees (beyond degree 600). In order to be consistent, the gravity values would have to be downward continued to the reference body of the geopotential model before applying the 2D-DFT procedure.

Additionally, the type of approximation chosen for the underlying mass distribution of a topography-implied SH model, i.e. spherical or ellipsoidal approximation, yields different energy levels in the spectrum according to an attenuation factor that is implicitly contained in the spherical harmonic coefficients. The spherical approximation, historically and even today, often plays an important role in forward modelling Newtonian gravity from the topographic masses (Balmino et al. 2012; Hirt and Kuhn 2014).

With the new empirical rule of thumb (Eq. 26), derived from two topographic potential spectra, one can transform the degree variance between its spherical and ellipsoidal representation (Fig. 9). The method is only approximate (~10 %) and derived from topographic potential models; thus it may yield larger discrepancies for geopotential models, especially at low-degree harmonics. Furthermore, the transformation applies in degree variance domain and is a good approximation at least for the degrees 150 to 2160.

The comparison of the degree variances shows that the spectral power of the ellipsoidal models is (seemingly) smaller than of the models in spherical approximation, and this effect becomes more pronounced as the harmonic degree increases (Fig. 7, particularly Fig. 9). This behavior of the

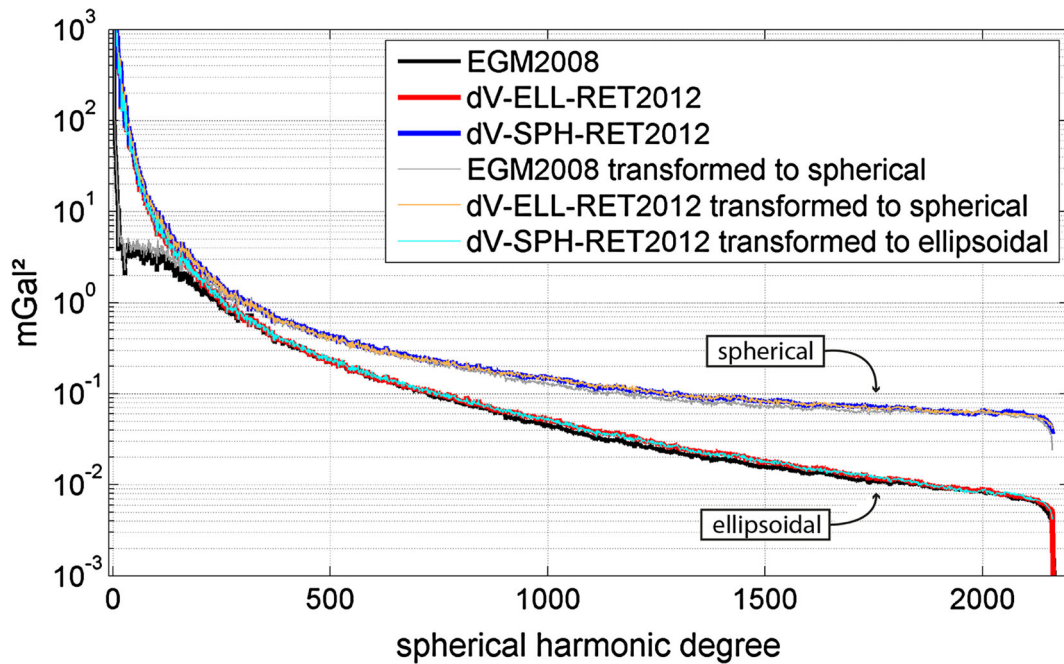


Fig. 9 Transformation of the degree variances of three selected spherical harmonic models between their ellipsoidal and their spherical approximation using the rule of thumb (Eq. 26)

degree variances reflects that the mass distribution in spherical approximation is close to the reference radius, while being up to ~ 20 km below the reference radius (at the poles) in ellipsoidal approximation. Because of the radial dampening of the field, the amplitudes of the degree variances are thus much lower in ellipsoidal approximation. This is both the case for EGM2008 and the topographic potential model dV-ELL-RET2012, both reflecting ellipsoidal mass distributions. The lower spectral energy associated with the ellipsoidal models (Fig. 9) does not represent a smoother gravity field, but rather the (ellipsoidal) location of field-generating masses w.r.t. to the reference radius of the spherical harmonic model.

Balmino et al. (2012) noted different energy levels between their topographic potential and the EGM2008 geopotential model at short spatial scales, down to degree 2160 (ibid, see Fig. 10). The authors find the spectral energy of the topographic potential to be “significantly larger” and attribute this to a “well known sign of a compensation mechanism such as isostasy”. However, our results show that the differences simply reflect two levels of approximation: While EGM2008 is in ellipsoidal approximation, their generated topographic potential coefficients are in spherical approximation as they reflect the topographic masses arranged on the surface of a sphere. Our work, especially the developed rule for the transformation between the two approximations (ellipsoid vs. sphere), can thus be seen as an extension to their work. We expect the developed rule to make their power spectrum more compatible to models in ellipsoidal approximation, such as EGM2008.

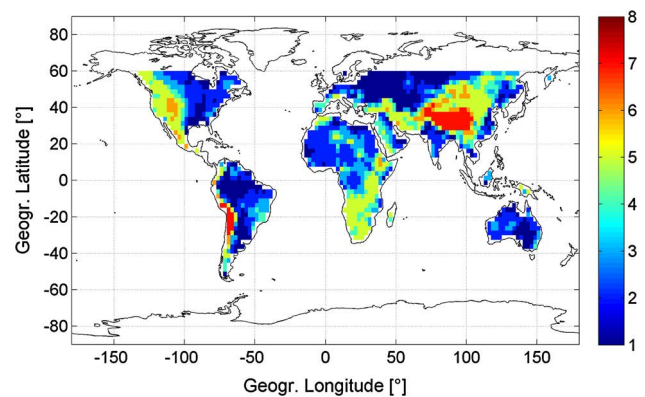


Fig. 10 Global coverage with utilized GGMplus $2.5^\circ \times 2.5^\circ$ tiles and their classification into seven terrain RMS classes

The 2D-DFT approach is capable of delivering spherically approximated spectra only. This is because it relies on the transformation of Forsberg (1984a), which uses a constant (mean) Earth radius (Eq. 13). Applying the 2D-DFT globally for recovery of gravity spectra yields pleasingly good results given the simplicity of the approach and taking into account that some 2D-DFT prerequisites are being violated (e.g. equidistant spacing, periodicity). This even holds true for working in small tiles and consecutive averaging over the spectra of all tiles. With the tiling procedure, the degree variances of a potential model can be retrieved from a global grid with discrepancies at the 10–20 % level over large parts of the spectrum by fitting an appropriate degree variance model to it. The tiling allows for the evaluation of degree variances

in selected regions of the Earth, e.g. the spectral energy over polar regions, continental landmasses, the oceans or areas of different terrain type. The method is, therefore, suited for the estimation of high-degree spherically approximated degree variances from GGMplus gravity grids (next section).

4 Approximation of the Earth's gravitational potential energy to ultra-short spatial scales

4.1 Data and processing

In this section information on the data and the workflow for an approximation of the power spectrum of the topographic potential as implied by the Earth's land topographic masses in terms of degree variances for the degrees 2160 up to 90,000 by 2D-DFT are provided.

For this purpose we make use of the GGMplus (Hirt et al. 2013) gravity maps. GGMplus is a set of digital gravity maps available for different gravity functionals with near-global coverage (all landmasses from -56° to 60° latitude). The gravity implied in the maps is a combination of satellite gravity, gravity as given by EGM2008 (Pavlis et al. 2012) and forward modelled topographic gravity up to ultra-short scale. In the low to mid-range frequencies (degrees $0 \dots \sim 180$) the maps rely on a combination of ITG-GRACE (Mayer-Gürr et al. 2010) and GOCE (Pail et al. 2010) satellite information (equivalent to GOCE-TIM4 release). Gravity information from EGM2008 (Pavlis et al. 2012) supersedes the satellite-only information in the maps near degree 190. EGM2008 is dominant in the degrees $200 \dots 2190$. From degree 2160 up to degree $\sim 90,000$, corresponding to spatial scales ranging from ~ 10 km down to ~ 220 m, the maps rely on forward modelled topographic gravity. The forward modelling is achieved assuming a standard rock-density of 2670 kg/m^3 and applying residual terrain modelling (RTM) procedures (Forsberg 1984b) based (mainly) on topographic information of the Shuttle Radar Topography Mission (SRTM) (Farr et al. 2007). More information on the computation of the GGMplus maps can be found in Hirt et al. (2013). The maps can be accessed at <http://ddfe.curtin.edu.au/models/GGMplus/>.

We have chosen GGMplus maps of gravity disturbances (radial derivative of the disturbing potential) which provide the anomalous part of the gravity acceleration with a formal resolution of 0.1 microGal ($1 \mu\text{Gal} = 10^{-8} \frac{\text{m}}{\text{s}^2}$) for the evaluation with the 2D-DFT. In principal, other functionals, e.g. quasi-geoid heights, could be used likewise for the evaluation. However, topographic gravity signals at scales of 250 m might not be represented fully by the provided data resolution of 1 mm for quasi-geoid heights.

The maps come in $5^\circ \times 5^\circ$ sized tiles with an equi-angular grid sampling of 7.2 arc-seconds. Inserting the tile size in

Eq. (15) and the sampling in Eq. (16), yields a minimum and maximum retrievable degree of ~ 36 and $\sim 90,000$, respectively. Hence, both the 2D-DFT method and the data allow the approximation of power spectra of the topographic potential between degree 2160 and $\sim 90,000$.

The processing of the GGMplus tiles exactly follows the procedure of our closed loop test performed with tiles of the topographic potential model dV-SPH-RET2012 (Sect. 3.1), except for the tile size which is decreased to 2.5° . The smaller tile size allows finer selection of ocean and non-ocean tiles, thus taking into account more gravity data closer to the shore line, extending the landmasses covered by our analyses (see Fig. 10). The degree variances are computed for each single $2.5^\circ \times 2.5^\circ$ inland tile and then all tiles are averaged to obtain an approximation of the topographic potential degree variances over the landmasses of the Earth.

As a refinement, this is also done for different types of terrain: from low- to high elevated terrain. The terrain type is determined by means of the root-mean-square (RMS) over the heights in each tile. We will refer to this indicator as Terrain RMS in the following. The colour of the degree variances is linked to the class colour attributed to each class in Fig. 10 that visualises the spatial distribution of the tiles by Terrain RMS. Seven groups of terrain roughness are defined given by the following thresholds for the Terrain RMS: 0–250 m (1), 250–500 m (2), 500–750 m (3), 750–1000 m (4), 1000–2000 m (5), 2000–3000 m (6), > 3000 m (7). The latter class contains parts of the Andes and Himalaya mountains as highest elevated areas of Earth.

Any tile containing non-available numbers (i.e., cells 10 km or more apart from the coast line) is excluded from the computation, as gravity is not provided offshore in GGMplus. Alternatively, (1) ocean tiles could have been filled with zeros which would underestimate the spectral power, or (2) marine gravity from altimetry could be filled in, which, however, does not resolve the field much below 4 arc-min scales.

Our derived degree variance models are based on the functional model of the Sanso/Sideris-type model (Eq. 20), with the coefficients A and B estimated using our least-squares fitting procedure (Sect. 3.2). This model has been identified to approximate the computed degree variances best, based on the least-square fit residuals. The computed degree variances of the topographic potential are an approximation of the Earth's actual geopotential spectra due to several reasons:

- The forward modelling in GGMplus uses uniform rock-density; the actual gravitational attraction caused by the topographic masses might therefore be over- or underestimated in some places.
- The topographic heights used in the forward modelling are from the SRTM model which is not free of errors (see, e.g. Rexer and Hirt 2014).

- Approximation errors of the 2D-DFT method for the computation of degree variances with respect to rigorous spherical harmonic modelling (about 10–20 % in terms of degree variances, see Sect. 3, Fig. 5).
- Non-global coverage; GGMplus is limited to the land-masses in between -56° and 60° latitude while degree variances of the spherical harmonic representation are per se defined in a truly global sense.

We note that GGMplus gravity values and thus also the derived spectra represent the gravity at the Earth's surface (on top of the topography), and not at some reference body (ellipsoid or sphere).

4.2 Results

4.2.1 Degree variances and models

In this section degree variances estimated from GGMplus gravity maps are presented following the procedures described above.

The black curve in Fig. 11a illustrates the average degree variance of all 1502 $2.5^\circ \times 2.5^\circ$ tiles. The signal of all averages shows (1) the decay of the signal with rising degree and (2) strong oscillations towards the ultra-high frequencies. The oscillations stem from the tiling of the global grid in 2.5° tiles (c.f. Sect. 3). As explained above, the oscillations are of lower frequency and of higher amplitude the smaller the tiles are. The oscillations showed not to have negative impact on the fit. The coloured degree variance curves in Fig. 11a reflect the average degree variances in our seven different classes of terrain. With this classification we can give estimates for the gravitational power of the topographic masses on small scales as a function of the terrain's elevation. The variances confirm that the higher the Terrain RMS (meaning: the larger the amount of the topographic masses) the higher the gravitational signal (meaning: higher variability of attraction). In addition, by grouping the tiles by the STD of the elevation instead of by RMS, we may say that the rougher the terrain (meaning: the more mountainous) the higher the gravitational signal, and the flatter the terrain the lower the gravitational signal (results not shown here in detail).

Fitting curves to the computed degree variances using the functional model of the Sanso/Sideris-type degree variance model (Eq. 20) yields the curves in Fig. 11b, with the (individual) model coefficients A and B reported in Table 3. Note that the values in the degree range $0 \dots 2160$ are extrapolations for the seven terrain class models, as the models are fitted from computed degree variances starting at degree 2160. The degrees below 2160 were neglected because the focus of this study lies upon the very high frequencies and including the lower degrees leads to a poorer fit in the upper part of the spectrum.

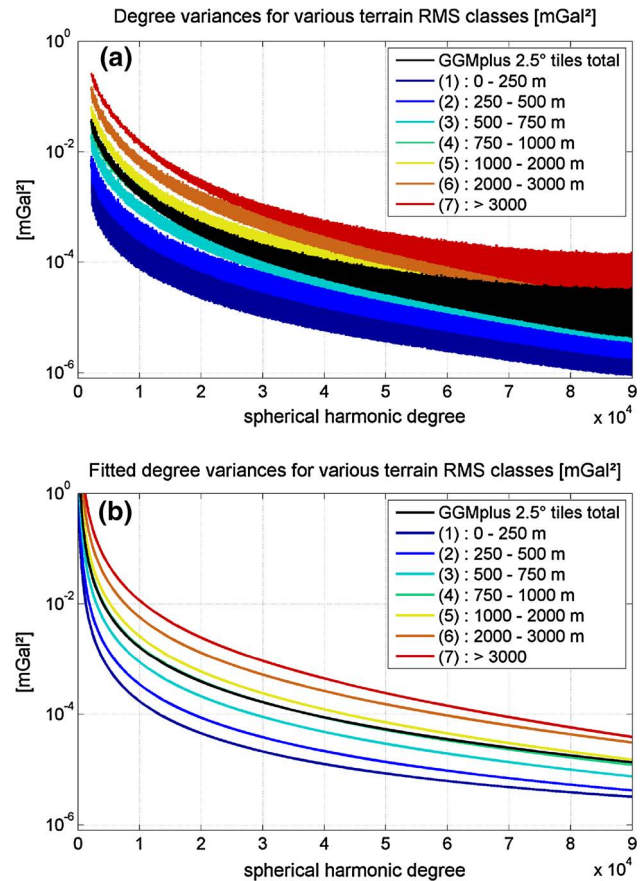


Fig. 11 Resulting GGMplus degree variances (total average : black line); **a** class averages of the degree variances computed in each tile by 2D-DFT; **b** fitted degree variance curves for each class by means of a best fitting Sanso/Sideris-type model (Eq. 20)

The fitted curves provide a clearer picture of the signal power at all scales. As expected, the average over all tiles (black curve) is found in the middle of the other curves, close to the equivalent of tiles with Terrain RMS of around 750 m.

4.2.2 Omission errors from computed degree variance models

Omission errors in physical geodesy denote the error associated with the truncation of the infinite series (of spherical harmonic functions) at some maximum degree. Degree variances calculated from degree variance models may easily be transformed into omission errors. The error ε_{OM} is defined as the sum over all squared spherical harmonic coefficients CS_{lm}^2 of degree $l > l_{max}$ and thus may be written as

$$\varepsilon_{OM} = \sum_{l=l_{max}+1}^{\infty} \sum_{m=-l}^l CS_{lm}^2 = \sum_{l=l_{max}+1}^{\infty} c_l^2. \quad (27)$$

In Table 4 the omission errors for three different truncation degrees ($l_{max} = 2160, 10,800, 21,600$) of popular degree variance models and of degree variance models computed

Table 3 Coefficients *A* and *B* of Sanso/Sideris-type degree variance models (Eq. 20) as estimated for different spherical harmonic potential models and for GGMplus gravity tiles via 2D-DFT. The degree variances c_l^2 , received when evaluated with Eq. (20), are dimensionless ($\Psi = 1$)

Source of degree variances	Valid for degrees	Number of tiles used	SS-type model	A	B
Sanso and Sideris (2013)—EGM2008	0...2160	—	Original	3.9e-8	0.999443
EGM2008 @ ellipsoid (corrected Sanso and Sideris model)	3...2160	—	This work	5.0e-8	0.999845
dV-ELL-RET2012 @ ellipsoid	3...2160	—	This work	8.69e-8	0.999528
dV-SPH-RET2012 @ sphere	3...2160	—	This work	9.65e-8	1.000475
GGMplus Tr 2.5°—all land tiles @ topography	4 ...90,000	1502	This work	1.79e-7	0.999995
GGMplus Tr 2.5°—only land: Terrain RMS 1	2160 ...90,000	330	This work	1.69e-8	1.0000053
GGMplus Tr 2.5°—only land: Terrain RMS 2	2160 ...90,000	408	This work	3.62e-8	0.9999997
GGMplus Tr 2.5°—only land: Terrain RMS 3	2160 ...90,000	221	This work	9.62e-8	0.9999953
GGMplus Tr 2.5°—only land: Terrain RMS 4	2160 ...90,000	143	This work	1.91e-7	0.9999931
GGMplus Tr 2.5°—only land: Terrain RMS 5	2160 ...90,000	291	This work	2.98e-7	0.9999905
GGMplus Tr 2.5°—only land: Terrain RMS 6	2160 ...90,000	49	This work	6.67e-7	0.9999895
GGMplus Tr 2.5° only land: Terrain RMS 7	2160 ...90,000	60	This work	1.42e-7	0.9999837

from the different GGMplus spectra are listed. The omission error here is evaluated up to degree 90,000 (and not up to infinity) in terms of gravity disturbances and geoid heights.

4.3 Interpretation and discussion of results

When comparing our degree variances to the spherical harmonic spectra of global geopotential models (or common degree variance models), we keep in mind that

- (a) for degrees higher than 2160, the computed degree variances reflect only the gravitational signal implied by the topographic masses,
- (b) our degree variances are not truly global (although represented in spherical harmonic domain) and
- (c) the degree variances represent gravity on top of the topography and not directly at any reference surface (e.g. a sphere or an ellipsoid). This makes our degree variances “incompatible” to those from global spherical harmonic models, which represent gravity downward-continued to some reference surface. Downward-continuation of the GGMplus gravity with procedures described in Pavlis et al. (2012) would make the spectra more mutually compatible, however this remains as a future task.

It was shown in Sect. 3.3.1 that (b) leads to an overestimation (as poles and oceans are excluded) and (c) to an underestimation of the power spectrum. Our calculated degree variances contain a mixture of both effects. This in turn suggests how the presented degree variances (models) are to be interpreted and used: they reflect the signal of the topography-implied gravity field over the continental landmasses, as sensed directly at its surface (the topography). Due to the generation procedure our degree variances are close to spherical approximations of the topographic potential, i.e. the underlying reference surface is a sphere (see Fig. 7).

As the central result of our study Fig. 12 shows the fitted GGMplus-based degree variances (solid red line) together with spectra of other selected degree variance models (Kaula, Tscherning/Rapp, Sanso/Sideris), and directly computed spectra from the spherical harmonic model coefficients (EGM2008, and of topographic potential models dV-SPH-RET2012 and dV-ELL-RET2012). For comparison purposes, the 2D-DFT recovered spectra from dV-SPH-RET2012 gravity (evaluated at the topography, over continental 5° × 5° sized tiles within ±60° latitude only, which is comparable to the GGMplus data area) is shown (dashed blue line). From Fig. 12, the models clearly group into ellipsoidal approximation (EGM2008, dV-ELL-RET2012, Sanso/Sideris) and spherical approximation (dV-SPH-RET2012, Kaula, Tscherning/Rapp). The latter sets of degree variances have somewhat more power

Table 4 Omission error from topographic potential degree variances (based on spherical approximation) computed in this study from GGMplus tiles and from popular degree variance models for various degree ranges in terms of geoid heights (m) and gravity disturbances (mGal)

Degree variance model	Underlying data		Omission error degree range (degree of truncation)			
	(mGal)	(cm)	(mGal)	(cm)	(mGal)	(cm)
Kaula: c_K^2	23.93	2.64	18.05	0.52	14.81	0.26
Tscherning/Rapp: $c_{T\ Rapp}^2$	11.18	2.31	1.17	0.06	0.11	$\sim 3e-3$
Sanso/Sideris: c_{SS}^2	1.38	0.32	0.03	$\sim 2e-3$	$\sim 9e-4$	$\sim 2e-5$
Corrected Sanso/Sideris: c_{SS}^2	3.12	0.64	0.56	0.02	0.12	$\sim 3e-3$
This work (average of all 2.5° tiles, all types of terrain)	8.62	1.53	3.51	0.13	2.23	0.02
Terrain RMS = 0–250 m	2.77	0.48	1.23	0.04	0.84	0.01
Terrain RMS = 250–500 m	3.95	0.70	1.68	0.06	1.10	0.02
Terrain RMS = 500–750 m	6.33	1.13	2.59	0.10	1.64	0.03
Terrain RMS = 750–1000 m	8.83	1.58	3.54	0.14	2.21	0.04
Terrain RMS = 1000–2000 m	10.93	1.96	4.29	0.17	2.63	0.05
Terrain RMS = 2000–3000 m	16.31	2.94	6.35	0.25	3.87	0.08
Terrain RMS > 3000 m	23.31	4.24	8.66	0.34	5.06	0.11
Maximum values of all 2.5° tiles (located in the Himalayas)	38.13	7.51	14.9	0.62	9.11	0.2

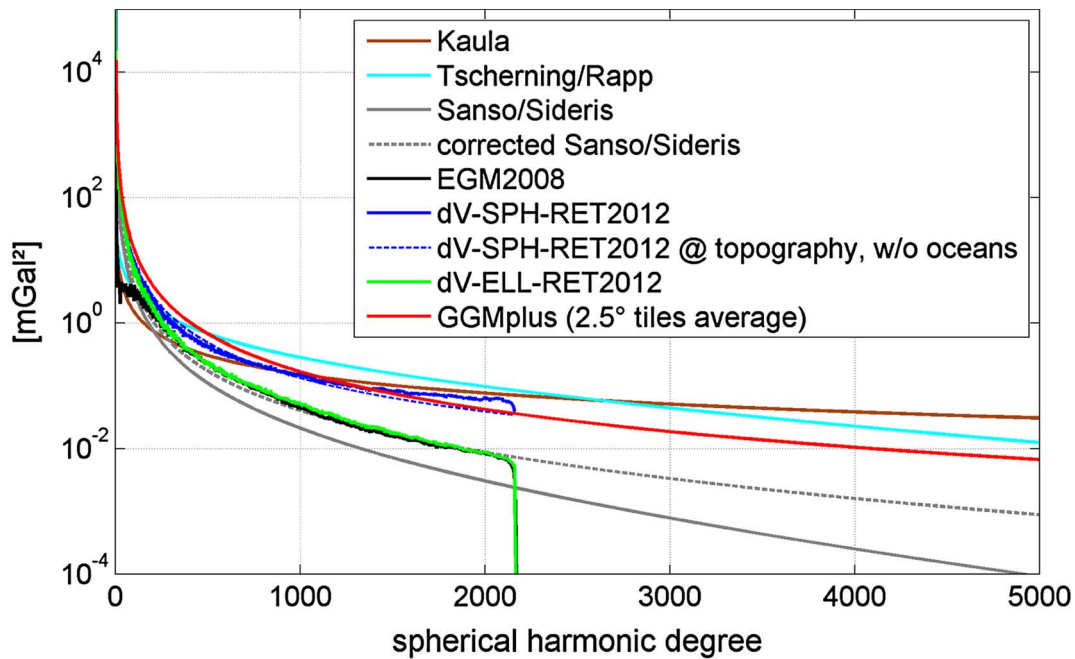


Fig. 12 Overview on computed GGMplus degree variances and selected well-known degree variances (from models) in terms of gravity disturbances (mGal^2); for degrees 0...5000

than those evaluated at the topography (GGMplus and dV-SPH-RET2012 at the topography).

4.3.1 GGMplus-based omission errors

Looking at the GGMplus-based omission errors (computed as averages over all 2.5° tiles) we find the signal strengths of omitted signals on the order of ~ 9 mGal for gravity (~ 1.5 cm for geoid effects) at scales of ~ 10 km, ~ 4 mGal (~ 1 mm) at scales of ~ 2 km and ~ 2 mGal (~ 0.2 mm) at scales of ~ 1 km. Our omission errors are lower than those of Kaula's rule and somewhat higher than those based on the Tscherning/Rapp (1974) degree variance model beyond degree 10,800 (Table 4).

4.3.2 Correction to Sanso and Sideris (2013)

The Sanso and Sideris (2013) degree variance model based on their numerical values $A = 3.9 \times 10^{-8}$ and $B = 0.999443$ (solid grey line) is shown in Fig. 12. This model is in clear disagreement with the EGM2008 spectrum. Instead, a least-squares fit of the EGM2008 degree variances is obtained with Sanso and Sideris' model along with coefficients $A = 5.0 \times 10^{-8}$ and $B = 0.999845$ (dashed grey line). We denote this as "corrected Sanso and Sideris model". Note that while the numerical coefficients listed in Sanso and Sideris (2013) are not correct, their figures and omission error estimates seem to be based on coefficients similar to our corrected model.

4.3.3 Ellipsoidal approximation underestimates omission errors

Importantly, the GGMplus omission error estimates are considerably larger than those based on EGM2008 spherical harmonic potential coefficients. Omission errors thus appear to be much underestimated in ellipsoidal approximation. For instance, the omission error beyond degree 2160 seemingly reduces from ~ 1.5 cm for GGMplus to ~ 0.6 cm (~ 0.3 cm) for the corrected (original) Sanso and Sideris model by virtue of the approximation level. This effect is much more pronounced for ultra-short scales, e.g., ~ 2.2 mGal (from GGMplus) versus ~ 0.12 mGal signal strength (corrected Sanso and Sideris model) beyond degree 21,600.

These results—to our understanding—show that the ellipsoidal approximation level of the spherical harmonic spectra is not compatible with the spherical computation of omission errors. This is corroborated by the observation that a ~ 0.6 cm geoid omission error for degree 2160 expansions is in contrast to practical results from omission error modelling (e.g., Jekeli et al. 2009; Hirt et al. 2010) showing this effect to be on the lower cm-level. Using models of spherical approximation type yields more realistic estimates of the short-scale spectral energy (e.g., Tscherning/Rapp: 2.3 cm, this work: 1.5 cm geoid signals) omitted by degree-2160 expansions. Another way to obtain realistic estimates of short-scale spectral energy would be to work entirely with ellipsoidal harmonics. The spectral energy of spherical harmonic models in spherical approximation is very close to the

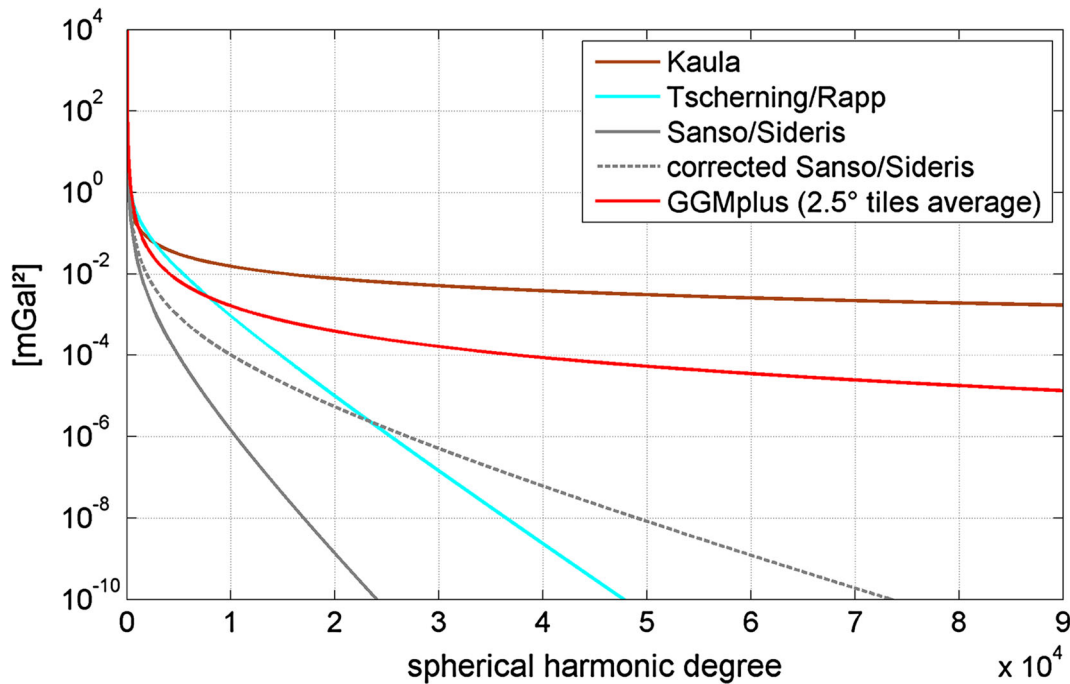


Fig. 13 Overview on computed GGMplus degree variances and selected well-known degree variances (from models) in terms of gravity disturbances (mGal^2)

energy of the truly ellipsoidal harmonic spectrum (compare, e.g. to Fig. 7, p. 24 in Pavlis et al. 2012).

On the other hand, EGM2008 represents truly global degree variances, while the GGMplus variances are only valid over land, where the gravity field power was shown to be larger than globally. As such, one would expect the true (albeit unknown) omission error to be somewhat lower than that derived from the GGMplus land data.

4.3.4 GGMplus-based omission errors for different types of terrain

Investigation of the omission error dependence on the Terrain RMS present in the tiles exhibits an increase in omission error with rising terrain elevation (Table 4). As expected, the error produced by the truncation of the spherical harmonic series at some degree >2160 in average is larger in regions of large topographic masses (Terrain RMS = 7) than in low elevated regions (Terrain RMS = 1). Although the gravity signal beyond degree $\sim 21,600$ becomes small ($\sim 2 \text{ mGal}$ and $< 1 \text{ mm}$) on average, there are regions on Earth where there is still significant contribution of topographic masses to the gravity signal. This can be concluded from the maximum omission error of all 1502 2.5° tiles per degree (bottom row in Table 4), which is found in the Himalayas (75°E – 77.5°E and 32.5°N – 35°N). The investigation of the maxima indicates that at scales less than $\sim 1 \text{ km}$ (degree 21,600) the omission

error can still be on the order of 9–10 mGal ($\sim 2 \text{ mm}$) over high elevated areas (bottom rows in Table 4).

4.3.5 Corroboration from dV-SPH-RET2012

The GGMplus degree variances are in close agreement with those from the topographic potential dV-SPH-RET2012 (2D-DFT recovered using a similar area as GGMplus) at short spatial scales and nearly coincide at degree 2160 (compare solid red and dashed blue lines in Fig. 13). The dashed blue line and the red line express signal strengths of the same gravity functional (gravity disturbances from topographic potential model evaluated at the top of the topography) and over the same region of Earth. Given that a large part of Earth's observed gravity field (i.e., GGMplus to degree 2160) is generated by the topographic masses at short scales, this good agreement between the 2D-DFT-recovered dV-SPH-RET2012 and GGMplus is within the expectations and indicates the consistency of our processing procedure.

4.3.6 Validation with Parseval's theorem

The validity of our processing is assessed by evaluating Parseval's theorem that states identical signal power in space and frequency domain and, hence, a lossless transformation between the domains (see, e.g. Papoulis 1984). Parseval's Theorem in our case can be written as

$$\sqrt{\int_0^{360} \int_{-90}^{90} |f(\varphi, \lambda)|^2 \cos \phi d\phi d\lambda} = \sqrt{\int_{n_{\min}}^{n_{\max}} c_n(l)^2 dl}, \quad (28)$$

where in our discrete case the left-hand side is equivalent to the root-mean-square of the function $f(\varphi, \lambda)$ (in space domain), here given on a grid, and the right-hand side corresponds to the omission error (in the frequency domain). From Hirt et al. (2014), Table 3 ibid, the total RMS of GGMplus gravity and geoid effects at spatial scales of ~ 10 km–220 m (where the model relies on topography-implied gravity only) is 1.6 cm in geoid height (10.59 mGal) in the space domain [left side of Eq. (28)]. This is in good agreement with the omission error from the 2D-DFT recovered GGMplus spectrum of 1.51 cm (8.62 mGal) from our computed degree variances for the degree range 2161...90,000 [right side of Eq. (28)]. The differences are less than 20 % (gravity) and below 10 % (geoid), which is commensurate with the approximation errors of the 2D-DFT method quantified in Sect. 3.

4.3.7 Comparison with classical degree variance models at ultra-short scales

Comparing all degree variance models in the short and the ultra-short wavelengths (Fig. 13) reveals strong divergence. This is not surprising as the classical degree variance models were developed based on long/medium-wavelength gravity data, so are extreme extrapolations in the ultra-high degrees. Beyond degree 8000 Kaula's rule shows the least decay, while the Tscherning/Rapp model indicate much faster decay of the gravity signal. The GGMplus-derived signal (representing continental, forward modelled gravity as synthesised on top of the topography) resides in between those of the classical models. Of all degree variance models in Fig. 13, it is only the GGMplus-based spectrum that is supported by gravity data (topography-implied) to ultra-fine scales of degree 90,000.

The extrapolation effect of the classical models at ultra-short scales is evident, e.g., from estimated omission errors beyond degree 21,600, where the Tscherning-Rapp model suggest 0.11 mGal gravity signal strengths which is a factor as large as 20 below those indicated by the GGMplus-based spectrum (2.2 mGal, cf. Table 4). Conversely, Kaula's rule significantly overestimates the gravity signal omission at these scales by a factor of 7 compared to GGMplus (cf. Table 4).

4.3.8 Comparison with literature results

Finally, comparing the estimated (spherical) omission errors from our new degree variance model (Table 4) with previous regional work we find our values in the same magnitude

range. Voigt and Denker (2007) have estimated the omission error from RTM gravity effects in three $1^\circ \times 1^\circ$ bins in Germany (German Alps, Harz and Franconia), representing rough and medium-elevated topographic areas. In those areas the omission error at degree 10,800 in terms of geoid heights ranges from 0.1 to 0.5 cm (this work: ~ 0.13 cm in average, ranging from 0.04 to 0.34 cm). For degree 21,600 their analyses yield a geoid RMS power of 0.0 to 0.1 cm (this work: ~ 0.045 cm in average, ranging from 0.01 to 0.1 cm).

5 Summary and outlook

This study started with some remarks on topographic gravity modelling and recapitulating the definition and meaning of degree variances and current degree variance models. For the approximation of signal powers of Earth's topographic potential from gridded gravitational field quantities in terms of degree variances we describe and investigate the 2D-DFT approach dating back to Forsberg (1984a) and Flury (2006) and discussed curve fitting based on the analytical functions of common degree variance models. Closed-loop experiments with the 2D-DFT approach on global scale revealed that

- (a) the approach can be used for recovery of degree variances with 10–20 % accuracy;
- (b) this holds true also for tiling of the global grid and consecutive averaging (and fitting) of the degree variances obtained in each tile;
- (c) the tiling and averaging leads to an oscillation of the signal around the original degree variance; the oscillation's frequency and magnitude are linked to the tile size;
- (d) the azimuth averaging procedure determines the smoothness and the spectral resolution of the computed degree variances.

As key result of this work, we applied the 2D-DFT procedure to GGMplus gravity maps, yielding a new degree variance model for gravity signal strengths at the surface of the topography:

$$c_{\text{GGMplus}}^2(l) = \frac{1.79 \cdot 10^{-7} \cdot (0.999995)^l}{(l-1)(l-2)(l+4)(l+17)} \quad (29)$$

This model is supported by about 3 billion points of GGMplus topography-implied gravity effects at spatial scales of 10 km to 220 m over all land areas where SRTM data is available. The model is thus defined for harmonic degrees up to 90,000 and allows for estimates of omission errors that are in the order of ~ 9 mGal (~ 1.5 cm) at scales of ~ 10 km (degree 2160 truncations), and ~ 3.5 mGal (~ 1 mm) at scales of ~ 2 km (degree 10,800 truncations). The approximation

errors caused by the 2D-DFT procedure (instead of rigorous spherical harmonic modelling) was found to be 20 % or less.

In comparison to degree variance models fitted to spectra of spherical harmonic coefficients/ geopotential models, the model in Eq. (29) has two major differences that make it incompatible to those (apart from the fact that the input GGMplus gravity data are not truly global).

First, it does not describe signal strengths of gravity downward-continued (amplified) to some reference surface (which is the case in spherical harmonic models of the topographic and gravitational potential). Instead, our new degree variance model describes gravity signal strengths as found at the surface of the topography. This is compatible with signal strengths of (unreduced in the sense of not continued) terrestrial gravity field observations and represents a more natural way for describing short-scale signal characteristics.

Second, the new degree variance model reflects a spherical approximation of the field-generating masses. It is thus not compatible with spherical harmonic degree variance models from geopotential models that reflect the field generating masses to be—in good approximation—ellipsoidal. Importantly, degree variance models relying on ellipsoidal approximation were shown to underestimate the spectral energy of gravity at short spatial scales. They, therefore, lead to unrealistically small omission errors. In this context an empirical rule has been developed to transform spherical harmonic spectra between spherical and ellipsoidal approximation. The spherical harmonic spectrum in spherical mass approximation is found to be very close to a truly ellipsoidal harmonic spectrum.

While building upon approximations and assumptions, it is hoped that the new GGMplus-based degree variance model provides an improved description of the Earth's gravity spectrum to ultra-fine spatial scales. Refining the chosen 2D-DFT approach through a more sophisticated estimation of the localized power spectrum, e.g. by multitaper spectral methods/Slepian tapers (e.g. Dahlen and Simons 2008; Szücs et al. 2014) and a more rigorous analysis of approximation errors warrant future research. It is also likely that in the next years spherical harmonic analysis procedures will be used up to ultra-short scales, yielding further improved estimates of the signal power at those scales in a truly global manner.

Acknowledgments With the support of the Technische Universität München—Institute for Advanced Study, funded by the German Excellence Initiative. We thank the Australian Research Council for funding via Grant DP120102441. We thank Roland Pail for sharing his knowledge on Fourier transforms, Reiner Rummel for directing us to Parseval's theorem, and Sten Claessens for the discussions related to degree variances. We are grateful for very constructive and thorough reviews received from four anonymous reviewers, improving the clarity of presentation and stimulating future research.

References

- Abyrkosov O, Förste C, Gruber C, Shako R, Barthelmes F (2012) Harmonic analysis of the DTU10 global gravity anomalies. In: Abbasi A, Giesen N (eds) EGU General Assembly Conference Abstracts, EGU General Assembly Conference Abstracts, vol 14, p 4945
- Balmino G, Vales N, Bonvalot S, Briais A (2012) Spherical harmonic modelling to ultra-high degree of Bouguer and Isostatic anomalies. *J Geod* 86(7):499–520. doi:10.1007/s00190-011-0533-4
- Claessens S, Hirt C (2013) Ellipsoidal topographic potential—new solutions for spectral forward gravity modelling of topography with respect to a reference ellipsoid. *J Geophys Res* 118(11):5991–6002. doi:10.1002/2013JB010457
- Dahlen FA, Simons FJ (2008) Spectral estimation on a sphere in geophysics and cosmology. *Geophys J Int* 147:774–807. doi:10.1111/j.1365-246X.2008.03854.x
- Farr T, Rosen P, Caro E, Crippen R, Duren R, Hensley S, Kobrick M, Paller M, Rodriguez E, Roth L, Seal D, Shaffer S, Shimada K, Umland J, Werner M, Oskin M, Burbank D, Alsdorf D (2007) The Shuttle Radar Topography Mission. *Rev Geophys* 45(RG2004). doi:10.1029/2005RG000183
- Flury J (2006) Short-wavelength spectral properties of the gravity field from a range of regional data sets. *J Geod* 79:624–640. doi:10.1007/s00190-005-0011-y
- Forsberg R (1984a) Local covariance functions and density distribution. OSU Report 356, Ohio State University
- Forsberg R (1984b) A study of terrain reductions, density anomalies and geophysical inversion methods in gravity field modelling. OSU Report 355, Ohio State University
- Grombein T, Luo X, Seitz K, Heck B (2014) A wavelet-based assessment of topographic-isostatic reductions for GOCE gravity gradients. *Surv Geophys* 1–24. doi:10.1007/s10712-014-9283-1
- Gruber C, Abrikosov O (2014) High resolution spherical and ellipsoidal harmonic expansions by Fast Fourier Transform. *Studia Geophysica et Geodaetica* 58. doi:10.1007/s11200-013-0578-3 (online first)
- Heller W, Jordan S (1976) A new self-consistent statistical gravity field model. In: *Eos Trans. AGU Fall Meeting, San Francisco*, vol 75, p 895
- Hirt C (2012) Efficient and accurate high-degree spherical harmonic synthesis of gravity field functionals at the Earth's surface using the gradient approach. *J Geod* 86(9):729–744. doi:10.1007/s00190-012-0050-y
- Hirt C, Kuhn M (2012) Evaluation of high-degree series expansions of the topographic potential to higher-order powers. *J Geophys Res Solid Earth* 117. doi:10.1029/2012JB009492
- Hirt C, Kuhn M (2014) A band-limited topographic mass distribution generates a full-spectrum gravity field—gravity forward modelling in the spectral and spatial domain revisited. *J Geophys Res Solid Earth* 119. doi:10.1002/2013JB010900
- Hirt C, Kuhn M, Claessens SJ, Pail R, Seitz K, Gruber T (2014) Study of the Earth's short-scale gravity field using the ERTM2160 gravity model. *Comput Geosci* 73:71–80. doi:10.1016/j.cageo.2014.09.00
- Hirt C, Featherstone W, Marti U (2010) Combining EGM2008 and SRTM/DTM2006.0 residual terrain model data to improve quasi-geoid computations in mountainous areas devoid of gravity data. *J Geod* 84(9):557–567. doi:10.1007/s00190-010-0395-1
- Hirt C, Claessens S, Fecher T, Kuhn M, Pail R, Rexer M (2013) New ultra-high resolution picture of Earth's gravity field. *Geophys Res Lett* 40(16):4279–4283. doi:10.1002/grl.50838
- Holmes S, Pavlis N (2008) EGM Harmonic Synthesis Software. National Geospatial-Intelligence Agency. <http://earth-info.nga.mil/GandG/wgs84/gravitymod/newegm/newegm.html>

- Jekeli C (1978) An investigation of two models for the degree variances of global covariance functions. OSU report 275, Department of Geodetic Science, Ohio State University
- Jekeli C, Yanh HJ, Kwon JH (2009) Evaluation of EGM08—globally and locally in South Korea. *Newton's Bull* 38–49
- Jekeli C (2010) Correlation modeling of the gravity field in classical geodesy. In: Freedon W, Nashed M, Sonar T (eds) *Handbook of the Geomathematics*. Springer, Berlin Heidelberg. doi:10.1007/978-3-642-01546-528
- Kaula W (1966) Theory of satellite geodesy. Blaisdel, Waltham
- Kuhn M, Seitz K (2005) Comparison of Newton's integral in the space and frequency domains. In: Sanso F (ed) *A window on the Future of Geodesy—IAG Symposia*, vol 128, pp 386–391
- Mayer-Gürr T, Kurtenbach E, Eicker A (2010) ITG-Grace2010 gravity field model. www.igg.unibonn.de/apmg/index.php?id=itg-grace2010
- Moritz H (1977) On the computation of a global covariance model. OSU 255, Department of Geodetic Science, Ohio State University
- Moritz H (2000) Geodetic reference system 1980. *J Geod* 74(1):128–162. doi:10.1007/s001900050278
- Novak P (2010) Direct modelling of the gravitational field using harmonic series. *Acta Geodyn Geomater* 7(1):35–47
- Pail R, Goiginger H, Mayrhofer R, Schuh WD, Brockmann JM et al (2010) GOCE gravity field model derived from orbit and gradiometry data applying the Time-Wise Method. *Proc ESA Living Planet Symp* 28 June–2 July (ESA SP-686)
- Pail R, Bruinsma S, Migliaccio F, Förste C, Goiginger H, Schuh WD, Höck E, Reguzzoni M, Brockmann JM, Abrikosov O, Veicherts M, Fecher T, Mayrhofer R, Krasbutter I, Sanso F, Tscherning CC (2011) First GOCE gravity field models derived by three different approaches. *J Geod* 85(11):819–843. doi:10.1007/s00190-011-0467-x (special issue: “GOCE - The Gravity and Steady-state Ocean Circulation Explorer”)
- Papoulis A (1984) *Signal analysis*. McGraw-Hil Book Company
- Pavlis NK, Rapp RH (1990) The development of an isostatic gravitational model to degree 360 and its use in global gravity modelling. *Geophys J Int* 100:369–378. doi:10.1111/j.1365-246X.1990.tb00691.x
- Pavlis N, Factor J, Holmes S (2007) Terrain-related gravimetric quantities computed for the next EGM. In: Dergisi H (ed) *Proceedings of the 1st International Symposium of the International Gravity Field Service*, vol 18, pp 318–323
- Pavlis N, Holmes S, Kenyon S, Factor J (2012) The development and evaluation of the Earth Gravitational Model 2008 (EGM2008). *J Geophys Res* 117. doi:10.1029/2011JB008916
- Rexer M, Hirt C (2014) Comparison of free high resolution digital elevation data sets (ASTER GDEM2, SRTM v2.1/v4.1) and validation against accurate heights from the Australian National Gravity Database. *Aust J Earth Sci* 1–15. doi:10.1080/08120099.2014.884983. <http://www.tandfonline.com/doi/abs/10.1080/08120099.2014.884983>
- Rummel R, Rapp R, Sünkel H, Tscherning C (1988) Comparisons of global topographic/isostatic models to the Earth's observed gravity field. OSU report 388, Ohio State University
- Sanso F, Sideris M (2013) *Geoid determination—Lecture Notes in Earth Sciences*, vol 110 (chap Harmonic Calculus and Global Gravity Models). Springer, Berlin Heidelberg
- Sneeuw N (1994) Global spherical harmonic analysis by least-squares and numerical quadrature methods in historical perspective. *Geophys J Int* 118(3):707–716. doi:10.1111/j.1365-246X.1994.tb03995.x
- Szücs E, Papp G, Benedek J (2014) A study of different wavelength spectral components of the gravity field derived from various terrestrial data sets. *Acta Geodaetica et Geophysica*. doi:10.1007/s40328-014-0061-9 (online first)
- Tapley BD, Bettadpur S, Watkins M, Reigber C (2004) The gravity recovery and climate experiment: mission overview and early results. *Geophys Res Lett* 31:L09607. doi:10.1029/2004GL019920
- Torge W (2001) *Geodesy*, 3rd edn. Walter de Gruyter
- Tscherning C, Rapp R (1974) Closed covariance expressions for gravity anomalies, geoid undulations, and deflections from the vertical implied by anomaly degree variance models. OSU report 208, Ohio State University
- Vassiliou A, Schwarz K (1987) Study of the high-frequency spectrum of the anomalous potential. *J Geophys Res* 92(B1):609–617
- Voigt C, Denker H (2007) A study of high frequency terrain effects in gravity field modelling. In: Dergisi H (ed) *1st International Symposium of the International Gravity Field Service*, “Gravity Field of the Earth”, Ankara, Turkey, vol 18, pp 342–347
- Wenzel H, Arabelos D (1981) Zur Schätzung von Anomalie-Gradvarianzen aus lokalen empirischen Kovarianzfunktionen. *Zeitschrift für Vermessungswesen* 106:234–243

P.2 Publication II: Earth2014: 1' shape, topography, bedrock and ice-sheet models - Available as gridded data and degree 10,800 spherical harmonics

Reference:

Hirt C., Rexer M.: Earth2014: 1' shape, topography, bedrock and ice-sheet models - Available as gridded data and degree 10,800 spherical harmonics; International Journal of Applied Earth Observation and Geoinformation, Vol. 39, pp 103-112, Elsevier, DOI: 10.1016/j.jag.2015.03.001, 2015

Copyright

This work originally has been published in International Journal of Applied Earth Observation and Geoinformation. The copyright has been transferred to Elsevier.

Short Summary

Gravity forward-modelling at high-resolution and other geodetic/geophysical techniques require reliable and densely sampled digital elevation models of Earth's topographic masses. The herein created model named Earth2014 is the most up-to-date global topographic model at 1 arc-min resolution, providing topography, ice-sheet, bedrock and shape geometries. Compared to ETOPO1, Earth2014 includes latest observations and models over Antarctica, Greenland and parts of the ocean. The different layers were expanded into series of surface spherical harmonic coefficients complete up to degree 10,800, allowing to study the spectral short-scale properties of Earth's different layer boundaries. For each set of coefficients a degree variance model has been parametrized. Earth2014 is freely available to the community.

Declaration of own contribution

(MR: Moritz Rexer; CH: Christian Hirt)

CH had the idea to Earth2014 and designed the entire study. CH contributed the largest share of numerical results, e.g. combination of different data sources. MR performed the harmonic analysis of the boundary functions (the Earth2014 layers BED, TBI, SUR, ICE and RET) to d/o 10,800. Additionally, MR fitted degree variance models to the spectra of all Earth2014 layers. CH is responsible for most of the interpretations and drafted most of the text. MR drafted the text to sections 3.3 and 4.2, created Fig. 5 and Table 3, while the remaining tables and figures were created by CH.

The overall own contribution of MR for P-II is estimated at 15 %, which is the (rounded) average value of the percentage values estimated for the six criteria listed in the table below (Tab. P.2).

Criteria	Estimated own contribution
Computation and results	20 %
Ideas and study design	0 %
Analysis and interpretation	10 %
Text	15 %
Figures	16 %
Tables	25 %
Total	14.3 %

Tab. P.2 – Criteria and estimated contribution share of Moritz Rexer for P-II

Confirmation by the First-Author

I hereby confirm the correctness of the declaration of own contribution by Moritz Rexer for the publication:

Hirt C., Rexer M.: Earth2014: 1' shape, topography, bedrock and ice-sheet models - Available as gridded data and degree 10,800 spherical harmonics; International Journal of Applied Earth Observation and Geoinformation, Vol. 39, pp 103-112, Elsevier, DOI: [10.1016/j.jaq.2015.03.001](https://doi.org/10.1016/j.jaq.2015.03.001), 2015.

Christian Hirt

Institut für Astronomische und Physikalische Geodäsie, Technische Universität München, Germany.

Signature: Christian Hirt Date: 27/01/2017

P.3 Publication III: Ultra-high-Degree Surface Spherical Harmonic Analysis Using the Gauss-Legendre and the Driscoll/Healy Quadrature Theorem and Application to Planetary Topography Models of Earth, Mars and Moon

Reference:

Rexer M., Hirt C.: Ultra-high-Degree Surface Spherical Harmonic Analysis Using the Gauss-Legendre and the Driscoll/Healy Quadrature Theorem and Application to Planetary Topography Models of Earth, Mars and Moon; *Surveys in Geophysics*, Vol. 36, Nr. 6, pp 803-830, Springer Netherlands, ISSN (Online) 0169-3298, DOI: 10.1007/s10712-015-9345-z, 2015.

Copyright

This work originally has been published in *Surveys in Geophysics*, available at <http://link.springer.com/>, and is reprinted here with permission of Springer. Copyright has been transferred to Springer Netherlands.

Short Summary

The quadrature theorems based on Driscoll/Healy (DH) and Gauss-Legendre (GL) weights are suitable candidates for high resolution spherical harmonic modelling, since they allow exact transforms and are efficient due to employing Fast Fourier Transforms (FFT). It is shown how numerical underflow/overflow occurring in the computation of the associated Legendre Functions (ALFs) can be avoided using arithmetically extended numbers (so called X-numbers) and how computation times can be reduced to acceptable level by parallelisation (parallel computing) of certain analysis steps. Both investigated quadrature techniques provide high accuracy up to some 10,000s of degrees. The GL quadrature is preferred in terms of computation times. The application of the techniques is demonstrated by harmonic analyses of the topographic functions of Earth up to degree 43,200, Mars up to degree 23,040 and Moon up to degree 46,080 as needed e.g. for high-resolution spectral gravity forward-modelling.

Declaration of own contribution

(MR: Moritz Rexer; CH: Christian Hirt)

MR had the idea to demonstrate high-resolution spherical harmonic analysis by quadrature and CH had the idea to test the procedures with planetary topography models. MR and CH mutually designed the study. MR developed the software and computed all numerical results. The analysis and interpretation of the results originate from MR and were improved by discussions with CH. MR drafted the entire text and created all figures and tables in the paper.

The overall own contribution of MR for P-III is estimated at 90 %, which is the (rounded) average value of the percentage values estimated for the six criteria listed in the table below (Tab. P.3).

Criteria	Estimated own contribution
Computation and results	100 %
Ideas and study design	50 %
Analysis and interpretation	90 %
Text	90 %
Figures	100 %
Tables	100 %
Total	88.3 %

Tab. P.3 – Criteria and estimated contribution share of Moritz Rexer for *P-III*


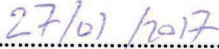
Confirmation by the Co-Author

I hereby confirm the correctness of the declaration of own contribution by Moritz Rexer for the publication:

Rexer M., Hirt C.: Ultra-high-Degree Surface Spherical Harmonic Analysis Using the Gauss-Legendre and the Driscoll/Healy Quadrature Theorem and Application to Planetary Topography Models of Earth, Mars and Moon; Surveys in Geophysics, Vol. 36, Nr. 6, pp 803-830, Springer Netherlands, ISSN (Online) 0169-3298, DOI: [10.1007/s10712-015-9345-z](https://doi.org/10.1007/s10712-015-9345-z), 2015.

Christian Hirt

Institut für Astronomische und Physikalische Geodäsie, Technische Universität München, Germany.

Signature:  Date: 

Ultra-high-Degree Surface Spherical Harmonic Analysis Using the Gauss–Legendre and the Driscoll/Healy Quadrature Theorem and Application to Planetary Topography Models of Earth, Mars and Moon

Moritz Rexer^{1,2} · Christian Hirt^{1,2,3}

Received: 3 July 2015 / Accepted: 3 October 2015
© Springer Science+Business Media Dordrecht 2015

Abstract In geodesy and geophysics, spherical harmonic techniques are popular for modelling topography and potential fields with ever-increasing spatial resolution. For ultra-high-degree spherical harmonic modelling, i.e. degree 10,000 or more, classical algorithms need to be extended to avoid under- or overflow problems associated with the computation of associated Legendre functions (ALFs). In this work, two quadrature algorithms—the Gauss–Legendre (GL) quadrature and the quadrature following Driscoll/Healy (DH)—and their implementation for the purpose of ultra-high (surface) spherical harmonic analysis of spheroid functions are reviewed and modified for application to ultra-high degree. We extend the implementation of the algorithms in the SHTOOLS software package (v2.8) by (1) the X-number (or Extended Range Arithmetic) method for accurate computation of ALFs and (2) OpenMP directives enabling parallel processing within the analysis. Our modifications are shown to achieve feasible computation times and a very high precision: a degree-21,600 band-limited (=frequency limited) spheroid topographic function may be harmonically analysed with a maximum space-domain error of 3×10^{-5} and 5×10^{-5} m in 6 and 17 h using 14 CPUs for the GL and for the DH quadrature, respectively. While not being inferior in terms of precision, the GL quadrature outperforms the DH algorithm in terms of computation time. In the second part of the paper, we apply the modified quadrature algorithm to represent for—the first time—gridded topography models for Earth, Moon and Mars as ultra-high-degree series expansions comprising more than 2

✉ Moritz Rexer
m.rexer@tum.de

Christian Hirt
c.hirt@tum.de

¹ Institute for Astronomical and Physical Geodesy, Technische Universität München, Arcisstrasse 21, 80333 Munich, Germany

² Institute for Advanced Study, Technische Universität München, Lichtenbergstr. 2 a, 85748 Garching, Germany

³ Western Australian Geodesy Group, Department of Spatial Sciences, The Institute for Geophysical Research, Curtin University of Technology, GPO Box U1987, Perth, WA 6845, Australia

billion coefficients. For the Earth's topography, we achieve a resolution of harmonic degree 43,200 (equivalent to ~ 500 m in the space domain), for the Moon of degree 46,080 (equivalent to ~ 120 m) and Mars to degree 23,040 (equivalent to ~ 460 m). For the quality of the representation of the topographic functions in spherical harmonics, we use the residual space-domain error as an indicator, reaching a standard deviation of 3.1 m for Earth, 1.9 m for Mars and 0.9 m for Moon. Analysing the precision of the quadrature for the chosen expansion degrees, we demonstrate limitations in the implementation of the algorithms related to the determination of the zonal coefficients, which, however, do not exceed 3, 0.03 and 1 mm in case of Earth, Mars and Moon, respectively. We investigate and interpret the planetary topography spectra in a comparative manner. Our analysis reveals a disparity between the topographic power of Earth's bathymetry and continental topography, shows the limited resolution of altimetry-derived depth (Earth) and topography (Moon, Mars) data and detects artefacts in the SRTM15 PLUS data set. As such, ultra-high-degree spherical harmonic modelling is directly beneficial for global inspection of topography and other functions given on a sphere. As a general conclusion, our study shows that ultra-high-degree spherical harmonic modelling to degree $\sim 46,000$ has become possible with adequate accuracy and acceptable computation time. Our software modifications will be freely distributed to fill a current availability gap in ultra-high-degree analysis software.

Keywords Spherical harmonic analysis · Quadrature · Gauss–Legendre · Driscoll/Healy · Topography · Digital elevation model · Earth · Mars · Moon

1 Introduction

1.1 Motivation

The application of spherical harmonic modelling has a long tradition in Earth and planetary sciences such as geodesy and geophysics (see e.g., Sneeuw 1994; Wieczorek 2007; Balmino et al. 2012; Wieczorek 2015). The representation of a function (e.g., gravity field functionals, topography and magnetic field strength) on a spheroid planet in spherical harmonics (SH) can be used to (1) explore the spectral constituents of a global function (e.g., through global power spectral densities), (2) spherical harmonic modelling [e.g., combination of satellite data and/with terrestrial data (Pail et al. 2011)], (3) enable transforms in the spectral domain [e.g., spectral forward modelling of the topographic potential (Claessens and Hirt 2013)] or (4) to interpolate between discrete points. The two mathematical processes to expand a function in the spatial domain into spherical harmonics, i.e. spherical harmonic coefficients (SHCs), and vice versa are known as the spherical harmonic analysis (SHA) and the spherical harmonic synthesis (SHS), respectively.

Today, many space-borne observation techniques are delivering high-resolution global data sets (i.e. 10 m to a few hundreds of metres in terms of global topographic data sets: TanDEM-X (Bartusch et al. 2008) surveyed the Earth with 12-m resolution, and LOLA (Smith et al. 2010) surveyed the Moon with up to 30-m resolution). Further, there is an environmentally and politically driven growing demand for geophysical and environmental modelling. In consequence, the requirements for spherical harmonic computations concerning (1) spatial resolution, (2) numerical accuracy and (3) computational aspects such as

memory and computation times steadily increase. For ultra-high-degree (i.e. spherical harmonic degrees of 10,800 and beyond) spherical harmonic synthesis, free software has become available with the MATLAB-based GrafLab by Bucha and Janák (2013). However, as far as the ultra-high-degree SHA is concerned, there is a demand to review the existing SHA methods, eventually providing suitable SHA algorithms and software with ultra-high-degree capability to the scientific community.

1.2 Past Work

The fast Fourier technique (FFT) (Walker 1996) for spherical harmonic analysis is a method of choice as it allows efficient evaluation of integrals in the frequency domain (with transformations between spatial and frequency domain). The most important prerequisite for the FFT is that the data are sampled on a regularly arranged grid. In general, a spherical harmonic analysis using FFT can be performed by numerical integration (=quadrature) following certain sampling theorems or by least-squares (LSQ) techniques (Sneeuw 1994). The advantage of the latter is that it is the only SHA technique that allows stochastic modelling and hence is capable of delivering variance–covariance information for the estimated spherical harmonic parameters. The major drawback of the LSQ technique is that for ultra-high spherical harmonic degrees, the normal equations become extremely large and require large-scale computational resources for its inversion [see e.g., Fecher et al. (2013)]. In comparison, quadrature techniques are more efficient to handle, as they usually (only) require a number fast Fourier transforms and series expansions (see also Sect. 2.1).

The theoretical foundations and derivations of quadrature techniques for SHA are well known. For a sound overview on most common methods and related literature, see Sneeuw 1994; Claessens 2006; Driscoll and Healy 1994. Few works exist on the implementation of ultra-high-resolution spherical harmonic analysis techniques. Recently, some works were published that comprise spherical harmonic computations up to degree 10,800 at maximum (Gruber et al. 2011; Abrykosov et al. 2012; Balmino et al. 2012), which is the lower limit of the degree range taken into consideration in this work.

In Balmino et al. (2012), 1 arc-min topography is analysed “by a standard quadrature method applied to $1' \times 1'$ equiangular mean values, and accelerated by the Longitude Recursion-Partial Sums algorithm”. Numerical stability of the computed integrals of associated Legendre functions (ALFs) above degree and order (d/o) 2700 is achieved by the authors by multiple application of a normalization factor which prevents overflow with respect to the IEEE limitations on real numbers (Balmino et al. 2012). Abrykosov et al. (2012) analyse a 1 arc-min gravity anomaly grid. The work relies on the 2D-FFT method by Gruber et al. (2014) that circumvents shifts of the FFT base by latitude-dependent phase lags, which occur when data are given in geodetic latitudes and cannot be treated efficiently by an FFT algorithm. The computation of ALFs in Gruber et al. (2011, 2014) is based on Fourier expansions of ALFs (Hofsommer and Potters 1960), modified as described in Gruber (2011).

The cited works and this work deal with the harmonic transformation based on spherical harmonic base functions. With respect to the rotationally flatness of most planets, the use of ellipsoidal harmonics (EH) is possible likewise (see, e.g., Dassios 2012). EH may even seem more natural; however, ellipsoidal harmonic tools are not (yet) widely used.

1.3 This Work

This paper primarily deals with the computational realization and validation of two numerical quadrature techniques for ultra-high-resolution (surface) spherical harmonic analysis (\geq degree 10,800): the Gauss–Legendre quadrature and the quadrature based on Driscoll/Healy's sampling theorem. As a second aspect, we exemplify the application of the methods to ultra-high-resolution planetary topography. We make use of the implementation of both techniques in the Fortran (F90)-based SHTOOLS v2.8 package (<http://SHTOOLS.ipgp.fr/>) written by Mark Wieczorek. The relevant routines are extended here with (1) stable algorithms for the computation of the fully normalized ALFs based on the Extended Range Arithmetic (ERA) approach (Fukushima 2012) and (2) parallel processing using OpenMP standards. First, the newly derived routines are validated in a closed-loop environment of consecutive analysis and synthesis up to spherical harmonic degree 21,600 (later during application, the routines are validated indirectly up to degree 46,080). Then, the routines are used to investigate the characteristics and differences in spectral energy of the planetary topography of Earth and Mars as well as the Moon's body up to ultra-fine scales based on SRTM15 PLUS and the available Planetary Data System (PDS) data sets. Major motivation for the analysis of the high-resolution topography is that surface spherical harmonic coefficients of different powers of the topography may be used to forward-model the gravitational potential in the spectral (i.e. the spherical harmonic) domain (see, e.g., Rummel et al. 1988; Wieczorek 2007; Balmino et al. 2012; Claessens and Hirt 2013; Hirt and Kuhn 2014) at scales far beyond the resolution of gravity-capturing satellite missions such as the *Gravity and steady-state Ocean Circulation Explorer* (GOCE) (ESA 1999), for Earth, or the *Gravity Recovery and Interior Laboratory* (Grail) (Lemoine et al. 2014), for the Moon.

The paper is outlined as follows: Sect. 2 briefly introduces the spherical harmonic series expansion and recapitulates the basic theory of numerical quadrature. In Sect. 3, the modifications for making the previously introduced algorithms suitable for ultra-high-degree SHA by extending the SHTOOLS package are described. Computation times, allocated memory and precision of the algorithms are discussed in Sects. 3.2 and 3.3. In Sect. 4, the procedures are applied to planetary topography models of Earth, Mars and Moon (Sect. 4.1), revealing their spectrum up to degree and order 43,200, 23,040 and 46,080, respectively. The application of our procedures is described in Sect. 4.2, and the results and the overall performance are discussed in Sects. 4.3 and 4.4, respectively. Finally, we summarize the main findings of this work and give an outlook on future work in Sect. 5.

2 Theory

2.1 Spherical Harmonic Analysis by Quadrature

Quadratures here denote methods that translate a function on a spheroid into its spectral constituents with respect to the spherical harmonic base functions by means of numerical integration. It is thus, in a more general view, a spherical harmonic analysis procedure such as SHA based on least-squares (Sneeuw 1994) or collocation techniques (Moritz 1978; Arabelos and Tscherning 1998). Sneeuw (1994) showed that an approximate quadrature can be derived from the least-squares collocation formulation. For fundamental mathematical relations

concerning spherical harmonic analysis, see, e.g., Hofsommer (1957), Colombo (1981) and Sneeuw (1994).

Following the explanations in Sneeuw (1994), in continuous space, the harmonic coefficients C_{nm} and S_{nm} may be defined by the two integrals

$$\begin{Bmatrix} A_m(\theta) \\ B_m(\theta) \end{Bmatrix} = \frac{1}{(1 + \delta_{m0})\pi} \int_0^{2\pi} f(\theta, \lambda) \begin{Bmatrix} \cos m\lambda \\ \sin m\lambda \end{Bmatrix} \partial\lambda \tag{1}$$

$$\begin{Bmatrix} \bar{C}_{nm} \\ \bar{S}_{nm} \end{Bmatrix} = \frac{1 + \delta_{m0}}{4} \int_0^\pi \bar{P}_{nm}(\cos \theta) \begin{Bmatrix} A_m(\theta) \\ B_m(\theta) \end{Bmatrix} \sin \theta \partial\theta \tag{2}$$

where f is the function on a sphere with spherical coordinates θ (co-latitude) and λ (longitude) and \bar{P}_{nm} are the fully normalized ALFs of the first kind with

$$\delta_{m0} = \begin{Bmatrix} 1, & m = 0 \\ 0, & m \neq 0 \end{Bmatrix}. \tag{3}$$

The spherical harmonic degree and order are n and m , respectively, while $\partial\lambda$ and $\sin \theta \partial\theta$ are the differentials indicating the integration variables.

Equations 1 and 2 can directly be translated into discrete space, giving the basic formulas for an approximate quadrature (here modified after Sneeuw 1994)

$$\begin{Bmatrix} A_m(\theta_i) \\ B_m(\theta_i) \end{Bmatrix} = s_i \frac{1}{N(1 + \delta_{m0} + \delta_{mL})} \sum_{j=0}^{2N-1} f(\theta_i, \lambda_j) \begin{Bmatrix} \cos m\lambda_j \\ \sin m\lambda_j \end{Bmatrix} \tag{4}$$

$$\begin{Bmatrix} \bar{C}_{nm} \\ \bar{S}_{nm} \end{Bmatrix} = \frac{1 + \delta_{m0}}{4} \sum_{i=1}^N \bar{P}_{nm}(\cos \theta_i) \begin{Bmatrix} A_m(\theta_i) \\ B_m(\theta_i) \end{Bmatrix} \tag{5}$$

where N denotes the number of latitude parallels (the equation holds for an equiangular grid, with $2N - 1$ meridian parallels) and s_i is a weight which is proportional to the sine of the co-latitude (akin to the $\sin\theta d\theta$ term in Eq. 2). The weights may be seen as a means to account for the meridian-convergence-implied distortion of the scaling in each latitude parallel.

2.1.1 Approximate Quadrature

According to Sneeuw (1994), the weights s_i may be chosen as

$$s_i = \frac{\pi}{N} \sin \theta_i, \tag{6}$$

or

$$s_i = \frac{2}{\sum_{k=1}^N \sin \theta_k} \sin \theta_i \tag{7}$$

and, inserted into Eqs. 5 and 4, may be used as formula for an approximate quadrature. However, the weights in Eqs. 6 and 7 do not account for the fact that some of the base functions, namely the Legendre functions, lose their orthogonality in the discrete case (Sneeuw 1994), and thus, applied in the quadrature, yield approximate values for the harmonic coefficients only. Two (known) possibilities to ensure the orthogonality of the

discretized Legendre functions by certain weighting and sampling schemes are presented in Sects. 2.1.2 and 2.1.3, leading to an exact harmonic retrieval of spherical functions by numerical integration.

2.1.2 Exact Quadrature Through Driscoll/Healy

Following the quadrature based on Driscoll and Healy's (DH) algorithm (Driscoll and Healy 1994), the geographic data have to be provided on a regular (quadratic) grid of $[2n_{\max} + 2 \times 2n_{\max} + 2] = [N \times N]$ grid points, where n_{\max} is the maximum spherical harmonic degree (and order) of the coefficients, with latitude parallel sampling of $\Delta\theta = 180^\circ/N$ and meridian sampling of $\Delta\lambda = 360^\circ/N$ or on a larger (truly) equiangular grid ($[N \times 2N]$) with $\Delta\theta = \Delta\lambda = 180^\circ/N$. The additional information in the larger grid is ignored by the algorithm; however, grids dimensioned with $N \times 2N$ are often used by global geographic data sets and therefore might be the more practicable grid size. The number of samples, N , must be even for this type of quadrature, and the spherical harmonic expansion is exact if the function represented by the grid is band-limited to degree $n_{\max} = N/2 - 1$. More precisely, the algorithm is based on the fact that "a function, whose Fourier transform has bounded support, may be recovered" from its uniformly arranged samples "with a frequency at least twice the bounding frequency" (Driscoll and Healy 1994).

To account for the fact that the sample points near the poles are closer to each other than they are near the equator, latitude-dependent sample weights are introduced (Driscoll and Healy 1994), achieving orthogonality of the base functions. The weights a_i are given in Driscoll and Healy (1994, eq. 9, p. 216) as

$$a_i = 4\pi \frac{2\sqrt{2}}{N} \sin\left(\frac{\pi i}{N}\right) \sum_{l=0}^{N/2} \frac{1}{2l+1} \sin\left((2l+1)\frac{\pi i}{N}\right) \quad \text{for } i = 0, \dots, N-1 \quad (8)$$

where the factor 4π additionally is introduced into the original equation, as Driscoll and Healy (1994) use unity normalized spherical harmonics and the quadrature is based on 4π -normalized spherical harmonics (as is common in geodesy). Then, the coefficients A_m and B_m within Driscoll and Healy's method for an equiangular grid become

$$\begin{Bmatrix} A_m(\theta_i) \\ B_m(\theta_i) \end{Bmatrix} = \frac{\sqrt{2}}{\pi} a_i \sum_{j=0}^{2N-1} f(\theta_i, \lambda_j) \begin{Bmatrix} \cos m\lambda_j \\ \sin m\lambda_j \end{Bmatrix} = \frac{\sqrt{2}}{\pi} a_i \begin{Bmatrix} \text{Re}(F_m(f(\theta_i, \lambda_1 \dots \lambda_{2N-1}))) \\ -\text{Im}(F_m(f(\theta_i, \lambda_1 \dots \lambda_{2N-1}))) \end{Bmatrix} \quad (9)$$

and, with Eq. 9 inserted into Eq. 5, the surface spherical harmonic coefficients may be retrieved. The variable F_m denotes the complex-valued fast Fourier transform which is computed for each i th latitude parallel of the gridded functional $f(\theta_i, \lambda_1, \dots, \lambda_{2N-1})$ and contains the Fourier coefficients [real (Re) and imaginary (Im) part of F_m]. The back and forward Fourier transformations are possible because of the periodicity of the function described by each latitude parallel and because of the orthogonality of the sine and cosine functions (c.f. Sneeuw 1994).

Note that due to the oversampling needed for the algorithm N or $2N$ complex Fourier coefficients are computed (for a quadratic or an equiangular grid, respectively) for each parallel, of which only $\frac{N}{2} - 1$ ($=n_{\max} = m_{\max}$) are used. All frequencies $n > \frac{N}{2} - 1$ are simply discarded as they would lead to aliasing.

2.1.3 Exact Quadrature Through Gauss–Legendre

Following the Gauss–Legendre quadrature (GLQ) (or *second Neumann method* in Sneeuw 1994), an irregular grid ($[n_{\max} + 1 \times 2n_{\max} + 1] = [N \times 2N - 1]$) with equidistant sampling along latitude parallels and variable sampling along meridians is established. On the meridians, grid points are at the zero-crossings of the associated fully normalized Legendre polynomials, i.e. $\bar{P}_{n_{\max}+1,m=0}(\cos \theta_i) := 0$. This grid is referred to as Gauss–Legendre grid or Gauss–Neumann grid (Sneeuw 1994).

Neumann’s latitude-dependent quadrature weights w_i (also called Legendre weights) ensure that the orthogonality of the discrete Legendre functions is guaranteed and is given, e.g., by Krylov (1962) in Sneeuw (1994)

$$w_i = \frac{2}{\left(1 - \cos(\theta_i)^2\right) \left(P'_{n_{\max}+1}(\theta_i)\right)^2} \quad \text{for } i = 0, \dots, N - 1, \quad (10)$$

where P' is the first derivative of the Legendre polynomial with respect to θ . Then, the coefficients A_m and B_m within the GLQ become

$$\left\{ \begin{array}{l} A_m(\theta_i) \\ B_m(\theta_i) \end{array} \right\} = 2w_i \sum_{j=0}^{2N-1} f(\theta_i, \lambda_j) \left\{ \begin{array}{l} \cos m\lambda_j \\ \sin m\lambda_j \end{array} \right\} = 2w_i \left\{ \begin{array}{l} \text{Re}(F_m(f(\theta_i, \lambda_1 \dots \lambda_{2N-1}))) \\ -\text{Im}(F_m(f(\theta_i, \lambda_1 \dots \lambda_{2N-1}))) \end{array} \right\} \quad (11)$$

and, with Eq. 11 inserted into Eq. 5, the surface spherical harmonic coefficients may be retrieved. The quadrature is exact when the function on the sphere is band-limited to degree $n_{\max} = N - 1$.

3 Computational Aspects

This section describes the implementation of the above algorithms for high-degree SHA under computational and numerical aspects. The starting point for the realization is existing (open-source) Fortran (F90) routines (<http://SHTOOLS.ipgp.fr/>) for both quadrature rules (DH and GLQ) in the SHTOOLS v2.8 package. The package written by Mark Wieczorek consists of a compilation of F90 routines dedicated to spherical harmonic computations (e.g., transformations, multitaper spectral analysis).

In SHTOOLS, the implementation of the two quadrature algorithms given above by Eqs. 9 and 11 inserted in Eq. 5 is done in a very efficient manner by (1) employing FFT for the evaluation of the sum over longitude-dependent cosine and sine arguments in each latitude parallel and by (2) exploiting the symmetry of the Legendre polynomials and ALFs about the equator [$P_{nm}(\cos \theta) = P_{nm}(\cos -\theta)$]. Due to the latter measure, ALFs are computed only once for corresponding latitude parallels on the northern and southern hemisphere. In effect, the loop for the summation in Eq. 5 halves (upper summation index then is $N/2 + 1$), leading to significant acceleration of the quadratures. Additionally, the ALF computation is embedded in the routines, which is time-saving as multiple initializations are omitted and no calls to external modules/routines are necessary (see SHTOOLS routines: SHExpandDH.f90, SHExpandGLQ.f90).

3.1 Computation of associated Legendre functions (ALFs)

The key aspect facilitating numerically accurate spherical harmonic computations up to ultra-high degree and order is numerical stability in the evaluation of the fully normalized ALFs to ultra-high degree. In contrast to the fully normalized associated Legendre polynomials (\bar{P}_{n0}), the ALFs (\bar{P}_{nm} with $m \neq 0$) are numerically inaccurate when evaluated with standard recursion formulas for high spherical harmonic degree and order. In the SHTOOLS package, the computation of the ALFs is realized via the modified forward-column method (Holmes and Featherstone 2002). This method is a modification of the standard forward-column recursion which prevents over-/underflow of the ALFs (held in double precision variables) by applying a scaling factor of 1^{-280} at the beginning of the recursion. This modification allows the stable computation of Legendre polynomials to degree 2700 (Holmes and Featherstone 2002).

Aiming at higher-degree computations, we incorporated the *Extended Range Arithmetic* (ERA) approach (Fukushima 2012), also known as *X-number* approach, for the computation of fully normalized ALFs, instead. In theory, the ERA allows the stable evaluation of ALFs up to arbitrary degree and order. Within the algorithm, under-/overflow problems are omitted by extending the exponent of floating point numbers, keeping the numbers in the numerical range of ordinary double precision (REAL*8) numbers. The ALF algorithms by Fukushima (2012) for the computation of the sectorial and tesseral ALFs are complemented by a standard forward-column method for the computation of the zonal Legendre polynomials (which are unaffected by over-/underflow issues at ultra-high degrees). The zonal ($m = 0$) fully normalized Legendre polynomials P_n follow the recursive description e.g., given in Holmes and Featherstone (2002) as

$$\begin{aligned}
 P_0 &= 1 \\
 P_1 &= \sqrt{3} \sin \theta \\
 P_n &= P_{n-1} \cdot \frac{\sqrt{(2n+1)(2n-1)}}{n} \cdot \cos \theta - P_{n-2} \cdot (n-1) \cdot \frac{\sqrt{2n+1}}{n \cdot \sqrt{2n-3}}, \quad \text{for } n > 1.
 \end{aligned}
 \tag{12}$$

To verify the accuracy of the implemented ALF algorithm, tests with exact identities that represent certain sums of ALFs may be used (see, e.g., identity tests provided in

Fig. 1 Identity error I^0 (Eq. 13) of the implemented ALF algorithm for various maximum degrees per latitude parallel. Note that the *green* and *blue* curves are very close together

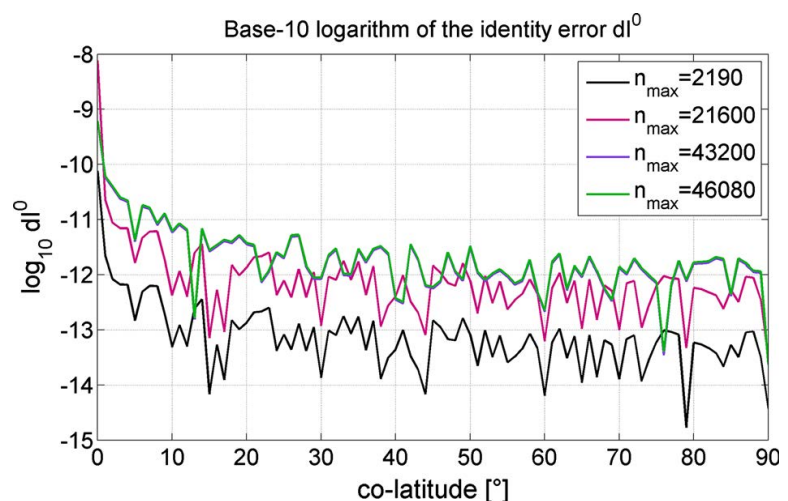


Table 1 SHA parameter, array and grid sizes for various maximum spherical harmonic degrees n_{\max}

n_{\max}	SHCs		Pnm/ALFs			DH-grid			GLQ-grid		
	Number (million)	Memory ^a (GB)	Number (million)	Memory ^b (GB)	Latitude parallels	Points (million)	Memory (GB)	Latitude parallels	Points (million)	Memory (GB)	
360	0.13	0.00	0.13	0.00	722	0.52	0.00	361	0.26	0.00	
2160	4.67	0.04	4.67	0.04	4322	18.68	0.15	2161	9.34	0.07	
5400	29.17	0.23	29.17	0.23	10,802	116.68	0.93	5401	58.34	0.47	
10,800	116.66	0.93	116.66	0.93	21,602	466.65	3.73	10,801	233.31	1.87	
21,600	466.65	3.73	466.65	3.73	43,202	1866.41	14.93	21,601	933.18	7.47	
43,200	1866.33	14.93	1866.33	14.93	86,402	7465.31	59.72	43,201	3732.61	29.86	
46,080	2123.46	16.99	2123.46	16.99	92,162	8483.83	67.95	47,081	4246.87	33.97	

DH Driscoll/Healy, GLQ Gauss–Legendre quadrature

^a In SHTOOLS twice the memory denoted here is needed for the SHCs, as cosine- and sine-assigned SHCs are stored in separate arrays of size $(n_{\max} + 1)^2$

^b In SHTOOLS, the Pnm/ALFs are computed on the fly for each latitude parallel, so a maximum number of n_{\max} Pnm/ALFs need to be held at the same time

Holmes and Featherstone 2002; Fukushima 2012). We use the identity error defined by

$$I^0 = \frac{\sum_{n=0}^M \sum_{m=0}^n P_{nm}(\cos \theta)^2}{(M + 1)^2} - 1 \tag{13}$$

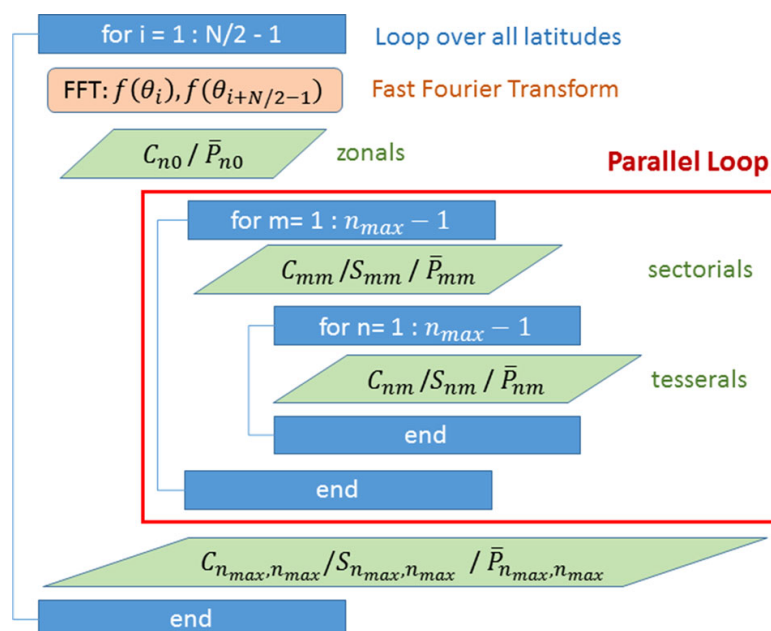
(cf. Holmes and Featherstone 2002), where the square-sum over all ALFs up to a certain maximum degree M for any θ in the interval $-90^\circ < \theta < 90^\circ$ must equal $(+1)^2$. Our tests (Fig. 1) show that for $M = 2190, 21,600, 43,200$ and $46,080$, the error stays well below 1^{-10} for $\theta > 5^\circ$ and below 1^{-8} for polar latitudes ($\theta < 5^\circ$). Note that for accurate computation of the identity error in Eq. 13, the variable holding the squared ALFs must be of quadruple precision (REAL*16).

We acknowledge other methods exist for the numerically stable computation of ALFs at ultra-high degree (see, e.g., Balmino et al. 2012 or Gruber 2011), which could be considered for implementation too.

3.2 Parallelization and Computation Times

Ultra-high-degree spherical harmonic computations require efficient parallel computation techniques. The reason is that the number of parameters and ALFs to be estimated or computed increases in a quadratic manner with the maximum degree, by $(n_{max} + 1)^2$. Simultaneously, the size of the grid increases quadratically, as raising the degree requires a finer sampling of the function to be analysed by the quadrature. An overview on the number of parameters, ALFs and grid points together with related memory allocation is given in Table 1 for selected spherical harmonic degrees. A degree-21,600 SHA thus requires the computation of 466.6 million spherical harmonic parameters and the same number of ALFs per latitude. Even when taking into account the symmetry of the ALFs to the equator a total of $\sim 10^{13}$ or $\sim 5 \times 10^{12}$ SHCs and ALFs need to be computed within the implementation of Driscoll/Healy’s quadrature (DH) and the Gauss–Legendre quadrature (GLQ), respectively. These large numbers already suggest that using a single CPU is

Fig. 2 Scheme of the general program structure of the SHTOOLS quadratures (applies for GLQ and DH) showing the location of the implemented OpenMP parallel loop directive in this work



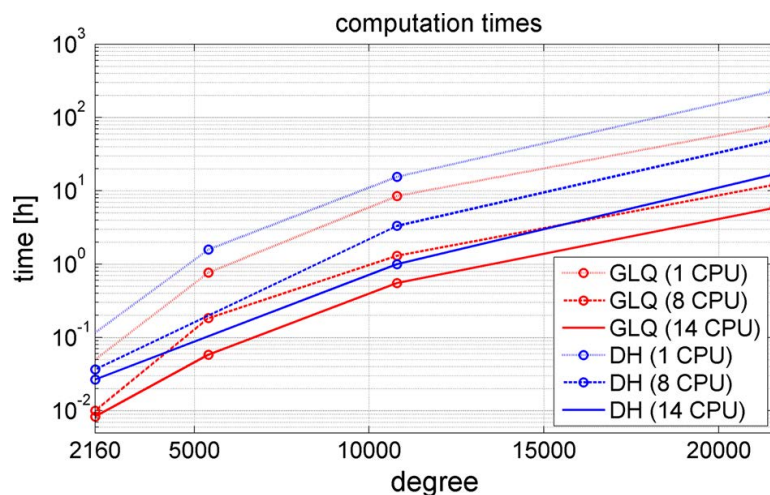
hardly sufficient for high-degree quadratures. Therefore, we make use of the *OpenMP* Application Program Interface (API) (www.openmp.org), which provides a flexible interface for certain CPU directives, enabling shared-memory parallel programming for multiple platforms in C/C++ and Fortran.

In a first attempt, we make use of the *OpenMP Parallel Loop* directive, which allows to share time-consuming loops among a predefined number of threads, i.e. CPUs. There are generally two major loops needed, one outer loop over all orders m and on inner loop over all degrees $n > m$, when it comes to the computation of all sectorial and tesseral SHCs associated with a certain latitude (and to its symmetrical counterpart) in Eq. 5 together with Eqs. 9 or 11. The parallel regions are embedded directly into the SHTOOL quadrature (and synthesis) routines (SHExpandGLQ.f95, SHExpandDH.f95, MakeGridGLQ.f95, MakeGridDH.f95) and embrace the computationally costly double loop (Fig. 2). Within the outer loop, the ALF routine is called $n_{\max} - 1$ times to calculate a vector containing all ALFs of the same order m , which is then multiplied with the corresponding Fourier coefficients (or with the corresponding spherical harmonic coefficients in case of SHS routines) within the inner loop over all degree n for $n > m$. The resulting $(n_{\max} - 1) + (n_{\max} - 1) \cdot (n_{\max})/2$ operations per latitude (e.g., ~ 233.3 million operations for $n_{\max} = 21,600$) are shared between the allocated CPUs.

With this kind of parallel processing, computation times of the GLQ quadrature could be reduced approximately by a factor of 6 and by a factor of 13 of the time needed by a single CPU using 8 and 14 CPUs, respectively. In the case of using the DH algorithm in the quadrature, the parallelization reduces to a fifth and a thirteenth of the time needed by a single CPU using 8 and 14 CPUs, respectively. Absolute computation times of both algorithms are illustrated in Fig. 3. The *CPU time* (=computation time times number of used CPUs) of the here-investigated SHA methods is significantly lower compared to, e.g., the method suggested by Gruber et al. (2011). A degree and order 10,800 analysis in Gruber et al. (2011) (c.f. Table 1) takes ≈ 170 CPU hours (in a 16 thread environment), while it takes ≈ 8 CPU hours using the here-implemented GLQ quadrature (in a 14 thread environment).

We note that at degree 2160 the computation times are about 8 times longer compared to the original SHTOOLS quadrature routine which is based on the standard forward-column recursion (47 vs. 376 s). The significant prolongation owes to (1) using the X-number routines for the computation of the ALFs, which are approximately a factor 2 more time-consuming than the modified forward-column recursion (personal comm. Fukushima 2015) and to (2) calling an external routine for the computation of the

Fig. 3 Computation times for spherical harmonic analysis using the Gauss–Legendre quadrature (GLQ) and the Driscoll/Healy quadrature (DH) as a function of maximum recovered degree and allocated CPUs



X-number ALFs. In the original SHTOOLS implementation, the ALF computation is embedded in between the lines of the quadrature routine which means initialization of parameters is only done once (and not m times) and storage of ALFs in large arrays is not required.

In a second attempt, we tried to assign a single core directly to the processing of a whole latitudinal parallel. This approach turned out to be not feasible because within each latitudinal parallel the CPUs have to update the array holding the SHCs. As the different CPUs may write (update) an allocated memory within the array at the same time, data integrity is not ensured. The OMP attribute clauses for shared variables, like ATOMIC or REDUCTION, would ensure this kind of integrity. Those attributes, however, only work for scalar variables. The variable holding the SHCs is an array of dimension $[2, n_{\max} + 1, n_{\max} + 1]$, and thus, the attributes are not applicable here.

3.3 Precision of Implemented Algorithms

The implemented DH (Sect. 2.1.2) and GLQ (Sect. 2.1.3) quadratures are exact algorithms, only, when applied to a band-/frequency-limited function that is discretized (or sampled) in the correct manner. In order to validate both algorithms, we use band-limited variants of Earth's relief (topography and bathymetry) and perform two consecutive analysis and synthesis to create a closed-loop experiment. First, DEM elevations are resampled according to the respective algorithms' sampling scheme (described above) by means of a 2D interpolation (cubically). The obtained grids are harmonically analysed via the implemented extended SHTOOLS quadratures. The computed spherical harmonic coefficients can then be used to create band-limited grids of DH or GLQ kind up to degree 21,600, via another synthesis. The synthesis step is validated externally with the freely available GrafLab software (Bucha and Janák 2013), a MATLAB-based synthesis for ultra-high spherical harmonic expansions. Our implementation of the synthesis based on SHTOOLS (see above) is in very good agreement with GrafLab, and errors in the space domain do not exceed 2×10^{-6} m at degree/order 21,600.

The numerical precision of the quadratures given by the maximum absolute error of analysis and consecutive synthesis of the created band-limited topography function in the space domain is given in Table 2 for selected maximum spherical harmonic degrees n_{\max} . The maximum residual errors of both approaches (GL and DH) are in the same order of magnitude, not exceeding 5×10^{-5} m even at maximum degree 21,600. This suggests that the implementation is well suited for ultra-high-degree spherical harmonic analysis. Error patterns in the residuals are shown and discussed in Sects. 4.4.1 and 4.4 up to maximum degree 46,080.

Table 2 Maximum absolute space-domain error of closed-loop experiments with band-limited variants of Earth's topography using the GLQ and the DH quadrature algorithm

n_{\max}	Gauss–Legendre (GLQ)	Driscoll and Healy (DH)
2160	3.09×10^{-9}	2.6×10^{-9}
10,800	2.10×10^{-6}	1.58×10^{-6}
21,600	2.63×10^{-5}	4.89×10^{-5}

Units are in metres

4 Application to Planetary Topography

In this section, the implementation of the GLQ quadrature (Sect. 3) is applied to planetary topography of different resolution and features, followed by a discussion of computational aspects and interpretation of results.

4.1 Data

The two planets Earth and Mars as well as the Earth's Moon are found to be suited to extensively test the numerical quadrature algorithms described in Sect. 2.1, mainly because high-resolution shape functions are available in public data sets, covering the bodies' surfaces in their entirety. Additionally, the bodies show very different characteristics and surface features at large, medium and small scales (Wieczorek 2007). On Earth, we have the clear and unique distinction between continents (topography) and oceans (bathymetry) along with plate margins accompanied by (active) rift, subduction and uplift zones. On Mars, we find a unique dichotomy—an asymmetry between low elevations in the northern and high elevations in the southern hemisphere—as well as large impact basins, rifts and the monumental regional peaks of the Tharsis volcanoes near the equator. Next to the Tharsis volcanoes located is the highest peak known as Olympus Mons reaching almost 22 km (Wieczorek 2007). The Lunar topography, with its heavily cratered farside and comparatively smooth nearside (reasoned by the young basaltic material and the Moon's Earth-bound rotation), is home to the largest known impact structure in the solar-system: the giant South Pole-Aitken impacts basin on the southern farside hemisphere with a total relief of over 10 km within a region of 2000 km diameter (Wieczorek 2007). At the same time, the central processes being responsible for the morphology are very different due to the very different outer conditions and forces present in the respective planetary system. Among others, the processes leading to unique surface structures are: exposure to solar radiation, existence and composition of atmosphere, tectonic and volcanic activity, existence of water and gravity.

Planetary topographic data sets are provided in terms of digital elevation models (DEMs) and have been used in spherical harmonic analyses in the past. To our knowledge, the maximum degree of available SHCs does not exceed 10,800 for Earth, 2600 for the Moon and 2600 for Mars. The corresponding data sets and references are listed in Table 3.

Within the publicly provided data sets, there generally exist limitations or inconsistencies which are independent of the provided data resolution. Those may, e.g., be related to the technique of measurement and blur our knowledge about the surface elevations of a

Table 3 Existing works on high-degree spherical harmonic analysis of planetary topography

Planet	Degree	SHC data set	Reference	Topographic data
Earth	10,800	Earth2014	Hirt and Rexer (2015)	SRTM30 PLUS v9, Bedmap2, SRTM v4.1, GBT v.3
Earth	10,800	ETOPO1	Balmino et al. (2012)	ETOPO1
Moon	2600	LOLA2600p	Wieczorek (2015)	LOLA
Mars	2600	MarsTopo2600	Wieczorek (2015)	MOLA

SRTM Shuttle Radar Topography Mission, *GBT* Greenland Bedrock Topography, *PDS* Planetary Data System, *LOLA* Lunar Orbiter Laser Altimeter, *MOLA* Mars Orbiter Laser Altimeter

planet. On Earth, for example, we have large differences between the quality of topographic elevations and seafloor (=bathymetric) elevations. The first of which can be measured with various terrestrial/airborne/space-borne sensors, while the latter is sensed directly only via local-scale ship soundings and determined globally indirectly via ties to the altimetric gravity field (Smith and Sandwell 1994). According to Sandwell et al. (2014), more than 50 % of the ocean is more than 10 km away from the next direct depth measurement. The highest resolution gravity field over the oceans is derived from satellite altimetry, and available models reach $\sim 1'$ ($\cong 2$ km) resolution (Andersen et al. 2013; Sandwell et al. 2014) at best. However, the actual resolution in these models is dependent on the spacing (or density) and the orientation of the satellite altimeter ground tracks. The available new altimeter data sets of CryoSat-2 and Jason-1 have a ground-track spacing of 2.5 and 7.5 km (Sandwell et al. 2014), respectively. When combined with altimeter data of older satellites (Geosat and ERS-1), the gravity data can be used to retrieve seamounts between 1 and 2 km height (Sandwell et al. 2014). But due to the attenuation of the shorter wavelength gravity signals, the estimation of bathymetric heights from gravity works best in the wavelength band from 12 to 160 km (Sandwell et al. 2014), which means it is of lower quality at scales <12 km. Further, the quality of the estimates decreases with the thickness of the seafloor (Sandwell et al. 2014).

On Mars and Moon, the actual resolution also is dependent on the across-track spacing of the laser altimeter ground tracks, and higher-resolution data products are released as soon as the measurement density is good enough that there are some samples per pixel accumulated (Neumann 2010). However, the track density is lowest near the equator and highest towards the poles due to the (near) polar orbit. Owing to this fact, there exist gaps of up to 12 km between neighbouring profiles at the equator in case of Mars. In the data products, these gaps are filled with interpolated values (Smith et al. 2003).

Further, deviations from the orbital inclination of 90° inherent to most orbiters lead to non- or poor observations in polar regions (see Farr et al. 2007 and Tachikawa et al. 2011a for Earth or Smith et al. 2003 for Mars) and can only partly be compensated by other missions or observation techniques.

4.1.1 Earth's Topography and Bathymetry

Earth's topography and bathymetry here are taken from the first version of the SRTM15 PLUS data set (ftp://topex.ucsd.edu/pub/srtm15_plus/). It is the 15 arc-sec nominal resolution (~ 0.5 km) successor of the well-known 30 arc-sec topography/bathymetry maps SRTM30 PLUS (Becker et al. 2009). SRTM15 PLUS contains a new combination of SRTM, ASTER and CryoSat-2 ice sheet data over land and is based on SRTM30 PLUS v11 over the oceans' bathymetry. The SRTM30 bathymetry was derived, in principle, from the anomalous gravity field as sensed by various satellite altimeters and was calibrated and augmented locally by ship-sounding data aggregated over 40-year time (Smith and Sandwell 1994). The bathymetric data in areas devoid of ship sounding have a resolution of ~ 12 km with a maximum resolution of 2 km, rather than the nominal 500-m resolution of SRTM15 PLUS (cf. Sandwell et al. 2014; Sect. 4.1). For more details on the creation of the bathymetry and its accuracy, the reader is referred to Smith and Sandwell (1994), Sandwell et al. (2014), Marks et al. (2010).

The elevations and depths are given in terms of orthometric heights (in metres) relative to the *EGM96* geoid, which is referenced to the *WGS84* ellipsoid and which in good approximation represents the mean sea level.

As the SRTM15 PLUS data refer to geodetic latitudes, it has to be transformed to geocentric latitudes in order to be used by the quadratures correctly. This is done by a 2D-spline interpolation using the simple relation

$$\tan \Theta = \frac{a^2}{b^2} \tan \phi \quad (14)$$

(see, e.g., Torge 2001, p. 95) between the spherical co-latitude Θ and the geodetic co-latitude ϕ , where a is the semi-major and b the semi-minor axis of the underlying ellipsoid, which is GRS80 (Moritz 2000) in this case.

Further, we found 6,194,174 NaN (not-a-number)-flagged pixels in the SRTM15 PLUS data set (0.17 % of all pixels). We filled these data gaps with SRTM30 PLUS information in order to get to a truly complete (=global) topography/bathymetry data set for Earth.

4.1.2 Martian Topography

The topography model for Mars originates from the Mars Orbiter Laser Altimeter (MOLA) which was part of the Mars Global Surveyor (MGS) mission. The MGS orbiter was operated between 1998 and 2006 in a near-polar orbit (inclination = 93°). We use the *Mission Experiment Gridded Data Record* (GDR)—digital topographic maps that are generated from the altimeter observation data accumulated over the entire primary mission—made available via NASA's *Planetary Data System* (PDS) (Smith et al. 2003). The maps are sampled at 128 pixel per degree (~460 m). The MOLA topography is referenced to an areoid, defining a surface of constant (gravitational and rotational) potential (12,652,804.7 m²/s² as the mean value at the equator at an average radius of 3396.000 km) (Smith et al. 2003). The areoid may be calculated by the Goddard Mars Gravity Model GGM-2B (Lemoine et al. 2001) evaluated to degree and order 50 (Smith et al. 2003). The MOLA topography then is the difference between the real planetary radius and areoid at a certain planetocentric longitude and latitude (IAU2000 coordinate system).

In the case of Mars, the polar regions (>+88° and <-88° latitude) are not covered by the gridded data products of 128 pixel per degree due to the spatially limited availability of MOLA observations. Therefore, we used the 64-pixel-per-degree elevation product in the polar regions instead and oversampled it by means of a bi-cubical interpolation to reach a nominal global resolution of 128 pixel per degree.

4.1.3 Lunar Topography

The Lunar topography originates from the Lunar Orbiter Laser Altimeter (LOLA) instrument of the Lunar Reconnaissance Orbiter (LRO) mission (Smith et al. 2010). The orbiter circulates the moon on a polar orbit since mid-2009. We use the NASA PDS *Gridded Data Record's* digital elevation model with 256-pixel-per-degree resolution (~120 m), provided in terms of an equidistant cylindrical map (Neumann 2010). The elevations are referenced to a reference sphere of 1737.4 km radius. A planetopotential topography, i.e. physically meaningful heights, similar to the Earth's and the Martian case could be derived for the Moon by subtracting a selenoid model from the planetary radius. The selenoid (=Lunar geoid) can be derived from any potential model for the Moon. However, this is not required for the purpose of the present study.

4.2 Processing

For the spherical harmonic analysis of the planetary topography, we choose the Gauss–Legendre quadrature as described and tested in Sects. 2.1.3 and 3.2. Both the GLQ and the DH algorithm would be qualified for this task in terms of precision (see Sect. 3.3), but because of comparatively long computation times the DH method is not efficient for ultra-high degrees ($>10,800$), see Sect. 3.2 and Fig. 3.

The spectral bandwidth of the real topography is unlimited, and the recoverable spherical harmonic bandwidth of the topography, however, is limited by its discretization (Sect. 2.1). Thus, the sampling of a discrete topographic function defines the degree of truncation in the spherical harmonic analysis (and leads associated truncation errors, see Sect. 4.3). The sampling and the associated maximum recoverable degree of each topographic data set (Sect. 4.1) are listed in Table 4. In order to apply the Gauss–Legendre quadrature, the latitude parallels have to coincide with the zero-crossings of the Legendre polynomials (Eq. 12). This was achieved by bi-cubically interpolating topographic height values at the respective latitudes using MATLAB's intrinsic 2D-interpolation method (cubic interpolater).

4.3 Results and Discussion

The harmonic analysis reveals the spectral composition of Earth's topography and bathymetry to degree 43,200 (=500 m half-wavelength), of the Martian topography to degree 23,040 (=460 m half-wavelength) and of the Lunar topography to degree 46,080 (=120 m half-wavelength). The degree variances are given in Figs. 4 and 5, as a function of harmonic degree and of the half-wavelength (=spatial resolution), respectively. At the same time, re-expanding the calculated harmonic coefficients to a grid—sampled in the same manner as the input grid—allows evaluation of the accuracy of the implemented GLQ quadrature for the different maximum degrees in a closed-loop scenario (Figs. 6, 10, 12).

4.3.1 Spectra of Planetary Topography Models

The topography of each planet exhibits different spectral energy towards ultra-short scales, and the degree variances also reveal different decay of the topographic signal with harmonic degree (Fig. 4).

Table 4 Spatial resolution (sampling), maximum harmonic degree and sources of the data used in the spherical harmonic analysis of planetary topography (see also Sect. 4.1) in this work

Planet	Sampling			Harmonic degree	Topographic data
	$\left(\frac{\text{pixels}}{\text{degree}}\right)$	(arc-sec)	(m)		
Earth	240	15	~ 500	43,200	SRTM15 PLUS v1
Mars	128	28.125	~ 460	23,040	MOLA
Moon	256	14.0625	~ 120	46,080	LOLA

SRTM Shuttle Radar Topography Mission, *LOLA* Lunar Orbiter Laser Altimeter, *MOLA* Mars Orbiter Laser Altimeter

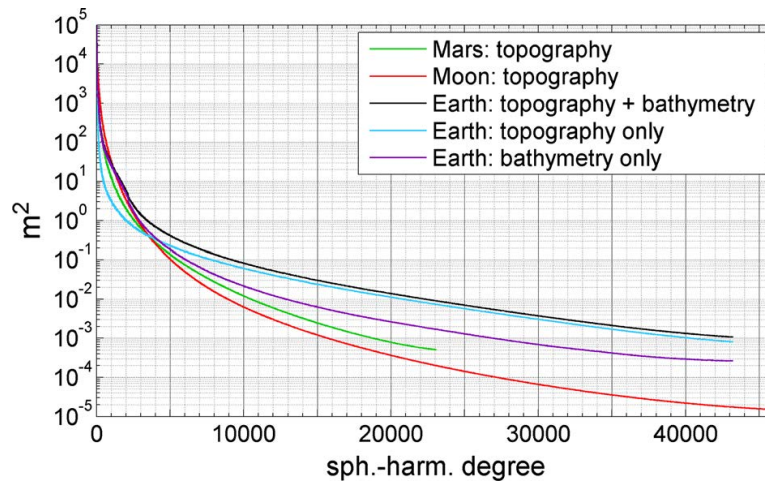


Fig. 4 Degree variances of planetary topography: Earth's topography and bathymetry in *black*, Earth's topography (ocean values set to zero) in *light blue*, Earth's bathymetry (continental values set to zero) in *magenta*, Lunar topography in *red* and the Martian topography in *green*; unit on y-axis is metres squared

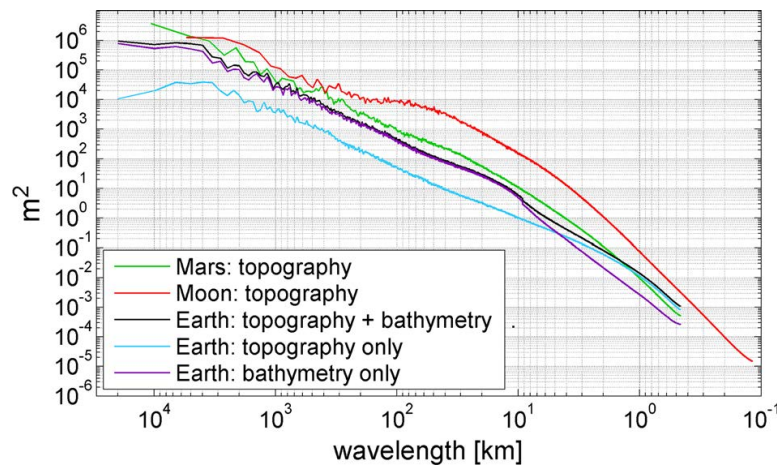


Fig. 5 Degree variances of planetary topography by associated spatial scale (half-wavelength in kilometres): Earth's topography and bathymetry in *black*, Earth's topography (ocean values set to zero) in *light blue*, Earth's bathymetry (continental values set to zero) in *magenta*, Lunar topography in *red* and Martian topography in *green*; unit on y-axis is metres squared

Notably, it is Earth that has highest topographic energy beyond degree ~ 1900 (black curve), exceeding the Moon's topographic energy by almost 2 orders of magnitude at degree 43,200. The major part of this short-scale energy is associated with Earth's continental topography. This can be seen from the harmonic analysis of the continental topography only (by setting all values below sea level to zero: light blue curve) and of the bathymetry only (by setting all values above sea level to zero: magenta curve). Bathymetry makes up most of the power in the black degree variance curve up to degree ~ 4000 , whereas continental topography dominates Earth's spectral harmonic power beyond this degree. Adding the degree variances of the magenta and the light blue curve would lead to the full (topography and bathymetry) signal and result in the black curve (Fig. 4).

The spectral properties of the Martian and Lunar topography are comparatively even (until degree 23,040). The Lunar degree variance curve (red) intersects with the Martian curve (green) near degree 4000, having more power beyond this degree. Due to the limited

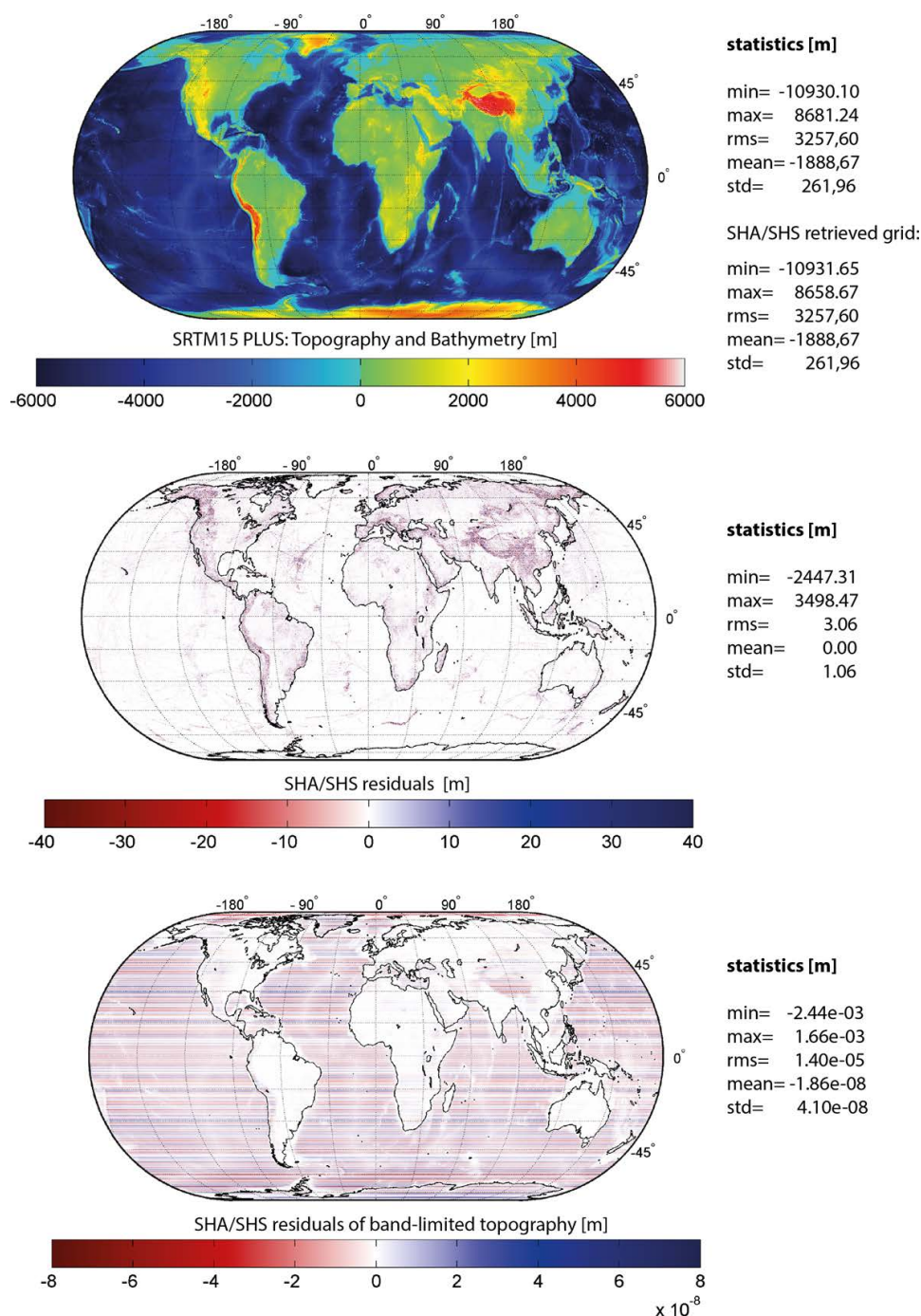


Fig. 6 Earth's topography and bathymetry (*upper plot*), closed-loop residuals with input topography after the first spherical harmonic analysis and synthesis (*middle plot*) and residuals of the analysis and synthesis of a band-limited input topography (to degree 43,200); unit is metres

grid resolution of the topographic data of Mars, only half of the spherical harmonic degrees could be recovered compared to the other two planets.

Translating the spherical harmonic degrees into spatial scales using each planet's natural half-wavelength (Fig. 5) allows to compare the spectral power in the degree variances of the different planets more intuitively, at the level of metric scales. Among the three bodies, the Moon's topography possesses the highest energy over all spatial scales, indicating that its planetary relief has a higher variability (and thus roughness). In particular, at spatial scales of ~ 80 to ~ 200 km, there are several pronounced topographic features on

the Moon (craters of similar size). This is to be seen in the degree variances of the Lunar topography, which remain at the level of $\sim 10 \times 10^4 \text{ m}^2$, while the power of the other topography models (Earth and Mars) steadily decreases in this spectral band. In the Lunar topography, this spectral bands represents several large-size class 1 craters classified as TYC type by Wood and Anderson (1978), e.g., Tycho (86 km diameter), Aristoteles (87 km diameter), Langrenus (132 km diameter) or Humboldt (207 km diameter). Those TYC craters are attributed multiple tiers of terraces, crenulated rim crest, large flat floor and a central peak (Wood and Anderson 1978). Compared to Earth, also the Martian topography possesses more power at low and medium scales. Only below scales of 1.5 km, the Martian topographic variability is below that of Earth's.

Compared with the topographic spectra of Moon and Mars, which show a very smooth decay (Fig. 4), the decay of Earth's topographic spectrum slows down in the band from $\sim 30 \text{ km}$ down to $\sim 10 \text{ km}$ (degree ~ 600 and 2160). Further, near degree 2160, a sudden drop in the power of the degree variances (see Fig. 4) or a change in tilt of the black curve (see Fig. 5), respectively, becomes visible. This behaviour is attributable to the bathymetry component of the SRTM15 PLUS model, which is seen from the intercomparison of the three Earth power spectra (black vs. blue vs. magenta curve). We interpret the change of tilt at degree 2160 ($\sim 9\text{--}10 \text{ km} \sim 4\text{--}5 \text{ arc-min}$) to indicate the limit of the full resolution of bathymetric depth data (the seafloor mapping is not complete anymore at shorter spatial scales). This is supported by the assessment of the bathymetric resolution in Sect. 4.1.

Note that the absolute power of the degree variances also depends on the sphere-aeroid and the sphere-geoid-separation, respectively, which has been treated differently for the planets or not at all in case of the Moon (see Sect. 4.1). However, this effect is relevant only at long and medium spatial scales because the underlying geoid models are of rather smooth nature (maximum degree is 360 for SRTM30 Plus and 50 for MOLA).

4.3.2 Analysis of Earth's Topography to $d/o 43,200$

For Earth, the topography could be harmonically analysed to degree 43,200. Using the computed SHCs for SHS, we can compare the resulting $15'' \times 15''$ grid with the SRTM15 PLUS input topography (Fig. 6, upper and middle plot). The standard deviation of the differences is about 1 m (RMS = 3.06 m) in the space domain. Much of the differences (here further denoted as *residual error* but also found denoted as *representation error* by

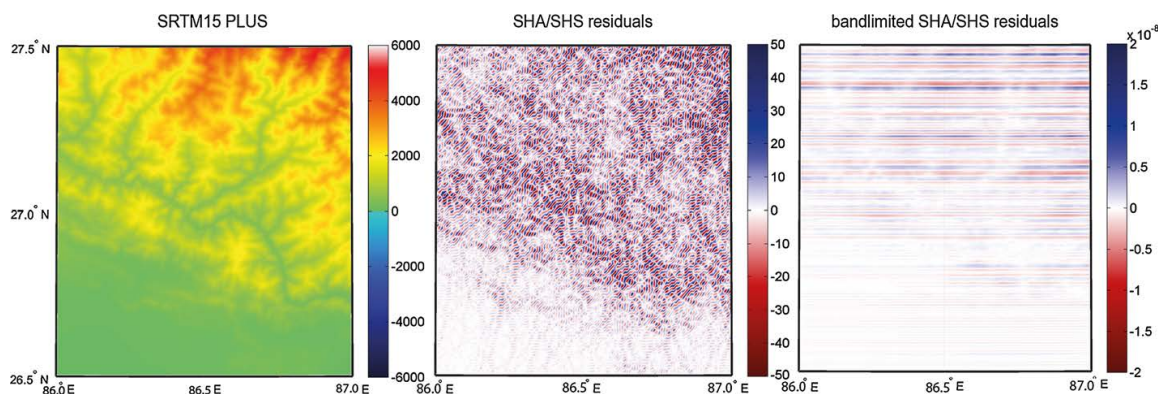


Fig. 7 Earth's topography (*left plot*), closed-loop residuals with respect to input topography after the first spherical harmonic analysis and synthesis (*middle plot*) and residuals of the analysis and synthesis of a band-limited input topography (*right plot*) to degree 43,200 over a selected region over the Himalayas; unit is metres

Balmino et al. 2012) occur in high elevated or rough terrain (e.g., in the Himalayas with amplitudes of about ± 50 m, see middle plot in Fig. 7), whereas flat terrain (e.g., Australia) shows very small residual errors. Interestingly, apart from the mid-oceanic ridges at the

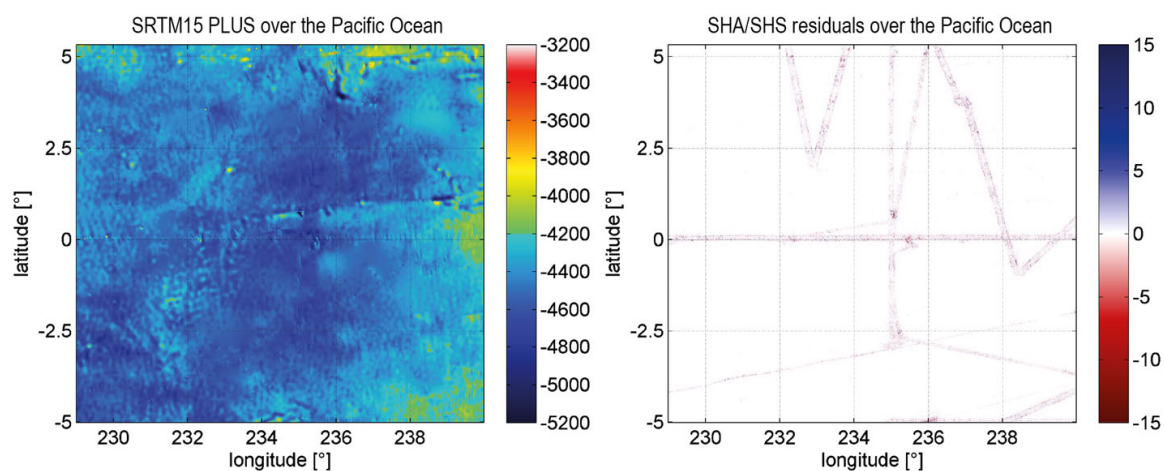


Fig. 8 Bathymetry over parts of the Pacific Ocean as contained in SRTM15 PLUS (*left*) and the SHA/SHS residual error over this region (*right*), clearly depicting the ship-sounding tracks; unit is metres

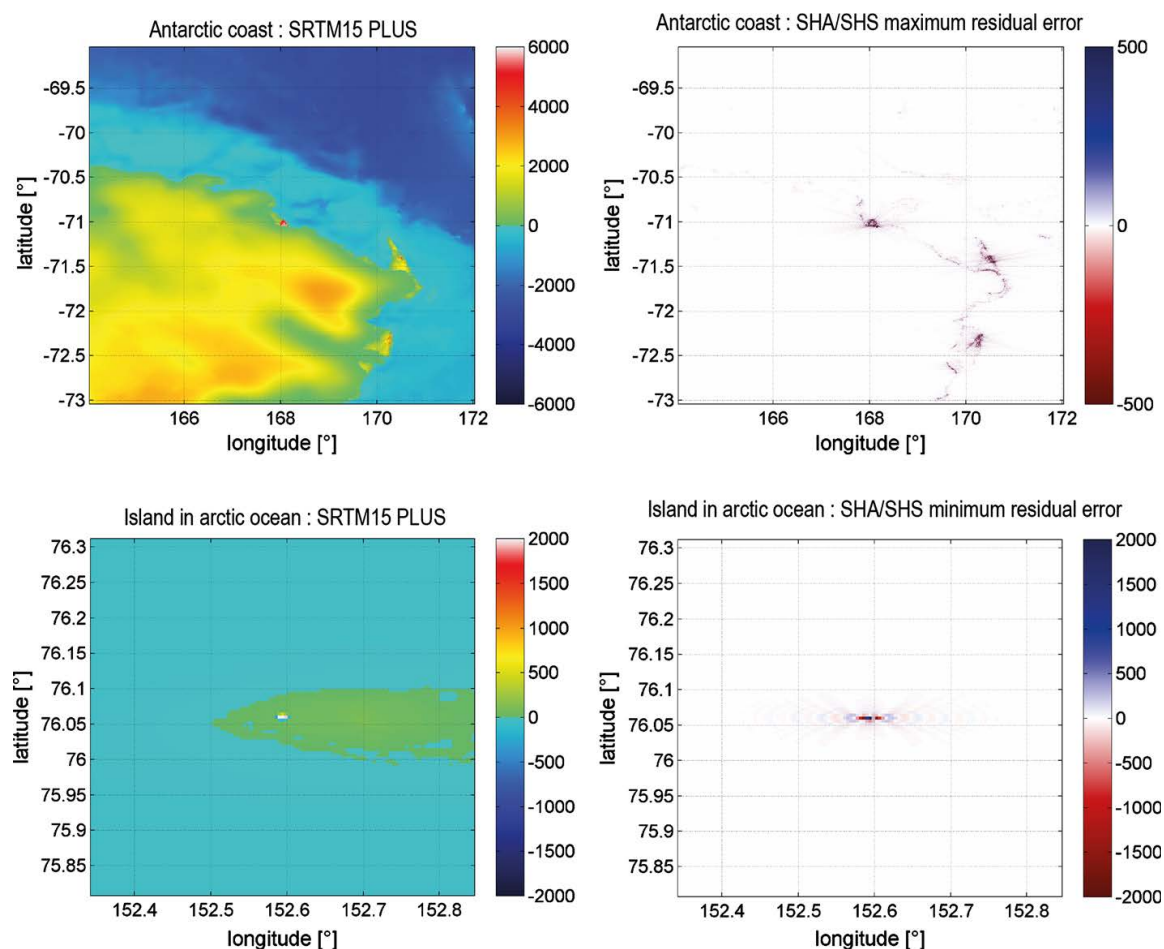


Fig. 9 Upper row area of minimum SHA/SHS residual error (-2447.31 m) in the SRTM15 PLUS data set; bottom row area of maximum SHA/SHS residual error (3498.47 m) in the SRTM15 PLUS data set (note that some of the pixels on the island were NaNs and are filled by SRTM30P values, see Sect. 4.1.1); unit is metres

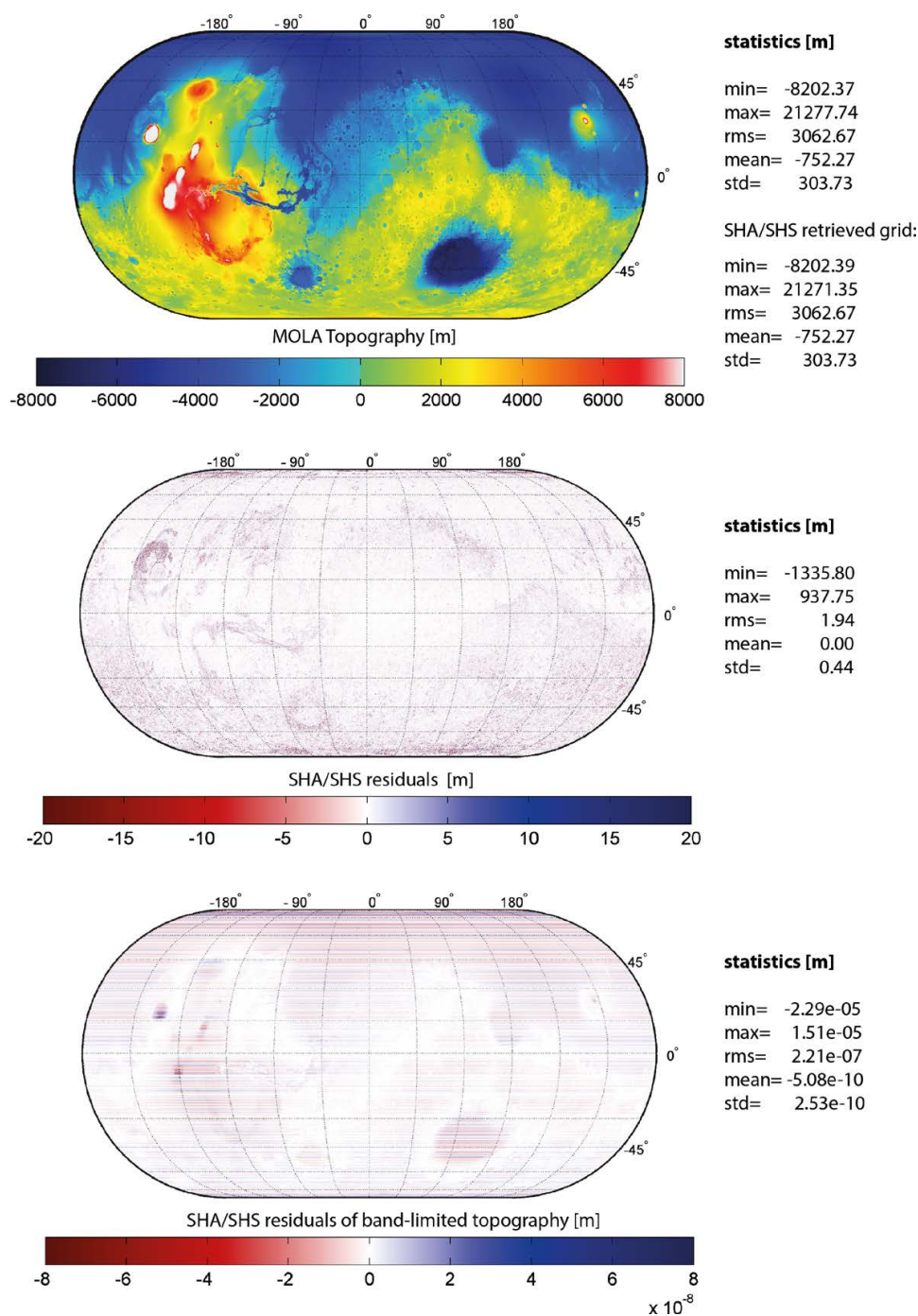


Fig. 10 Martian topography (*upper plot*), closed-loop residuals with input topography after the first spherical harmonic analysis and synthesis (*middle plot*) and residuals of the analysis and synthesis of a band-limited input topography (to degree 23,040); unit is metres

floor of the oceans, also linear residual error patterns become visible over the oceans. These linear errors seem to coincide with the ship routes that contributed the sounding data which was used to calibrate the SRTM15 PLUS bathymetry (Fig. 8). Obviously, these ship tracks create sharp edges in the modelled bathymetric surface. A much higher sampling frequency and higher degree in the analysis would be needed to adequately represent those features in spherical harmonics. These residual errors together with the residual errors that appear in the areas of steep slopes (mountains, trenches) are here classified as truncation errors.

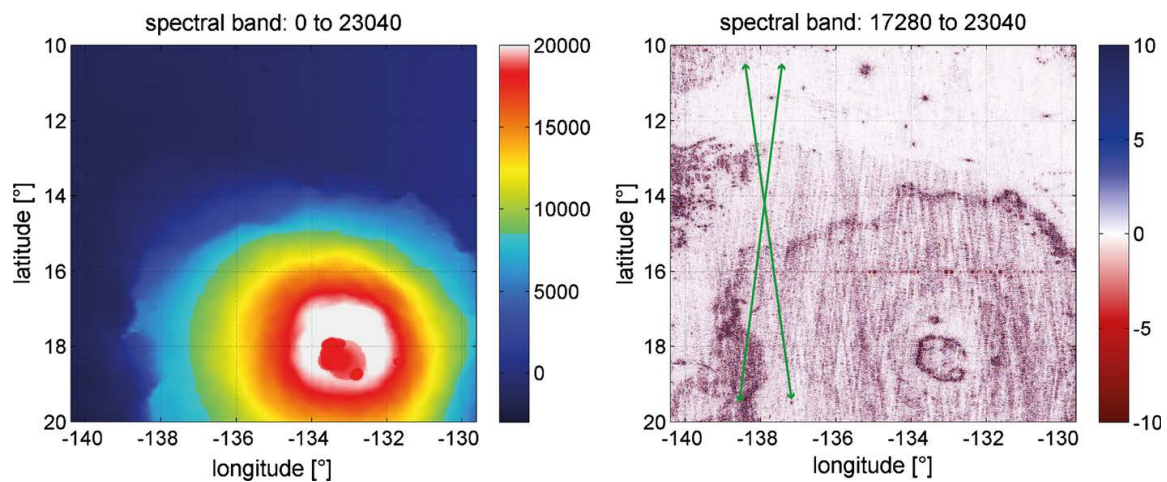


Fig. 11 Elevations around Olympus Mons obtained from a analysis and synthesis of MOLA data in the spectral band 0. . .23,040 (left) and 17,280. . .23,040 (right); the green arrows indicate the direction of the visible striping pattern; unit is metres

The minimum and maximum residual SHA/SHS error (-2447.31 and 3498.47 m, respectively) is very high compared to the analysis of Mars and Moon (see further down). Importantly, they are the result of artefacts with sharp edges (or single pixel errors) detected in the SRTM15 PLUS data set (Fig. 9) and are no sign for deficiencies in the quadrature algorithm.

4.3.3 Analysis of the Martian Topography to d/o 23,040

For Mars, the topography could be harmonically analysed to degree 23,040 with a truncation error of about 0.4 m in terms of STD (RMS = 1.94 m) in the space domain (Fig. 10, upper and middle plot). High residual errors are found around the highest elevated peaks (but not directly over the peaks), at the edges of some of the impact craters and along the deep rift valley such as the east-west-aligned Vallis Marineris. The minimum and maximum errors are -1335.80 and 937.75 m, respectively, less than in Earth's case.

Investigating different spectral bands of the MOLA topography by SHS reveals a slightly inclined striping in the MOLA data (with ~ 5 – 10 m amplitude in the spectral band 17,280. . .23,040, Fig. 11). The stripes are also visible in the spectral band 11,541. . .17,279 (not shown here). Most probably, the stripes are related to the ground tracks and ground coverage of the MOLA/MGS orbiter and illustrate the domain where MOLA DEM offers full resolution. Observation gaps existing between neighbouring ground tracks are filled by interpolation (Smith et al. 2003 and see also Sect. 4.1) and might thus be an explanation for the visible inconsistencies.

4.3.4 Analysis of the Lunar Topography to d/o 46,080

For Moon, the topography could be harmonically analysed to degree 46,080 with a standard deviation of about 0.2 m (RMS = 0.91 m) in the space domain (Fig. 12, upper and middle plot). The residuals on Moon show less co-location with topographic rough features (such as impact craters) and are generally of lower amplitude compared to those of the other planets analysed in this work. However, we find the amplitudes of the residuals slightly rising towards the poles.

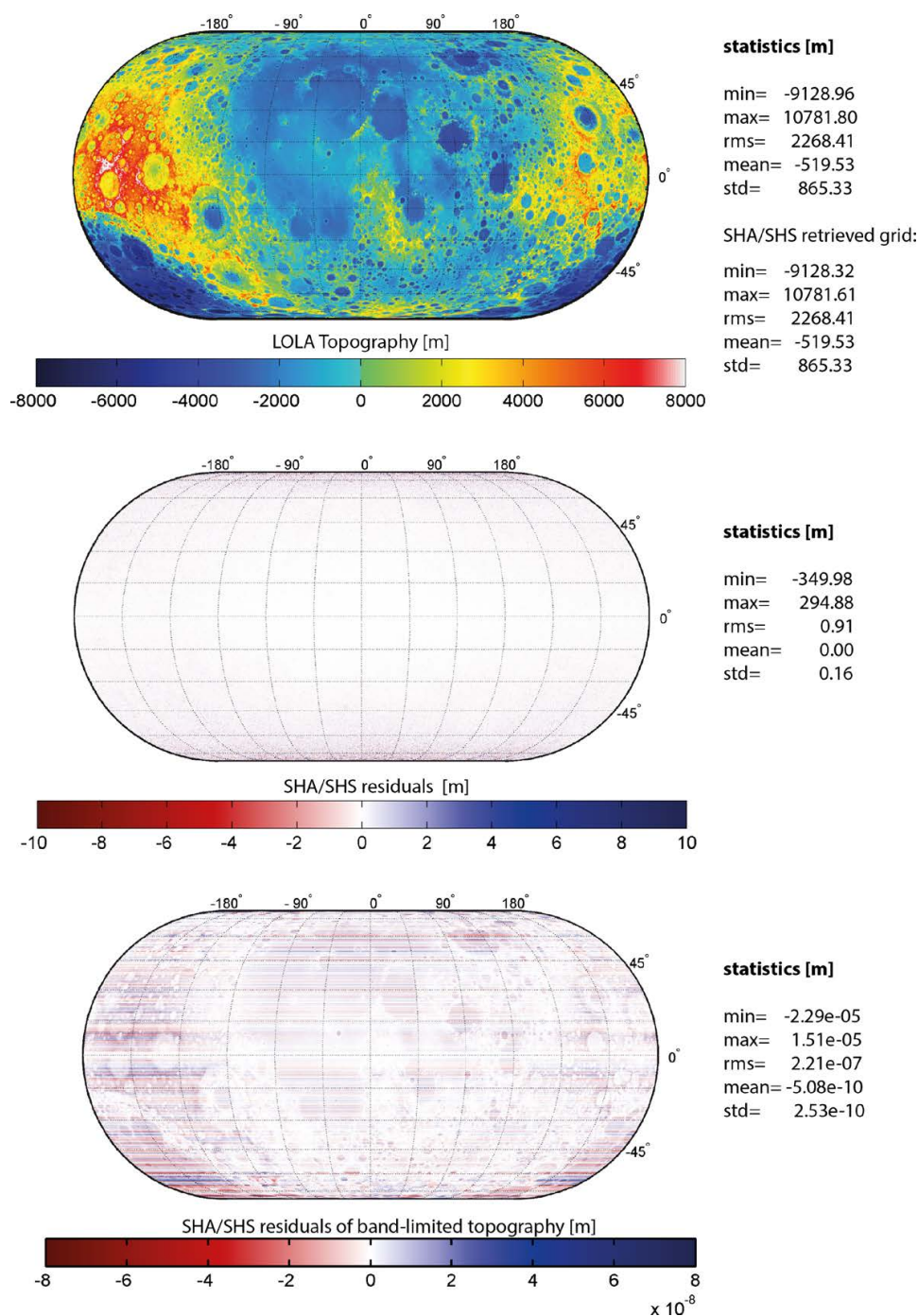


Fig. 12 Lunar topography (*upper plot*), closed-loop residuals with input topography after the first spherical harmonic analysis and synthesis (*middle plot*) and residuals of the analysis and synthesis of a band-limited input topography (to degree 46,080); unit is metres

By performing a synthesis in various spectral bands, we find certain bands affected by striping. In contrast to the striping in the MOLA data set, the stripes in LOLA data are north–south aligned and thus in along-track direction of the LRO spacecraft that was navigated on a polar orbit. In the band 23,081. . .34,620, the stripes have amplitudes at the 5- to 15-m level (Fig. 13), indicating the limit in the resolution for the LOLA data.

MOLA/MGS has an inclined orbit, and thus, also the stripes are inclined against the north–south direction. We suspect the reason for LOLA and MOLA stripes to be of similar kind and to be related to the ground track/ coverage of the laser altimeters.

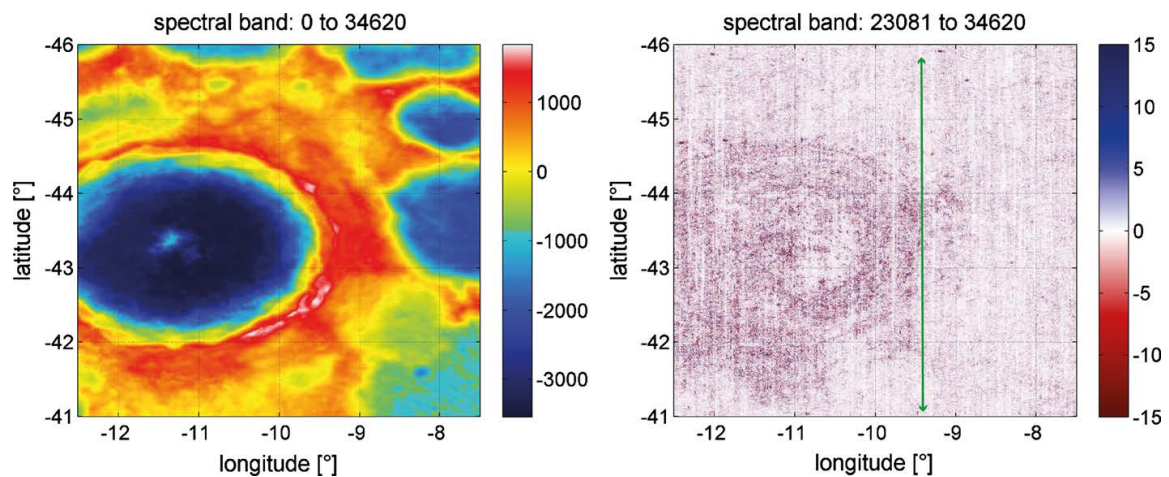


Fig. 13 Elevations around Tycho crater obtained from a analysis and synthesis of LOLA data in the spectral band 0...34,620 (*left*) and 23,081...34,620 (*right*); the *green arrows* indicate the direction of the visible striping pattern; unit is metres

4.4 Quadrature Performance at Ultra-high Degrees

4.4.1 Accuracy and Truncation Errors of the Analysis of Planetary Topography

The accuracy of the quadrature is not critically deteriorated by the choice of a higher spherical harmonic degree (see also Sect. 3.3), as the Moon's much higher resolved topography is much better represented in spherical harmonics than Earth's topography. Instead, by interpreting the residuals (=differences to input topography shown in the middle plots of Figs. 6, 10, 12) as truncation error, we learn that the choice of a higher harmonic degree in case of the Lunar topography (and the finer sampling intervals of the grid) leads to a lower truncation error (as expected). Taking the global topographic function's standard deviations as indicator for the overall roughness of a planet's topography, the Moon shows the highest variability (STD = 865.33 m), followed by Mars (STD = 303.73 m) and Earth (STD = 261.96 m). Although Earth features the smoothest surface on average, it shows the highest truncation error.

Further, we find that the accuracy of the quadrature locally is dependent on the topographic surface function itself, i.e. smoothness/roughness of the terrain, because the residuals coincide with the locations of mountains, steep slopes or edges (such as the ship-sounding data tracks in Earth's bathymetry). This was also found by Balmino et al. (2012).

4.4.2 Precision of the Quadrature at Ultra-high Degrees

The residuals of each topographic input grid with respect to the topographic grid synthesized from its computed spherical harmonic coefficients reveal the quality (i.e. accuracy) by which the topographic surface functions are represented in the spherical harmonic domain through the GLQ quadrature (Sects. 4.3.2, 4.3.3, 4.3.4) and may be interpreted as truncation errors (Sect. 4.4.1).

By performing another harmonic analysis and synthesis using band-limited topographic input grids of the three planets (obtained by synthesis using the SHCs from the initial SHA), we can investigate the precision of the GLQ quadrature in closed-loop manner (similar to the experiments done for the DH and the GLQ algorithm in Sect. 3.2 up to degree 21,600). The results—space-domain residual errors—are shown in the bottom plot

of Figs. 6, 10 and 12. The absolute amplitudes of the errors (Earth: <3 mm; Mars: <0.03 mm; Moon: <1 mm) suggest that the GLQ algorithm works very precise even at the ultra-high harmonic degrees and that the precision is not the limiting factor for the application of the algorithm to planetary topography in this work.

All residual plots from band-limited input topography reveal a striping pattern along latitude parallels, which is interrupted by white areas (indicating less or no errors) that show some obvious correlation to the topography. Similar striping patterns can be investigated for using the DH algorithm instead (not shown here). This striping is entirely non-critical for the application to digital elevation data of the planetary topography done here; nevertheless, it deserves some close-up investigation. In case of Earth, this pattern can be characterized as follows: ocean and continental areas of about ± 2000 -m elevation are free of the striping pattern; higher or lower elevated areas are affected by the striping. Thus, the floor of the large oceans (except for the ridges), the Himalayas, but also Olympus Mons on Mars are covered by striping. Due to the strict east–west alignment of the striping pattern, the error must originate from the zonal harmonic coefficients. Those are, e.g., dependent on the Legendre polynomials (LPs). However, the LPs are determined accurately using exact identities (see Sect. 3.1). Nevertheless, at very high or very low elevated points, the algorithm must be at the edge of arithmetic over-/underflow, setting the limits for the precision of the quadrature and leading to the characteristic error patterns in the spatial domain. This may be an issue for extremely high-resolution quadratures (e.g., up to some hundred thousands of degrees) some day in the future.

5 Summary and Outlook

In this work, two known algorithms—the Gauss–Legendre quadrature and the quadrature following Driscoll/Healy—and their implementation for the purpose of ultra-high (surface) spherical harmonic analysis of spheroid functions were presented in detail. We extended the implementation of the algorithms found in the SHTOOLS software package by (1) the X-number (or ERA) method for accurate computation of ALFs and (2) OpenMP directives enabling parallel computing for feasible computation times. A degree 21,600 quadrature (of a degree 21,600 band-limited topographic function) that involves the computation of over 466×10^6 parameters, shows a precision of at least 3×10^{-5} and 5×10^{-5} m in the space domain for the GL and DH algorithm, respectively. Sharing the degree-21,600 quadrature between 8 or 14 CPUs, the computation times could be reduced approximately to a sixth (to ~ 12.1 h) or a thirteenth (to ~ 5.9 h) of the single-thread time in case of the GL algorithm and to a fifth (to ~ 49.5 h) or thirteenth (to ~ 16.9 h) of the single-thread time in case of the DH algorithm. Hence, the Gauss–Legendre algorithm can be considered computationally more effective, although neither algorithm is inferior in terms of numerical precision.

The implementation of the GL quadrature was then used to harmonically analyse the Earth's topography and bathymetry (from the SRTM15 PLUS data set) to degree 43,200, the Martian topography (from MOLA data products) to degree 23,040 and the Lunar topography (from LOLA data products) to degree 46,080. The retrieved spherical harmonic coefficients gave spectral insights into the different short and ultra-short wavelength characteristics of the topography of the three bodies. Degree variances reveal that the power (variability) of the Moon's topography is significantly larger compared to the planets at all spatial scales (at least down to a half-wavelength of 500 m), especially below

scales of 200 km. The representation of the Earth's bathymetry (only) and topography (only) in terms of degree variances reveals irregularities in the bathymetry data of SRTM15 PLUS data set. The bathymetric degree variance curve exhibits a change in the decay of the spectral power around degree 2160, which indicates the limit of full resolution in contemporary bathymetry data, based on inversion of gravity from satellite altimetry. Neglecting these irregularities, we find the ocean floors making up most of the Earth's topographic variability at scales above 5 km and the continental topography making up most power below scales of 5 km (\sim degree 4000).

Importantly, the residuals and the ultra-high bands of the spectral representation may also be used to reveal artefacts and systematics/characteristics of the observation techniques used for the creation of the elevation data. In case of SRTM15 PLUS, ship tracks become clearly visible in the bathymetry and an artefact over Antarctica and the Arctic ocean was detected. In case of MOLA and LOLA, the synthesis of certain spectral bands (e.g., 2160–10,800) reveals the ground tracks of the orbiters that carried the laser altimeters.

The accuracy of the representation of the planets' topography in spherical harmonics was investigated in terms of residual errors in the space domain. The global STD of the residuals are 3.06 m for Earth (d/o 43,200), 1.94 m for Mars and 0.91 m for Moon. Apart from the rather high residuals in case of Earth, the results corroborate that choosing a higher degree in the analysis minimizes the truncation error. Among others, artefacts and ship-track edges in the SRTM15 PLUS data set might be responsible for comparatively high residuals in the case of Earth. The residuals in all cases generally show a high correlation with the topography, and most errors are found over areas of steep (or rough) terrain (e.g., mountains, trenches, crater edges). Investigation of the quadrature precision for the three cases of high-degree spherical harmonic analysis in closed-loop manner shows east-west-aligned stripes (caused by the zonal coefficients) which are pronounced in high and low elevated areas at the 1×10^{-7} m level, with the absolute errors not exceeding 3 mm for Earth, 0.03 mm for Mars and 1 mm for the Moon. As the key conclusion, both algorithms and their implementation are suitable for efficient and accurate ultra-high-degree spherical harmonic analysis of spheroidal functions, tested here up to degree 46,080. The Gauss–Legendre algorithm outperforms the Driscoll/Healy algorithm in terms of computation times and therefore is preferable.

The extension of the algorithms for solid spherical harmonic analysis (e.g., of a functional of the gravitational field) is possible and would certainly extend the applicability of the algorithms in geophysics and geodesy.

Acknowledgments This study was supported by the Australian Research Council (Grant DP12044100) and through funding from Curtin University's Office of Research and Development. Further, it was created with the support of the Technische Universität München—Institute for Advanced Study, funded by the German Excellence Initiative. We gratefully acknowledge the thorough work of Mark Wieczorek who developed SHTOOLS in the first place and distributes the code freely to the community. We also want to thank all the colleagues who were involved in the construction or contributed to any of the planetary topography data sets used in this work.

References

- Abrykosov O, Förste C, Gruber C, Shako R, Barthelmes F (2012) Harmonic analysis of the DTU10 global gravity anomalies. In: Abbasi A, Giesen N (eds) EGU General Assembly conference abstracts, vol 14, p 4945

- Andersen O, Knudsen P, Kenyon S, Factor J, Holmes S (2013) The dtu13 global marine gravity field—first evaluation. Technical report, DTU Space - National Space Institute
- Arabelos D, Tscherning C (1998) The use of least squares collocation method in global gravity field modeling. *Phys. Chem. Earth* 23(1):1–12. doi:[10.1016/S0079-1946\(97\)00234-6](https://doi.org/10.1016/S0079-1946(97)00234-6)
- Balmino G, Vales N, Bonvalot S, Briais A (2012) Spherical harmonic modelling to ultra-high degree of Bouguer and isostatic anomalies. *J Geodesy* 86(7):499–520. doi:[10.1007/s00190-011-0533-4](https://doi.org/10.1007/s00190-011-0533-4)
- Bartusch M, Berg H, Siebertz O (2008) The TanDEM-X Mission. In: 7th European conference on synthetic aperture radar (EUSAR), pp 1–4
- Becker J, Sandwell D, Smith W, Braud J, Binder B, Depner J, Fabre D, Factor J, Ingalls S, Kim SH, Ladner R, Marks K, Nelson S, Pharaoh A, Trimmer R, Von Rosenberg J, Wallace G, Weatherall P (2009) Global bathymetry and elevation data at 30 arc seconds resolution: Srtm30_plus. *Mar Geodesy* 32(4):355–371. doi:[10.1080/01490410903297766](https://doi.org/10.1080/01490410903297766)
- Bucha B, Janák J (2013) A MATLAB-based graphical user interface program for computing functionals of the geopotential up to ultra-high degrees and orders. *Comput Geosci* 56:186–196
- Claessens S (2006) Solutions to ellipsoidal boundary value problems for gravity field modelling. PhD thesis, Curtin University of Technology
- Claessens S, Hirt C (2013) Ellipsoidal topographic potential—new solutions for spectral forward gravity modelling of topography with respect to a reference ellipsoid. *J Geophys Res* 118(11):5991–6002. doi:[10.1002/2013JB010457](https://doi.org/10.1002/2013JB010457)
- Colombo O (1981) Numerical methods for harmonic analysis on the sphere. Technical report. Report no. 310, The Ohio State University
- Dassios G (2012) Ellipsoidal harmonics. Cambridge University Press, Cambridge. doi:[10.1017/CBO9781139017749](https://doi.org/10.1017/CBO9781139017749)
- Driscoll J, Healy D (1994) Computing Fourier transforms and convolutions on the 2-sphere. *Adv. Appl. Math.* 15(2):202–250. doi:[10.1006/aama.1994.1008](https://doi.org/10.1006/aama.1994.1008)
- ESA (1999) Gravity field and steady-state ocean circulation mission. Report for the mission selection of the four candidate earth explorer missions (ESA SP-1233(1)), European Space Agency
- Farr T, Rosen P, Caro E, Crippen R, Duren R, Hensley S, Kobrick M, Paller M, Rodriguez E, Roth L, Seal D, Shaffer S, Shimada K, Umland J, Werner M, Oskin M, Burbank D, Alsdorf D (2007) The shuttle radar topography mission. *Rev Geophys* 45:RG2004. doi:[10.1029/2005RG000183](https://doi.org/10.1029/2005RG000183)
- Fecher T, Pail R, Gruber T (2013) Global gravity field modeling based on GOCE and complementary gravity data. *Int J Appl Earth Obs Geoinf* 35:120–127. doi:[10.1016/j.jag.2013.10.005](https://doi.org/10.1016/j.jag.2013.10.005)
- Fukushima T (2012) Numerical computation of spherical harmonics of arbitrary degree and order by extending exponent of floating point numbers. *J Geodesy* 86(4):271–285. doi:[10.1007/s00190-011-0519-2](https://doi.org/10.1007/s00190-011-0519-2)
- Fukushima T (2015) Personal communication, IUGG Prague
- Gruber C (2011) A study on the Fourier composition of the associated Legendre functions; suitable for applications in ultra-high resolution. Scientific technical report 11/04, German Research Centre for Geosciences (GFZ), Potsdam. doi:[10.2312/GFZ.b103-11041](https://doi.org/10.2312/GFZ.b103-11041)
- Gruber C, Novak P, Sebera J (2011) FFT-based high-performance spherical harmonic transformation. *Stud Geophys Geod* 55:489–500
- Gruber C, Barthelmes F, Flechtner F, Novak P (2014) Derivation of topographic potential from global DEM models. In: Rizos C, Willis P (eds) *Earth on the edge: science for a sustainable planet: proceedings of the IAG General Assembly, Melbourne, Australia, 28 June–2 July 2011*, vol 139. Springer, Berlin, pp 535–542
- Hirt C, Kuhn M (2014) A band-limited topographic mass distribution generates a full-spectrum gravity field—gravity forward modelling in the spectral and spatial domain revisited. *J Geophys Res Solid Earth* 119(4):3646–3661. doi:[10.1002/2013JB010900](https://doi.org/10.1002/2013JB010900)
- Hirt C, Rexer M (2015) Earth 2014: 1' shape, topography, bedrock and ice-sheet models—available as gridded data and degree 10,800 spherical harmonics. *Int J Appl Earth Obs Geoinf* 39:103–112. doi:[10.1016/j.jag.2015.03.001](https://doi.org/10.1016/j.jag.2015.03.001)
- Hofsommer D (1957) On the expansion of a function in a series of spherical harmonics. Technical report. Report no. R344A, Computation Department of the Mathematical Centre, Amsterdam
- Hofsommer D, Potters M (1960) Table of Fourier coefficients of associated Legendre functions. Report r 478. knaw, Computational Department of the Mathematical Centre, Amsterdam
- Holmes S, Featherstone W (2002) A unified approach to the Clenshaw summation and the recursive computation of very high degree and order normalised associated Legendre functions. *J Geodesy* 76:279–299. doi:[10.1007/s00190-002-0216-2](https://doi.org/10.1007/s00190-002-0216-2)
- Krylov V (1962) Approximate calculation of integrals. MacMillan, New York

- Lemoine F, Smith DE, Rowlands D, Zuber M, Neumann G, Chinn D, Pavlis D (2001) An improved solution of the gravity field of Mars (GMM-2B) from Mars Global Surveyor. *J Geophys Res* 106:23,359–23,376
- Lemoine FG, Goossens S, Sabaka TJ, Nicholas JB, Mazarico E, Rowlands DD, Loomis BD, Chinn DS, Neumann GA, Smith DE et al (2014) Grgm900c: a degree 900 lunar gravity model from grail primary and extended mission data. *Geophys Res Lett* 41(10):3382–3389
- Marks K, Smith W, Sandwell D (2010) Evolution of errors in the altimetric bathymetry model used by Google Earth and GEBCO. *Mar Geophys Res* 31(3):223–238
- Moritz H (1978) Least-squares collocation. *Rev Geophys* 16(3):421–430. doi:[10.1029/RG016i003p00421](https://doi.org/10.1029/RG016i003p00421)
- Moritz H (2000) Geodetic Reference System 1980. *J Geodesy* 74(1):128–162. doi:[10.1007/s001900050278](https://doi.org/10.1007/s001900050278)
- Neumann G (2010) 2009 Lunar Orbiter Laser Altimeter raw data set, lro-l-lola-4-gdr-v1.0, pds. Technical report, NASA
- Pail R, Goiginger H, Schuh W, Höck E, Brockmann J, Fecher T, Mayer-Gürr T, Kusche J, Jäggi A, Rieser D, Gruber T (2011) Combination of GOCE data with complementary gravity field information (GOCO). In: Proceedings of 4th international GOCE user workshop, Munich, 31 March 2011
- Rummel R, Rapp R, Sünkel H, Tscherning C (1988) Comparisons of global topographic/isostatic models to the Earth's observed gravity field. OSU report 388, Ohio State University
- Sandwell DT, Müller RD, Smith WH, Garcia E, Francis R (2014) New global marine gravity model from CryoSat-2 and Jason-1 reveals buried tectonic structure. *Science* 346(6205):65–67
- Smith WH, Sandwell DT (1994) Bathymetric prediction from dense satellite altimetry and sparse shipboard bathymetry. *J Geophys Res Solid Earth* (1978–2012) 99:21803–21824
- Smith DE, Zuber M, Neumann G, Guinness E, Slavney S (2003) Mars global surveyor laser altimeter mission experiment gridded data record (mgs-m-mola-5-megdr-l3-v1.0). Technical report, NASA Planetary Data System
- Smith DE, Zuber M, Jackson G, Cavanaugh J, Neumann G, Riris H, Sun X, Zellar R, Coltharp C, Connelly J, Katz R, Kleyner I, Liiva P, Matuszeski A, Mazarico E, McGarry J, Novo-Gradac AM, Ott M, Peters C, Ramos-Izquierdo L, Ramsey L, Rowlands D, Schmidt S, Scott I VStanley, Shaw G, Smith J, Swinski JP, Torrence M, Unger G, Yu A, Zagwodzki T (2010) The Lunar Orbiter Laser Altimeter investigation on the Lunar Reconnaissance Orbiter mission. *Space Sci Rev* 150(1–4):209–241. doi:[10.1007/s11214-009-9512-y](https://doi.org/10.1007/s11214-009-9512-y)
- Sneeuw N (1994) Global spherical harmonic analysis by least-squares and numerical quadrature methods in historical perspective. *Geophys J Int* 118:707–716
- Tachikawa T, Hato M, Kaku M, Iwasaki A (2011) Characteristics of ASTER GDEM version 2. In: IEEE international geoscience and remote sensing symposium (IGARSS). IEEE, pp 3657–3660
- Torge W (2001) *Geodesy*, 3rd edn. Walter de Gruyter, Berlin
- Walker JS (1996) *Fast Fourier transforms*, vol 24. CRC Press, Boca Raton
- Wieczorek M (2007) Gravity and topography of the terrestrial planets. *Treatise Geophys* 10:165–206. doi:[10.1016/B978-0-444-52748-6/00156-5](https://doi.org/10.1016/B978-0-444-52748-6/00156-5)
- Wieczorek M (2015) Gravity and topography of the terrestrial planets. In: Schubert G (ed) *Treatise Geophys*, vol 10, 2nd edn. Elsevier, Oxford, pp 153–193. doi:[10.1016/B978-0-444-53802-4.00169-X](https://doi.org/10.1016/B978-0-444-53802-4.00169-X)
- Wood C, Anderson L (1978) New morphometric data for fresh lunar craters. *Lun Planet Sci Conf Proc* 9:3669–3689

P.4 Publication IV: Layer-based modelling of the Earth's gravitational potential up to 10km-scale in spherical harmonics in spherical and ellipsoidal approximation

Reference:

Rexer M., Hirt C., Claessens S., Tenzer R. : Layer-based modelling of the Earth's gravitational potential up to 10km-scale in spherical harmonics in spherical and ellipsoidal approximation; *Surveys in Geophysics*, DOI: 10.1007/s10712-016-9382-2, 2016.

Copyright

This work originally has been published in *Surveys in Geophysics*, available at <http://link.springer.com/>, and is reprinted here with permission of Springer. Copyright has been transferred to Springer.

Short Summary

Spectral forward-modelling with respect to a reference ellipsoid, leading to the ellipsoidal topographic potential (ETP), is less affected by mapping effects and provides the gravity spectra compatible to observation-based geodetic gravity models. The recently developed harmonic combination (HC) method that computes the ETP is conceptually extended for application with multiple volumetric mass layers, allowing a better approximation of Earth's mass distribution. Additionally to efficient integral solutions based on binominal series, also the rigorous expressions for layer-based modelling w.r.t. a reference ellipsoid are given. Further, often ignored aspects such as aliasing and convergence behavior are of great importance for correct spectral forward modelling. The provided new expressions are used with the Earth2014 boundary data up to degree 2160/90. Computed potential models are validated using gravity observations over Antarctica. Benefits of layer-modelling as compared to single-layer (rock-equivalent-topography) modelling are detected using GOCE-satellite observations. Studying geometric and gravity differences between modelling w.r.t to a spherical or ellipsoidal references confirms characteristic spectral differences. Since space domain differences are rather small (up to ~ 3 mGal), modelling with an ellipsoidal reference is mainly necessary for applications requiring high accuracy or high-resolution.

Declaration of own contribution

(MR: Moritz Rexer; CH: Christian Hirt; SC: Sten Claessens; RT: Robert Tenzer)

RT initially encouraged to develop a layer approach with the HC-method. CH and SC pursued and thought through the idea and offered the development of such a method to MR. MR then designed the study in reconciliation with CH and SC and developed the presented methods for the most parts. MR set up the software and adapted the HC-program developed by SC to multiple layers. MR prepared the data and created all numerical results. The interpretation and analysis was initially done by MR and improved by the co-authors. MR drafted the entire text and created all figures and tables.

The overall own contribution of MR for P-IV is estimated at 85 %, which is the (rounded) average value of the percentage values estimated for the six criteria listed in the table below (Tab. P.4).

Criteria	Estimated own contribution
Computation and results	100 %
Ideas and study design	35 %
Analysis and interpretation	80 %
Text	90 %
Figures	100 %
Tables	100 %
Total	84.1 %

Tab. P.4 – Criteria and estimated contribution share of Moritz Rexer for *P-IV*

Confirmation by the Co-Authors

We hereby confirm the correctness of the declaration of own contribution by Moritz Rexer for the publication:

Rexer M., Hirt C., Claessens S., Tenzer R. : *Layer-based modelling of the Earth's gravitational potential up to 10km-scale in spherical harmonics in spherical and ellipsoidal approximation; Surveys in Geophysics*, DOI: [10.1007/s10712-016-9382-2](https://doi.org/10.1007/s10712-016-9382-2), 2016.

Christian Hirt

Institut für Astronomische und Physikalische Geodäsie, Technische Universität München, Germany.

Signature: Christian Hirt Date: 27/01/2017

Sten Claessens

Department of Spatial Sciences, The Institute for Geoscience Research, Curtin University, Perth, Australia.

Signature: S.J. Claessens Date: 18/11/2016

Robert Tenzer

New Technologies for the Information Society, University of West Bohemia, Plzeň, Czech Republic.

Signature: Robert Tenzer Date: 18 November, 2016

Layer-Based Modelling of the Earth's Gravitational Potential up to 10-km Scale in Spherical Harmonics in Spherical and Ellipsoidal Approximation

Moritz Rexer¹ · Christian Hirt¹ · Sten Claessens² · Robert Tenzer^{3,4}

Received: 29 March 2016 / Accepted: 10 August 2016
© Springer Science+Business Media Dordrecht 2016

Abstract Global forward modelling of the Earth's gravitational potential, a classical problem in geophysics and geodesy, is relevant for a range of applications such as gravity interpretation, isostatic hypothesis testing or combined gravity field modelling with high and ultra-high resolution. This study presents spectral forward modelling with volumetric mass layers to degree 2190 for the first time based on two different levels of approximation. In spherical approximation, the mass layers are referred to a sphere, yielding the spherical topographic potential. In ellipsoidal approximation where an ellipsoid of revolution provides the reference, the ellipsoidal topographic potential (ETP) is obtained. For both types of approximation, we derive a mass layer concept and study it with layered data from the Earth2014 topography model at 5-arc-min resolution. We show that the layer concept can be applied with either actual layer density or density contrasts w.r.t. a reference density, without discernible differences in the computed gravity functionals. To avoid aliasing and truncation errors, we carefully account for increased sampling requirements due to the exponentiation of the boundary functions and consider all numerically relevant

✉ Moritz Rexer
m.rexer@tum.de

Christian Hirt
c.hirt@tum.de

Sten Claessens
s.claessens@curtin.edu.au

Robert Tenzer
rtenger@sgg.whu.edu.cn

¹ Institute of Astronomical and Physical Geodesy, Institute for Advanced Study, Technische Universität München, 21, Arcisstrasse, 80333 Munich, Germany

² Department of Spatial Sciences, The Institute for Geoscience Research, Western Australian Geodesy Group, Curtin University, GPO Box U1987, Perth, WA 6845, Australia

³ The Key Laboratory of Geospace Environment and Geodesy, Wuhan University, Wuhan, China

⁴ New Technologies for the Information Society (NTIS), University of West Bohemia, Plzeň, Czech Republic

terms of the involved binominal series expansions. The main outcome of our work is a set of new spectral models of the Earth's topographic potential relying on mass layer modelling in spherical and in ellipsoidal approximation. We compare both levels of approximations geometrically, spectrally and numerically and quantify the benefits over the frequently used rock-equivalent topography (RET) method. We show that by using the ETP it is possible to avoid any displacement of masses and quantify also the benefit of mapping-free modelling. The layer-based forward modelling is corroborated by GOCE satellite gradiometry, by in-situ gravity observations from recently released Antarctic gravity anomaly grids and degree correlations with spectral models of the Earth's observed geopotential. As the main conclusion of this work, the mass layer approach allows more accurate modelling of the topographic potential because it avoids 10–20-mGal approximation errors associated with RET techniques. The spherical approximation is suited for a range of geophysical applications, while the ellipsoidal approximation is preferable for applications requiring high accuracy or high resolution.

Keywords Gravity forward modelling · Ellipsoidal topographic potential · Harmonic combination method · Spherical harmonics · Spherical approximation · Ellipsoidal approximation · Layer concept · Earth2014

1 Introduction

1.1 Motivation and Related Work

Global modelling of the Earth's gravitational potential from its underlying mass distribution in spherical harmonics is a classical problem in geophysics and geodesy (e.g., Balmino et al. 1973; Rapp 1982; Rummel et al. 1988; Wieczorek 2007, 2015). The solution to this problem can be used for testing of topographic/isostatic hypothesis (Rummel et al. 1988; Göttl and Rummel 2009; Hirt et al. 2012; Grombein et al. 2014), modelling of Bouguer gravity (Balmino et al. 2012; Wieczorek 2015; Rexer et al. 2015), smoothing or reduction of the Earth's gravity field and its observations [as, for example, needed for Stokes' geodetic boundary value problem or improved interpolation/prediction with remove-compute-restore techniques (Grombein et al. 2014)], computation of fill-in gravity for combined gravity field models (Pavlis et al. 2007, 2012; Fecher et al. 2013), omission error modelling (Hirt et al. 2011; Rexer and Hirt 2015a) and the evaluation of digital elevation models (Rexer et al. 2015).

For some of the listed applications, a forward model that is as close as possible to the actual gravity field is desirable. Aiming at such a “perfect” synthetic gravitational model, an accurate mass model of the Earth is required. Mass models deliver information about the physical geometry of Earth along with density information about its interior. A perfect mass model would be able to describe the masses in terms of infinitesimal small bodies (such as rectangular prisms or tesseroids) at all 3D positions of Earth. Together with an adequate implementation of Newton's law of gravitation, which means numerical integration over all masses (see, for example, Kuhn and Seitz 2005; Grombein et al. 2014), this mass model would allow to accurately determine the gravitational potential of Earth. However, such a mass model in reality is not practicable as the computational requirements are very challenging, and more prohibitively, because the required density and geometric information is neither available globally nor in 3D with adequate resolution. Today,

globally consistent physical surface information (usually provided in terms of digital elevation models) at best is given with a resolution of ~ 12 m [TanDEM-X satellite mission: Bartusch et al. 2008] and a vertical accuracy of ~ 4 m (Rexer and Hirt 2016). At short scales (~ 10 km or less), it is mainly the masses of the crust—the upper part of the lithosphere—and hydrosphere that cause substantial anomalous gravitational signals. The anomalous potential that originates from the Earth's interior (upper mantle or below) has long-wavelength character. Satellite-borne and terrestrial observation techniques result in complete (global) high-resolution models of the topographic elevation and to some extent also of the bathymetric depth, water bodies and ice sheets (Hirt and Rexer 2015), making forward modelling of short-scale (=crustal) gravity signals possible to ultra-high resolution, e.g., up to ~ 2 km scale (Balmino et al. 2012) and up to ~ 200 m scale (Hirt et al. 2013).

In contrast, available density information for the lithosphere (crust and upper mantle, down to about 30 km depth) is limited to a lateral resolution of about 110 km [CRUST1.0 (Laske et al. 2012) and LITHO1.0 (Pasyanos et al. 2014)]. Considering the density profile (vertical resolution), which is derived mainly from seismic tomography, presently available models only distinguish between 8 and 10 different layers, assuming that the density is not varying vertically within each layer. This short review of mass models already suggests that it is convenient and practicable to model Earth's masses in terms of layers since layers are a natural way to describe the structure of the physical Earth.

Forward modelling can either be conducted by Newtonian integration over Earth's masses in the space domain, e.g., by using rigorous analytical integration formulas for rectangular prisms (Nagy et al. 2000, 2002) or tesseroids (Grombein et al. 2013; Heck and Seitz 2007), or in the spectral domain, by using relations among surface spherical harmonic coefficients of the geometric boundary surfaces. Historically (Lee and Kaula 1967; Balmino et al. 1973; Rummel et al. 1988) and recently (Wieczorek 2007, 2015; Forsberg and Jensen 2015; Hirt et al. 2015) forward modelling approaches were often used in combination with “single-density” mass models, also known as rock-equivalent topography (RET) models. RET modelling involves a compression of all masses to a layer of constant (rock) density, resulting in approximation errors in the order of several dozens of mGal; see, for example, Grombein et al. (2016) and Kuhn and Hirt (2016). Therefore, it is very useful to have forward modelling approaches that are adapted to rigorous modelling of mass layers. These are available for spatial domain modelling in spherical (Kuhn and Seitz 2005) and ellipsoidal (Grombein et al. 2014) approximation. In spherical approximation, the topographic masses are forward modelled relative to a mass sphere. Correspondingly, in ellipsoidal approximation, a mass ellipsoid as a much closer approximation of the real Earth is used to provide the reference for the forward modelling. For spectral domain modelling a layer-based approach only was formulated in spherical approximation (Pavlis and Rapp 1990; Tenzer et al. 2010, 2015; Root et al. 2016). The spectral approach has mainly been used to create low resolution models, e.g., in

- Pavlis and Rapp (1990): to d/o 360, distinguishing between 6 different terrain types corresponding to the explicit modelling of 4 layers—topography, ocean, ice sheets/glaciers and lake water—as represented by the OSUJAN89 topographic database
- Tenzer et al. (2010): to d/o 90, only ice layer based on the CRUST2.0 model and the surface heights in GTOPO30 (US Geological Survey, released 1996)
- Tenzer et al. (2015): to d/o 180 based on the CRUST1.0 model as contained in the 9 layers—topography, ocean, polar ice sheets, sediments (3 layers) and consolidated crust (3 layers)—of *Earth's spectral crustal model* (ESCM180: Chen and Tenzer 2014)

- Tenzer et al. (2016): to d/o 360 based on 4 layers—topography, ocean, inland lakes/seas and ice sheets—of the Earth2014 model (Hirt and Rexer 2015)
- Root et al. (2016): to d/o 1800 based on 2 layers—topography and ocean—of GTOPO30

and also for ultra-high-resolution modelling [Balmino et al. (2012): d/o 10800 based on four layers—topography, ocean, inland lakes/seas and ice sheets—of the ETOPO1 model (Amante and Eakins 2009)]. Note that in the work of Balmino et al. (2012), Tenzer et al. (2010) and Root et al. (2016) the integration is facilitated using a binominal series. In these cited works, the series expansion is evaluated only up to the third-order term resulting in (unknown) truncation errors (see Sect. 2.3), while Pavlis and Rapp (1990) present a rigorous integration which is more accurate but computationally more demanding, especially for high resolutions.

Recently, Claessens and Hirt (2013) have developed a spherical harmonic technique to model the Earth's gravitational potential in ellipsoidal approximation, i.e. with respect to a reference ellipsoid. In contrast to the spherical concepts of Rummel et al. (1988); Pavlis and Rapp (1990); Balmino et al. (2012); Wiczorek (2015); Tenzer et al. (2015)—where the topographic masses are considered relative to a reference sphere—the *Harmonic Combination Method* (HCM) (Claessens and Hirt 2013) models the topographic masses considered relative to a reference ellipsoid. Thus, the HCM provides the gravity spectrum to the same level of approximation (w.r.t. the same reference) as most spherical harmonic gravity field models based on observations available at IAG's International Center for Global Earth Models (ICGEM: <http://icgem.gfz-potsdam.de/ICGEM/>). This, as will be shown, is a major advantage especially when it comes to combining and comparing the forward models with satellite data or other terrestrial data.

We may thus define—because of the underlying ellipsoidal approximation—Claessens and Hirt (2013) to provide a solution to the *ellipsoidal topographic potential* (ETP) while the methods based on a spherical approximation of the Earth's masses provide a solution to the *spherical topographic potential* (STP).

Tenzer et al. (2015) and Root et al. (2016) provide the framework for layer-based modelling of the STP. For the ETP, such a framework is still missing. The HCM as formulated in Claessens and Hirt (2013) is designed for a single-density mass model, but it can be reformulated to adopt layer-based mass models, as will be shown in this contribution.

1.2 This Work: Contributions to Spectral Forward Modelling

In this contribution, we formulate a new spherical harmonic approach to compute the ETP from arbitrary volumetric layers having laterally varying density. The approach is based on the *Harmonic Combination Method* (Claessens and Hirt 2013) and allows the layers to be referenced to the surface of some reference ellipsoid. The new approach is then validated by modelling the Earth's gravitational potential as implied by the masses of layers of the solid crust, ocean water, lake water and ice sheets up to spherical harmonic degree 2190 (~ 10 km).

First, we recapitulate known expressions for layer-based spherical harmonic modelling of the STP (with layers referenced to the sphere) (Sect. 2.1). In the next step, we make the transition from the spherical to the ellipsoidal case and formulate new expressions for layer-based spherical harmonic modelling of the ETP (with layers referenced to the ellipsoid) (Sect. 2.2). Then, a layer concept based on the layers of the Earth2014 (Hirt and

Rexer 2015) data set (Sect. 3) and two ways of applying it within the previously introduced forward modelling approaches are defined (Sect. 3.1 and 3.2). The gravitational spectra and signals of the layer-based ETP are computed with 10-km spatial resolution (Sect. 4.1) and validated using GOCE satellite gradiometry (Sect. 4.2), other gravity field models (Sect. 4.3) and terrestrial observations (Sect. 4.4). Finally, differences between the ETP and the STP are elaborated in detail (Sect. 4.5) and conclusions are drawn (Sect. 5).

2 Spectral Forward Modelling of the Gravitational Potential Based on Volumetric Layers of Laterally Varying Density

Let $V(P)$ be the gravitational potential at a point P exterior to the Earth's body B . Following Newton's law of gravitation and neglecting the presence of atmospheric masses, it may be written as the integral over the Earth's mass distribution (see, for example, Heiskanen and Moritz 1967; Sanso and Sideris 2013)

$$V(P) = G \int_B \frac{\rho(Q)}{l_{PQ}} dB \tag{1}$$

where G is the Newtonian gravitational constant, $\rho(> 0)$ is the density value associated with the infinitesimal volume element $dB = r_B^2 \sin \theta dr d\theta d\lambda$ at Q with $Q \in B$ and l_{PQ} being the Euclidean distance between P and the respective mass element at Q . In order to get Eq. 1 in a spherical coordinate system (P and Q are then defined by the coordinate triplet: geocentric distance r , longitude λ , co-latitude θ), the reciprocal distance $1/l_{PQ}$ has to be replaced by its spherical harmonic expansion. Rummel et al. (1988) show that Eq. 1 can then be represented as spherical harmonic series of the form

$$V(P) = \frac{GM}{R} \sum_{n=0}^{\infty} \sum_{m=-n}^n \left(\frac{R}{r_P}\right)^{n+1} \times \left\{ \frac{1}{M(2n+1)} \int_B \left(\frac{r_Q}{R}\right)^n \rho(Q) \bar{Y}_{nm}(\theta_Q, \lambda_Q) dB \right\} \bar{Y}_{nm}(\theta_P, \lambda_P) \tag{2}$$

with the mass of Earth M , its mean radius R , the geocentric radii of the computation point r_P and the source point r_Q , the spherical harmonic degree n and order m . \bar{Y}_{nm} denote the well-known set of fully normalised Laplace's surface spherical harmonic functions

$$\bar{Y}_{nm}(\theta, \lambda) = \bar{P}_{nm}(\cos \theta) \begin{cases} \cos(m\lambda) & \text{for } m \leq 0 \\ \sin(m\lambda) & \text{for } m > 0 \end{cases} \tag{3}$$

with \bar{P}_{nm} being the fully normalised (4π -normalised) associated Legendre functions of the first kind. The term in curly brackets in Eq. 2 now contains the integration over the Earth's mass distribution and can alternatively be represented as a set of dimensionless fully normalised coefficients

$$\bar{V}_{nm} = \frac{3}{\bar{\rho}R^3(2n+1)} \frac{1}{4\pi} \int_B \left(\frac{r_Q}{R}\right)^n \rho(Q) \bar{Y}_{nm}(\theta_Q, \lambda_Q) dB, \tag{4}$$

that can be subdivided into their cosine- and sine-assigned equivalents, C_{nm} and S_{nm} , according to Eq. 3, where M is replaced by $\frac{4}{3}\pi\bar{\rho}R^3$ and with $\bar{\rho}$ being the mean density of Earth. Then, Eq. 2 can be rewritten conveniently as

$$V(P) = \frac{GM}{R} \sum_n^\infty \sum_{m=-n}^n \left(\frac{R}{r_p}\right)^{n+1} \bar{V}_{nm} \bar{Y}_{nm}(\theta_P, \lambda_P). \tag{5}$$

Now, let's consider an Earth that is subdivided into a set of volumetric mass layers Ω_ω ($\omega = [1, 2, \dots, \omega_{\max}]$) fulfilling the following requirements:

- (i) ρ varying only in the lateral direction in each layer ($\rho^{(\Omega_\omega)}$ is radially invariant: $\rho^{(\Omega_\omega)}(\theta, \lambda)$),
- (ii) each layer having a defined upper bound (UB) and lower bound (LB) $(r_{\text{LB}}^{(\Omega_\omega)} \leq r_{\text{UB}}^{(\Omega_\omega)})$,
- (iii) the layer's boundaries being entirely inside Earth's body $(r_{\text{UB}}^{(\Omega_\omega)} \leq r_B)$
- (iv) the layers being uniquely separated by their boundaries $(\Omega_\omega \cap \Omega_{\omega+1} \equiv \emptyset)$
- (v) and the set of layers (including the remaining volumetric body inside the lower most layer boundary) forms a complete subset of Earth's body $(\sum_\omega \Omega_\omega \equiv B)$.

Then, the gravitational potential $V(P)$ in Eq. 5 may be written as a sum of the gravitational potential of each layer $V(P)^{(\Omega_\omega)}$

$$\begin{aligned} V(P) &= \sum_\omega V(P)^{(\Omega_\omega)} = \frac{GM}{R} \sum_n^\infty \sum_{m=-n}^n \left(\frac{R}{r_p}\right)^{n+1} \bar{V}_{nm}^{(\Omega_1)} \bar{Y}_{nm}(\theta_P, \lambda_P) \\ &+ \frac{GM}{R} \sum_n^\infty \sum_{m=-n}^n \left(\frac{R}{r_p}\right)^{n+1} \bar{V}_{nm}^{(\Omega_2)} \bar{Y}_{nm}(\theta_P, \lambda_P) \\ &+ \dots + \frac{GM}{R} \sum_n^\infty \sum_{m=-n}^n \left(\frac{R}{r_p}\right)^{n+1} \bar{V}_{nm}^{(\Omega_{\max})} \bar{Y}_{nm}(\theta_P, \lambda_P) \\ &= \frac{GM}{R} \sum_n^\infty \sum_{m=-n}^n \left(\frac{R}{r_p}\right)^{n+1} \sum_\omega \bar{V}_{nm}^{(\Omega_\omega)} \bar{Y}_{nm}(\theta_P, \lambda_P). \end{aligned} \tag{6}$$

Thus, the fully normalised coefficients in Eqs. 4 and 9 are the sum of the respective coefficients of all layers

$$\bar{V}_{nm} = \sum_\omega \bar{V}_{nm}^{(\Omega_\omega)} \tag{7}$$

The fully normalised potential coefficients of a layer $\bar{V}_{nm}^{(\Omega_\omega)}$ are given by the global radial integration of the layer's masses

$$\begin{aligned} \bar{V}_{nm}^{(\Omega_\omega)} &= \frac{3}{\bar{\rho}R^3(2n+1)} \frac{1}{4\pi} \int_{\Omega_\omega} \left(\frac{r_Q}{R}\right)^n \rho^{(\Omega_\omega)}(\theta_Q, \lambda_Q) \bar{Y}_{nm}(\theta_Q, \lambda_Q) d\Omega_\omega \\ &= \frac{3}{\bar{\rho}R^3(2n+1)} \frac{1}{4\pi} \int_{\lambda=0}^{2\pi} \int_{\theta=0}^{\pi} \int_{r_{\text{LB}}^{(\Omega_\omega)}}^{r_{\text{UB}}^{(\Omega_\omega)}} \left(\frac{r_Q}{R}\right)^n \\ &\quad \times \rho^{(\Omega_\omega)}(\theta_Q, \lambda_Q) \bar{Y}_{nm}(\theta_Q, \lambda_Q) r_Q^2 \sin\theta dr d\theta d\lambda \end{aligned} \tag{8}$$

where $\rho^{(\Omega_\omega)}$ denotes the layers density distribution. With moving the reference radius outside the integrals, we then write (see Rummel et al. 1988)

$$\bar{V}_{nm}^{(\Omega_\omega)} = \frac{3}{\bar{\rho}R(2n+1)} \frac{1}{4\pi} \int_{\lambda=0}^{2\pi} \int_{\theta=0}^{\pi} \Omega^{(\omega)} \bar{Y}_{nm}(\theta_Q, \lambda_Q) \sin \theta d\theta d\lambda \quad (9)$$

where $\Omega^{(\omega)}$ denotes the radial integration of the layer's masses

$$\Omega^{(\omega)} = \int_{r_{LB}^{(\Omega_\omega)}}^{r_{UB}^{(\Omega_\omega)}} \left(\frac{r_Q}{R}\right)^{n+2} \rho^{(\Omega_\omega)}(\theta_Q, \lambda_Q) dr. \quad (10)$$

Since $\rho^{(\Omega_\omega)}$ is assumed to be a function of λ and θ only (and thus constant in radial direction within each layer), the solution of the integral in Eq. 10 yields

$$\Omega^{(\omega)} = \rho^{(\Omega_\omega)}(\theta_Q, \lambda_Q) \frac{R}{n+3} \left[\left(\frac{r_{UB}^{(\Omega_\omega)}}{R}\right)^{n+3} - \left(\frac{r_{LB}^{(\Omega_\omega)}}{R}\right)^{n+3} \right]. \quad (11)$$

Then, consider that the integral in Eq. 10 can also be defined with respect to the ellipsoidal radius by two separate integrals, e.g., by

$$\Omega^{(\omega)} = \int_{r=r_{LB}^{(\Omega_\omega)}}^{r_e} \left(\frac{r_Q}{R}\right)^{n+2} \rho^{(\Omega_\omega)}(\theta_Q, \lambda_Q) dr + \int_{r=r_e}^{r_{UB}^{(\Omega_\omega)}} \left(\frac{r_Q}{R}\right)^{n+2} \rho^{(\Omega_\omega)}(\theta_Q, \lambda_Q) dr. \quad (12)$$

The above (split) integral solution holds for all possible vertical arrangements of layer boundaries (where all, none or only a part of the masses of a layer are located within the reference ellipsoid), as shown in Claessens and Hirt (2013) for single-layer modelling. Then, with $\rho^{(\Omega_\omega)}$ being radially invariant, the solution to the integral in Eq. 12 becomes

$$\begin{aligned} \Omega^{(\omega)} &= \rho^{(\Omega_\omega)}(\theta_Q, \lambda_Q) \frac{R}{n+3} \\ &\times \left(\left[\left(\frac{r_{UB}^{(\Omega_\omega)}}{R}\right)^{n+3} - \left(\frac{r_e}{R}\right)^{n+3} \right] - \left[\left(\frac{r_{LB}^{(\Omega_\omega)}}{R}\right)^{n+3} - \left(\frac{r_e}{R}\right)^{n+3} \right] \right), \end{aligned} \quad (13)$$

which essentially is the same as Eq. 11, since $\left(\frac{r_e}{R}\right)^{n+3}$ cancels out in Eq. 13. Starting from this solution to the radial integral of the masses within a layer Ω_ω —which will turn out to be of mathematically convenient form—we will derive the potential $V(P)^{(\Omega_\omega)}$ of a volumetric layer in spherical approximation in Sect. 2.1 and in ellipsoidal approximation in Sect. 2.2.

2.1 Layer-Based Modelling with Respect to a Reference Sphere

The potential based on volumetric layers of laterally variable density as given by Eq. 6 modelled with respect to a reference sphere means—in simple words—a spherical approximation of Earth's masses and yields the *spherical topographic potential* V^{STP} . A solution to the layer-based STP was given already by Pavlis and Rapp (1990), Tenzer et al. (2015) and other works (see Sect. 1) and is recapitulated in own notation here.

The first spherical approximation that is introduced is setting

$$r_e = R \quad (14)$$

in Eq. 13, which yields the spherical approximated mass of the layer

$$\Omega^{(STP,\omega)} = \rho^{(\Omega_\omega)}(\theta_Q, \lambda_Q) \frac{R}{n+3} \left(\left[\left(\frac{r_{UB}^{(\Omega_\omega)}}{R} \right)^{n+3} - 1 \right] - \left[\left(\frac{r_{LB}^{(\Omega_\omega)}}{R} \right)^{n+3} - 1 \right] \right). \quad (15)$$

The second spherical approximation is made by describing the layer's boundaries with respect to the reference sphere as

$$\begin{aligned} r_{UB}^{(\Omega_\omega)} &= R + H_{UB}^{(\Omega_\omega)} \\ r_{LB}^{(\Omega_\omega)} &= R + H_{LB}^{(\Omega_\omega)} \end{aligned} \quad (16)$$

where $H_{UB}^{(\Omega_\omega)}$ and $H_{LB}^{(\Omega_\omega)}$ denote the orthometric height of the upper and the lower boundary of Ω_ω , respectively. We may then introduce the well-known binominal expansion for both terms in square brackets in Eq. 15 (see Rummel et al. 1988)

$$\begin{aligned} \left(\frac{r_{UB}^{(\Omega_\omega)}}{R} \right)^{n+3} - 1 &= \sum_{k=1}^{n+3} \binom{n+3}{k} \left(\frac{H_{UB}^{(\Omega_\omega)}}{R} \right)^k = \sum_{k=1}^{n+3} \frac{1}{k!} \prod_{i=1}^k (n+4-i) \left(\frac{H_{UB}^{(\Omega_\omega)}}{R} \right)^k \\ \left(\frac{r_{LB}^{(\Omega_\omega)}}{R} \right)^{n+3} - 1 &= \sum_{k=1}^{n+3} \binom{n+3}{k} \left(\frac{H_{LB}^{(\Omega_\omega)}}{R} \right)^k = \sum_{k=1}^{n+3} \frac{1}{k!} \prod_{i=1}^k (n+4-i) \left(\frac{H_{LB}^{(\Omega_\omega)}}{R} \right)^k \end{aligned} \quad (17)$$

and yield

$$\begin{aligned} \Omega^{(STP,\omega)} &= \rho^{(\Omega_\omega)}(\theta_Q, \lambda_Q) \frac{R}{n+3} \left(\sum_{k=1}^{n+3} \binom{n+3}{k} \left(\frac{H_{UB}^{(\Omega_\omega)}}{R} \right)^k - \sum_{k=1}^{n+3} \binom{n+3}{k} \left(\frac{H_{LB}^{(\Omega_\omega)}}{R} \right)^k \right) \\ &= \rho^{(\Omega_\omega)}(\theta_Q, \lambda_Q) \frac{R}{n+3} \sum_{k=1}^{n+3} \binom{n+3}{k} \left(\left(\frac{H_{UB}^{(\Omega_\omega)}}{R} \right)^k - \left(\frac{H_{LB}^{(\Omega_\omega)}}{R} \right)^k \right). \end{aligned} \quad (18)$$

Inserting Eq. 18 into Eq. 9 gives, after moving the double integral into the binominal series, the solution to the layer's spherical topographic potential

$$\begin{aligned} \bar{V}_{nm}^{(STP,\Omega_\omega)} &= \frac{3}{\bar{\rho}(2n+1)(n+3)} \sum_{k=1}^{n+3} \binom{n+3}{k} \frac{1}{4\pi} \int_{\lambda=0}^{2\pi} \int_{\theta=0}^{\pi} \rho^{(\Omega_\omega)}(\theta_Q, \lambda_Q) \\ &\quad \times \left(\left(\frac{H_{UB}^{(\Omega_\omega)}}{R} \right)^k - \left(\frac{H_{LB}^{(\Omega_\omega)}}{R} \right)^k \right) \bar{Y}_{nm}(\theta_Q, \lambda_Q) \sin \theta d\theta d\lambda \end{aligned} \quad (19)$$

where the height function (HF) to the power k within the double integral, scaled by the density $\rho^{(\Omega_\omega)}(\theta_Q, \lambda_Q)$ in each cell, can be expressed as a series of (fully normalised) surface spherical harmonic coefficients of the layer's height density function (HDF)

$$\begin{aligned} \overline{\text{HDF}}_{knm}^{(STP,\Omega_\omega)} &= \frac{1}{4\pi} \int_{\lambda=0}^{2\pi} \int_{\theta=0}^{\pi} \rho^{(\Omega_\omega)}(\theta_Q, \lambda_Q) \\ &\quad \times \left(\left(\frac{H_{UB}^{(\Omega_\omega)}}{R} \right)^k - \left(\frac{H_{LB}^{(\Omega_\omega)}}{R} \right)^k \right) \bar{Y}_{nm}(\theta_Q, \lambda_Q) \sin \theta d\theta d\lambda. \end{aligned} \quad (20)$$

Then, we arrive at a concise expression of the layer's spherical topographic potential

$$\overline{V}_{nm}^{(STP, \Omega_\omega)} = \frac{3}{\bar{\rho}(2n+1)(n+3)} \sum_{k=1}^{n+3} \binom{n+3}{k} \overline{\text{HDF}}_{knm}^{(STP, \Omega_\omega)}. \quad (21)$$

Note that the radial integration (Eq. 10) can also be done rigorously (without using binominal series expansions), as shown, for example, by Pavlis and Rapp (1990). However, the rigorous integration is much less efficient compared to an integration based on binominal series expansions (Rummel et al. 1988). Therefore, especially for large n_{\max} , the rigorous approach may become excessively computationally demanding. The rigorous expressions in our notation are found in Appendix 1.

2.2 Layer-Based Modelling with Respect to a Reference Ellipsoid

Next, the potential based on volumetric layers of laterally variable density as given by Eq. 6 is modelled with respect to a reference ellipsoid. This procedure yields the *ellipsoidal topographic potential* V^{ETP} . In contrast to the spherical variant described in Sect. 2.1, this modelling technique defines the layered masses with respect to a reference ellipsoid. The Earth is thus not approximated by a sphere and the true physical shape of Earth can be preserved.

The solution to the layer-based ETP discussed next is based on the HC method derived in Claessens and Hirt (2013), who applied the HC method only to compute the ETP from a single-density (RET) model.

The starting point is Eq. 13 that is a solution to the radial integral of a layer's masses (Eq. 10) with respect to an ellipsoid, which can also be written as follows:

$$\Omega^{(\text{ETP}, \omega)} = \rho^{(\Omega_\omega)}(\theta_Q, \lambda_Q) \frac{R}{n+3} \left(\frac{r_e}{R}\right)^{n+3} \left(\left[\left(\frac{r_{\text{UB}}^{(\Omega_\omega)}}{r_e}\right)^{n+3} - 1 \right] - \left[\left(\frac{r_{\text{LB}}^{(\Omega_\omega)}}{r_e}\right)^{n+3} - 1 \right] \right). \quad (22)$$

The layer's boundaries in the ellipsoidal case may be described by their pseudo-ellipsoidal heights $h'_{\text{UB}}^{(\Omega_\omega)}$ and $h'_{\text{LB}}^{(\Omega_\omega)}$ following

$$\begin{aligned} r_{\text{UB}}^{(\Omega_\omega)} &= r'_e + h'_{\text{UB}}^{(\Omega_\omega)} \\ r_{\text{LB}}^{(\Omega_\omega)} &= r'_e + h'_{\text{LB}}^{(\Omega_\omega)} \end{aligned} \quad (23)$$

measured along the direction towards the origin of the ellipsoid, akin to the geocentric coordinates needed for spherical harmonics [denoted approximate ellipsoidal height in Claessens and Hirt (2013)]. In approximation, the layer's boundaries may be described by $d_{\text{UB}}^{(\Omega_\omega)}$ and $d_{\text{LB}}^{(\Omega_\omega)}$ denoting the ellipsoidal height h taken in the direction towards the geocenter and thus yields

$$\begin{aligned} r_{\text{UB}}^{(\Omega_\omega)} &= r_e + d_{\text{UB}}^{(\Omega_\omega)} \\ r_{\text{LB}}^{(\Omega_\omega)} &= r_e + d_{\text{LB}}^{(\Omega_\omega)}. \end{aligned} \quad (24)$$

The error of this ellipsoidal approximation, when $d_{\text{UB}}^{(\Omega_\omega)}$ and $d_{\text{LB}}^{(\Omega_\omega)}$ are used instead $h'_{\text{UB}}^{(\Omega_\omega)}$ and $h'_{\text{LB}}^{(\Omega_\omega)}$, is investigated in Sect. 4.5.

Both square brackets terms in Eq. 22 can—equivalent to the spherical case (Eq. 17)—be expressed by the binominal series expansions

$$\begin{aligned} \left(\frac{r_{\text{UB}}^{(\Omega_\omega)}}{r_e}\right)^{n+3} - 1 &= \sum_{k=1}^{n+3} \binom{n+3}{k} \left(\frac{d_{\text{UB}}^{(\Omega_\omega)}}{r_e}\right)^k = \sum_{k=1}^{n+3} \frac{1}{k!} \prod_{i=1}^k (n+4-i) \left(\frac{d_{\text{UB}}^{(\Omega_\omega)}}{r_e}\right)^k \\ \left(\frac{r_{\text{LB}}^{(\Omega_\omega)}}{r_e}\right)^{n+3} - 1 &= \sum_{k=1}^{n+3} \binom{n+3}{k} \left(\frac{d_{\text{LB}}^{(\Omega_\omega)}}{r_e}\right)^k = \sum_{k=1}^{n+3} \frac{1}{k!} \prod_{i=1}^k (n+4-i) \left(\frac{d_{\text{LB}}^{(\Omega_\omega)}}{r_e}\right)^k. \end{aligned} \tag{25}$$

Inserting Eq. 25 and Eq. 22 into Eq. 9 gives a preliminary solution to the ETP of a layer

$$\begin{aligned} \bar{V}_{\text{nm}}^{(\text{ETP}, \Omega_\omega)} &= \frac{3}{\bar{\rho}(2n+1)(n+3)} \sum_{k=1}^{n+3} \binom{n+3}{k} \\ &\times \frac{1}{4\pi} \int_{\lambda=0}^{2\pi} \int_{\theta=0}^{\pi} \left(\frac{r_e}{R}\right)^{n+3} \rho^{(\Omega_\omega)}(\theta_Q, \lambda_Q) \left(\left(\frac{d_{\text{UB}}^{(\Omega_\omega)}}{r_e}\right)^k - \left(\frac{d_{\text{LB}}^{(\Omega_\omega)}}{r_e}\right)^k \right) \\ &\times \bar{Y}_{\text{nm}}(\theta_Q, \lambda_Q) \sin \theta d\theta d\lambda. \end{aligned} \tag{26}$$

In order to get a practicable solution for the ETP that is independent of any term with degree n in the exponent, Claessens and Hirt (2013) have introduced a second (infinite) binominal series for $\left(\frac{r_e}{R}\right)^{n+3}$ that has been derived in Claessens (2006):

$$\left(\frac{r_e}{R}\right)^{n+3} = \left(\frac{b}{R}\right)^{n+3} (1 - e^2 \sin^2 \theta)^{\left(-\frac{n+3}{2}\right)} = \left(\frac{b}{R}\right)^{n+3} \sum_{j=0}^{\infty} (-1)^j \binom{-\frac{n+3}{2}}{j} e^{2j} \sin^{2j} \theta \tag{27}$$

where b is the semi-minor axis of the ellipsoid and e^2 is the squared first numerical eccentricity. With the help of fully normalised *sinusoidal Legendre weight functions* $\bar{K}_{\text{nm}}^{2i, 2j}$ [see, for example, Appendix 1 in Claessens and Hirt (2013) for more details on the recursion relations], it is evident that

$$\sin^{2j} \theta \bar{Y}_{\text{nm}} = \sum_{i=-j}^j \bar{K}_{\text{nm}}^{2i, 2j} \bar{Y}_{n+2i, m}. \tag{28}$$

Inserting Eqs. 28 and 27 in 26 yields coefficients of the ellipsoidal topographic potential $V_{\text{nm}}^{(\text{ETP}, \Omega_\omega)}$ of the layer Ω_ω :

$$\begin{aligned} \bar{V}_{\text{nm}}^{(\text{ETP}, \Omega_\omega)} &= \frac{3}{\bar{\rho}(2n+1)(n+3)} \left(\frac{b}{R}\right)^{n+3} \sum_{k=1}^{n+3} \binom{n+3}{k} \sum_{j=0}^{\infty} (-1)^j \binom{-\frac{n+3}{2}}{j} e^{2j} \sum_{i=-j}^j \bar{K}_{\text{nm}}^{2i, 2j} \\ &\times \frac{1}{4\pi} \int_{\lambda=0}^{2\pi} \int_{\theta=0}^{\pi} \rho^{(\Omega_\omega)}(\theta_Q, \lambda_Q) \left(\left(\frac{d_{\text{UB}}^{(\Omega_\omega)}}{r_e}\right)^k - \left(\frac{d_{\text{LB}}^{(\Omega_\omega)}}{r_e}\right)^k \right) \\ &\bar{Y}_{n+2i, m}(\theta_Q, \lambda_Q) \sin \theta d\theta d\lambda \end{aligned} \tag{29}$$

Again, the term within the double integral, scaled by the density $\rho(\theta_Q, \lambda_Q)$ in each cell, can be expressed as a series of (fully normalised) surface spherical harmonic coefficients of the layer's (ellipsoidal) height density function

$$\overline{\text{HDF}}_{\text{klm}}^{(\text{ETP}, \Omega\omega)} = \frac{1}{4\pi} \int_{\lambda=0}^{2\pi} \int_{\theta=0}^{\pi} \rho^{(\Omega\omega)}(\theta_Q, \lambda_Q) \left(\left(\frac{d_{\text{UB}}^{(\Omega\omega)}}{r_e} \right)^k - \left(\frac{d_{\text{LB}}^{(\Omega\omega)}}{r_e} \right)^k \right) \times \bar{Y}_{\text{lm}}(\theta_Q, \lambda_Q) \sin \theta d\theta d\lambda \quad (30)$$

where $l = n + 2i$ and we arrive at a compact expression for the layer's ellipsoidally approximated potential

$$\bar{V}_{\text{nm}}^{(\text{ETP}, \Omega\omega)} = \frac{3}{\bar{\rho}(2n+1)(n+3)} \left(\frac{b}{R} \right)^{n+3} \sum_{k=1}^{k_{\text{max}}} \binom{n+3}{k} \sum_{j=0}^{j_{\text{max}}} (-1)^j \binom{-\frac{n+3}{2}}{j} e^{2j} \times \sum_{i=-j}^j \bar{K}_{\text{nm}}^{2i, 2j} \overline{\text{HDF}}_{\text{klm}}^{(\text{ETP}, \Omega\omega)} \quad (31)$$

where $k_{\text{max}} \leq n + 3$ and $j_{\text{max}} < \infty$ denote the maximum orders of the binominal series expansions. While k_{max} and j_{max} are much smaller than the maximum harmonic degree of the model n_{max} , generally, the number of binominal terms that are required to avoid truncation errors for different modelling parameters (e.g. spatial resolution) is discussed next. The rigorous expressions for the ETP of mass layers (devoid of binominal series expansions) are given in Appendix A.

2.3 Convergence of Binominal Series Expansions

As shown above, Eq. 31 contains two binominal series expansions, one incrementing by k and one by j . The convergence of the first series (Eq. 25), which is also found in the solution of the STP for $r_e = R$ (Eq. 17), has been thoroughly studied, for example, by Sun and Sjöberg (2001) for various resolutions. Commonly, $k_{\text{max}} = 7$ is considered sufficient for degree 2160. We have studied the relative amplitudes in Eq. 17 since the series additionally depends on r_e in case of the ETP. However, for $a = 6,378,137$ m and $b = 6,356,752$ m (where $a \geq r_e \geq b$), an identical number of terms were found to be required for different r_e . Our investigations show $k_{\text{max}} = 10$ is needed to achieve convergence at the 1 % level (i.e. less than 1 % truncation error) at degree 2160 (Table 1). Note that Root et al. (2016) showed that the convergence may be problematic for deep layers (e.g., upper mantle layers), with the boundaries' lower bound $\ll R$. According to Root et al. (2016), the problem can be overcome by reducing the reference radius R during the forward modelling of the affected layer and a subsequent rescaling of the computed coefficients.

The second series (Eq. 27), a function of degree n and the co-latitude Θ , occurs in the ETP only. Despite its infinite summations, it was shown to always converge (Claessens 2006). Looking at the amplitudes of the series's terms in a relative manner, at least $j_{\text{max}} = 18$ should be used to achieve convergence at the 1 % level for degree 2160 and $\theta \in [0; \frac{\pi}{2}]$ (Table 2).

2.4 Sampling Requirements of Height Density Functions

Special attention is required for the harmonic analysis of the layer's height density functions [e.g., by means of quadrature (Rexer and Hirt 2015b)] that is needed to derive the surface spherical harmonic coefficients $\overline{\text{HDF}}_{\text{knm}}^{(\text{STP}, \Omega\omega)}$ or $\overline{\text{HDF}}_{\text{klm}}^{(\text{ETP}, \Omega\omega)}$. Due to the exponentiation of the height function by k , the bandwidth (expressed by the maximum degree N

Table 1 Order of truncation k_{\max} of the first binominal series (Eq. 25) at various resolutions (harmonic degree n) and locations of the layer boundary required to reduce the relative error below the 1 %-level, where $a = 6,378,137 \text{ m} \geq r_e \geq b = 6,356,752 \text{ m}$

n	Distance to reference surface (H or d)		
	$\pm 9 \text{ km}$	$\pm 4.5 \text{ km}$	$\pm 1 \text{ km}$
10	2	2	2
360	4	4	3
2160	10	7	4
2190	10	7	4
5400	17	11	5
10,800	29	17	7

Table 2 Order of truncation j_{\max} of the second binominal series (Eq. 27) at various resolutions (harmonic degree n) and co-latitude θ required to reduce the relative error below the 1 %-level, where $b = 6,356,752 \text{ m}$ and $R = 6,378,137 \text{ m}$

n	$\theta = 0^\circ$	$\theta = 10^\circ$	$\theta = 30^\circ$	$\theta = 45^\circ$	$\theta = 60^\circ$	$\theta = 80^\circ$	$\theta = 90^\circ$
10	1	2	3	3	3	3	3
360	1	3	4	5	6	7	7
2160	1	4	8	12	15	18	18
2190	1	4	8	12	15	18	18
5400	1	5	13	21	27	33	34
10,800	1	7	21	34	46	56	57

of the original height function) increases proportionally with k , following Hirt and Kuhn (2014),

$$N(k) = kN. \tag{32}$$

Importantly, Eq. 32 implies that the gridded height functions need to be sampled according to k_{\max} (see Sect. 2.3) in order to avoid any aliasing effects. Computing the STP to degree 2160 with $k_{\max} = 7$ in an experiment (not shown here), with the grid sampling limiting the maximum degree to degree 2700, yields aliasing errors of up to $\sim 20 \text{ mGal}$ and a global root mean square (RMS) of 0.17 mGal . In all computations in this contribution, the increased sampling requirements are thus fully taken into account. A more detailed study of the aliasing effect is outside the scope of this paper.

3 Layer Concept Based on Earth2014

The mass layer concept using the STP and ETP framework presented in Sect. 2 can be applied with the four (geophysical) volumetric layers

- Ω_1 : Ice
- Ω_1 : Lakes
- Ω_1 : Ocean
- Ω_1 : Crust (solid rock)

while different rock types or sediment layers shall not be considered. It is of course possible to include more layers, but relevant global data sets at resolutions < 111 km are not available (see Sect. 1.1). Note that vertical density functions (e.g., given by some polynomial) for the integration of ocean water columns (Tenzer et al. 2015) or radially varying mass density distributions in general (Root et al. 2016) were not integrated into the layer concept (although possible), as this is not the scope of this paper.

The layer's boundaries are generated from the Earth2014 data set (Hirt and Rexer 2015) that provides a suite of self-consistent surface layers and masks which can be used to distinguish between ice, lake, ocean and solid Earth surface at 1' resolution (~ 2 km). Earth2014 is a freely available composite model combining up-to-date digital elevation data with other gridded surface data products from different sources in terms of mean-sea-level heights. As such Earth2014 can be considered an up-to-date, higher resolution and more detailed version of the OSUJAN89 (Pavlis and Rapp 1990), DTM2002 (Saleh and Pavlis 2002) and ETOPO1 (Amante and Eakins 2009) topographic databases that in principle provide the same terrain types (see, for example, Fig. 1 in Pavlis and Rapp 1990). We refer to Hirt and Rexer (2015) for a full account on Earth2014 data.

In Fig. 1, a scheme of the layer concept is given based on Earth2014 layers: *bedrock layer* (BED) describing the boundary of solid rock (green lines), *surface layer* (SUR) which is defined as the boundary between atmosphere and Earth (red lines) and the *ice thickness layer* (ICE). The difference between SUR and ICE describes an Earth free of ice cover/sheets and is indicated by the orange lines. Here, a total of ten different cases (A)–(J) are given showing the most common arrangement of layers w.r.t. mean sea level (MSL). Those cases and examples for occurrences on Earth are described in Table 3. Note that in both above described approaches the layer's boundaries are subject to approximation since they are defined by the orthometric height w.r.t. the respective reference surface in a spherical harmonic frame. Effectively, thus, the geoid height is neglected and the reference surface conforms with the MSL line in Fig. 1. The geometry and approximation error due to height assumptions is further discussed in Sect. 4.5.

Two different possibilities exist for the choice of the densities, leading to the following two different approaches for layer-based forward modelling

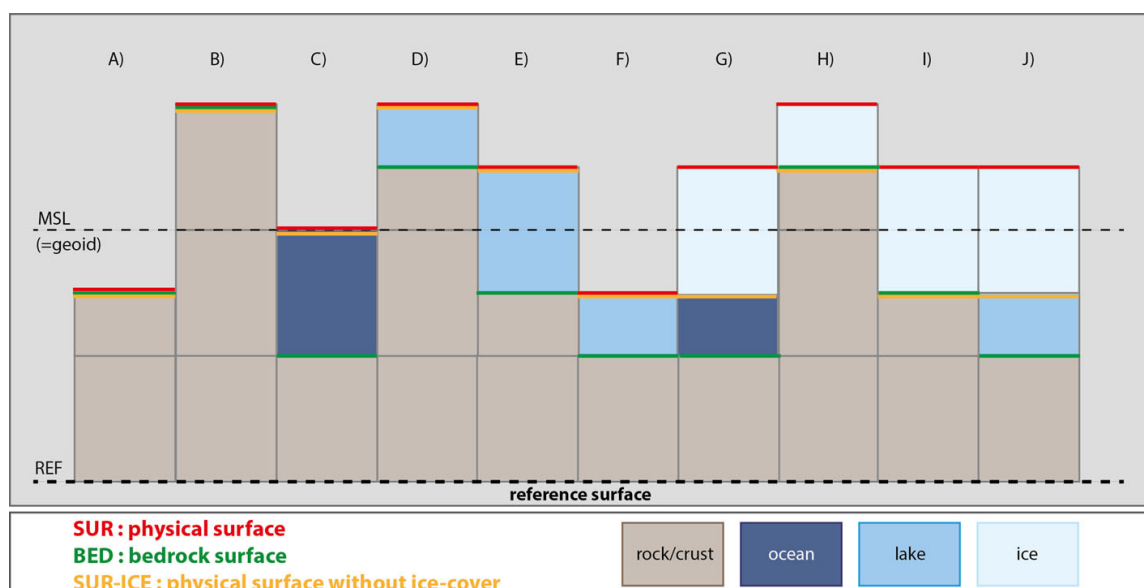


Fig. 1 Simplified scheme of the four geophysical layers extracted from the Earth2014 data set

Table 3 Cases of layer arrangements shown in Fig. 1 and their occurrences on Earth

Case	Type	Occurrence
A	Dry land—bedrock below MSL	e.g., Death Valley
B	Dry land—bedrock above MSL	Most continental areas
C	Ocean	All open oceans
D	Lake—bedrock and lake surface above MSL	e.g., shallow parts of Great Lakes and Lake Baikal
E	Lake—bedrock below MSL, lake surface above MSL	e.g., deep parts of Great Lakes and Lake Baikal
F	Lake—bedrock and lake surface below MSL	e.g., Caspian Sea
G	Ice shelf—ice above ocean	e.g., shorelines of Antarctica and Greenland
H	Ice-/snow-covered bedrock above MSL	e.g., continental glaciers, Antarctica, Greenland
I	Ice-/snow-covered bedrock below MSL	e.g., Antarctica
J	Ice-/snow-covered lake	e.g., Lake Vostok

Table 4 Description of layer boundaries and densities in the *LCA approach* using Earth2014 data

Layer name	Density (kg/m ³)	Layer boundary type	Over land	Over ocean and shelf ice	Over lakes	Over ice
Ice layer	917	UB	SUR	SUR	SUR	SUR
		LB	SUR-ICE	SUR-ICE	SUR-ICE	SUR-ICE
Lakes layer	1000	UB	SUR-ICE	SUR-ICE	SUR-ICE	SUR-ICE
		LB	SUR-ICE	SUR-ICE	BED	SUR-ICE
Ocean layer	1030	UB	SUR-ICE	SUR-ICE	SUR-ICE	SUR-ICE
		LB	SUR-ICE	BED	SUR-ICE	SUR-ICE
Crust layer	2670	UB	BED	BED	BED	BED
		LB	REF	REF	REF	REF
Cases (c.f. Fig. 1)			A, B	C, G	D, E, F, J	H, I

SUR, Earth2014 surface layer; ICE, Earth2014 ice thickness layer; BED, Earth2014 bedrock layer; ICE-SUR, Earth2014 surface removed for ice sheets (see yellow lines in Fig. 1); REF, reference surface

1. LCA: layer correction approach with actual layer densities (c.f. Table 4)
2. LRA: layer reduction approach with density contrasts (c.f. Table 5)

which are described in the following.

3.1 Layer Correction Approach (LCA)

In this approach, the gravitational potential generated by each mass layer is modelled with its actual density. Each layer thus makes a (positive) contribution to the final model, i.e. the total topographic potential, that can be thought of as a *correction* in geodetic sense. Then, the total topographic potential is the sum of the potential contributions of all layers. In the LCA, the layer boundaries and densities for the four layers are selected from the Earth2014 database as listed in Table 4. The LCA can be best understood as bottom-up approach as

Table 5 Description of layer boundaries and densities in the *LRA approach* using Earth2014 data

Layer name	Density/ -contrast (kg/m ³)	Layer boundary type	Over land	Over ocean and shelf ice	Over lakes	Over ice
Crust layer	2670	UB	SUR	SUR	SUR	SUR
		LB	REF	REF	REF	REF
Ice layer	−1753	UB	SUR	SUR	SUR	SUR
		LB	SUR−ICE	SUR−ICE	SUR−ICE	SUR−ICE
Lakes layer	−1670	UB	SUR−ICE	SUR−ICE	SUR−ICE	SUR−ICE
		LB	SUR−ICE	SUR−ICE	BED	SUR−ICE
Ocean layer	−1640	UB	SUR−ICE	SUR−ICE	SUR−ICE	SUR−ICE
		LB	SUR−ICE	BED	SUR−ICE	SUR−ICE
Cases (c.f. Fig. 1)			A,B	C,G	D,E,F,J	H,I

SUR, Earth2014 surface layer; ICE: Earth2014 ice thickness layer; BED, Earth2014 bedrock layer; ICE−SUR, Earth2014 surface removed for ice sheets (see yellow lines in Fig. 1); REF, reference surface

each layer from the reference surface to the surface of Earth is modelled one after another. This is different from the approach described next.

3.2 Layer Reduction Approach (LRA)

One can best imagine the LRA approach as a top-down approach: the crustal potential is modelled using the uppermost boundary layer (the physical surface of Earth) and is then reduced for the effect of mass density anomalies expressed by density contrasts (w.r.t. the assumed crustal density) that exist in each layer beneath the surface, down to the reference surface. The layer boundaries and density contrasts in the LRA approach are listed in Table 5. When using negative density contrasts for the layers, the total topographic potential is the sum of the gravitational effects of each layer.

3.3 LRA Versus LCA

Theoretically, both approaches should yield the same potential and neither of the approaches is preferable in terms of computational expense. However, practically small differences may remain between the approaches, mainly due to spherical harmonic representation errors as will be shown (see Sect. 4.1). In the literature, often only the LRA approach based on density contrasts is considered. In Tenzer et al. (2015), for example, so-called *striping corrections* to the topographic correction are computed based on density contrasts, so their procedure corresponds to the LRA approach.

The cross-validation of the results of both approaches is a valuable tool for detecting inconsistencies of the used mass models. For example, consider

- (a) a layer A intersecting with another layer B (Fig. 2a)—then, the overlapping space would be modelled twice in the LCA approach and in the LRA approach, leading to different potentials: in case of LCA, the overlapping space would be corrected using both layers' densities; in case of LRA, the overlapping space would be reduced for both layers' density contrasts. In general, the error ϵ associated with this kind of inconsistency depends on ρ_B if UB_B is wrong and on ρ_A if LB_A is wrong. However,

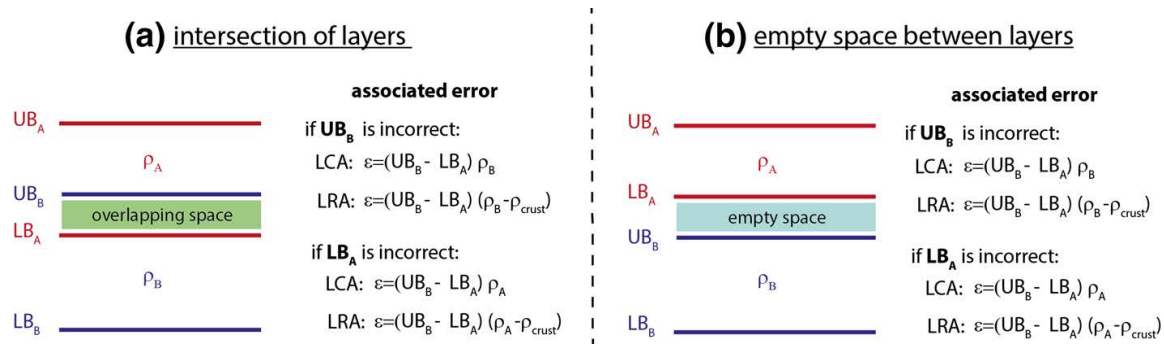


Fig. 2 Scheme and associated error of (a) intersecting layers or (b) empty space between layers in the LCA and the LRA approach

no error will occur in case of the LRA if UB_B is wrong and layer B happens to be the crustal layer ($\rho_B = \rho_{crust}$).

- (b) a not modelled (volumetric) empty space between two layers A and B (Fig. 2b)—then, this space is not accounted for in the LCA approach at all, while the space is implicitly filled and modelled with crustal density in the LRA approach. Again, no error will occur in case of the LRA if UB_B is wrong and layer B happens to be the crustal layer ($\rho_B = \rho_{crust}$).

Note that it is likewise possible (and associated with less computational costs) to detect inconsistencies in the mass models by applying the (purely) geometric conditions listed under (ii) to (v) in Sect. 2.

4 Results

This section presents a numerical study based on the ellipsoidal layer-based forward modelling technique (Sect. 2.2) using the volumetric layers defined in Sect. 3. It also shows the results of the layer-based forward modelling in spherical approximation (Sect. 2.1) for comparison purposes.

4.1 Global Gravitational Potential from Volumetric Layers in Ellipsoidal Approximation

The above presented techniques allow modelling the topographic gravitational potential of a single layer as well as the combined (total) effect of several layers via corrections or reductions. For the sake of clarity, an overview on the computed potential fields together with their approximation level and acronyms is given in Table 6.

The dimensionless degree variances

$$c_n = \sum_{m=-n}^n \bar{V}_{nm}^2 \tag{33}$$

of the ETP of all layers computed using the constants given in Table 7 are shown in Fig. 3. While the single layers' potentials (coloured lines) are different (by a constant scale factor) for the LRA and the LCA approach, the sum of all layer's potentials (black lines) yields similar spectra for both approaches. The difference is at least five orders of magnitude below the signal (Fig. 4, left plot), corresponding to a root mean square (RMS) of

Table 6 Acronyms of computed potential models in the numerical study together with used layers, type of approximation, layer approach and maximum spherical harmonic degree

Acronym	Approximation	Layer	Layer approach	Max. degree
dV_ELL_Earth2014_lca	Ellipsoidal/ETP	All	LCA	2190
dV_ELL_Earth2014_lra	Ellipsoidal/ETP	All	LRA	2190
dV_ELL_ICE2014_lca	Ellipsoidal/ETP	Ice layer	LCA	2190
dV_ELL_ICE2014_lra	Ellipsoidal/ETP	Ice layer	LRA	2190
dV_ELL_LAKES2014_lca	Ellipsoidal/ETP	Lakes layer	LCA	2190
dV_ELL_LAKES2014_lra	Ellipsoidal/ETP	Lakes layer	LRA	2190
dV_ELL_OCEAN2014_lca	Ellipsoidal/ETP	Ocean layer	LCA	2190
dV_ELL_OCEAN2014_lra	Ellipsoidal/ETP	Ocean layer	LRA	2190
dV_ELL_CRUST2014_lca	Ellipsoidal/ETP	Crust layer	LCA	2190
dV_ELL_CRUST2014_lra	Ellipsoidal/ETP	Crust layer	LRA	2190
dV_ELL_RET2014	Ellipsoidal/ETP	All	RET	2190
dV_SPH_Earth2014_lca	Spherical/STP	All	LCA	2160
dV_SPH_Earth2014_lra	Spherical/STP	All	LRA	2160
dV_SPH_ICE2014_lca	Spherical/STP	Ice layer	LCA	2160
dV_SPH_ICE2014_lra	Spherical/STP	Ice layer	LRA	2160
dV_SPH_LAKES2014_lca	Spherical/STP	Lakes layer	LCA	2160
dV_SPH_LAKES2014_lra	Spherical/STP	Lakes layer	LRA	2160
dV_SPH_OCEAN2014_lca	Spherical/STP	Ocean layer	LCA	2160
dV_SPH_OCEAN2014_lra	Spherical/STP	Ocean layer	LRA	2160
dV_SPH_CRUST2014_lca	Spherical/STP	Crust layer	LCA	2160
dV_SPH_CRUST2014_lra	Spherical/STP	Crust layer	LRA	2160
dV_SPH_RET2014	Spherical/STP	All	RET	2160

ETP, ellipsoidal topographic potential; STP, spherical topographic potential; LCA, layer correction approach; LRA, layer reduction approach; RET, rock-equivalent topography (=single-density modelling)

~0.001 mGal in terms of gravity disturbances evaluated at the surface of Earth (Fig. 5). The largest differences are found above the inland lakes, which are accompanied by error patterns distributed approximately along great arcs. We believe those differences stem from spherical harmonic representation errors (Gibbs effect) that occur over small areas with large variations in height/depth (e.g., Lake Baikal). The corresponding coefficient differences are given in Fig. 4 (right plot).

We have computed a 5° global grid of gravity disturbances from the new dV_ELL_Earth2014_lca model in spectral band of degrees 0 to 2190 at the Earth's surface as represented by the Earth2014 SUR layer. This was done by using the isGrafLab software (Bucha and Janák 2014) along with the gradient approach for 3D harmonic synthesis (Hirt 2012). In Fig. 6, the gravity disturbances from the dV_ELL_Earth2014_LCA model vary approximately between -802 and 624 mGal with an average signal strength (RMS) of ~350 mGal.

The area of Antarctica has been selected to show the gravitational contribution of each layer to the total gravitational effect of the Earth2014 based mass model (Fig. 7), as each layer has a significant contribution over that region. The largest contributions are given by the crust layer and ocean layer, while the ice layer and lake layer have smaller (but still) significant contributions. Note especially that, for example, the ocean layer has significant

Table 7 Constants and modelling parameters used for the numerical study

Symbol	Description	LCA	LRA
$\rho^{(\Omega_1)}$	Ice layer density/contrast	917 kg/m ³	-1753 kg/m ³
$\rho^{(\Omega_2)}$	Lakes layer density/contrast	1000 kg/m ³	-1670 kg/m ³
$\rho^{(\Omega_3)}$	Ocean layer density/contrast	1030 kg/m ³	-1640 kg/m ³
$\rho^{(\Omega_4)}$	Crust layer density/contrast	2670 kg/m ³	2670 kg/m ³
$\bar{\rho}$	Earth's mean density	5495.30635355977 kg/m ³	
R	Reference radius	6,378,137.0 m	
a	Semi-major axis of GRS80	6,378,137.0 m	
e^2	Square of first eccentricity of GRS80	0.00669438002290	
M	Earth's mass	5.972581×10^{24} kg	
GM	Mass \times Gravitational constant	3.986005×10^{14} m ³ /s ⁻²	
k_{\max}	Maximum power	12	
j_{\max}	Maximum summation index	30	
n_{\max}	Maximum degree	STP:2160; ETP:2190	
$n_{\max,DEM}$	maximum degree of input Earth2014 DEM resolution/sampling of input Earth2014 DEM	2160 25"	

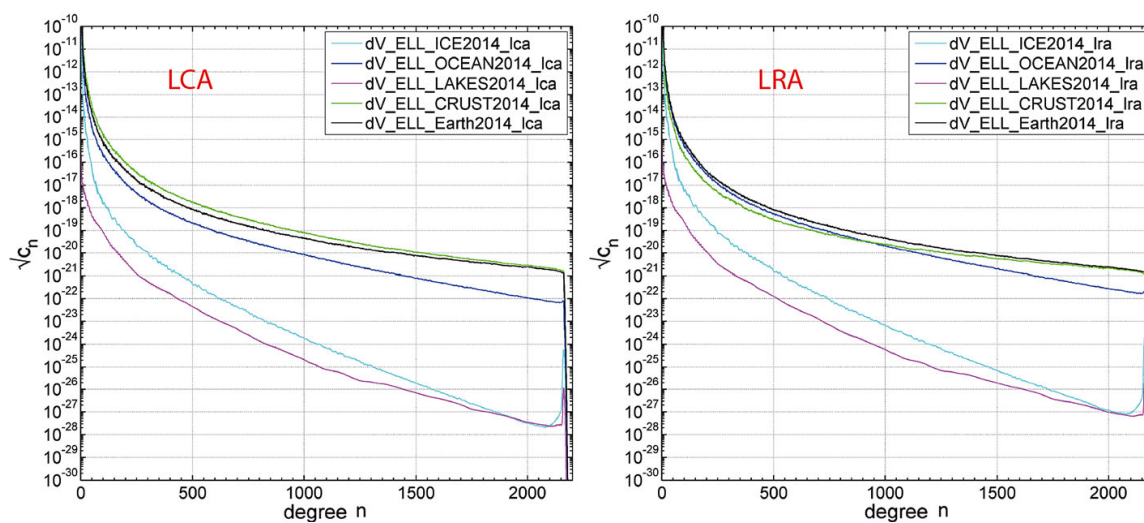


Fig. 3 Degree variances of the ellipsoidal topographic potential models and their layers using the LCA approach (*left*) and the LRA approach (*right*)

contributions over continental Antarctica (and over other continents) which underlines the importance of explicitly modelling the ocean's masses in order to retrieve a good approximation of the gravitational potential over land.

The benefit of layer-based modelling, as done here, compared to RET-based (single-density models) modelling obviously is largest over ice- and water-covered parts of Earth where discrepancies are of the order of ~ 10 – 20 mGal (Fig. 8). Especially over the mid-oceanic ridges and deep ocean trenches (but also over many other areas), notable differences are present which all can safely be interpreted as RET approximation errors (see

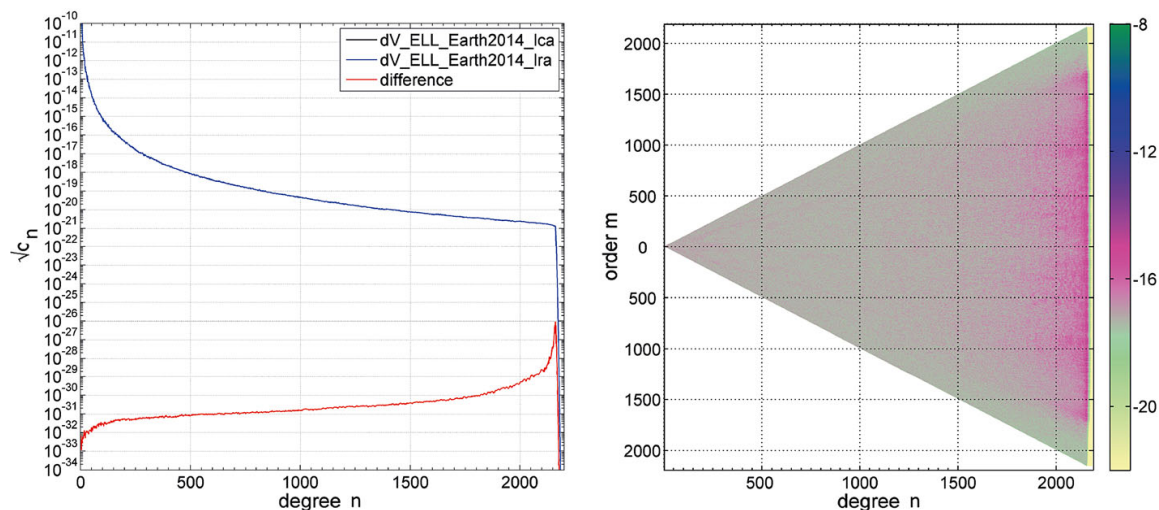


Fig. 4 LCA versus LRA approach: difference between the respective spectra of layer-based ETP in terms of degree variances (*left*) and dimensionless coefficient differences (*right*)

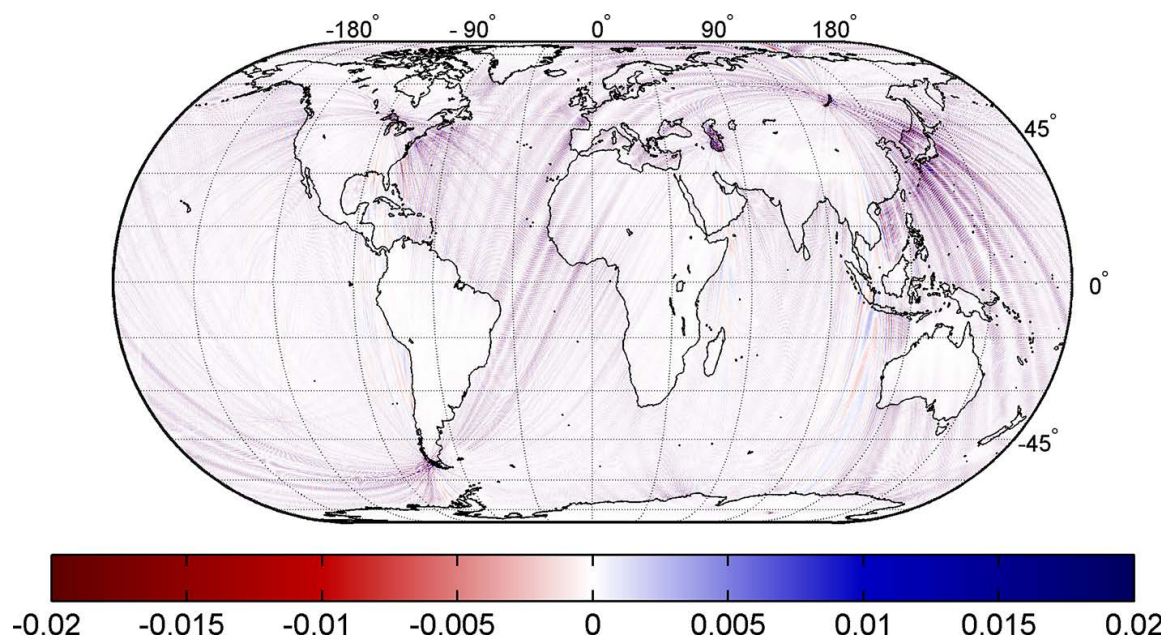


Fig. 5 LCA versus LRA approach: difference of layer-based ETP ($dV_{ELL_Earth2014_ica} - dV_{ELL_Earth2014_ira}$) in terms of gravity disturbances evaluated at the surface of the Earth, d/o 0..2190 (unit is in mGal). RMS = 0.001 mGal; min = -0.06 mGal; max = 0.07 mGal; mean = 0.00 mGal

Sect. 4.2). The discrepancies shown in Fig. 8 are in good agreement with the findings by Grombein et al. (2016) and Kuhn and Hirt (2016).

4.2 Validation of Layer-Based Modelling Using GOCE Satellite Gradiometry

The successful operation of a gradiometer on board of ESA satellite *Gravity Field and steady-state Ocean Circulation Explorer* (GOCE) resulted in global gravity gradient observations which currently are the most consistent and accurate source for Earth's gravity at scales up to $\sim 70\text{--}80$ km. Its observations as incorporated in the GOCE-only gravity field model *GO_CONS_GCF_2_TIM_R5* (EGM_TIM_R5) (Brockmann et al. 2014) are totally independent of any of the computed topographic potential models in this

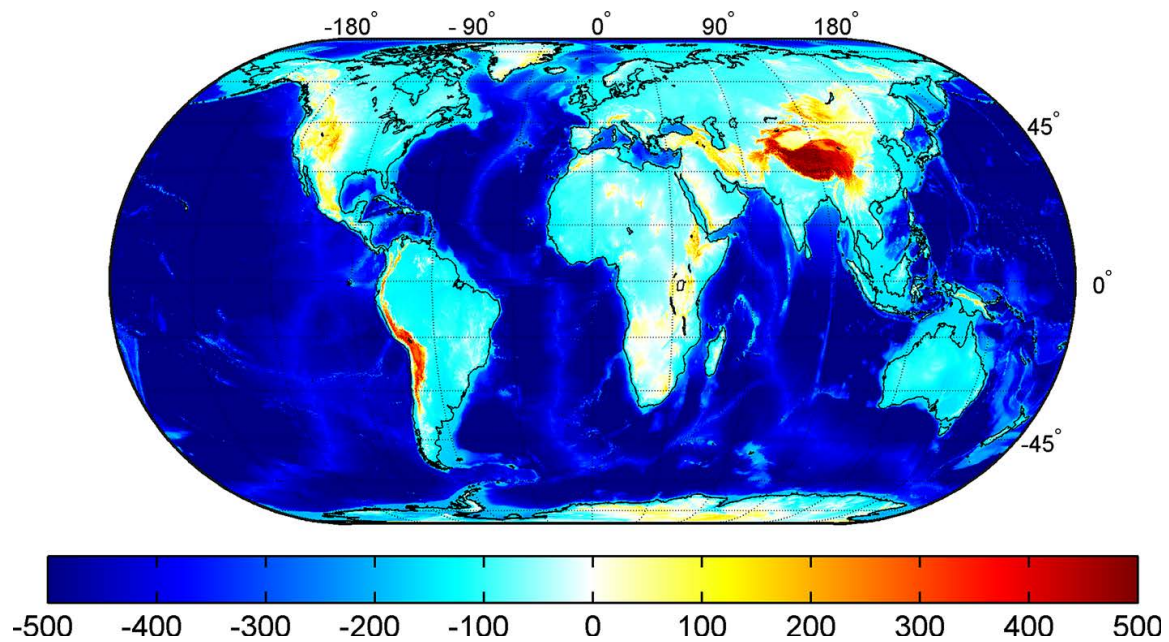


Fig. 6 Gravity of layer-based ETP ($dV_ELL_Earth2014_lca$) in terms of gravity disturbances evaluated at the surface of the Earth, d/o 0..2190 (unit is in mGal). RMS = 349.45 mGal; min = -802.07 mGal; max = 623.63 mGal; mean = -283.58 mGal

work and can therefore be used to quantify the benefits of layer-based modelling over RET-based modelling, thus corroborating our spectral layer approach. In this regard, we compute regional *reduction rates* (RR) (Hirt et al. 2012) from $1^\circ \times 1^\circ$ blocks of band-limited gravity disturbances δg globally at the reference ellipsoid following

$$\begin{aligned}
 RR_{\text{layer}} &= 100 \cdot \left(1 - \frac{RMS(\delta g_{dV_ELL_Earth2014} - \delta g_{EGM_TIM_R5})}{RMS(\delta g_{EGM_TIM_R5})} \right) \\
 RR_{\text{RET}} &= 100 \cdot \left(1 - \frac{RMS(\delta g_{dV_ELL_RET2014} - \delta g_{EGM_TIM_R5})}{RMS(\delta g_{EGM_TIM_R5})} \right)
 \end{aligned}
 \tag{34}$$

and investigate their differences $RR_{\text{layer}} - RR_{\text{RET}}$ (Fig. 9). The limitation of the investigation to the spectral band $n = 160 \dots 250$ is reasoned as follows: the GOCE gravity model contains the effects of isostatic compensation that are not modelled in this work. Since isostatic effects are predominantly of long-wavelength character, we exclude all degrees $n < 160$. We further exclude all degrees $n > 250$ since Brockmann et al. (2014) showed that this is where the signal-to-noise ratio of the gradiometer observations becomes 1. RMS denotes the root mean square operator, applied on the respective gravity disturbances. The RR visualise to what extend the forward modelled gravity in the ETP models can be reduced (i.e. explained) by the satellite's observations. Blue areas in Fig. 9 thus are areas where the layer modelling—in simple words—agrees better with GOCE observations than RET-based modelling. Moreover, it is interesting to see that above the continents—predominantly above near-coastal land areas—significant improvement through the layer-based modelling was achieved, although the mass model over the continents is the same (except of lakes) in the case of RET-based and layer-based modelling. The reason for this behaviour of course is that the gravitational signal of a bounded density contrast (which in this case is the ocean) leaks over its physical boundaries.

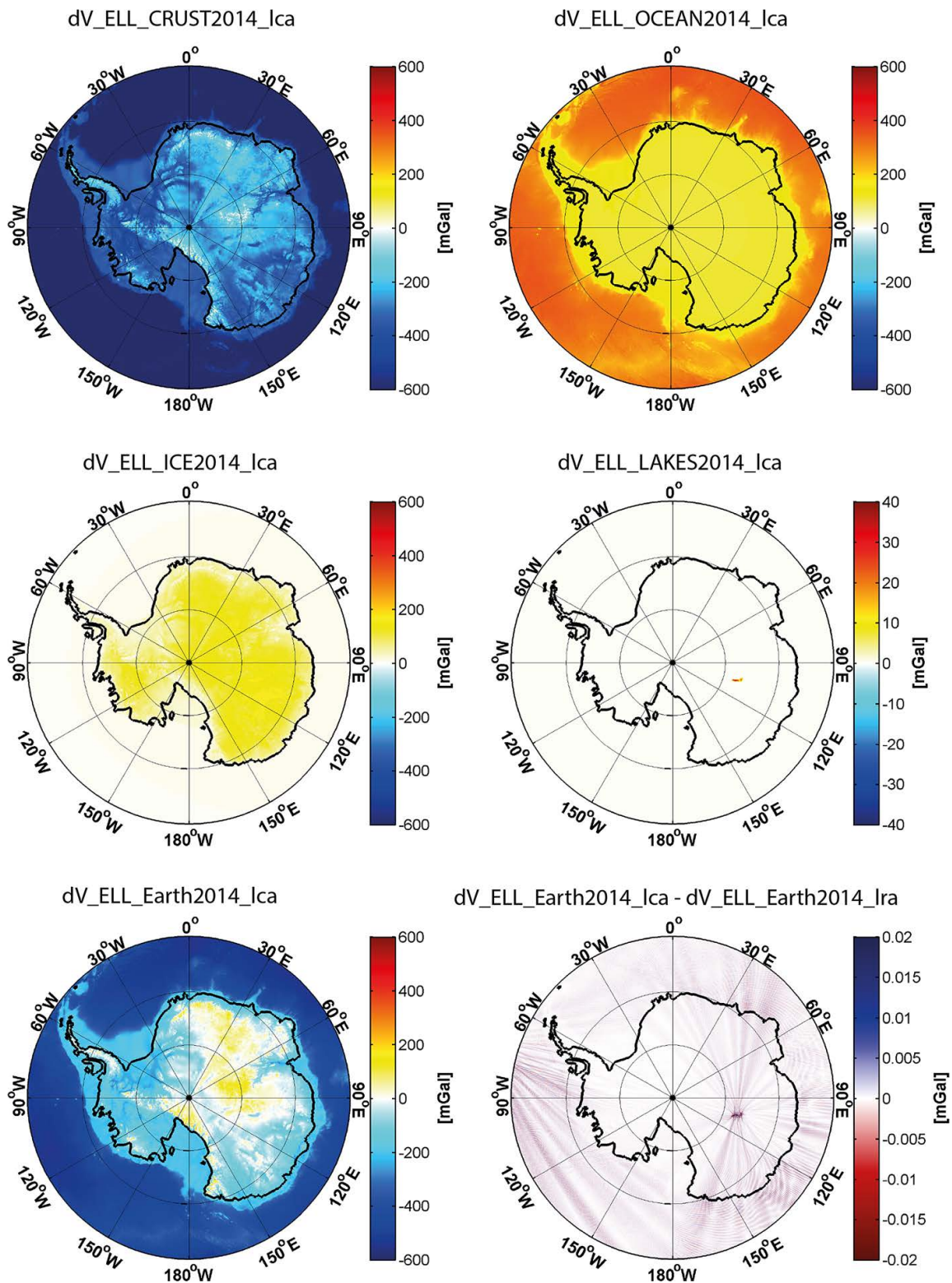


Fig. 7 Gravity contribution in terms of gravity disturbances (mGal) of the single layers, their combined effect and the difference between LCA and LRA approach over the area of Antarctica

4.3 Corroboration of Layer-Based Modelling Using Other GGMs

Any existing global gravitational model (GGM) may be used to investigate the quality of the suggested layer-based forward modelling. We restrict our investigations to two models which are

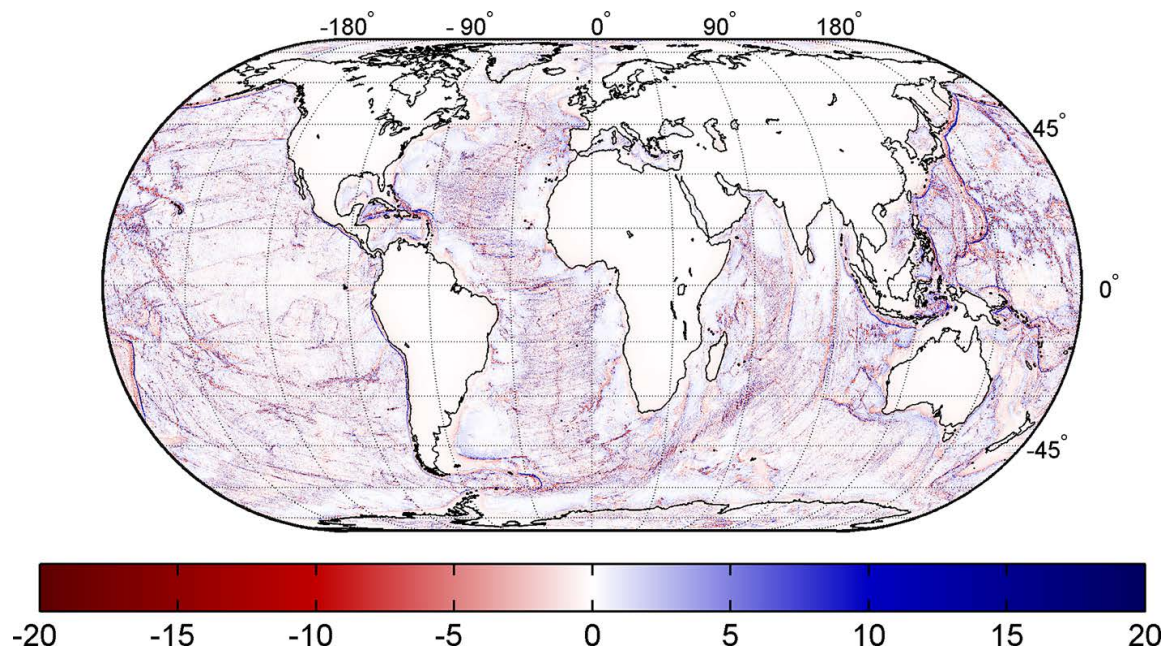


Fig. 8 Layer-based modelling versus RET-based (single-density) modelling: difference between the layer-based ETP and the RET-based ETP in terms of gravity disturbances evaluated at the reference ellipsoid (unit is in mGal). RMS = 1.79 mGal; min = -45.67 mGal; max = 65.91 mGal; mean = -0.05 mGal

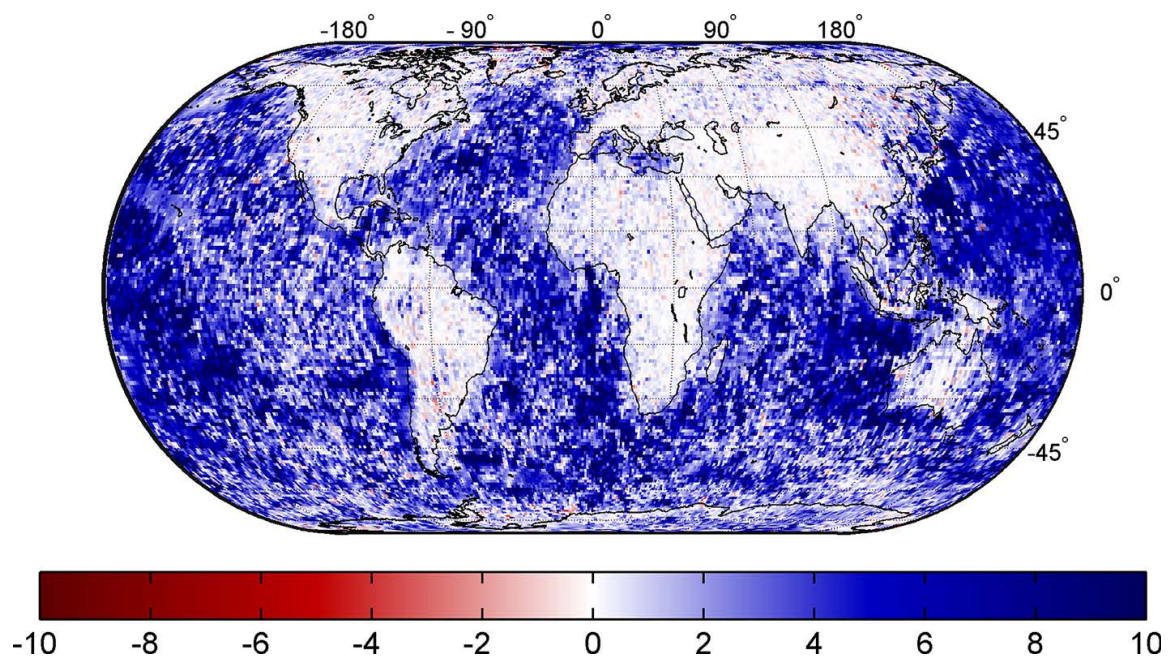


Fig. 9 Layer-based modelling versus RET-based (single-density) modelling: reduction rate differences (Eq. 34) in $1^\circ \times 1^\circ$ blocks using gravity from the GOCE-only model *GO_CONS_GCF_2_TIM_R5* in the band from degree 160 to 250. Positive values denote a better agreement between layer-based modelling and GOCE observations (unit is in percent). RMS = +5.47%; average = +3.25 %

1. EGM2008: the Earth Gravitational Model 2008 (Pavlis et al. 2012) which is a combined GGM using satellite observations, terrestrial observations and residual terrain fill-in gravity complete up to degree and order (d/o) 2190. EGM2008 incorporates the most complete (and up-to-date) set of terrestrial gravity observations of any available GGM and is therefore the best candidate to investigate the layer-based modelling at short scales with real observations.

2. RWI_TOPO_2015: the Rock–Water–Ice topographic model 2015 (Grombein et al. 2016) is a forward model based on layers of solid rock, water and ice derived from the same data set (Earth2014) as used for the layer-based ETP models in this work. Contrary to this work RWI_TOPO_2015 has been generated from an integration in the space domain using a tesseroïd approach (see Grombein et al. 2013) and was transformed into the spectral domain by a subsequent spherical harmonic analysis. The model is also complete up to d/o 2190 and is perfectly suited for a cross-validation with the suggested spectral approach in this work.

Consequently, the comparison with EGM2008 will allow us to judge how closely the computed models approximate the observable gravity field at short scales while the comparison to RWI_TOPO_2015 will provide independent feedback on the modelling technique as such. The *degree correlation* (DC) y_n (see, for example, Wieczorek 2007) of a GGM w.r.t. EGM2008 is given by

$$y_n = \frac{cx_n(\text{EGM2008, GGM})}{\sqrt{c_n(\text{EGM2008}) \cdot c_n(\text{GGM})}} \quad (35)$$

and indicates the degree of correlation ($[-1; 1]$) between the signal contained in coefficients of equal degree of EGM2008 and the GGM under evaluation, where cx_n is the cross-degree variance

$$cx_n(\text{EGM2008, GGM}) = \sum_{m=-n}^n \bar{V}_{nm}(\text{EGM2008}) \cdot \bar{V}_{nm}(\text{GGM}). \quad (36)$$

As expected, the computed layer-based ETP models (dV_ELL_Earth2014_lca/lra) and RWI_TOPO_2015 show a higher correlation with EGM2008 than the RET-based model (Figs. 10, 11). However, the degree correlation computed from the (original) spherical harmonic models reaches a maximum correlation of 0.93 near degree ~ 1000 , after which the correlations decrease again (and stay above 0.8). This is against all expectations, since the short-scale signals of the gravity field are driven by the topographic masses. Hence, an increase in the correlation is to be expected. The reason for this behaviour is that spherical harmonic models in ellipsoidal approximation (like EGM2008 and most other models found at ICGEM) cannot be used in small bands (band limited) because of dependencies

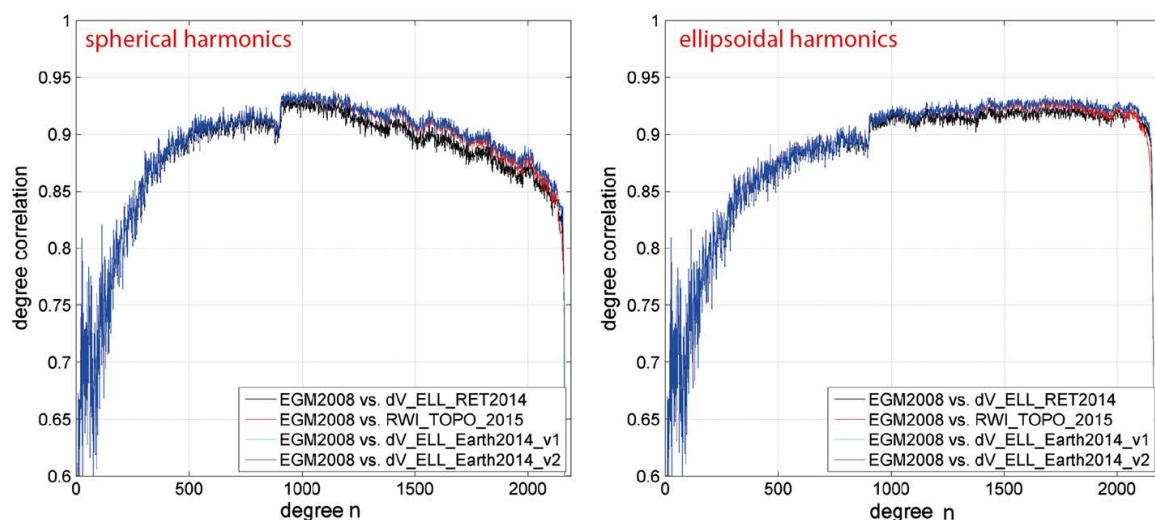


Fig. 10 Degree correlation w.r.t. EGM2008 in terms of spherical harmonic models (*left panel*) and in terms of their ellipsoidal harmonic equivalents (*right panel*)

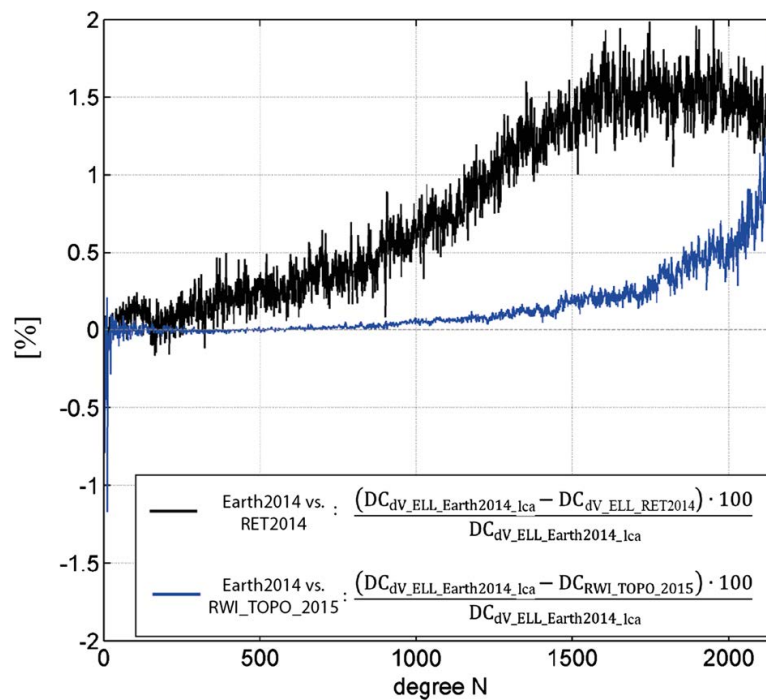


Fig. 11 Differences between the (spherical harmonic) degree correlation w.r.t. EGM2008 of RWI_TOPO_2015 (*blue*) and dV_ELL_RET2014 (*black*) versus the degree correlation of the layer model computed in this work (dV_ELL_Earth2014_lca) in per cent. Positive values denote a higher correlation of dV_ELL_Earth2014_lca

among the coefficients that effect the ellipsoidal approximation. For instance, EGM2008 and other such models constructed in ellipsoidal approximation have to be synthesised up to degree 2190 to avoid erroneous striations increasing with latitude (also see Hirt et al. (2015), Fig. 13 *ibid*). However, by transforming the spherical harmonic models into truly ellipsoidal harmonic models using Jekeli's transform (Jekeli 1988), a band-limited investigation of the GGMs becomes possible. Then, the degree correlations stay at a high level (~ 0.92) even beyond degree ~ 1000 (c.f. Fig. 10, right panel), indicating that the computed layer-based ETP models agree well with the short-scale gravity as contained in EGM2008.

The difference of respective DCs reveals that the computed layer-based ETP models of this work show an increasingly higher correlation beyond degree 800 or so (up to 2% near degree 2160) compared to the RWI_TOPO_2015 model (Fig. 11). Note that a higher correlation with EGM2008 is not necessarily a valid indicator for a better quality since EGM2008 itself (a) has incomplete observations over some areas (e.g., it contains only GRACE over Antarctica) and contains fill-in gravity and (b) is not error-free. However, we find the degree correlations in Fig. 10 together with the findings in the previous Sect. (4.2) to corroborate the layer-based modelling approach in this work, since the agreement with EGM2008 is at least as good as that of RWI_TOPO_2015.

4.4 Combination with Satellite Data and Validation over Antarctica

For external validation with ground truth data, we have computed combination models with GOCE and GRACE gravity observation data. A combination is necessary to be able to directly compare the computed layer-based forward models (see Table 6) with ground truth data, particularly at short scales. Also, because isostatic effects have rather long-wave-length character (c.f. Grombein et al. 2014) and were not taken into account in the forward

modelling, satellite observations are used here as an accurate source of such information. We use precomputed normal equation matrices for GRACE [ITG-Grace2010: Mayer-Gürr et al. (2010)] and GOCE [fifth release of time-wise method: Brockmann et al. (2014)] along with the combination strategy described in Hirt et al. (2015) (Eqs. 5–8) to create a combined model of (1) a layer-based ETP model and (2) GRACE and GOCE information that is optimal over the area of Antarctica (and to be used with care outside this area, since the ETP is likely to possess a too strong weight in some spectral bands there). The combination in principle means a regularisation of (non-regularised) GOCE and GRACE normal equations using ETP coefficients with empirically designed regularisation weights. We choose the weighting scheme *A* in Hirt et al. (2015), which was found superior especially within the polar gap region of GOCE. The combination of GRACE and GOCE with the model `dV_ELL_RET2014` and `dV_ELL_Earth2014_lca` is named `SatGravRet2014` and `SatGravEarth2014`, respectively. Importantly, a combination of this kind is not possible with spherically approximated (STP) models, since the levels of approximation of the satellite component and the topography component would not be consistent (see Sect. 4.5).

We compared the combined models with gravity observations as contained in the newly released Antarctic gravity anomaly grids (AGAG) (Scheinert et al. 2016). The AGAG data set is based on 13 million observations and covers an area of 1×10^7 km², corresponding to 73 % of the Antarctic continent (Fig. 12). We therefore synthesise the gravity anomaly at each AGAG point of height *h* above the reference surface from both combination models up to their maximum degree of resolution (d/o 2190). We also compute the gravity anomaly from the model EGM2008 (Pavlis et al. 2012) and the satellite-only model GOCO05s (Pail et al. 2011; Mayer-Gürr et al. 2015). The residuals—the differences between the AGAG data and the synthesised gravity—are taken here as an indicator of how close the observed potential (via AGAG) is represented by the different modelling variants. In case of the combination models, the differences between the AGAG gravity and modelled gravity can also be interpreted as short-scale Bouguer gravity: the AGAG observations are (more or less) completely reduced by the observed satellite gravity in the long wavelengths; in the short wavelengths, the AGAG gravity is reduced for the gravitational effect of the visible topographic masses (=Bouguer gravity).

For the entire AGAG data set (181,443 grid points) and a subset of the most accurate grid points (24,315 grid points with standard deviation (STD) < 2 mGal) the residuals reveal that the herein created combination model based on the layer approach (`SatGravEarth2014`) performs better than the other models under investigation (Table 8). The improvement in `SatGravEarth2014` w.r.t. EGM2008 is 15 % using all AGAG points and 25 % using the more accurate subset of points, while it improves over GOCO05s with 8 % using all points and 18.5 % in the subset. The improvement in layer-based modelling w.r.t. RET modelling is about 2 % over both areas in Antarctica, which corresponds to an RMS/STD of ~ 0.3 mGal. The improvement is not very large in absolute terms but still indicative, given the differences between `SatGravRet2014` and `SatGravEarth2014` gravity at the AGAG points (Fig. 12) have an RMS of ~ 1 mGal only. Further, the positive effect of layer-based modelling is more notable over the ocean (5 % improvement) than over land/continental Antarctica (1% improvement). Globally, this tendency is shown already in Fig. 9. Note that EGM2008 shows a better performance over the ocean than the other investigated models. This is to be expected and reflects that AGAG data and EGM2008 are observation based down to short scales. EGM2008 has DTU altimetry data included over the oceans while AGAG over the oceans presumably relies on ship-track-based observations; hence, both data sets are observation based and thus in closer agreement than the

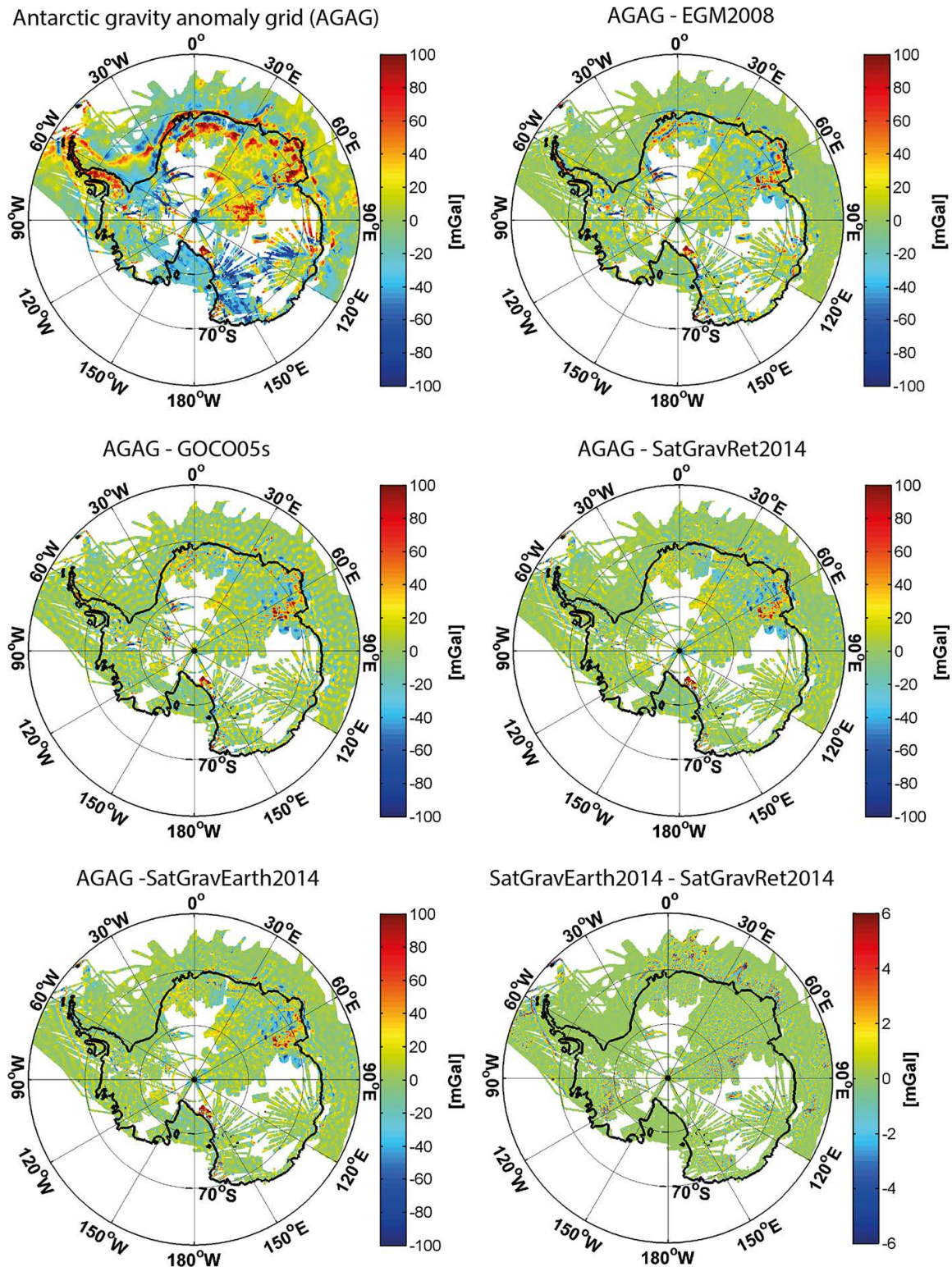


Fig. 12 Antarctic gravity anomaly grid (*upper left plot*) and residuals with gravity anomalies synthesised from various GGMs (unit is in mGal)

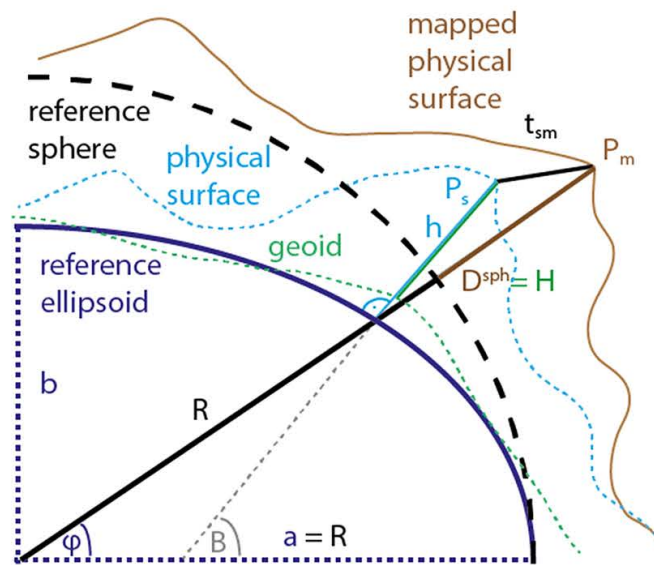
AGAG observations with forward models. Also, this finding reveals limitations in currently available Antarctic bathymetry data.

The sum of (1) GOCO05s taken (from $n = 0$) up to degree 280 and (2) ETP model ($dV_ELL_RET2014$ or $dV_ELL_Earth2014$) taken in the band $281 \leq n \leq 2190$ shows less agreement with AGAG data (~ 1 mGal more in terms of RMS/STD, see Table 8) than the

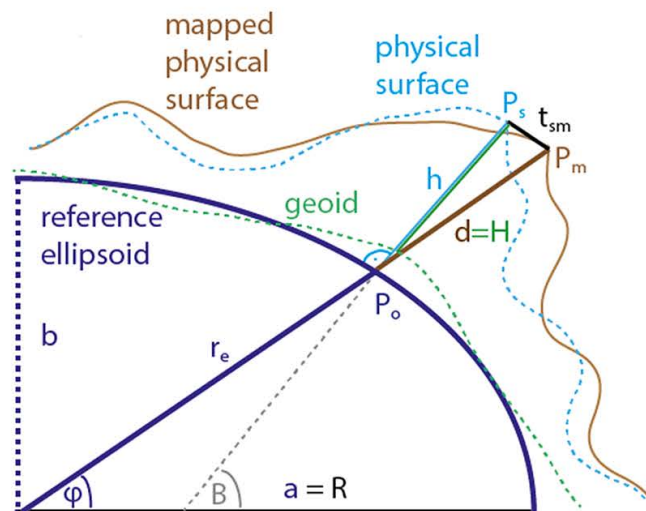
Table 8 Descriptive statistics of residual gravity between Antarctic gravity anomaly grid (AGAG) points and various gravitational models for four different AGAG gravity data subsets

AGAG pts (#)	Model	Min (mGal)	Max (mGal)	Mean (mGal)	RMS (mGal)	STD (mGal)	Relative to EGM2008 (%)	Relative to GOCO05s (%)	
	0..280	281..2190							
Total (181,443)	EGM2008	-356.73	219.13	-0.02	19.61	19.61	-	-	
	GOCO05s	-356.30	193.31	0.22	18.10	18.10	7.7	-	
	GOCO05s	dV_ELL_RET2014	-343.15	217.33	0.28	17.90	17.90	8.7	1.1
	GOCO05s	dV_ELL_Earth2014	-342.98	217.26	0.28	17.59	17.59	10.3	2.8
	SatGravRET2014		-355.01	221.47	0.45	17.02	17.01	13.3	6.0
	SatGravEarth2014		-354.90	221.61	0.45	16.67	16.66	15.0	8.0
	EGM2008		-356.73	219.13	0.02	24.56	24.56	-	-
	GOCO05s		-356.30	193.31	0.21	21.56	21.56	12.2	-
	GOCO05s	dV_ELL_RET2014	-343.16	217.33	0.14	20.63	20.63	16.0	4.3
	GOCO05s	dV_ELL_Earth2014	-342.99	217.26	0.14	20.39	20.39	17.0	5.4
	SatGravRET2014		-355.01	221.47	0.34	19.91	19.91	18.9	7.7
	SatGravEarth2014		-354.89	221.61	0.34	19.66	19.66	20.0	8.8
	EGM2008		-129.40	132.03	-0.07	10.89	10.89	-	-
	GOCO05s		-85.93	104.46	0.24	12.69	12.69	-16.5	-
Only ocean (82,033)	GOCO05s	dV_ELL_RET2014	-124.57	125.06	0.45	13.87	13.87	-27.4	-9.3
	GOCO05s	dV_ELL_Earth2014	-110.40	123.17	0.46	13.41	13.40	-23.0	-5.6
	SatGravRET2014		-129.81	134.08	0.59	12.65	12.63	-16.0	0.5
	SatGravEarth2014		-120.34	133.18	0.59	12.07	12.06	-10.7	5.0
	EGM2008		-119.99	141.34	-0.01	19.10	19.10	-	-
	GOCO05s		-98.68	139.69	-0.29	17.52	17.52	8.3	-
	GOCO05s	dV_ELL_RET2014	-201.79	96.60	-0.17	15.76	15.76	17.5	10.1
	GOCO05s	dV_ELL_Earth2014	-200.29	93.12	-0.17	15.43	15.43	19.2	11.9
	SatGravRET2014		-206.96	103.41	0.17	14.65	14.65	23.3	16.4
	SatGravEarth2014		-205.40	99.22	0.18	14.30	14.30	25.1	18.4
	AGAG STD ≤ 2 mGal (24,315)								

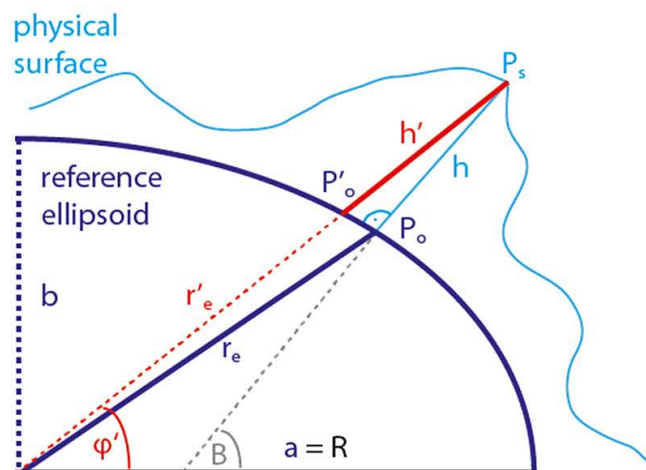
(a) STP mapping: spherical approximation



(b) ETP mapping: ellipsoidal approximation



(c) ETP without mapping



◀ **Fig. 13** Scheme of mapping of the Earth’s physical surface in the investigated modelling techniques: mapping situation in STP modelling in spherical approximation (a), mapping situation in ETP modelling in ellipsoidal approximation (b) and mapping-free situation in ETP modelling without approximation by using pseudo-ellipsoidal heights h' at their respective latitudes φ' (c); φ : geocentric latitude; B : geodetic latitude; r_e : ellipsoidal radius to P_o ; r'_e : ellipsoidal radius to P'_o ; a, b : semi-major/minor axis of ellipsoid; R : spherical radius; H : orthometric height; h : ellipsoidal height; D^{sph} : mapped spherical height; d : mapped ellipsoidal height; P_s : surface point; P_m : mapped surface point; t_{sm} : distance $\overline{P_s P_m}$

combination models that also comprise gravity from GRACE, GOCE and ETP model (SatGravRET2014 and SatGravEarth2014). Thus, a quite simple combination of the ETP and observed gravity, e.g., as done here by means of a regularisation, is better than omission error modelling, since the latter leads to higher residuals. Omission error modelling means the estimation of short-scale gravity signals that are not contained in a GGM (i.e. signals beyond the maximum degree N of the model) by band-limited information that can, for example, be computed from a residual terrain model (RTM modelling, c.f. Forsberg 1984) or taken from a (abrupt) truncation of a topographic potential model, as done here.

4.5 Modelling Differences Between the Spherical and Ellipsoidal Approach

The spherically approximated (see Sect. 2.1) and ellipsoidally approximated (see Sect. 2.2) layer-based forward modelling of the potential in spherical harmonics—leading to solutions of the STP and ETP, respectively—is to be treated and interpreted differently. The STP and ETP are inherently different regarding the spectral and spatial domain characteristics as will be shown next.

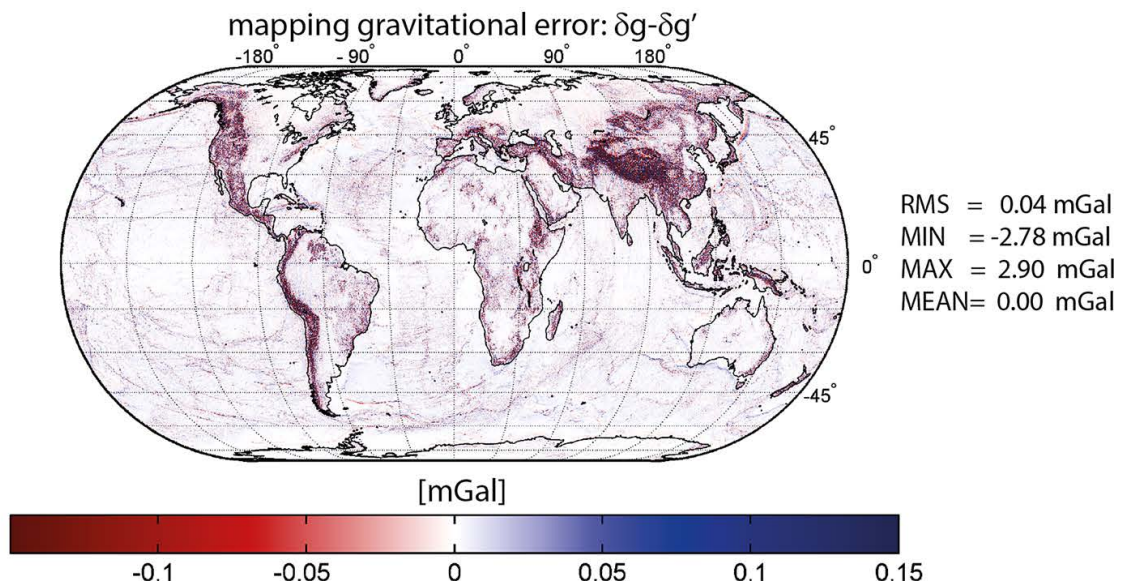
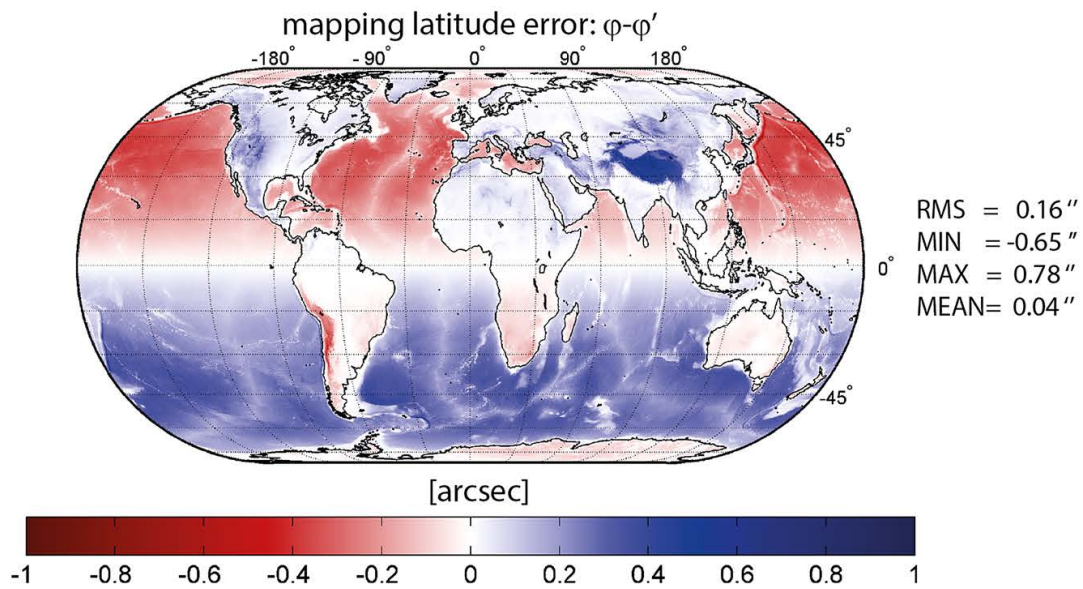
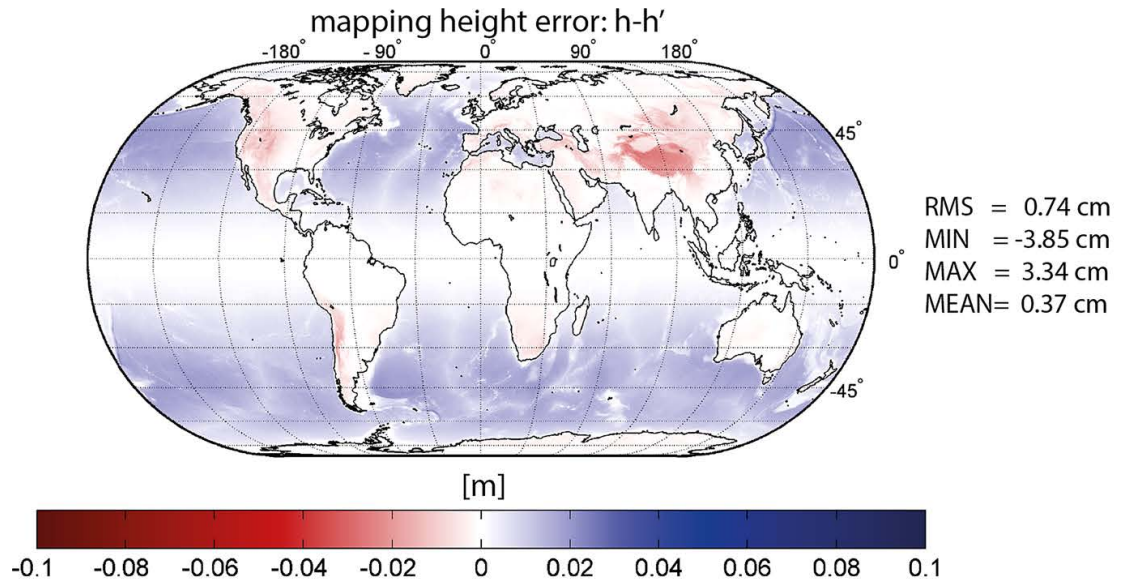
4.5.1 Geometric Differences and Mapping of the Layer Boundaries

Essentially, both STP and ETP are different representations of the (same) potential that is generated by the same masses which are defined by volumetric layers (see Sects. 2, 3). The spherical approach assumes the boundaries of the layers to be referenced to some reference

Table 9 Definition of heights and their usage in this work (see also Fig. 13)

Symbol	Term	Direction	Meaning	Use in this work
N	Geoid height	Normal to ellipsoid	Diff. between h and H	None
\tilde{H}	Mean-sea-level height	Aprpr. normal to geoid	Distance: MSL to P_s	Given by DEMs and used for H
H	Orthometric height	Normal to geoid	Distance: geoid to P_s	Used to approximate the heights in STP and ETP modelling
h	Ellipsoidal height	Normal to ellipsoid	Distance: ellipsoid to P_s	Unusable in the modelling because of direction
d	Mapped ellipsoidal height	Direction to geocenter	Distance: ellipsoid to P_m	In ETP modelling under ellipsoidal approximation
h'	Pseudo-ellipsoidal height	Direction to geocenter	Distance: ellipsoid to P_s	Can be used in ETP modelling to avoid mapping
D^{sph}	Mapped spherical height	Direction to geocenter	Distance: sphere to P_m	In STP modelling under spherical approximation
H^{sph}	Spherical height	Direction to geocenter	Distance: sphere to P_s	In STP modelling (theoretically)

P_s , surface point; P_m , mapped surface point; MSL, mean sea level



◀ **Fig. 14** Mapping effects in the ETP in terms of height differences $h - h'$ (in metres, *upper plot*), latitude differences $\varphi - \varphi'$ (in arc-seconds, *middle plot*) and the resulting gravity disturbance differences $\delta_g - \delta'_g$ (in mGal, *lower plot*) of both geometric effects. Note, the effects are also contained in the mapping within the STP, but projected onto the sphere

sphere. This is accomplished with the orthometric height serving as an approximation for the distance between sphere and surface point (referred to as mapped spherical height). The ellipsoidal approach assumes the layers to be referenced to some reference ellipsoid using the orthometric height as approximation for the distance between ellipsoid and surface point (referred to as mapped ellipsoidal height). See also Table 9 for an overview of the used heights, their definitions and use. Neither of the approaches thus takes into account the geoid–ellipsoid separation (i.e. the geoid height), which shall not be further looked at here, nor the fact that orthometric heights are not measured along the direction to the geocenter, which is implicitly assumed in the spherical harmonic framework.

The result of the latter is a displacement (often referred to as mapping) of the Earth's physical surface and of all layer boundaries (Fig. 13). In case of the spherical approximation (STP), the approximation error introduced by the mapping is hard to be determined/interpreted, since the masses and computation point P_S are rearranged w.r.t. a spherical reference (Fig. 13a) and there is no workaround to avoid a displacement of masses. In case of the ellipsoidal approximation (ETP), the displacement due to mapping is largest at mid-latitudes and becomes zero at the poles and the equator (Fig. 13 B and Fig. 14). These displacements are also a part of the mapping within the STP, but (additionally) projected onto the sphere. At maximum, consider a point P_s with extreme elevation of $h = 9$ km above or $h = -10$ km below the ellipsoid and at a latitude of $B = 45^\circ$, the displacement given by the distance $t_{sm} = \overline{P_s P_m}$ between surface point P_s and its mapped equivalent P_m becomes ~ 30 m or 33 m, respectively (i.e. $\varphi - \varphi' \sim 0.9''$ and $h - h' \sim 5$ cm). This confirms similar the findings by Balmino et al. (2012). In view of 10-km resolution models as computed in this model, mass displacements of this order hardly play a role. Nevertheless, in case of the ETP, displacement can be avoided by working with what we denote pseudo-ellipsoidal heights h' (c.f. Appendix 1 for their computation). They are given at their respective geocentric latitudes φ' that are defined along the direction towards the geocenter (Fig. 13c). Working with the pseudo-ellipsoidal heights instead of mapped ellipsoidal heights within layer-based modelling to degree 2190 yields differences in the order of ± 3 mGal or RMS=0.04 mGal (see Fig. 14). Accounting for the mapping is thus only required for applications of high accuracy or high resolution.

4.5.2 Differences in the Spectral Domain

The spherical harmonic coefficients of STP and ETP differ notably as can be seen from their degree variances (Fig. 15). The degree variances of the STP (dV_SPH_Earth2014_lca/lra) follow Kaula's rule (Kaula 1966) closely, which itself is close to the truly ellipsoidal harmonic spectrum of the gravity field (Rexer and Hirt 2015a). The degree variances of the ETP (dV_ELL_Earth2014_lca/lra) run below those of STP. They are comparable to commonly used gravity field models (e.g., those listed at ICGEM). This has already been found by Rexer and Hirt (2015a), who empirically derived an approximate rule of thumb that allows to transform degree variances from a spherically approximated model (STP) into their ellipsoidally approximated equivalents (ETP) (and vice versa). All spherical harmonic GGMs (of $N > 2000$) that (implicitly) assume an ellipsoidal Earth are accompanied by a "tail" of 30 degrees (from degree 2160 to 2190) with rapidly decreasing

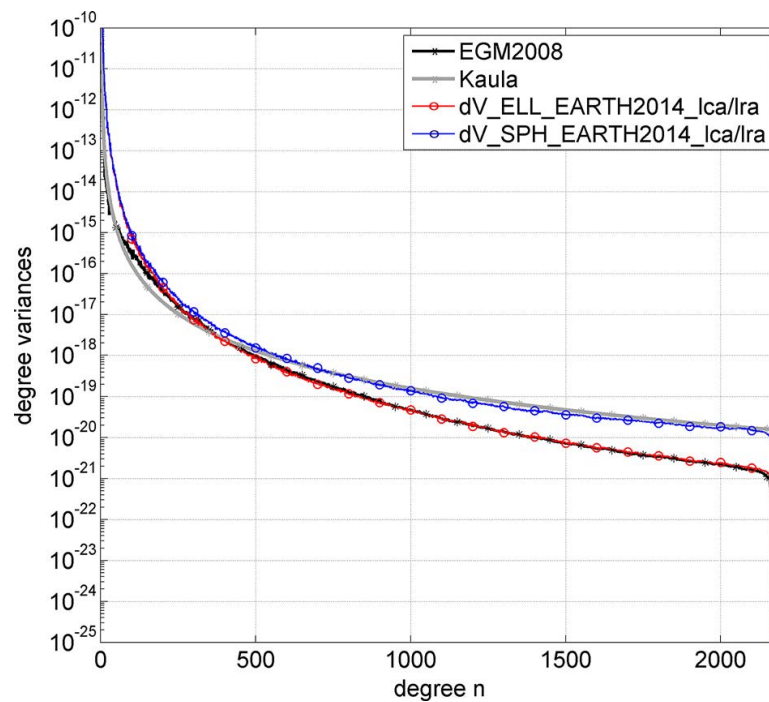


Fig. 15 Spectral characteristics of the spherically ($dV_SPH_Earth2014_lca/lra$) and the ellipsoidally ($dV_ELL_Earth2014_lca/lra$) approximated potential models in terms of degree variances, together with those of EGM2008 and Kaula's rule of thumb

energy, which are needed for a proper representation of the potential. This is the very reason why band-limited investigation is not possible with this kind of models (see Sect. 4.3) without suffering from erroneous striations increasing with latitude (see also Claessens and Hirt 2013; Pavlis et al. 2012). Spherical harmonic models in spherical approximation allow band-limited investigations akin to truly ellipsoidal harmonic models (see Sect. 4.3).

4.5.3 Differences in the Space Domain

In the space domain, rather long-wavelength differences appear between the STP and the ETP at the level of few mGals (Fig. 16). Note that for a comparison of ETP and STP in the space domain, the ETP was evaluated on the surface of the reference ellipsoid while the STP was evaluated on the surface of the reference sphere. Similar differences were already found to reflect different mass arrangements between ETP and STP by Claessens and Hirt (2013) (ibid. Fig. 6a) who applied the HC method to a single-density mass model. At the Earth's surface, the effect is almost of the same dimension with marginally smaller amplitudes and similar RMS (Fig. 17). The differences in Figs. 16 and 17 also contain the effect of mapping discussed above (h vs. h' and φ vs. φ'), but they are dominated by the additional mapping of the masses from the ellipsoid onto the sphere.

The differences notably differ from the *ellipsoidal correction* (Fig. 12 in Balmino et al. 2012) which is thought to correct a STP model for the difference between integrating Earth's masses w.r.t. spherical instead of an ellipsoidal reference. The range of the *ellipsoidal correction* in Balmino et al. (2012) is much smaller (~ 0.005 mGal vs. ~ 8 mGal)—even when investigating the differences in Fig. 16 in the same spectral band ($0 \leq n \leq 120$)—and is predominated by a zonal J_2 effect. Possibly, their correction, which is only computed to the second order, is a part of the true difference between a topographic forward model in spherical and ellipsoidal approximation.

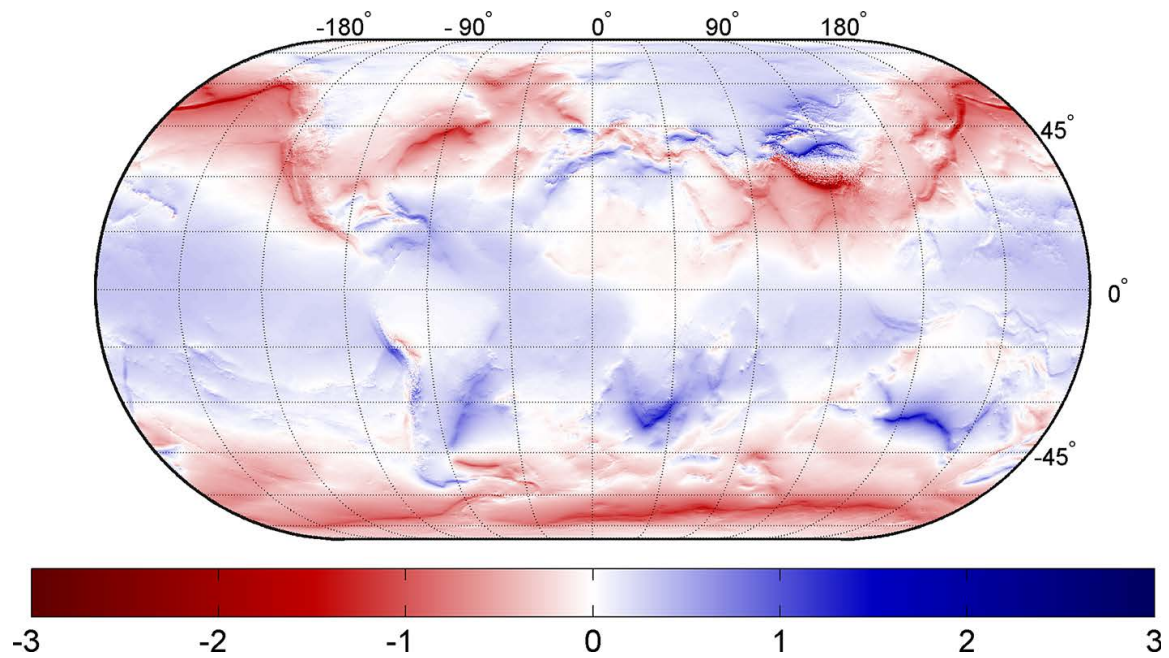


Fig. 16 Gravity difference between the spherically ($dV_SPH_Earth2014_lca/lra$) and the ellipsoidally ($dV_ELL_Earth2014_lca/lra$) approximated potential models in terms of gravity disturbances evaluated *at the respective reference surface (sphere and ellipsoid, respectively)*; RMS = 0.35 mGal; min = -4.66 mGal; max = 2.84 mGal; mean = -0.08 mGal (unit is in mGal)

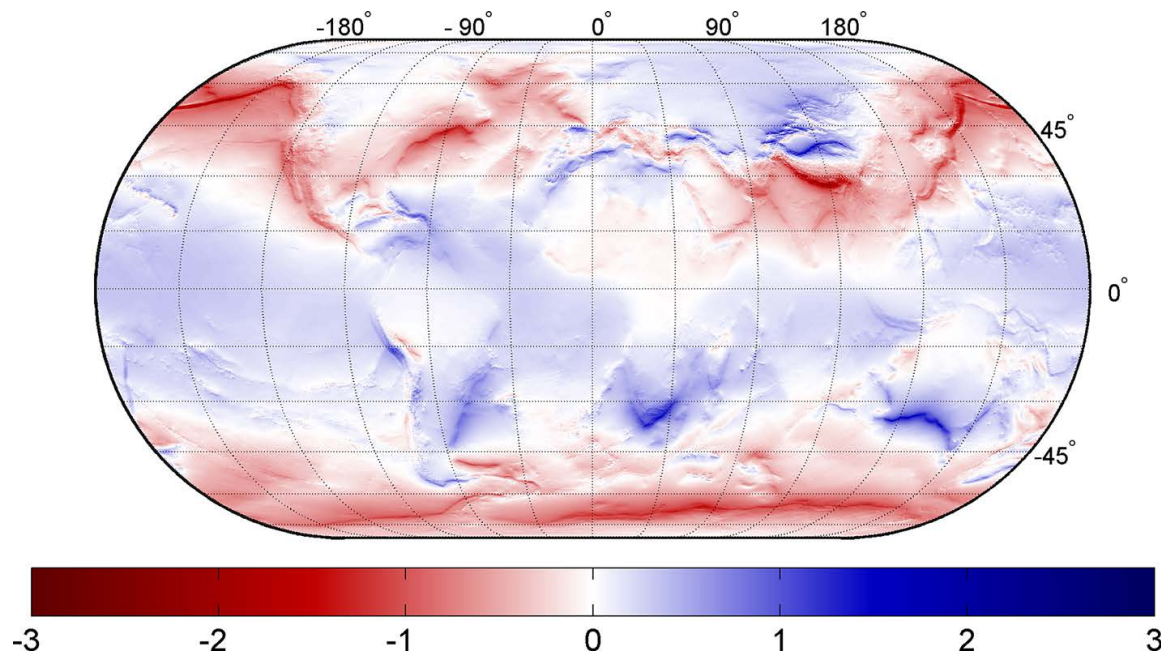


Fig. 17 Gravity difference between the spherically ($dV_SPH_Earth2014_lca/lra$) and the ellipsoidally ($dV_ELL_Earth2014_lca/lra$) approximated potential models in terms of gravity disturbances evaluated *at the Earth's surface*; RMS = 0.36 mGal; min = -2.89 mGal; max = 2.11 mGal; mean = -0.08 mGal (unit is in mGal)

5 Conclusions and Outlook

We presented spectral forward modelling based on volumetric mass layers to d/o 2190 at two different levels of approximation (spherical and ellipsoidal) and took full account of increased sampling requirements and all relevant terms of the involved binomial series expansions, avoiding aliasing and truncation errors due to early truncation of the series.

Based on the HCM method, we derived a new spherical harmonic approach that allows us to rigorously and efficiently compute the ellipsoidally approximated topographic potential based on volumetric layers of laterally varying density that are referenced to an ellipsoid. A layer concept has been established with the layers' boundaries taken from the Earth2014 model, separating the masses of ice sheets, water in inland lakes/seas, ocean water and solid rock with 1' resolution. Applying the layer concept in two ways—in a correction approach with actual densities or in a reduction approach with density contrasts—leads to equivalent potentials, with negligible differences (RMS ~ 0.001 mGal) that are caused by the spherical harmonic representation of the respective layer boundaries. The layer-based modelling approach reaches over 90% correlation with EGM2008 in the band $900 \leq n \leq 2150$ with significantly higher correlations compared to single-density (RET) modelling. Further, it was shown to be at least equivalent to state-of-the-art layer-based forward modelling in the space domain. A validation with ground truth gravity data over Antarctica shows that layer-based modelling improves over single-density modelling by $\sim 2\%$, with the improvement being largest over the ocean ($\sim 5\%$). The latter was also confirmed globally by computing reduction rates with GOCE satellite observations as contained in GO_CONS_GCF_2_TIM_R5. For the validation, we computed a combination model, combining computed spherical harmonic coefficients in ellipsoidal approximation with satellite observations from GOCE and GRACE satellite, which is necessary in order to mitigate the problem of isostatically uncompensated masses in the forward models. The combination was done by means of an empirical regularisation of GOCE and GRACE normal equations. Using solely the most accurate ground truth observations (STD < 2 mGal) available, the combination model was found superior to EGM2008 and the satellite-only model GOCO05s (by ~ 25 and $\sim 8\%$ in terms of RMS). The comparison with ground truth data also showed that a combination of satellite data with the topographic potential, e.g., by means of a regularisation, is to be preferred compared to omission error modelling in general.

Depending on the level of approximation—spherical or ellipsoidal—we provided the framework to the spherical topographic potential (STP) or the ellipsoidal topographic potential (ETP), which were found to have substantially different spectral characteristics, yet rather small differences in the space domain. Evaluated at the respective reference surface or at surface of Earth, the STP and ETP show differences at the level of $\sim \pm 5$ mGal (RMS = 0.4 mGal) that mainly stem from a different arrangement of masses (mapping) due to different geometric assumptions in the approaches. In ellipsoidal approximation, the mapping, which was found to cause a rearrangement of masses by 30 m at maximum, can completely be avoided by using pseudo-ellipsoidal heights that are measured towards the geocenter. The error introduced by the mapping is in the order of mGal and should be taken into account in applications requiring ultra-high-resolution or high accuracy topographic gravity.

In the spectral domain, the STP shows substantially larger energy at short scales (comparable to that predicted by Kaula's rule of thumb or to the truly ellipsoidal harmonic spectrum of EGM2008) than the ETP. The ETP shows short-scale energy comparable to other spherical harmonic GGMs that make an (implicit) ellipsoidal assumption of Earth, e.g., EGM2008. This feature makes the ETP coefficients suitable for a combination with satellite data, e.g., as done in this work. The dependencies among the spherical harmonic coefficients in ellipsoidal approximation prevent application of the harmonic models in a band-limited manner (i.e. no truncations at $n < 2190$). In contrast, spherical harmonic models in spherical approximation and truly ellipsoidal harmonic models are free of such dependencies and may be used in band-limited form (i.e. truncated at $n < 2190$).

In conclusion, the choice between spherical and ellipsoidal approximation in spectral forward modelling depends on the application of the final models. While STP models may be good enough for a wide range of geophysical applications, ETP models are more accurate and needed for high-resolution applications. Current observation-based gravitational models conform spectrally with the ellipsoidal topographic potential which is inevitable for geodetic applications, such as a combination with satellite and terrestrial data by means of regularisation. The herein computed models are available at: http://ddfe.curtin.edu.au/models/Earth2014/potential_model/.

Acknowledgments This study received support from the German National Research Foundation (DFG), project n° Hi 1760/1. It was also supported by the Technische Universität München - Institute for Advanced Study, funded by the German Excellence Initiative (and the European Union Seventh Framework Programme under grant agreement n° 291763). We also acknowledge the Czech Ministry of Education, Youth and Sport for a financial support by the National Program of Sustainability, Project No.: LO1506. We thank Simon Holmes and NGA for the distribution of the land/ocean masks used in the creation of EGM2008. We further thank Simon Holmes for generously sharing the software facilitating Jekeli's transform with us. We thank Torsten Mayer-Gürr and Jan-Martin Brockmann for providing the satellite gravity normal equations for this study. We further acknowledge the work of all other producers of data used in this work. Finally, we thank two anonymous reviewers for their detailed reviews.

Appendix 1: Rigorous Expressions—Direct Solution to the Radial Integral in Modelling of the ETP and the STP

In contrast to the above presented solutions to the STP (Sect. 2.1) and ETP (Sect. 2.2) that rely on a binominal series expansion for the solution of the radial integral (Eq. 17), and in case of the ETP also on the binominal series expansion in Eq. 27, here the rigorous expressions are given.

The direct (rigorous) solution to the radial integral over the masses in a layer (Eq. 10) was given already in Eq. 11 or (in more generalised form) in Eq. 13, respectively.

Rigorous Solution to the STP of a Volumetric Mass Layer

In case of the STP, the direct integral solution to the radial integral from the lower to the upper layer bound in spherical approximation reads

$$\Omega^{(STP,\omega)} = \rho^{(\Omega_\omega)}(\theta_Q, \lambda_Q) \frac{R}{n+3} \left(\left(\frac{R + H_{UB}^{(\Omega_\omega)}}{R} \right)^{n+3} - \left(\frac{R + H_{LB}^{(\Omega_\omega)}}{R} \right)^{n+3} \right). \quad (37)$$

Inserting Eq. 37 into Eq. 9 the rigorous expression of the STP of a volumetric mass layer is

$$\hat{V}_{nm}^{(STP,\Omega_\omega)} = \frac{3}{\bar{\rho}(2n+1)(n+3)} \times \frac{1}{4\pi} \int_{\lambda=0}^{2\pi} \int_{\theta=0}^{\pi} \rho^{(\Omega_\omega)}(\theta_Q, \lambda_Q) \times \left(\left(\frac{R + H_{UB}^{(\Omega_\omega)}}{R} \right)^{n+3} - \left(\frac{R + H_{LB}^{(\Omega_\omega)}}{R} \right)^{n+3} \right) \bar{Y}_{nm}(\theta_Q, \lambda_Q) \sin \theta d\theta d\lambda, \quad (38)$$

and with

$$\overline{HDF}_{\text{nm}}^{(\text{STP}, \Omega\omega)} = \frac{1}{4\pi} \int_{\lambda=0}^{2\pi} \int_{\theta=0}^{\pi} \rho^{(\Omega\omega)}(\theta_Q, \lambda_Q) \left(\left(\frac{R + H_{\text{UB}}^{(\Omega\omega)}}{R} \right)^{n+3} - \left(\frac{R + H_{\text{LB}}^{(\Omega\omega)}}{R} \right)^{n+3} \right) \overline{Y}_{\text{nm}}(\theta_Q, \lambda_Q) \sin \theta d\theta d\lambda. \tag{39}$$

we arrive at the more concise form

$$\hat{V}_{\text{nm}}^{(\text{STP}, \Omega\omega)} = \frac{3}{\bar{\rho}(2n+1)(n+3)} \overline{HDF}_{\text{nm}}^{(\text{STP}, \Omega\omega)}. \tag{40}$$

As mentioned above, rigorous expressions for the STP of a layer in principle are known already in different notation, e.g., by Pavlis and Rapp (1990). The disadvantage of the rigorous expression in Eq. 40 is that it needs n_{max} spherical harmonic analyses of the surface function $\overline{HDF}_{\text{nm}}^{(\text{STP}, \Omega\omega)}$, while the expression relying on a binominal series expansion (Eq. 21) only needs k_{max} analyses, where $k_{\text{max}} \ll n_{\text{max}}$ in general (see Sect. 2.3 for convergency behaviour of the binominal series).

Rigorous Solution to the ETP of a Volumetric Mass Layer

In case of the ETP, the direct integral solution to the radial integral from the lower to the upper layer bound in ellipsoidal approximation reads

$$\Omega^{(\text{ETP}, \omega)} = \rho^{(\Omega\omega)}(\theta_Q, \lambda_Q) \frac{R}{n+3} \left(\frac{r_e}{R} \right)^{n+3} \left(\left(\frac{r_e + d_{\text{UB}}^{(\Omega\omega)}}{r_e} \right)^{n+3} - \left(\frac{r_e + d_{\text{LB}}^{(\Omega\omega)}}{r_e} \right)^{n+3} \right). \tag{41}$$

Inserting Eq. 41 into Eq. 9, the rigorous expression of the ETP of a volumetric mass layer is

$$\begin{aligned} \hat{V}_{\text{nm}}^{(\text{ETP}, \Omega\omega)} &= \frac{3}{\bar{\rho}(2n+1)(n+3)} \\ &\times \frac{1}{4\pi} \int_{\lambda=0}^{2\pi} \int_{\theta=0}^{\pi} \rho^{(\Omega\omega)}(\theta_Q, \lambda_Q) \left(\frac{r_e}{R} \right)^{n+3} \left(\left(\frac{r_e + d_{\text{UB}}^{(\Omega\omega)}}{r_e} \right)^{n+3} - \left(\frac{r_e + d_{\text{LB}}^{(\Omega\omega)}}{r_e} \right)^{n+3} \right) \\ &\times \overline{Y}_{\text{nm}}(\theta_Q, \lambda_Q) \sin \theta d\theta d\lambda, \end{aligned} \tag{42}$$

and with

$$\begin{aligned} \overline{HDF}_{\text{nm}}^{(\text{ETP}, \Omega\omega)} &= \frac{1}{4\pi} \int_{\lambda=0}^{2\pi} \int_{\theta=0}^{\pi} \rho^{(\Omega\omega)}(\theta_Q, \lambda_Q) \left(\frac{r_e}{R} \right)^{n+3} \\ &\times \left(\left(\frac{r_e + d_{\text{UB}}^{(\Omega\omega)}}{r_e} \right)^{n+3} - \left(\frac{r_e + d_{\text{LB}}^{(\Omega\omega)}}{r_e} \right)^{n+3} \right) \overline{Y}_{\text{nm}}(\theta_Q, \lambda_Q) \sin \theta d\theta d\lambda. \end{aligned} \tag{43}$$

we arrive at the more concise form

$$\hat{V}_{\text{nm}}^{(\text{ETP}, \Omega\omega)} = \frac{3}{\bar{\rho}(2n+1)(n+3)} \overline{HDF}_{\text{nm}}^{(\text{ETP}, \Omega\omega)}. \tag{44}$$

The disadvantage of the rigorous expression in Eq. 44 is that it needs n_{\max} spherical harmonic analyses of the surface function $\overline{HDF}_{\text{nm}}^{(\text{ETP}, \Omega\omega)}$, while the expression relying on binominal series expansions (Eq. 31) only needs k_{\max} analyses, where $k_{\max} \ll n_{\max}$ in general (see Sect. 2.3 for convergency behaviour of the binominal series).

Appendix 2: Computation of the Pseudo-Ellipsoidal Height h' and Its Latitude φ' of the Surface Point P_S

Given a surface point P_S with ellipsoidal height h , geodetic latitude B and geocentric distance r defined by

$$r^2 = (r'_e + h')^2 \tag{45}$$

the pseudo-ellipsoidal height h' that is running along the direction towards the geocenter (Fig. 18) can be computed using the cosine rules

$$r^2 = c^2 + ((N - e^2N) + h)^2 - 2c((N - e^2N) + h) \cdot \cos(\pi - B) \tag{46}$$

where

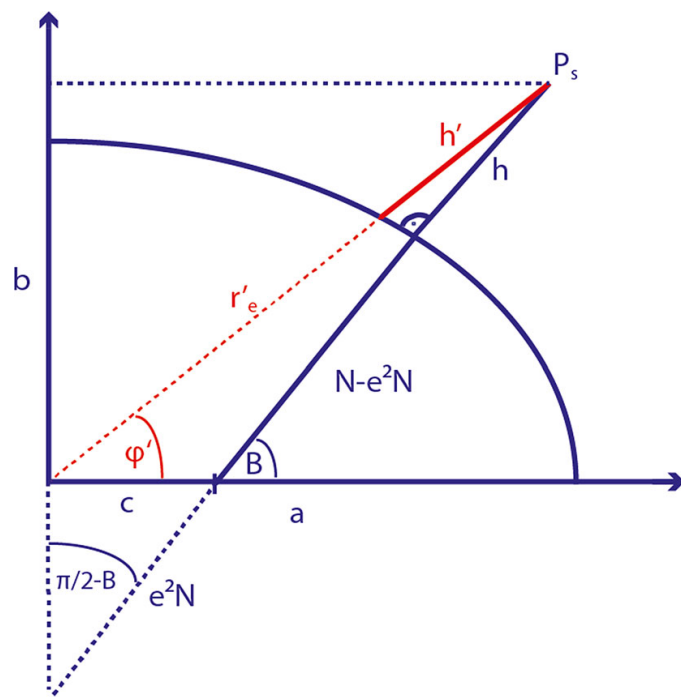
$$c = e^2N \cos B, \tag{47}$$

$$N = \frac{a}{\sqrt{1 - e^2 \cdot \sin^2 B}} \tag{48}$$

and

$$r'^2_e = a^2 \frac{1 - e^2}{1 - e^2 \cdot \cos^2 \varphi'}. \tag{49}$$

Fig. 18 Ellipsoidal height h and pseudo-ellipsoidal height h'



The (geocentric) latitude ϕ' can be computed using the sine rule

$$\sin \phi' = \left(\frac{((N - e^2 N) + h) \cdot \sin(\pi - B)}{r} \right). \quad (50)$$

Then, the pseudo-ellipsoidal height is retrieved with

$$h' = r - r'_e. \quad (51)$$

References

- Amante C, Eakins B (2009) ETOPO1 1 arc-minute global relief model: procedures, data sources and analysis. NOAA Technical Memorandum NESDIS NGDC-24, National Geophysical Data Center, NOAA
- Balmino G, Lambeck K, Kaula W (1973) A spherical harmonic analysis of the earth's topography. *J Geophys Res* 78(2):478–521
- Balmino G, Vales N, Bonvalot S, Briais A (2012) Spherical harmonic modelling to ultra-high degree of bouguer and isostatic anomalies. *J Geodesy* 86(7):499–520. doi:[10.1007/s00190-011-0533-4](https://doi.org/10.1007/s00190-011-0533-4)
- Bartusch M, Berg H, Siebertz O (2008) The TanDEM-X mission. In: 2008 7th European conference on synthetic aperture radar (EUSAR), pp 1–4
- Brockmann J, Zehentner N, Höck E, Pail R, Loth I, Mayer-Gürr T, Schuh W (2014) EGM_TIM_RL05: an independent geoid with centimeter accuracy purely based on the GOCE mission. *Geophys Res Lett* 41(22):8089–8099. doi:[10.1002/2014GL061904](https://doi.org/10.1002/2014GL061904)
- Bucha B, Janák J (2014) A MATLAB-based graphical user interface program for computing functionals of the geopotential up to ultra-high degrees and orders: efficient computation at irregular surfaces. *Comput Geosci* 66:219–227
- Chen W, Tenzer R (2014) Harmonic coefficients of the Earth's spectral crustal model 180–ESCM180. *Earth Sci Inf* 8(1):147–159. doi:[10.1007/s12145-014-0155-5](https://doi.org/10.1007/s12145-014-0155-5)
- Claessens S (2006) Solutions to ellipsoidal boundary value problems for gravity field modelling. Ph.D. thesis, Curtin University of Technology
- Claessens S, Hirt C (2013) Ellipsoidal topographic potential—new solutions for spectral forward gravity modelling of topography with respect to a reference ellipsoid. *J Geophys Res* 118(11):5991–6002. doi:[10.1002/2013JB010457](https://doi.org/10.1002/2013JB010457)
- Fecher T, Pail R, Gruber T (2013) Global gravity field modeling based on GOCE and complementary gravity data. *Int J Appl Earth Obs Geoinf* 35(Part A):120–127. doi:[10.1016/j.jag.2013.10.005](https://doi.org/10.1016/j.jag.2013.10.005)
- Forsberg R (1984) A study of terrain reductions, density anomalies and geophysical inversion methods in gravity field modelling. OSU Report 355, Ohio State University
- Forsberg R, Jensen T (2015) New geoid of Greenland: a case study of terrain and ice effects. GOCE and the use of local sea level data. International association of geodesy symposia. doi:[10.1007/1345_2015_50](https://doi.org/10.1007/1345_2015_50)
- Göttl F, Rummel R (2009) A geodetic view on isostatic models. *Pure Appl Geophys* 166:1247–1260. doi:[10.1007/s00024-004-0489-x](https://doi.org/10.1007/s00024-004-0489-x)
- Grombein T, Seitz K, Heck B (2013) Optimized formulas for the gravitational field of a tesseroid. *J Geodesy* 87:645–660. doi:[10.1007/s00190-013-0636-1](https://doi.org/10.1007/s00190-013-0636-1)
- Grombein T, Luo X, Seitz K, Heck B (2014) A wavelet-based assessment of topographic-isostatic reductions for GOCE gravity gradients. *Surv Geophys*. doi:[10.1007/s10712-014-9283-1](https://doi.org/10.1007/s10712-014-9283-1)
- Grombein T, Seitz K, Heck B (2016) The rock–water–ice topographic gravity field model *RWI_TOPO_2015* and its comparison to a conventional rock-equivalent-version. *Surv Geophys* 37(5):937–976. doi:[10.1007/s10712-016-9376-0](https://doi.org/10.1007/s10712-016-9376-0)
- Heck B, Seitz K (2007) A comparison of the tesseroid, prism and point-mass approaches for mass reductions in gravity field modelling. *J Geodesy* 81:121–136. doi:[10.1007/s00190-006-0094-0](https://doi.org/10.1007/s00190-006-0094-0)
- Heiskanen W, Moritz H (1967) *Physical Geodesy*. W.H. Freeman Company, London
- Hirt C (2012) Efficient and accurate high-degree spherical harmonic synthesis of gravity field functionals at the Earth's surface using the gradient approach. *J Geodesy* 86(9):729–744
- Hirt C, Kuhn M (2014) A band-limited topographic mass distribution generates a full-spectrum gravity field—gravity forward modelling in the spectral and spatial domain revisited. *J Geophys Res Solid Earth* 119(4):3646–3661. doi:[10.1002/2013JB010900](https://doi.org/10.1002/2013JB010900)

- Hirt C, Rexer M (2015) Earth 2014: 1° shape, topography, bedrock and ice-sheet models—available as gridded data and degree 10,800 spherical harmonics. *Int J Appl Earth Obs Geoinf*. doi:[10.1016/j.jag.2015.03.001](https://doi.org/10.1016/j.jag.2015.03.001)
- Hirt C, Gruber T, Featherstone W (2011) Evaluation of the first GOCE static gravity field models using terrestrial gravity, vertical deflections and EGM2008 quasigeoid heights. *J Geodesy* 85:723–740
- Hirt C, Kuhn M, Featherstone W, Göttl F (2012) Topographic/isostatic evaluation of new-generation GOCE gravity field models. *J Geophys Res Solid Earth* 117:B05407. doi:[10.1029/2011JB008878](https://doi.org/10.1029/2011JB008878)
- Hirt C, Claessens S, Fecher T, Kuhn M, Pail R, Rexer M (2013) New ultra-high resolution picture of Earth's gravity field. *Geophys Res Lett* 40. doi:[10.1002/grl.50838](https://doi.org/10.1002/grl.50838)
- Hirt C, Rexer M, Scheinert M, Pail R, Claessens S, Holmes S (2015) A new degree-2190 (10 km resolution) gravity field model for Antarctica developed from GRACE, GOCE and Bedmap2 data. *J Geodesy* 90:105–127. doi:[10.1007/s00190-015-0857-6](https://doi.org/10.1007/s00190-015-0857-6)
- Jekeli C (1988) The exact transformation between ellipsoidal and spherical harmonic expansions. *Manuscr Geod* 13(2):106–113
- Kaula W (1966) *Theory of satellite geodesy*. Blaisdel, Waltham
- Kuhn M, Hirt C (2016) Topographic gravitational potential up to second-order derivatives: an examination of approximation errors caused by rock-equivalent topography (RET). *J Geodesy* 90(9):883–902. doi:[10.1007/s00190-016-0917-6](https://doi.org/10.1007/s00190-016-0917-6)
- Kuhn M, Seitz K (2005) Comparison of Newton's integral in the space and frequency domains. In: Sanso F (ed) *A window on the future of geodesy—IAG symposia*, vol 128, pp 386–391
- Laske G, Masters G, Ma Z, Pasyanos M (2012) CRUST1. 0: an updated global model of Earth's crust. *Geophys Res Abs* 14
- Lee W, Kaula W (1967) A spherical harmonic analysis of the Earth's topography. *J Geophys Res* 72:753–758
- Mayer-Gürr T, Kurtenbach E, Eicker A (2010) ITG-Grace2010 gravity field model. <http://www.igg.uni-bonn.de/apmg/index.php?id=itg-grace2010>
- Mayer-Gürr T, Pail R, Gruber T, Fecher T, Rexer M, Schuh WD, Kusche J, Brockmann JM, Rieser D, Zehentner N, Kvas A, Klinger B, Baur O, Höck E, Krauss S, Jäggi A (2015) The combined satellite gravity field model goco05s. In: *Presentation at EGU 2015, Vienna, April 2015*
- Nagy D, Papp G, Benedek J (2000) The gravitational potential and its derivatives for the prism. *J Geodesy* 74:552–560. doi:[10.1007/s00190-006-0094-0](https://doi.org/10.1007/s00190-006-0094-0)
- Nagy D, Papp G, Benedek J (2002) Correction to “the gravitational potential and its derivatives for the prism”. *J Geodesy* 76:475. doi:[10.1007/s00190-002-0264-7](https://doi.org/10.1007/s00190-002-0264-7)
- Pail R, Fecher T, Jäggi A, Goiginger H (2011) Can GOCE help to improve temporal gravity field estimates? In: Ouwehand L (ed) *Proceedings of the 4th international GOCE user workshop*, ESA Publication SP-696
- Pasyanos M, Masters T, Laske G, Ma Z (2014) LITHO1.0: an updated crust and lithospheric model of the Earth. *J Geophys Res Solid Earth* 119(3):2153–2173
- Pavlis N, Factor J, Holmes S (2007) Terrain-related gravimetric quantities computed for the next EGM. In: Dergisi H (ed) *Proceedings of the 1st international symposium of the international gravity field service*, vol 18, pp 318–323
- Pavlis N, Holmes S, Kenyon S, Factor J (2012) The development and evaluation of the earth gravitational model 2008 (EGM2008). *J Geophys Res*. doi:[10.1029/2011JB008916](https://doi.org/10.1029/2011JB008916)
- Pavlis NK, Rapp R (1990) The development of an isostatic gravitational model to degree 360 and its use in global gravity modelling. *Geophys J Int* 100:369–378
- Rapp R (1982) Degree variances of the Earth's potential, topography and its isostatic compensation. *Bull Géod* 65:84–94
- Rexer M, Hirt C (2015a) Spectral analysis of the Earth's topographic potential via 2D-DFT: a new data-based degree variance model to degree 90,000. *J Geodesy* 89(9):887–909. doi:[10.1007/s00190-015-0822-4](https://doi.org/10.1007/s00190-015-0822-4)
- Rexer M, Hirt C (2015b) Ultra-high-degree surface spherical harmonic analysis using the Gauss-Legendre and the Driscoll/Healy quadrature theorem and application to planetary topography models of Earth, Mars and Moon. *Surv Geophys* 36:803–830. doi:[10.1007/s10712-015-9345-z](https://doi.org/10.1007/s10712-015-9345-z)
- Rexer M, Hirt C (2016) Evaluation of intermediate TanDEM-X digital elevation data products over Tasmania using other digital elevation models and accurate heights from the Australian National Gravity Database. *Aust J Earth Sci*(accepted for publication)
- Rexer M, Hirt C, Claessens S, Braitenberg C (2015) Use of topography in the context of the GOCE satellite mission—some examples. In: Ouwehand L (ed) *Proceedings of '5th international GOCE user workshop', Paris, France, 25–28 November 2014*, ESA Communications, ESA SP-728

- Root B, Novák P, Dirkx M, Kaban M, van der Wal W, Vermeersen L (2016) On a spectral method for forward gravity field modelling. *J Geodyn* 97:22–30. doi:[10.1016/j.jog.2016.02.008](https://doi.org/10.1016/j.jog.2016.02.008)
- Rummel R, Rapp R, Sünkel H, Tscherning C (1988) Comparisons of global topographic/isostatic models to the Earth's observed gravity field. OSU report 388, Ohio State University
- Saleh J, Pavlis N (2002) The development and evaluation of the global digital terrain model DTM2002. In: 3rd meeting of the international gravity and geoid commission, Thessaloniki, Greece
- Sanso F, Sideris M (2013) Harmonic calculus and global gravity models. In: Geoid determination. Lecture notes in earth sciences, vol 110, Springer, Berlin
- Scheinert M, Ferraccioli F, Schwabe J, Bell R, Studinger M, Damaske D, Jokat W, Aleshkova N, Jordan T, Leitchenkov G, Blankenship DD, Damiani TM, Young D, Cochran JR, Richter TD (2016) New Antarctic gravity anomaly grid for enhanced geodetic and geophysical studies in Antarctica. *Geophys Res Lett* 43(2):600–610. doi:[10.1002/2015GL067439](https://doi.org/10.1002/2015GL067439)
- Sun W, Sjöberg L (2001) Convergence and optimal truncation of binominal expansions used in isostatic compensations and terrain corrections. *J Geodesy* 74:627–636
- Tenzer R, Abdalla A, Vajda P, Hamayun (2010) The spherical harmonic representation of the gravitational field quantities generated by the ice density contrast. *Contrib Geophys Geod* 40(3):207–223
- Tenzer R, Chen W, Tsoulis D, Bagherbandi M, Sjöberg L, Novák P, Jin S (2015) Analysis of the refined CRUST1.0 crustal model and its gravity field. *Surv Geophys* 36(1):139–165
- Tenzer R, Hirt C, Novák P, Pitoňák M, Šprlák M (2016) Contribution of mass density heterogeneities to the quasigeoid-to-geoid separation. *J Geodesy* 90(1):65–80. doi:[10.1007/s00190-015-0858-5](https://doi.org/10.1007/s00190-015-0858-5)
- Wieczorek M (2007) The gravity and topography of the terrestrial planets. *Treatise Geophys* 10:165–206. doi:[10.1016/B978-0-444-52748-6/00156-5](https://doi.org/10.1016/B978-0-444-52748-6/00156-5)
- Wieczorek M (2015) 10.05—Gravity and topography of the terrestrial planets. In: Schubert G (ed) *Treatise on geophysics*, 2nd edn. Elsevier, Oxford, pp 153–193. doi:[10.1016/B978-0-444-53802-4.00169-X](https://doi.org/10.1016/B978-0-444-53802-4.00169-X), <http://www.sciencedirect.com/science/article/pii/B978044453802400169X>

P.5 Publication V: A new degree-2190 (10 km resolution) gravity field model for Antarctica developed from GRACE, GOCE and Bedmap2 data

Reference:

Hirt C., Rexer M., Scheinert M., Pail R., Claessens S., Holmes S.: A new degree-2190 (10 km resolution) gravity field model for Antarctica developed from GRACE, GOCE and Bedmap2 data; Journal of Geodesy, Vol. 90, Nr. 2, pp 105-127, Springer Berlin Heidelberg, ISSN (Online) 0949-7714, DOI: 10.1007/s00190-015-0857-6, 2016.

Copyright

This work has been published in Journal of Geodesy and is available at <http://link.springer.com/>. Copyright has been transferred to Springer Berlin Heidelberg.

Short Summary

Continental Antarctica happens to be one of the few areas on Earth where gravitational variations are not resolved down to ~ 10 km scales by current high-resolution combined gravity field models, such as EGM2008 and EIGEN6C4. Antarctica lacks homogenous terrestrial gravity observations, thus the models are entirely based on satellite gravimetry. In this work latest satellite gravity data from GRACE (ITG-GRACE2010) and GOCE (TIM5) satellite as contained in the respective normal equations are combined with forward-modelled gravity originating from the rock-equivalent-topography given by the Antarctic Bedmap2 data set by means of regularization. The new combined potential model (SatGravRET2014) shows significantly higher agreement with the IAG Sub-commission 2.4f 'Gravity and Geoid in Antarctica' (AntGG) database compared to satellite-only models and thus demonstrates the value of Bedmap2 topographic data. The combination, however, is not optimal in global sense and different weighting schemes for the regularization are tested and discussed. SatGravRET2014 is thought of as reference for future gravity modelling efforts over Antarctica.

Declaration of own contribution

(MR: Moritz Rexer; CH: Christian Hirt; MS: Mirko Scheinert; RP: Roland Pail; SC: Sten Claessens; SH: Simon Holmes) CH had the idea to the study and drafted its design. MR helped developing the design of the study as far as the combination schemes is concerned. The other co-authors contributed little to the idea and design of the study. CH created most of the numerical results, e.g. the dV_ELL_RET2014 and the dV_ELL_ETOPO1 model and all comparisons with ground truth data. MR performed all the combinations in the study (GOCE/GRACE, SatGravRET2014/A/B/C, SatGravETOPO1/A/B/C) and designed the combination weights. MR calculated the relative contributions of data types in the combinations. MR calculated the degree variances and computed the localized degree variances over Antarctica. MS prepared and selected the ground truth gravity anomaly data over Antarctica. RP contributed with his knowledge to the combinations. SC contributed with his knowledge and software to the computation of the topographic potential models. The data analysis and interpretation was done by CH. CH drafted almost the entire text. MR drafted section 3.2.1 and 3.2.2. Further, MR created figures 6, 7, 8 and 14. All other figures and tables were created by CH.

The overall own contribution of MR for P-V is estimated at 15 %, which is the average (rounded) value of the percentage values estimated for the six criteria listed in the table below (Tab. P.5).

Criteria	Estimated own contribution
Computation and results	25 %
Ideas and study design	10 %
Analysis and interpretation	10 %
Text	12 %
Figures	33 %
Tables	0 %
Total	15.5 %

Tab. P.5 – Criteria and estimated contribution share of Moritz Rexer for *P-V*

Confirmation by the First-Author

I hereby confirm the correctness of the declaration of own contribution by Moritz Rexer for the publication:

Hirt C., Rexer M., Scheinert M., Pail R., Claessens S., Holmes S.: A new degree-2190 (10 km resolution) gravity field model for Antarctica developed from GRACE, GOCE and Bedmap2 data; Journal of Geodesy, Vol. 90, Nr. 2, pp 105-127, Springer Berlin Heidelberg, ISSN (Online) 0949-7714, DOI: [10.1007/s00190-015-0857-6](https://doi.org/10.1007/s00190-015-0857-6), 2016.

Christian Hirt

Institut für Astronomische und Physikalische Geodäsie, Technische Universität München, Germany.

Signature: Christian Hirt Date: 27/01/2017

P.6 Publication VI: Topographic gravity modelling for global Bouguer maps to degree 2,160: Validation of spectral and spatial domain forward modelling techniques at the 10 microgal-level

Reference:

Hirt C., Reußner E., Rexer M., Kuhn, M.: Topographic gravity modelling for global Bouguer maps to degree 2,160: Validation of spectral and spatial domain forward modelling techniques at the 10 microgal-level; Journal of Geophysical Research: Solid Earth, Vol. 121, DOI: 10.1002/2016JB013249, 2016.

Copyright

This work originally has been published in Journal of Geophysical Research: Solid Earth, available at <http://sites.agu.org/>, and is a publication of the American Geophysical Union (AGU). Copyright has been transferred to AGU.

Short Summary

The evaluation of Newton's integral in the space and in the spectral domain are both valid and commonly used domains for forward modelling of the topographic masses in geodesy and geophysics. For a perfect agreement between both modelling approaches it is necessary 1) to take into account multiple integer powers and multiples of the input band-width of the topographic function in spectral domain modelling and 2) to work with high spatial resolution in order to reduce discretisation errors in space domain modelling. For a degree-2160 (≈ 10 km) topography the spectral method requires 15 integer powers and modelling of short-scale gravity signals to ultra-high degree 21,600 (≈ 1 km) in order to reach an agreement at the microGal level with space domain modelling. Space domain modelling is found to be associated with a higher computational effort, however, the convergence behavior in spectral domain modelling indicates that convergence may not always be guaranteed at ultra-short scales.

Declaration of own contribution

(MR: Moritz Rexer; CH: Christian Hirt; ER: Elisabeth Reußner; MK: Michael Kuhn)

CH had the idea to the global validation study and designed most parts. ER contributed more than the other co-authors since she performed a local study in her master thesis. MR provided the software for the challenging spherical harmonic analysis which was parallelised using the LRZ-Linux Cluster resources and computed the surface spherical harmonic coefficients from the 11th to the 25th power of the RET topography to degree 21,600. ER computed the 1st to the 10th power of the RET topography, performed the forward modelling and synthesized on the topography. MK did the space domain forward modelling. CH did the joint analysis and created the outcomes of the study. CH did the data analysis and drafted all interpretations. MR and the other co-authors improved the interpretation in discussions with CH. MR created Fig 2 and 3. CH created the rest of the figures. CH created all tables and drafted most of the manuscript text with the exception of Sect. 3 and 4 where all co-authors made textual contributions.

The overall own contribution of MR for P-VI is estimated at 10 %, which is the average (rounded) value of the percentage values estimated for the six criteria listed in the table below (Tab. P.6).

Criteria	Estimated own contribution
Computation and results	15 %
Ideas and study design	5 %
Analysis and interpretation	10 %
Text	3.3 %
Figures	20 %
Tables	0 %
Total	8.9 %

Tab. P.6 – Criteria and estimated contribution share of Moritz Rexer for *P-VI*

Confirmation by the First-Author

I hereby confirm the correctness of the declaration of own contribution by Moritz Rexer for the publication:

Hirt C., Reußner E., Rexer M., Kuhn M.: Topographic gravity modelling for global Bouguer maps to degree 2,160: Validation of spectral and spatial domain forward modelling techniques at the 10 microgal-level; Journal of Geophysical Research: Solid Earth, Vol. 121, DOI: [10.1002/2016JB013249](https://doi.org/10.1002/2016JB013249), 2016.

Christian Hirt

Institut für Astronomische und Physikalische Geodäsie, Technische Universität München, Germany.

Signature: Christian Hirt Date: 27/01/2017